Improving Electrical Impedance Tomography of brain function with a novel servo-controlled electrode helmet

James Peter Avery

A dissertation submitted in partial fulfilment
of the requirements for the degree of
Doctor of Philosophy
of
University College London.

Department of Medical Physics & Biomedical Engineering
University College London

June 17, 2015

Declaration

I, James Peter Avery, confirm that the work presented in this thesis is my own. Where information has been derived from other sources, I confirm that this has been indicated in the thesis.

Signed:

Acknowledgements

Conducting PhD research over the past four years has allowed me to make a living through investigating problems I find interesting, for which I feel extremely privileged. I am profoundly grateful to the people who supported me during this work, without whom this thesis would not have been possible. First I would like to thank my supervisors Prof. David Holder and Dr. Ben Hanson for offering me the opportunity to work on such a stimulating project, this work is a testament to their patience, encouragement, and experience.

Good research is collaborative and I am indebted to all of my friends in the UCL EIT group for their assistance, without their contributions none of the work would have been possible. I am especially thankful to Dr. Kirill Aristovich, whose advice and support in nearly every aspect in the project was invaluable, particularly in helping with the Sisyphean task of 3D printer maintenance. I would like to thank Dr. Thomas Dowrick who developed the UCL EIT system used in this project, and Bishal Karki who dedicated many hours to helping me with the KHU EIT system. Throughout the project I utilised software written by Dr. Gustavo Sato dos Santos, Dr. Aristovich and Markus Jehl for calculation of the forward solution and image reconstruction. The work on the head tank with skull is particularly indebted to Tugba Doru who first demonstrated the methodology. Dr. Brett Packham was a great support to me on innumerable tasks, but the advice and perspective on my research were especially appreciated. I must also acknowledge all past and present members of the UCL EIT group, whose work laid the foundations for my own.

I would also like to thank Dr. Aristovich, Nir Goren and Dr. Santos for helping me maintain my sanity and sharing horror stories during the early days of becoming a father. Finally I am grateful to my partner Catherine Evans, and my parents and sister, for their support and unwavering confidence in my abilities. I would like to dedicate this work to my son, Isaac, whose arrival brought things into perspective, albeit a hazy sleep deprived one.

Abstract

Electrical Impedance Tomography (EIT) is a medical imaging technique which reconstructs the internal conductivity of an object from boundary measurements. EIT has the potential to provide a novel means of imaging in acute stroke, epilepsy or traumatic brain injury. Previous studies, whilst demonstrating the potential of the technique, have not been successful clinically. The work in this thesis aims to address fundamental limitations including measurement drift in electronic hardware, lack of an anatomically realistic tank phantom for rigorous testing, poor electrode-skin contact and mis-location of scalp electrodes. Chapter 1 provides an introduction of the principles of bioimpedance and EIT, as well as a review of previous clinical studies. Chapter 2 details the development of a novel anatomically realistic head phantom, simulating the human adult head with scalp electrodes, using a 3D printer and cylindrical holes to provide simulated conductivity. This replicated the varying spatial conductivity of the skull within 5 % of the true value. Two multifrequency EIT systems with parallel voltage recording were optimised for recording in the adult head with scalp electrodes, in chapter 3. Measurement drift was reduced by better case design and temperature control and data quality was improved with an updated interface to the current source and signal processing. The UCL ScouseTom system, performed best, with lower noise in all resistor and tank measurements, but the differences were masked during scalp recordings. Further, both systems produced similar results in the realistic adult head tank from chapter 2. Recent advances in EIT imaging coupled with the developments in chapters 2 and 3 provided opportunity to reassess the feasibility of monitoring epilepsy with EIT. Biologically representative perturbations was localised to within 8 mm in the head tank, with less than half the image error of previous studies. However, the key limitations of application time and measurement drift with scalp electrodes had yet to be addressed. Therefore the focus of the work in chapter 5 and chapter 6 was the design and testing of a novel self-adjusting electrode helmet. Skin-electrode impedance was continuously optimised by constant pressure, rotation and feedback control, and position sensors returned the co-ordinates of electrode tips. Finally, experiments with this helmet were undertaken to assess the feasibility of future clinical recordings.

Contents

1 Introduction and review 1
1.1 Brain Pathologies 2
1.1.1 Acute stroke 2
1.1.2 Traumatic Brain Injury 2
1.1.3 Epilepsy 3
1.2 Electrical Impedance Tomography 5
1.2.1 Bioimpedance 5
1.2.2 Instrumentation 6
1.2.3 Protocols and data acquisition 8
1.2.4 Imaging principle 10
1.2.5 Imaging modalities 11
1.2.6 Modelling errors in EIT 13
1.3 EIT of brain pathologies 16
1.3.1 Bioimpedance of stroke 16
1.3.2 Bioimpedance of intracranial bleeding 17
1.3.3 Bioimpedance of epilepsy 18
1.3.4 Data collection and electrode localisation 19
1.3.5 Summary of previous studies 20
1.4 Biomedical electrodes 20
1.4.1 Electrode - tissue interface and contact impedance 20
1.4.2 Measurement Drift 24
1.4.3 Electrodes and electrode placement 26
1.5 Rationale 30
1.5.1 Intended application 30
1.5.2 Helmet specification 31
1.6 Purpose 32
1.7 Statement of originality 34

2 Novel head tanks for EIT 37
2.1 Introduction 37
2.1.1 Skull conductivity 38
2.1.2 Head phantoms in EIT 41
2.1.3 Modelling conductivity 44
2.1.4 Reproducibility of tanks 45
2.1.5 Purpose 46
2.1.6 Experimental Design 46

2.2 Methods 47
  2.2.1 Segmentation to Solid Model 47
  2.2.2 Electrode Positioning 48
  2.2.3 Tank design 49
  2.2.4 Anatomically realistic skull design 50
  2.2.5 Construction 54
  2.2.6 Geometry testing 58
  2.2.7 Comparison to simulation 59
2.3 Results 60
  2.3.1 Geometry analysis 60
  2.3.2 Comparison to simulation 60
2.4 Discussion 65
  2.4.1 Geometry of phantoms 65
  2.4.2 Comparison to simulation 66
  2.4.3 Assessment of tanks 68
  2.4.4 Reproducibility and limitations of method 69
  2.4.5 Technical considerations 70
  2.4.6 Recommendations for Further Work 70

3 Comparison of two EIT systems **71**
3.1 Introduction 71
  3.1.1 EIT systems 72
  3.1.2 Purpose 76
  3.1.3 Experimental Design 77
3.2 Methods 78
  3.2.1 KHU Modifications 78
  3.2.2 ScouseTom Modifications 86
  3.2.3 Resistor Phantom Measurements 91
  3.2.4 Tank Measurements 95
  3.2.5 Scalp Recordings 98
  3.2.6 Test object complexity 99
3.3 Results 99
  3.3.1 Resistor Phantom Measurements 99
  3.3.2 Head Tank 104
  3.3.3 Scalp Recordings 111
  3.3.4 Test Object Complexity 112
3.4 Discussion 115
  3.4.1 System Comparison 115
  3.4.2 Technical considerations 117
  3.4.3 Implications for future experiments 118
  3.4.4 Recommendations for future work 119

4 Feasibility of imaging epileptic seizures with EIT **121**
4.1 Introduction 121
  4.1.1 Previous tank experiments 121
  4.1.2 Neonatal Tank Studies 123
  4.1.3 Purpose 123

4.1.4 Experimental Design 124
4.2 Methods 125
4.2.1 Tank Study 125
4.2.2 Simulation Study 128
4.3 Results 129
4.3.1 Adult Head Tank 129
4.3.2 Neonatal Head Tank 132
4.3.3 Localisation Accuracy 137
4.3.4 Signal Size 140
4.4 Discussion 142
4.4.1 Summary of results 142
4.4.2 Tank study 143
4.4.3 Simulation study 143
4.4.4 Assessment of regularisation algorithms 144
4.4.5 Study limitations 145
4.4.6 Recommendations for future work 146

5 Characterisation of abrasion 149
5.1 Introduction 149
5.1.1 Purpose 150
5.1.2 Experimental Design 151
5.2 Methods 152
5.2.1 Test object: skin analogue 152
5.2.2 Overview of prototype and test rig 154
5.2.3 Force control 154
5.2.4 Rotary Actuation 160
5.2.5 Impedance Measurement 163
5.2.6 Electrode 165
5.2.7 Methods validation 167
5.2.8 Test protocol 173
5.3 Results 176
5.3.1 Characterisation of manual abrasion 176
5.3.2 Contact impedance as a function of applied force 177
5.3.3 Impedance during abrasion over a range of applied forces 177
5.3.4 Impedance during abrasion for minimum and maximum applied torque 180
5.3.5 Proof of principle on human skin 182
5.4 Discussion 184
5.4.1 Summary of results 184
5.4.2 Prototype performance 186
5.4.3 Technical considerations 187
5.4.4 Future work: implications for future designs 189
5.5 Conclusion 189

6 Servo electrode helmet for EIT 191
6.1 Introduction 191
6.1.1 Background 191
6.1.2 Purpose 194
6.1.3 Experimental Design 194
6.2 Methods 194
6.2.1 Electrode Unit 194
6.2.2 Controller 199
6.2.3 32 Channel Helmet 205
6.2.4 Experimental Protocol 208
6.3 Results 209
6.3.1 Single Unit 209
6.3.2 Four channel system 210
6.3.3 32 Channel Helmet 210
6.4 Discussion 212
6.4.1 Summary of results 212
6.4.2 Assessment of helmet design 213
6.4.3 Technical Considerations 214

7 Discussion and future work 217
7.1 Summary of studies 217
7.2 Head tanks 217
7.3 EIT systems 218
7.4 Time difference imaging in the head 218
7.5 Electrode helmet 218
7.6 Future work 219

Bibliography 221

List of Figures

1.1 Equivalent circuit of a cell **(a)**, extracellular resistance R_e in parallel with the intracellular resistance R_i and the capacitance of the cell membrane C_m,**(b)** Cole-Cole plot of this circuit 6

1.2 Equivalent circuit of measurement in EIT adapted from Boone and Holder [41]. Is: current source, C_{out}: output capacitance, R_{out}: output resistance, C_{ed} (C_{er}): electrode capacitance on driving (receiver) electrode, R_{ed} (R_{er}): electrode resistance on driving (receiver) electrode, R_1-R_4: load resistance under the measurement, R_i: input resistance, C_i: input capacitance, and V_{cm}: common-mode voltage 7

1.3 **(a)** Improved Howland Circuit iHCP from Franco [47], **(b)** equivalent model of current source 7

1.4 Two EIT systems used in the UCL group,**(a)** the serial UCL Mk2.5 designed by McEwan, Romsauerova, Yerworth, *et al.* [48] and **(b)** the fully parallel KHU Mk 2 by Oh, Wi, Kim, *et al.* [49] 8

1.5 EIT electrode positions, **(a)** EEG 31 protocol, 27 electrodes placed according to the extended EEG 10-20 psotions from Tidswell, Gibson, Bayford, *et al.* [53], **(b)** Spiral16, a subset of 16 electrodes chosen by Fabrizi, McEwan, Oh, *et al.* [54] 9

1.6 Finite element models in EIT, fig. 1.6a mesh from CT and MRI segmentation of the head by Jehl, Dedner, Betcke, *et al.* [63], fig. 1.6b rat brain mesh by Aristovich, Santos, Packham, *et al.* [61] 13

1.7 Existing tanks used in experiments in the UCL group, **(a)** a 2D cylindrical tank and **(b)** a head shaped tank created by Tidswell, Gibson, Bayford, *et al.* [74] . 14

1.8 Comparison of simulated and measured voltages in cylindrical tank 14

1.9 Artefacts due to modelling errors during experiments by Malone, Sato Dos Santos, Holder, *et al.* [71] in a 2D cylindrical tank 15

1.10 Comparison of simulated and measured voltages in UCL head tank [74] 16

1.11 Change in conductivity over frequency of normal brain tissue, ischaemic brain tissue and blood, adapted from [82] 17

1.12 Example of data collection for stroke EIT, photogrammetry markers are visible above elastic cap 19

1.13 Simple equivalent circuit model of electrode-gel-skin interface from [95] 21

1.14 Equivalent electrical circuit of the epidermis from [102] 22

1.15 Frequency characteristics of skin impedance from from [102] represented as values for the equivalent circuit in figure 1.14. Number of tape strippings given by numbers in parenthesis, Roman numerals denote corresponding data in R_p and C_p 22

1.16 Effect of abrasion of electrode site on the resultant contact impedance. Impedance values taken from [102] for zero and 9 strippings 23
1.17 Simulated reconstruction of Extradural Haematoma, **pert** is ideal reconstruction, **No N** is the reconstruction without any noise, the remaining columns correspond to the images with realistic measurement drift added 25
1.18 Example of traditional cup and paste EEG electrodes 27
1.19 Self abrading electrode from [113] 27
1.20 Quinton Quik-prep system for ECG electrodes [114] 28
1.21 Principle of dry microsprike electrode 29
1.22 Example EEG headnets. Clockwise from top left: Easycap, EEG electrodes, geodesic headnet and Physiometrix headcap from [78] 29

2.1 various skull conductivities 38
2.2 Skull samples demonstrating tri-layered structure, with two outer "compact" bone layers and a inner spongey layer of diploe, from Tang, You, Cheng, *et al.* [128] 39
2.3 Scatter plots demonstrating the correlation of skull resistivity with **(a)** thickness $r = -0.596$ and **(b)** percentage of diploe $r = -0.917$ from Tang, You, Cheng, *et al.* [128] 39
2.4 3D head phantoms for EIT, **(a)** spherical tank from Liston, Bayford, and Holder [127], **(b)** four shell agar tank from Sperandio, Guermandi, and Guerrieri [141], **(c)** EEG phantom from Collier, Kynor, Bieszczad, *et al.* [143] and **(d)** anatomically realistic phantom from Li, Tang, Dai, *et al.* [144] 42
2.5 Neonatal head phantoms. **(a)** spherical tank by Tang, Oh, and Sadleir [140], **(b)** smoothed head shaped tank by Tang and Sadleir [36] 44
2.6 Simulation of current flow through surface mimicking skull resistivity, from Doru, Avery, Aristovich, *et al.* [77] 45
2.7 Workflow to create solid models from an MRI segmentation for the design of the adult tank 48
2.8 Workflow to create solid models from a CT segmentation for the design of the neonatal tank 48
2.9 Design of tank models. **(a)** the scalp model is duplicated and scaled by 10%, **(b)** the inner scalp surface is removed and the shell split below in inion-nasion line, **(c)** the model is trimmed and the walls vertically extended 1cm, **(d)** models of the electrodes with clearance are positioned according to 2.2.2, **(e)**, the clearance electrodes are removed from the tank volume, **(f)** Supports add and model is finalised 50
2.10 Completed tank models for **(a)** adult head and **(b)** neonatal head 51
2.11 Design of skull models. **(a)** the skull model is split below in inion-nasion line along the same plane as fig. 2.9, **(b)** the model is trimmed and the walls vertically extended 1cm to match the height of the tank walls, **(c)** a support base is added which is used to position the skull precisely in the tank, **(d)** cylinders are created centred around the points defined in 2.2.4 normal to the surface, **(e)**, the cylinders are removed from the tank volume giving the final skull model 51
2.12 Conductivity distribution of adult skull 52

2.13 Calculation of hole location and size for the adult skull, **(a)** equispatial points, **(b)** cylinders aligned normal to model surface at each point 53
2.14 Comparison of σ values for target and adjusted adult skull 53
2.15 Skull conductivities from the literature in comparison with target and adjusted adult skull conductivities 54
2.16 Completed skull models for **(a)** adult head and **(b)** neonatal head 55
2.17 The 3D printer used to create the tanks, The Makerbot Replicator 2 from Makerbot Ind. 56
2.18 Completed phantoms for **(a)** adult head and **(b)** neonatal head 57
2.19 Mesh of adult tank produced by 3D scanning 59
2.20 Deviation analysis of head shaped tank 60
2.21 Comparison of voltages in adult head tank with optimal protocol 61
2.22 Error Across injections in adult head tank with optimal protocol $R = 0.9985$ . . 61
2.23 Comparison of simulated and measured voltages in neonatal head tank $R = 0.9992$ 62
2.24 Error in measured voltages across injections in neonatal head tank 62
2.25 Comparison of voltages in adult head tank with skull with optimal protocol $R = 0.9985$ 63
2.26 Error Across injections in adult head tank and skull with optimal protocol . . . 63
2.27 Comparison of simulated and measured voltages in neonate head tank including skull phantom $R = 0.9972$ 64
2.28 Error in measured voltages across injections in neonate head tank including skull phantom 64
2.29 Percentage errors in measured voltages 65

3.1 Drift across an hour recording on the head with the UCH mk2.5, as percentage of baseline mean plus standard deviation 72
3.2 Internal view of 16 channel KHU Mk 2 system, from which the 32 channel KHU Mk 2.5 system used in this study is descended, from Oh, Wi, Kim, *et al.* [49] . 72
3.3 Function blocks of the KHU Impedance Measurement Module (IMM), from Oh, Wi, Kim, *et al.* [49] 73
3.4 Commercial components of the ScouseTo, EIT system, **(a)** BioSemi ActiveTwo EEG Amplifier and **(b)** Keithley 6221 Current Source 74
3.5 Programming ST switch network. Source and sink channels set by pulses on +chn and -chn pins, injections pairs switched when sync pin set to high 76
3.6 Resistor set up for preliminary testing of the 32 channel KHU Mk 2.5 EIT system 79
3.7 Noise in voltages recorded on 1.1 kΩ resistor during preliminary testing of the 32 channel KHU Mk 2.5 EIT system 79
3.8 Comparison of the amplitude of the sine wave across 1.1 kΩ resistors, top: as calculated from the rms of voltage collected with a NI USB DAQ, bottom: the output from the KHU system 80
3.9 Updated regulator board for 32 Channel KHU Mk. 2.5, **(a)** circuit diagram . . 81
3.10 Improved power supply design for KHU 32 channel system 81
3.11 PSD of the voltage from KHU +5V regulator for original and new design, **(a)** with system idle **(b)** with system in scan mode 82
3.12 PSD of the voltage from KHU 3.3 V regulator for original and new design with system in scan mode 83

3.13 **(a)** Improved case for KHU Mk 2.5 system, **(b)** section view demonstrating fan alignment 84
3.14 Comparison of signal to noise ratio of injected current for the KHU mk2.5 with increasing current level setting 85
3.15 Switch Network Controller for ST EIT system: Switch network PCB and Arduino Uno with shield in 3D printed housing 87
3.16 Overview of ScouseTom EIT system. Current source and switch network controlled via Serial communication and Matlab interface. Switching indicators sent to BioSemi Digital Input channels 88
3.17 Ringing artefact in ScouseTom demodulation 90
3.18 Effect of increasing truncation samples for 3rd and 5th order IIR filters and increasing N 90
3.19 Four terminal measurement set-up. Injecting electrodes connected to terminals 1 and 2, measurement electrodes connected to terminals 3 and 4 91
3.20 Circuit diagram of SwissTom Resistor Phantom [165] 92
3.21 Example four terminal recording with both systems. KHU begins to overheat after 220 repeats 93
3.22 Section view of conductivities in hexahedral mesh of head tank. **(a)** baseline conductivity of saline and skull, **(b)** "ideal" perturbation in posterior location 96
3.23 Three locations of perturbations used in tank study, based on positions from Malone, Jehl, Arridge, *et al.* [59] 96
3.24 Scalp electrode locations, based on the `spiral_16` protocol by Fabrizi, McEwan, Oh, *et al.* [58] 99
3.25 Noise in four-terminal measurements across expected load range, comparison of ST and KHU systems 100
3.26 Variation across current of transimpedance $\frac{V}{A}$ recorded on SwissTom resistor phantom with the ST and KHU EIT systems. Top: average transimpedance across all channels, bottom : standard deviation transimpedance across channels101
3.27 PSD of ScouseTom and KHU EIT systems with 1kHz and 1.125 kHz current injection respectively 101
3.28 Variations of the voltages measured on the SwissTom resistor phantom across frequency with the ST and KHU EIT system 102
3.29 Noise in hour long recording on resistor phantom 103
3.30 Mean and standard deviation of drift across channels over one hour recording on SwissTom phantom with ST and KHU systems 103
3.31 Inter channel variations in one hour long recording on four separate protocol combinations, expressed as relative standard deviation. R_{load} = 4.48 for combination 1 and 2, R_{load} = 15.8 for combinations 3 and 4 104
3.32 Comparison of baseline voltages measured in adult head tank with ST and KHU systems to respective simulations 105
3.33 Percentage errors of measurements from ST and KHU systems in comparison to simulation 105
3.34 Standard deviation of recordings in adult head phantom 106

3.35 Differences in sensitivity with ST and KHU measurement protocol, positive changes correspond to greater sensitivity with ST, negative to greater sensitivity with KHU. **(a)** full range highlighting skull sensitivity with ST, **(b)** narrower range displaying differences inside skull and **(c)** expressed as a percentage change 106
3.36 Simulated reconstructed perturbations for corresponding measurement protocol in comparison to ideal perturbation 107
3.37 Section views of image of simulated reconstruction with **posterior** perturbation for ST and KHU measurement protocols 108
3.38 Section views of image of simulated reconstruction with **central** perturbation for ST and KHU measurement protocols 108
3.39 Section views of image of simulated reconstruction with **lateral** perturbation for ST and KHU measurement protocols 109
3.40 Image error metrics for simulated reconstructions compared to “ideal” perturbations, for **(a)** ScouseTom Protocol and **(b)** KHU protocol 110
3.41 Reconstructed perturbations in adult tank with both ST and KHU systems, in comparison to ideal reconstructions 110
3.42 Section views of image of experimental reconstructions with **posterior** perturbation for ST and KHU measurement protocols 111
3.43 Section views of image of experimental reconstruction with **central** perturbation for ST and KHU measurement protocols 112
3.44 Section views of image of experimental reconstruction with **lateral** perturbation for ST and KHU measurement protocols 113
3.45 Image error metrics for experiments compared to simulated perturbations for **(a)** ScouseTom Protocol and **(b)** KHU protocol 113
3.46 Standard deviation of recordings in adult head phantom 114
3.47 Proportional noise as % of mean across all experiments, resistor phantom, saline tank and scalp 114

4.1 Lateral perturbation reconstructions in anatomically realistic head tanks. True 3D reconstructions, **(a)** 30 % contrast Fabrizi, McEwan, Oh, *et al.* [58], **(b)** 90 % contrast without skull Packham, Koo, Romsauerova, *et al.* [68] and **(c)** 90 % contrast with skull. 2D reconstructions, **(d)** 176 % contrast Li, Tang, Dai, *et al.* [144] and **(e)** 2000 % contrast Dai, Li, Hu, *et al.* [16] 122
4.2 Time difference image of 50 % contrast representing intraventricular haemorrhage in neonatal head tank without skull Tang and Sadleir [36] 123
4.3 Perturbation locations used in tank study, **(a)** adult tank based on positions from Malone, Jehl, Arridge, *et al.* [59] and **(b)** neonatal tank with two additional locations 125
4.4 Perturbations in adult tank, reconstructed with both zeroth and first order Tikhonov, in comparison to ideal reconstructions 130
4.5 Section views of image of experimental reconstructions with **posterior** perturbation with both zeroth and first order Tikhonov regularisation 131
4.6 Section views of image of experimental reconstructions with **central** perturbation with both zeroth and first order Tikhonov regularisation 131

4.7 Section views of image of experimental reconstructions with **lateral** perturbation with both zeroth and first order Tikhonov regularisation 132
4.8 Image quantification results in adult tank, **(a)** zeroth order and **(b)** first order Tikhonov regularisation 133
4.9 Perturbations in neontal tank, reconstructed with both zeroth and first order Tikhonov, in comparison to ideal reconstructions 134
4.10 Section views of image of experimental reconstructions with **anterior** perturbation with both zeroth and first order Tikhonov regularisation 135
4.11 Section views of image of experimental reconstructions with **posterior** perturbation with both zeroth and first order Tikhonov regularisation 135
4.12 Section views of image of experimental reconstructions with **lateral** perturbation with both zeroth and first order Tikhonov regularisation 136
4.13 Section views of image of experimental reconstructions with **central** perturbation with both zeroth and first order Tikhonov regularisation 136
4.14 Section views of image of experimental reconstructions with **caudal** perturbation with both zeroth and first order Tikhonov regularisation 137
4.15 Image quantification results in neonatal tank, **(a)** zeroth order and **(b)** first order Tikhonov regularisation 138
4.16 Localisation error (mean±std) of the simulated perturbations in **(a)** adult and **(b)** neonatal head, with and without noise present, for both regularisations, expressed as norm of vector distance in mm, and as a percentage of mesh dimensions 138
4.17 Spatial distribution of localisation error in mm in adult head for both zeroth and first order Tikhonov regularisations, for simulated perturbations with and without realistic noise added 139
4.18 Spatial distribution of localisation error in mm in neonatal head for both zeroth and first order Tikhonov regularisations, for simulated perturbations with and without realistic noise added 140
4.19 Median voltage change μV for 10 % contrast perturbations across the adult head, **(a)** sagittal section and **(b)** axial section 140
4.20 Percentage of measurable voltages for a given minimum signal size in μV across all perturbations p_{ijk} in adult head, expressed as percentiles of the perturbation distribution 141
4.21 Median voltage change μV for 10 % contrast perturbations across the neonatal head, **(a)** sagittal section and **(b)** axial section 141
4.22 Percentage of measurable voltages for a given minimum signal size in μV across all perturbations p_{ijk} in neonatal head, expressed as percentiles of the perturbation distribution 142

5.1 Diagram of experimental set up to determine expected load impedances 152
5.2 Impedance of orange peel sections before and after abrasion 153
5.3 Overview of test rig, highlighting force control, rotary actuation and impedance measurement components 154
5.4 Schematic of force control components in prototype 155
5.5 Free body diagram of force control system, with generic test object 157

5.6 Simulation of transmissibility for MSD model showing the change with increasing damping ratio ζ. Human skin has $\zeta \approx 0.8$ 158
5.7 Limit cycling example 159
5.8 Block Diagram of stepper feedback control, with dead band 160
5.9 Limit cycling example 160
5.10 Schematic of rotary actuation components 161
5.11 Schematic of rotary actuation components, front view highlighting the transmission from DC motor to spindle 161
5.12 Quadrature endcoder location, mounting hidden 162
5.13 Phototransistor output for different codewheel track numbers. 10 and 20 track codewheels reliably decreased irradiance below threshold 163
5.14 Block diagram of impedance measurement circuit 164
5.15 Schematic of electrode design 165
5.16 Comparison of electrode impedances of brass electrode and silver reference electrode 166
5.17 Schematic of electrical connection of reference and actuated electrode, slip ring highlighted 166
5.18 Power spectral density of noise from spindle and slip ring 167
5.19 Error in resistance measurements with impedance measurement module (R_{IMM}) and Hewlett Packard 4284A Impedance Analyser (R_{HP}) 168
5.20 Impedance of RC circuit, comparison of simulated and measured values 168
5.21 Resistance of RC circuit, comparison of simulated and measured values 169
5.22 Reactance of RC circuit, comparison of simulated and measured values 169
5.23 Averaged step response of orange peel 170
5.24 Comparison of orange skin impedance before and after abrasion, and impedance of human skin with 0,9, and 15 strippings from [102]. Reduced frequency range in orange peel results due to limitations in measurement system 171
5.25 Speed profile of electrode rotation 172
5.26 Experimental setup to determine stall torque T_{stall} of motor from maximum force F_{max} 172
5.27 Stall torque (maximum torque available) profile of electrode rotation as a function of duty cycle 173
5.28 Experimental setup to measure force applied during manual abrasion, and resultant impedance 174
5.29 Experimental setup to measure impedance decrease during abrasion of the human 175
5.30 Force profile during manual abrasion of test sample with abrasive paste and cotton bud 176
5.31 Impedance spectra of orange skin test samples before and after manual abrasion 176
5.32 Impedance as a function of force applied normal to surface 177
5.33 Impedance decrease with respect to the number of rotations of the electrode, for a range of incident forces 178
5.34 Impedance decrease with respect to abrasion time, for a range of incident forces 178
5.35 Impedance decrease per sixth of a rotation, for a range of incident forces . . . 179
5.36 Impedance spectra of orange skin test samples before and after 20 seconds automated abrasion with 7.5 N applied force and 90 % duty cycle 179

5.37 Force control results: Measured applied force during abrasion, for set forces of 2,3,5,7.5 and 10 N 180
5.38 Comparison of impedance decrease for 5 N applied force with respect to number of rotations for both minimum and maximum applied torque 180
5.39 Comparison of impedance decrease for 5 N applied force with respect abrasion time for both minimum and maximum applied torque 181
5.40 Minimum torque necessary to rotate electrode across range of applied forces . 181
5.41 Impedance decrease on human forearm with respect to the number of rotations of the electrode, with and without abrasive conductive paste. Note motion artefact at 1.5 rotations for without paste 182
5.42 Impedance spectra measured on human forearm: before and after abrasion without paste (dashed); before and after abrasion with paste, and with the addition of paste only (solid) 183
5.43 Comparisons of corrected impedance spectra after abrasion was complete for both wet and dry abrasion in comparison with the impedance after 9 and 15 strips from [102] 183

6.1 Comparison of mean and standard deviation of head measurements in anthropometric surveys 193
6.2 Miniaturised servo electrode unit. **(a)**, overview of components, **(b)** concentric rotary actuation via servo motor with pain bearing and plain bearing, **(c)** feedback of electrode position X_E through measurement of displacement X_P, **(d)** units placed in rigid helmet at known positions, **(e)** isometric view of complete unit 195
6.3 Off the shelf components adapted for electrode unit, **(a)** Tower Pro MG90s Servo Motor, **(b)** BEI 9605 spring return linear position sensor 196
6.4 Characterisation of spring return linear sensor. Stepper motor advances to compress spring onto load cell. Measurements of displacement obtained from laser displacement sensor 197
6.5 Characterisation of spring potentiometer, **(a)** voltage across compression mean±std, **(b)**, force as function of distance mean±std 198
6.6 Abrasive electrode patterns 198
6.7 Wiring path to electrode 199
6.8 Overview of helmet controller. Labview software controlling Arduino Due through wireless serial communication. Ardruino controls impedance measurement, servo rotation and electrode position measurements 200
6.9 Control of 32 Servos using PCA9685 breakout boards 201
6.10 Adafruit 815 servo controller in 3D printed casing 201
6.11 Control of 32 Servos using PCA9685 breakout boards 202
6.12 Impedance measurement circuit for helmet controller 202
6.13 Standard deviation of impedance measurement for frequency of 20 and 100 Hz for increasing number of periods averaged 203
6.14 Validation of impedance measurement circuit based on Arduino Due. **(a)**, mean±std across expected measurement range compared to ideal, **(b)** percentage error 204
6.15 Housing for four electrode units for testing on the shin 204

6.16 Visualisation of the positions of the electrodes in the helmet on the reference model . . . 205
6.17 Design of electrode bearing helmet **(a)** the scalp model is scaled to match the nominal head dimensions section 6.1.1 and model trimmed below in inion-nasion line, **(b)** helmet frame constructed from 10 mm offset of nominal scalp surface, **(c)** electrode blocks are added to model and spacers then removed to create housings for each electrode unit aligned to the points in fig. 6.16, **(d)** electrode units added to complete model . . . 206
6.18 Comparison of mean and standard deviation of head measurements in anthropometric surveys . . . 207
6.19 Final helmet model inclusive of electrode assemblies . . . 208
6.20 Abrasion with single miniature unit on orange skin test rig, for both pyramidal electrode as in chapter 5, and smoothed electrode . . . 209
6.21 Abrasion with four channel system with application of abrasive Nuprep paste and with EleFix EEG gel and Nuprep paste . . . 210
6.22 Long term recording with four channel system, with two actuated electrodes and two conventional EEG electrodes, application of abrasive Nuprep paste and with EleFix EEG gel and Nuprep paste only . . . 211
6.23 Abrasion with 32 channel helmet on the scalp . . . 211
6.24 Minimum impedance with abrasion across range of compressions . . . 212

List of Tables

1.1 Summary of approximate head tissue conductivities below 1 MHz from Horesh [82] . . . 17

2.1 Conductivities of human skull from Tang, You, Cheng, *et al.* [128] measured at 1 kHz . . . 52

3.1 BioSemi ActiveTwo, EEG system specifications . . . 75
3.2 Keithley 6221 AC current source, system specifications . . . 75
3.3 Comparison of EIT systems used in this study . . . 76
3.4 SNR of injected current on the SwissTom resistor phantom as measured with the BioSemi EEG system . . . 102

5.1 Orange Peel Impedances . . . 153
5.2 Load Cell Errors . . . 156
5.3 RMS error of force control system during abrasion . . . 177

Chapter 1

Introduction and review

Electrical Impedance Tomography is a tomographic medical imaging technique which produces the internal electrical impedance of a subject from multiple impedance measurements using surface electrodes. Images are reconstructed by modelling electric fields within a Finite Element Model (FEM) of the subject and applying inverse algorithms. EIT has been proposed for a multitude of imaging techniques in the brain, including acute stroke and epilepsy. Electrodes must be placed onto the scalp before data acquisition, and the quality of the contact of the electrodes with the skin is an important factor in determining the signal to noise ratio of the EIT measurements. Conventional EEG cup electrodes, approximately 1 cm across, are commonly used in EIT studies on the head. The electrode site is prepared by an expert technician through removal of the top layer < 1 mm of skin, through abrasion with an applicator and abrasive paste. To enable imaging of acute stroke in an ambulance or other acute setting, electrodes must be applied rapidly by unskilled personnel, the conventional methods are time consuming and labour intensive and are thus not practical. The purpose of this project was to design an electrode bearing helmet which automatically applies electrodes onto the scalp of the patient, achieving and maintaining a low contact impedance in a safe manner. Methodological developments in other areas of EIT were also undertaken as part of this work, in both the design of realistic head tanks, and modification of newly developed hardware for use in scalp recordings. Whilst the primary purpose of the helmet is to rapidly apply electrodes for imaging acute stroke, it also enabled control of the electrode contact throughout recordings, which is beneficial for a number of other EIT applications. Epilepsy monitoring with EIT was revaluated in light of the developments in imaging and hardware within the UCL group and this thesis, and the suitability of the helmet design assessed with respect to this application alongside the primary purpose of imaging acute stroke.

1.1 Brain Pathologies

1.1.1 Acute stroke

Stroke is a major health problem, it is a leading cause of morbidity and disability in industrialised nations [1] and the Department of Health estimates the annual direct cost to the NHS as £2.8 billion [2]. Stroke is caused by a lack of oxygen to part of the brain, and has two main causes: ischaemic, where bloody supply is interrupted due to a blood clot, and haemorrhagic due to a vascular rupture. Ischaemic strokes can be treated through the use of thrombolytic (or clot-dissolving) agents, but these are deleterious, or even potentially fatal, to patients suffering from haemorrhagic stroke. It is necessary therefore to be certain in the differentiation between the two types of stroke, which cannot be achieved without neuroimaging. The earlier the treatment through thrombolytics the better the outcome with the benefits limited to the first 3 to 6 hours after onset [3]. Therefore it is essential that neuroimaging and hence treatment is performed as soon as possible. However, studies have shown that transport to CT or MRI scanner and completion and reporting of the scan take at least an hour [4], and that the majority of stroke patients are arriving at emergency departments after 3 hours [5]. In the UK the NHS uses the time taken for “FAST positive” patients (*i.e.* those with a suspected stroke) to reach a hyperacute stroke centre as a quality indicator **DeptartmentofHealth2012** The most recent statistics for October 2011 show that 68.4 % of FAST positive patients arrived at the stroke centre within one hour of the call to the emergency services. The National Institute for Health and Clinical Excellence (NICE) clinical guidelines stipulates that brain imaging should be performed “immediately (within the hour)” for patients with a suspected stroke [6]. Therefore even if patients arrive at the unit within the one hour guideline, they are unlikely to have a CT or MRI taken within the treatment guidelines, which are also an hour. It is clear therefore that faster imaging of acute stroke is vital to prevent patients being denied essential treatment during this timeframe. Electrical Impedance Tomography has been proposed as a solution to enable early neuroimaging in ambulances or diagnostic centres without other scanning systems [7].

1.1.2 Traumatic Brain Injury

Traumatic brain injury (TBI) is defined as an insult or trauma to the brain from an external force [8]. TBI is a major health issue and is one of the leading causes of death and long term disability, with 1000 patients per 100,000 attend A & E with TBI, and 10 in 100,000 fatalities [8], [9]. TBI is the most common cause of death and disability in people aged 1-40 in the UK. The majority of fatal outcomes are in moderate or severe groups of the Glasgow Coma Scale (GCS) [10] which comprise of only 5 % of TBI patients [11]. Thus clinicians need to identify a relatively small number of patients who will go onto develop serious acute intracranial problems. The majority of brain injuries could be detected in the first CT scan performed at emergency units with an established screening protocol to determine the urgency for each patient [11]. However, commonly there are secondary injuries with a delayed onset, such as Extradural Haematoma (EDH), subdural haematoma (SDH), and intracerebral Haemorrhage (ICH) which are not visible in the initial scans [11], [12]. In some of these cases, patients may have a normal initial CT scan, a high rating on the GCS indicating no alarming clinical signs, yet deteriorate and present significant findings in a subsequent CT scan. This delayed injury can be severe, even resulting in death. These delayed onsets are most likely to occur in the first two to three days after the primary injury, but have been known to occur weeks afterwards [12]. Monitoring these delayed onset brain injuries has been an application of EIT proposed early on the in the development of the technique [13]. Recently, studies by Manwaring, Moodie, Hartov, *et al.* [14] and Dai, Wang, Xu, *et al.* [15] have shown reproducible images of injected arterial blood in swine models with scalp electrodes. The most recent developments have shown in vivo images of injected irrigating fluid (5% dextrose in water) used in treatment of SDH [16]. Whilst this represents a step towards detection of intracranial bleeding, the dextrose mixture was injected in a known position, and has a conductivity contrast ten times greater than that expected through bleeding.

1.1.3 Epilepsy

Epilepsy is a neurological condition in which synchronised neuronal firing causes unpredictable recurring seizures. It is the most common neurological disorder, affecting approximately 50 million people globally [17], and accounts for 0.5% of the global burden of disease [18]. There are over 30 different types of epilepsy, and their categorisation and characterisation is still a cause for debate [19], [20]. Generally they can be categorised into *focal* (or *partial*) seizures, which are generated in and affect only a single area of the brain ranging from part of a lobe up to an entire hemisphere, and *generalised* seizures which occur in both hemispheres of the brain [19]. Generalised seizures originate in networks which are distributed bilaterally *i.e.* both hemispheres, and have onsets which can appear localised within in a single seizure, but are not consistently localised or lateralised between seizures. Focal seizures however, are constrained to networks within a single hemisphere and the ictal (seizure) onset is consistent between seizures, and are the most common type of seizure [21]. Generalised and focal seizures can occur both in superficial cortical structures of the brain, as well as deeper subcortical areas. Anti-epileptic drugs (AEDs) are the initial treatment for epilepsy patients, however they are not effective in 20-30 % of chronic cases [22], with approximately 60 % of patients with partial epilepsy entering remission with AED alone [23]. Patients who are not responding to AEDs, can potentially be treated through resective surgery, wherein the epileptogenic zone, the area of cortex generating the seizures, is removed or disconnected [24]. The outcomes of these patients undergoing resective surgery is generally good, with 30 to 85 % remaining seizure free. However, surgery is only considered if the focus is clearly identified and subsequently deemed resectable if it is located in a accessible area of the brain and removal will not significantly impair brain function [25]. Therefore, there is a clear clinical need for accurate foci localisation in epilepsy patients. This is routinely localised with prolonged video-EEG monitoring, which provides EEG recordings and seizure semiology for generating a hypothesis as to the seizure onset zone. Often, for improved localisation, patients undergo intracranial EEG recordings (ECoG) with electrodes placed on the surface of the cortex where the epileptogenic focus is suspected to be, based on the scalp EEG [25], [26]. Although free of the attenuation and distortions of the skull and scalp, these ECoG recordings still have drawbacks relating to the fact that it is a *summated* potential recorded on the surface [27]. As such, activity may not have an EEG correlate if the source is located deep in the brain, or is orientated tangentially to the scalp, or cancelled out by an opposing source in the sulci. Depth electrodes can be placed to overcome these issues but as they damage brain tissue, are necessarily limited in their number and spacing [26]. Improved localisation of epileptic foci has been proposed as a potential application of EIT [28], [29], as an adjunct modality to conventional EEG or ECoG recordings [30].

Neonatal Epilepsy

Seizures in full term infants have been shown to occur in 0.5-3 per live 1000 births, and up to 13% of very low birth weight infants [31]. Swift intervention is important as continued seizures are linked with permanent cerebral damage and long-term neuro-developmental delay [32], [33]. The majority of neonatal seizures are acute and arise as symptoms of another brain injury, the most common of which are Hypoxic-ischaemic encephalopathy and intracranial haemorrhage [34]. A major challenge in the diagnosis of epilepsy in infants is electroclinical dissociation, *i.e.* there may be seizures visible in EEG recordings but not clinically and visa-versa. The exact incident of clinically silent seizures is as yet unknown [31]. The physiology of the neonatal brain presents additional challenges alongside the problems of attenuation and source orientation of conventional EEG. The incomplete myelinisation (insulation layer) and arborisation (branching) of axons and dendrites within the neonatal brain result in small, isolated, weakly propagated seizures, the activity of which may not spread to surface EEG electrodes [31]. This has been proposed as an explanation of the electroclinical dissociation, as the symptoms of the seizures are clinically observed, but the electrical activity does not propagate to the surface electrodes. A further explanation is that certain seizures may not be epileptic, but occur in the primitive brain stem or spinal motor cord, and thus are unlikely to have an EEG correlate [31]. Unlike in adult patients, resective surgery is uncommon in neonates with intractable epilepsy due to the associated risks [35]. Therefore the need for accurate localisation is less clearly defined as in adult patients. However, EIT has been proposed as a method of both locating the activity in deeper structures [33], which could offer insight into the problem of electroclinical dissociation, as well as imaging intracranial haemorrhage, the major cause of seizures [36].

1.2 Electrical Impedance Tomography

Electrical Impedance Tomography (EIT) is an non-invasive imaging technique which exploits differences or changes in electrical properties of biological tissues to obtain structural or functional information. An array of electrodes are placed on the surface of the body, insensitive current is then injected and the resultant voltages are recorded. Images of the impedance distribution in two or three dimensions are reconstructed using an algorithm based on a formulation of Ohm's law for current flow in a volume [37], [38]. The advantages of EIT, particularly in the case of imaging acute stroke, lie in the portability and low cost of the instrumentation and the high temporal resolution. The limitations however, are low spatial resolution and sensitivity to errors in modelling and instrumentation.

1.2.1 Bioimpedance

The impedance Z describes the electrical properties of a biological tissue when a current or voltage is applied. The extent to which the charge transport is opposed within the tissue is described by its resistance R, and the capacitance C describes the ability of the tissue to store charge. Current is conducted through ion diffusion within the conductive extra and intra cellular spaces within the cell, which can be modelled as resistances R_e and R_i, whereas the lipid cell membrane can be modelled as a capacitance C_m [39]. The cell can thus be modelled as a simple parallel circuit, fig. 1.1a with frequency dependent impedance

$$Z(\omega) = \frac{R_e R_i + \dfrac{R_e}{j\omega C_m}}{R_e + R_i + \dfrac{1}{j\omega C_m}}. \tag{1.1}$$

At low frequencies no current crosses the cell membrane C_m as it is predominantly fully charged

$$\lim_{\omega \to 0} Z(\omega) = R_e. \tag{1.2}$$

As the frequency ω increases, more current is diverted away from the extracellular resistance into the intracellular space, increasing the phase angle. At high frequencies the membrane capacitance C_m becomes negligible, so $Z(\omega)$ again becomes purely resistive

$$\lim_{\omega \to 0\infty} Z(\omega) = \frac{R_e R_i}{R_e + R_i}. \tag{1.3}$$

This frequency dependence is commonly displayed in a *cole-cole* plot, fig. 1.1b, named after Cole and Cole [40] who extensively studied the frequency response of dielectrics.

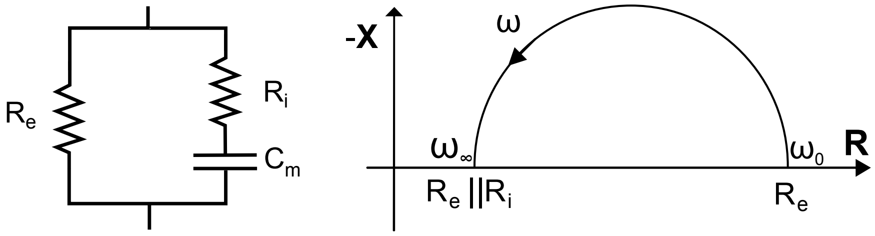

(a) **(b)**

Figure 1.1: *Equivalent circuit of a cell* ***(a)****, extracellular resistance R_e in parallel with the intracellular resistance R_i and the capacitance of the cell membrane C_m,* ***(b)*** *Cole-Cole plot of this circuit*

The value generally reconstructed in EIT is the *conductivity* σ, the inverse of the *resistivity* ρ. It is the variations of the conductivity between brain tissues which is used in EIT to provide information regarding structure and function within the brain.

1.2.2 Instrumentation

The measurement problem in EIT can be modelled as an equivalent circuit, fig. 1.2. Most common EIT systems comprise of a constant current drive (Is) and a differential voltage measurement side. Impedance measurements are usually made using four electrodes in tetrapolar configuration (also known as Kelvin sensing), with alternating current injected between one pair of electrodes and the remaining pair used to measure voltage [41]. The precision of the instrumentation is a crucial factor in the accuracy of the reconstructed images. Due to the ill posed nature of the EIT inverse problem, small errors in voltage measurements can result in large changes in the reconstructed conductivity [42]. The majority of the errors in an EIT system arise from the impedance C_{ed} R_{ed} which arises at the interface of the electrode with the boundary of the subject, known as the *contact impedance*, the causes of which are discussed in detail in section 1.4.

The majority of constant current sources in EIT systems are based on the improved Howland current pump (iHCP) fig. 1.3a [43]–[46], due to its robust performance with only a few passive components. With an ideal current source the injected boundary current is independent from the transfer-impedance of the subject and the electrode impedance, R_1-R_4 and C_{ed} R_{ed} in fig. 1.2 respectively. In reality, the actual current amplitude injected is determined by the ratio between the finite output impedance Z_{out} (which is comprised of the output resistance R_{out} in parallel with the output capacitance C_{out}) to the tissue impedance (which includes electrode impedance), fig. 1.3b. Coupled with this current divider effect, at high frequencies, stray capacitance C_{stray} adds in parallel to C_{out} resulting in increased current leakage [44]. The output resistance R_{out} of the iHCP in fig. 1.3a is maximised by matching $R_1 = R_3$ and

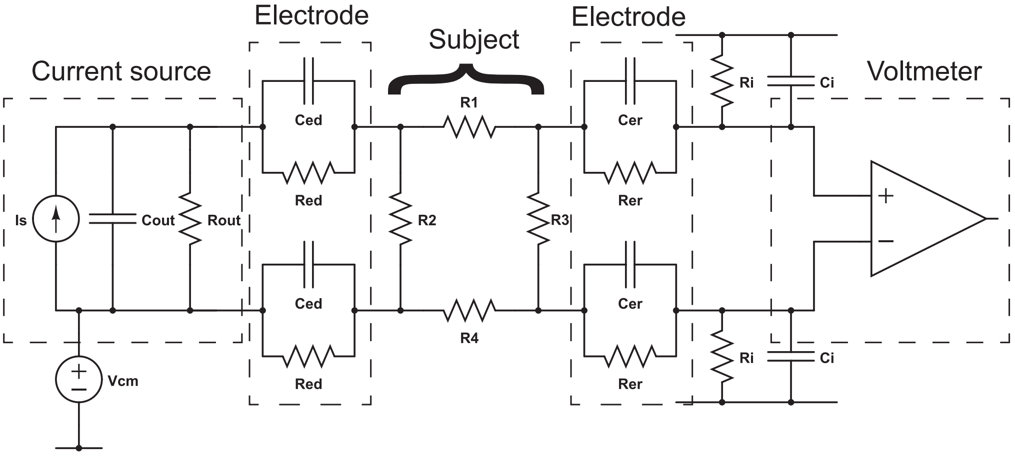

Figure 1.2: *Equivalent circuit of measurement in EIT adapted from Boone and Holder [41]. Is: current source, C_{out}: output capacitance, R_{out}: output resistance, C_{ed} (C_{er}): electrode capacitance on driving (receiver) electrode, R_{ed} (R_{er}): electrode resistance on driving (receiver) electrode, R_1-R_4: load resistance under the measurement, R_i: input resistance, C_i: input capacitance, and V_{cm}: common-mode voltage*

$R_4 = R_{2A} + R_{2B}$. To attempt to cancel out C_{out} and C_{stray}, Cook, Saulnier, Gisser, *et al.* [43] suggested a negative capacitance converter after the iHCP and more recently generalised impedance converters (GIC) have been implemented by Ross, Saulnier, Newell, *et al.* [44] and Oh, Woo, and Holder [45] to create a tunable inductance. Additionally, the alternating current source should be correctly balanced, as any injected DC offset current that flows to ground via a finite impedance will result in a common-mode voltage at the measuring side.

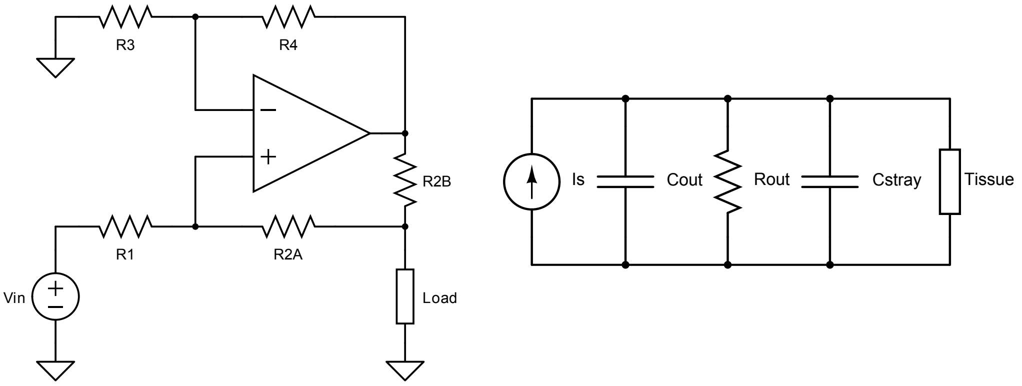

(a) *iHCP* **(b)** *Equivalent model*

Figure 1.3: ***(a)*** *Improved Howland Circuit iHCP from Franco [47],* ***(b)*** *equivalent model of current source*

The instrumentation amplifier is also subject to errors as a consequence of the finite input impedance R_i and C_i. A voltage divider is created between the input impedance (R_i in parallel with C_i) and the contact impedance (R_{er} in parallel with C_{er}), the ratio of which increases with frequency. Thus, for a finite input impedance, the amount of current which sinks through the amplifier is dependent upon the contact impedance, resulting in a load dependent Common

Mode Rejection Ratio (CMMR).

(a) *UCL Mk2.5* **(b)** *KHU Mk2*

Figure 1.4: *Two EIT systems used in the UCL group,**(a)** the serial UCL Mk2.5 designed by McEwan, Romsauerova, Yerworth,* et al. *[48] and **(b)** the fully parallel KHU Mk 2 by Oh, Wi, Kim,* et al. *[49]*

EIT systems can be generally classified by the strategy used to collect voltage measurements: serial, semi-parallel and fully parallel [50]. Serial systems such as the UCL Mk2.5, fig. 1.4a have a single current injection circuit, and a single differential amplifier and ADC on the record side, both of which are independently multiplexed to connect the circuits to the electrodes. Serial systems are the most flexible as it is possible to define a different measurement protocol for each current injection. However, the frame rate of these systems is low as the voltage measurements must be collected sequentially, and the multiplexers introduce errors through channel dependent parasitic capacitance. Semi-parallel systems such as the KHU Mk 1 [45] increase the acquisition rate through simultaneous recording of the voltages with a separate differential amplifier and ADC for each electrode pair. As with a serial system, a single current source is multiplexed between pairs of electrodes. The increased frame rate comes at the cost of a fixed measurement protocol as the differential inputs are hard-wired and not arbitrarily addressable. Fully parallel systems such as the KHU Mk 2 [49] fig. 1.4b , have separate independently controlled current sources, enabling simultaneous injection at multiple frequencies. The increased complexity of semi and fully parallel systems increase the burden upon correct system calibration to ensure symmetry between injecting and recording channels.

1.2.3 Protocols and data acquisition

An important part of EIT measurements is the *protocol*, which describes which electrodes are addressed by the current injection and voltage measurement channels within the system. An injection of current through a single pair of electrodes or multiple electrodes is referred to as a *current pattern*. The sequence of current patterns is known as the *current protocol*, with $N-1$ possible independent patterns for N electrodes. A *single measurement* (sometimes referred to as a *combination*) is the voltage measurement between two electrodes, known collectively as the *measurement protocol* for each current pattern. The *full protocol* is thus the combined current and measurement protocols, which defines the order of all the measurements. The spatial distribution of the sensitivity of the measurements to perturbations is greatly influenced by the choice of current patterns. The *adjacent* protocol used in the Sheffield systems [51], wherein current is injected sequentially through neighbouring electrodes, has low sensitivity in the centre as most of the current passes around the surface. Another common protocol is *polar* injection through opposite electrodes which increases the sensitivity in the centre, but reduces the number of independent injections in a cylindrical object to $N/2$. For such "quasi 2D" applications with symmetrical electrode arrangements, Adler, Gaggero, and Maimaitijiang [52] proposed a "just off" opposite current injection protocol.

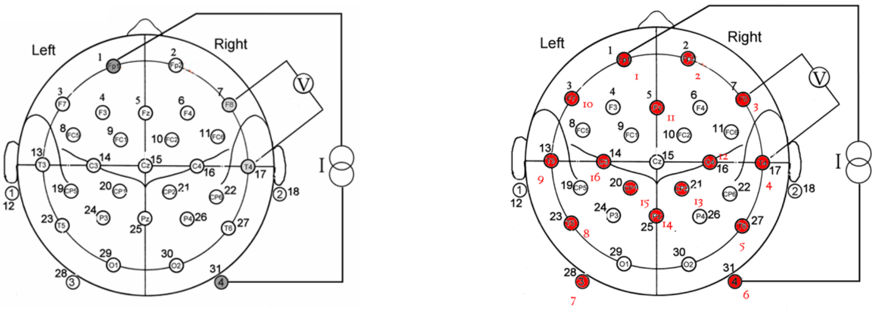

(a) *EEG31*

(b) *Spiral16*

Figure 1.5: *EIT electrode positions,* ***(a)*** *EEG 31 protocol, 27 electrodes placed according to the extended EEG 10-20 psotions from Tidswell, Gibson, Bayford,* et al. *[53],* ***(b)*** *Spiral16, a subset of 16 electrodes chosen by Fabrizi, McEwan, Oh,* et al. *[54]*

Correct current protocol is particularly important for EIT applications of the head as current is shunting through the highly conductive scalp. Maximal current density in the middle of the brain was observed in a head tank with half skull when current driving electrodes were directly opposite each other [55]. For this reason, diametric current patterns have been designed for EIT studies in the head, in which current is injected between diametrically opposing pairs of electrodes, and voltages measured between adjacent pairs of electrodes (excluding the driving pair). Commonly, electrodes are placed on the head according to the international EEG 10-20 system to provide an even coverage of the scalp [56]. The current protocol *EEG31*, fig. 1.5a was designed empirically by Gibson [57] for a 32-channel serial system such as the UCL Mk2.5, wherein current is injected between polar and close to polar electrode pairs and voltages measured between close to adjacent pairs around the circumference of the head and along the apex. Similarly, Fabrizi, McEwan, Oh, *et al.* [54] experimentally designed a 16-channel protocol for a semi-parallel system fig. 1.5b using a subset of the 31 electrodes used in EEG31, to give the same localisation error whilst reducing electrode application time [58]. More recently, Malone, Jehl, Arridge, *et al.* [59] designed an *optimal* current injection protocol wherein the injecting pairs of electrodes are chosen to maximize the distance between the electrodes, while acquiring the maximum number of independent measurements. This was achieved by finding the maximum spanning tree of the electrodes, weighted by the distance between the electrodes.

1.2.4 Imaging principle

The forward problem in EIT consists of the quasistatic Maxwell equations with the complete electrode model boundary conditions for pairs of electrodes [60]

$$\nabla \cdot \boldsymbol{\sigma} \nabla \boldsymbol{u} = 0, \tag{1.4}$$

$$\boldsymbol{\sigma} \frac{\delta \boldsymbol{u}}{\delta \boldsymbol{n}} = 0 \quad \text{off} \quad \bigcup_{l=1}^{2} e_l, \tag{1.5}$$

$$\boldsymbol{u} + z_l \boldsymbol{\sigma} \frac{\delta \boldsymbol{u}}{\delta \boldsymbol{n}} = V_l, \quad l = 1, 2 \tag{1.6}$$

where $\boldsymbol{u}$ is the electric potential, $\boldsymbol{\sigma}$ is the conductivity, n is the normal vector to the boundary, e_l is the lth electrode boundary, z_l is the contact impedance on the lth electrode, and V_l is the measured voltages. This forward problem is solved using the finite element method, which utilises a discretised mesh of the modelled object and a numerical solution of a matrix form of eq. (1.4) for all elements. This is repeated for all electrode injection pairs, with the voltages at all other electrode calculated. An important assumption is that the measured voltage changes are linear with respect to the conductivity changes in the volume [61]. Changes in conductivity $\delta\boldsymbol{\sigma}$ correspond to a particular set of boundary voltage measurements $\delta\boldsymbol{u}$, through a Jacobian or sensitivity matrix $\boldsymbol{J}$ given by the equation

$$\delta \boldsymbol{u} = \boldsymbol{J} \delta \boldsymbol{\sigma} \tag{1.7}$$

The sensitivity matrix describes the contribution of each voxel to the voltages recorded on the surface of the model, which is dependent upon the impedance in the voxel, the amount of current and the distance of the voxel to the electrode. In this manner it is possible to calculate the expected voltages at each electrode for a given conductivity distribution. Calculation of the forward solution is commonly performed through the open source finite element solvers, EIDORS [62] or the newly developed Parallel EIT solver (PEITS) by Jehl, Dedner, Betcke, *et al.* [63] within the UCL group. However, the goal is to obtain images of conductivity based on the voltage measurements obtained experimentally. Therefore the inverse equation must be solved, known as the inverse problem, given by the equation:

$$\delta \boldsymbol{\sigma} = \boldsymbol{J}^{\dagger} \delta \boldsymbol{u} \tag{1.8}$$

where $J^{\dagger}$ is the pseudo-inverse of the sensitivity matrix. Due to the ratio of electrode combinations (usually numbering in the hundreds) to the number of elements in the mesh (often of the order of 10^5 or above) the inversion problem is severely ill-posed [38]. Successful image reconstruction requires stabilisation through *regularisation*, common methods include truncated singular value decomposition [64] or Tikhonov regularisation [65].

1.2.5 Imaging modalities

There are three broad categories of EIT image reconstruction: *absolute*, *time difference* (TD) and *frequency difference* (FD). Absolute imaging involves mapping the measured voltages directly to a conductivity distribution within the object [66]. However, absolute imaging is prone to error and often results in noisy images, as shown by Kolehmainen, Vauhkonen, Karjalainen, *et al.* [67], when there is a mismatch between the model and the experimental reality. The inverse problem in EIT is severely ill-posed, small errors in the modelling result in large artefacts in the reconstructed images. Most EIT imaging, rather than using the absolute values, refer the voltage measurements to a baseline and produce images of *changes* in conductivity. Producing these contrast images has the advantage over absolute images in that errors caused by experimental and modelling inaccuracies are suppressed.

Time difference

Time difference imaging compares the measured voltages at time t to the voltages at a chosen baseline time point t_0. The change in conductivity between these two time steps can be reconstructed using the inverted Jacobian matrix J:

$$\delta\sigma = J^{-1}(V_t - V_{t_0}). \tag{1.9}$$

Inherent within this calculation using J is the assumption that the conductivity changes are small and localised such that the linear approximation of the relationship of conductivity and voltage changes is valid. As a baseline measurement is required, time difference is limited to applications where physiological changes occur over a short time scale, preferably with a known onset, such as lung ventilation, epilepsy, and neural activity.

Frequency difference

Multi-frequency EIT is based on the differences between the impedance spectra of tissues. The frequency of injected current ω_i is varied and are referred to a baseline frequency of ω_0

$$\Delta V_{FD} = V_{\omega_i} - V_{\omega_0} \tag{1.10}$$

Frequency difference EIT enables imaging without a reference recording, which is necessary for diagnostic situations where it is not possible to have a reference image. This is true for stroke, where an image of the patients healthy brain before stroke onset is not available. The simple frequency difference algorithm (FD) assumes that the conductivity of the background does not change over frequency and that the frequency dependence of the contact impedance and EIT system performance is negligible. Images can be reconstructed in a manner analogous to TD with a Jacobian matrix computed reference frequency ω_0.

$$\delta\sigma = J(\omega_0)^{-1}(V_{\omega_i} - V_{\omega_0}). \tag{1.11}$$

However, anomalies can only be reconstructed in simple FD for a frequency independent background, and given the characteristics of most cells described in section 1.2.1, its applications are extremely limited [68]. Therefore more complicated algorithms are necessary for biomedical frequency difference imaging.

Weighted frequency difference The more robust weighted frequency difference (WFD) algorithm was proposed by Seo, Lee, Kim, *et al.* [69] which enables reconstruction of perturbations in a frequency dependent background. The voltages are weighted such that the conductivity change in the background is suppressed:

$$\alpha = \frac{\langle V_{\omega_i}, V_{\omega_0} \rangle}{V_{\omega_0}, V_{\omega_0} \rangle} \longrightarrow \Delta V_{WFD} = V_{\omega_i} - \alpha V_{\omega_0} \tag{1.12}$$

This has been shown to be successful in frequency dependent homogeneous backgrounds [68], [70]. However, in the case of EIT in the head, the background is not homogeneous due to the differing conductivities of scalp, skull and brain, rendering the assumptions of WFD invalid.

Fraction reconstruction To overcome the limitations of WFD, the fraction reconstruction algorithm, developed for diffuse optical tomography, was adapted for multi-frequency EIT by Malone, Sato Dos Santos, Holder, *et al.* [71]. Measurements at a range of frequencies are combined to reconstruct volume fractions for each defined tissue

$$\sigma(\omega_i) = \sum_{j=1}^{T} f_{nj} \cdot \epsilon_{ij} \tag{1.13}$$

where n is the finite element index, T is the number of tissues within the object, the fraction of a given tissue in each element is $0 \leq f_{nj} \leq 1$ and ϵ_{ij} is the conductivity of the tissue j and frequency ω_i. To create images of the tissue fractions within each tissue the objective function is extended to incorporate all tissues T and measurement frequencies M:

$$\Phi(\boldsymbol{F}) = \sum_{i=1}^{M} \left\| A\left(\sum_{j=1}^{T} \boldsymbol{f}_j \cdot \epsilon_{ij}\right) - A\left(\sum_{j=1}^{T} \boldsymbol{f}_j \cdot \epsilon_{0j}\right) - (V_{\omega_i} - V_{\omega_0}) \right\|^2 + \tau\Psi(\boldsymbol{F}) \tag{1.14}$$

Where A is the forward map, τ is the regularisation hyperparameter for the regularisation function $\Psi(\boldsymbol{F})$. This objective function is then minimised iteratively using Markov random field regularisation, τ selected via the L-curve method [72]. Given a sufficiently accurate estimate of the conductivity spectra of the tissues within the subject, this method has been shown to be successful in tank experiments with simple geometry [71] and simulations of the adult head with realistic tissue conductivities [59]. This more advanced approach has a disadvantage in the complexity and computation required, which limits the number of elements possible in the FEM compared to TD or WFD.

1.2.6 Modelling errors in EIT

In order to obtain an accurate numerical solution, it is important that the experimental geometry and electrode position are correctly represented in the finite element model. Failure to do so can result in significant distortions to the resultant reconstructed images [73]. In tank experiments, the geometry and electrode positions are known *a priori*, whereas for measurements on subjects they must be measured and the forward model adjusted to match. Mesh optimisation has seen considerable focus within the UCL group, with work by Aristovich, Santos, Packham, *et al.* [61] enabling FEMs of over 10 million elements to be generated to more accurately represent the complex geometry of both the human head, as well as the rat brain.

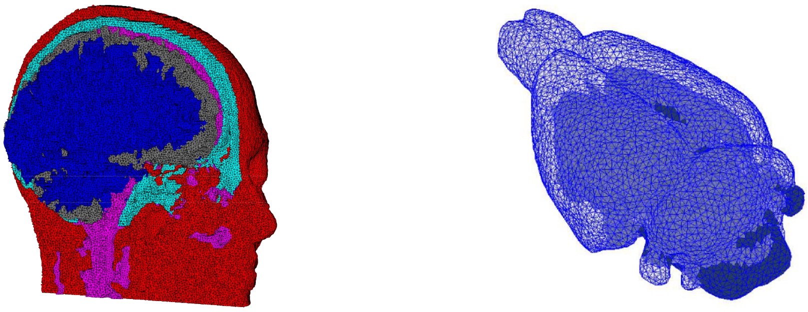

(a) **(b)**

Figure 1.6: *Finite element models in EIT, fig. 1.6a mesh from CT and MRI segmentation of the head by Jehl, Dedner, Betcke,* et al. *[63], fig. 1.6b rat brain mesh by Aristovich, Santos, Packham,* et al. *[61]*

Errors in representing the shape, conductivity, electrode positions and other factors effecting the current distribution in the forward solution are often grouped under the term "Modelling errors" [61], [71]. Minimisation of these errors is critical due to ill-posed and ill-conditioned inverse solution, thus comparatively small errors in the forward model can result in large errors in the inverse solution. Phantom experiments are important for any application of EIT, as these modelling errors are minimised as the geometry/conductivity of the object under test are known *a priori*, to a high precision. Further it is possible to test the robustness of the imaging to modelling errors by altering the phantom in a controlled manner.

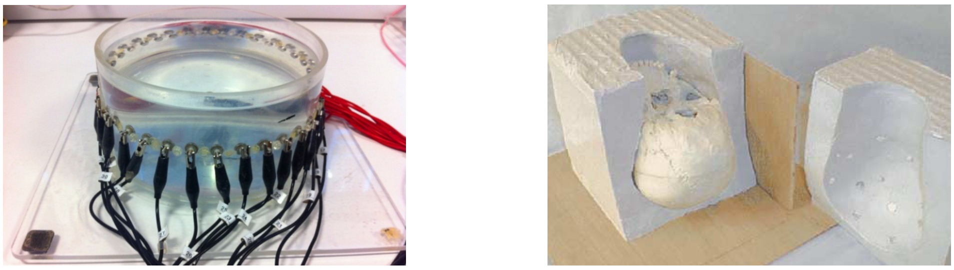

(a) *2D Tank* **(b)** *3D Tank*

Figure 1.7: *Existing tanks used in experiments in the UCL group,* ***(a)*** *a 2D cylindrical tank and* ***(b)*** *a head shaped tank created by Tidswell, Gibson, Bayford,* et al. *[74]*

A common tank used in EIT is a 2D cylindrical tank as an approximation of the human thorax [65], or the human head [54], [68], [75], [76]. This simple geometry also simplifies mesh generation and limits the number of elements required in the FEM. Therefore it should be expected that the modelling errors in these simple tanks are minimised, as the geometry is easy to fabricate both in simulation and experimentally. However as demonstrated in fig. 1.8, there are large errors between the experimental voltages collected by Packham, Koo, Romsauerova, *et al.* [68] in a 32 channel cylindrical tank to simulation. The roots of this problem lay in both the phantom and the mesh used. The electrodes in the phantom protruded into the main body, instead of flush against the side walls as in the mesh. Similarly the mesh was not sufficiently refined around the electrode positions, so the electrode area varied between each electrode in the mesh, whereas it was constant in the tank. Many of these modelling errors in the forward solution have been solved recently by improved meshing [61] and a faster parallel solver capable of handling significantly larger meshes [63].

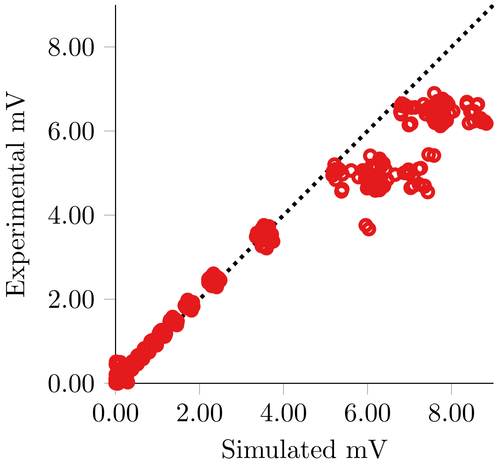

Figure 1.8: *Comparison of simulated and measured voltages in cylindrical tank*

It is important to note that these modelling errors do not preclude successful image reconstruction in tank experiments. These errors are largely time and frequency independent, they affect datasets equally and are thus cancelled out during difference imaging. However there is still often a large artefact in these electrode locations, as found by Malone, Sato Dos Santos, Holder, *et al.* [71] during frequency difference imaging shown in fig. 1.9.

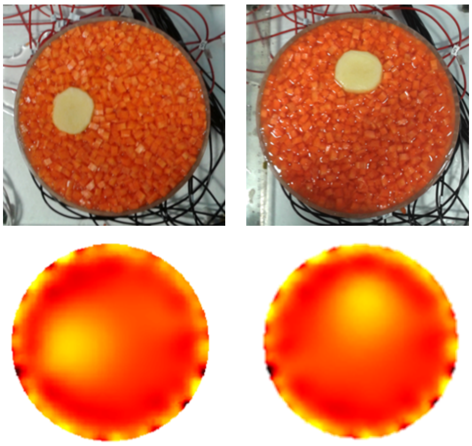

Figure 1.9: *Artefacts due to modelling errors during experiments by Malone, Sato Dos Santos, Holder,* et al. *[71] in a 2D cylindrical tank*

These results demonstrate that even phantoms with simple geometries can have modelling errors sufficient enough to cause artefacts in reconstructions. Therefore it is to be expected that the complex morphology of the head would result in greater modelling errors when conducting experiments in head phantoms. The comparison of simulated voltages to those experimentally collected by Doru, Avery, Aristovich, *et al.* [77] in the UCL head phantom created by Tidswell, Gibson, Bayford, *et al.* [74] shown in fig. 1.10, demonstrate large modelling errors, in some cases over 300 %. Studies have been carried out successfully in this phantom, both with [53], [74], [78] and without the skull present [68], [77]. The data collected with this phantom often required careful *post-hoc* data rejection of unsuitable channels [68], [77], [79] which may have coincidentally removed channels with the largest modelling errors. However this process is not described in the original studies with this phantom [53], [78] which suggests this may not be the case, although no comparison plots of the voltages as in fig. 1.10 were given. Another possibility is that the phantom has deteriorated though multiple uses over time and the properties no longer match those of the mesh used. This data highlights the necessity for a new head phantom for EIT, with stable properties over time as well as realistic geometry and conductivity.

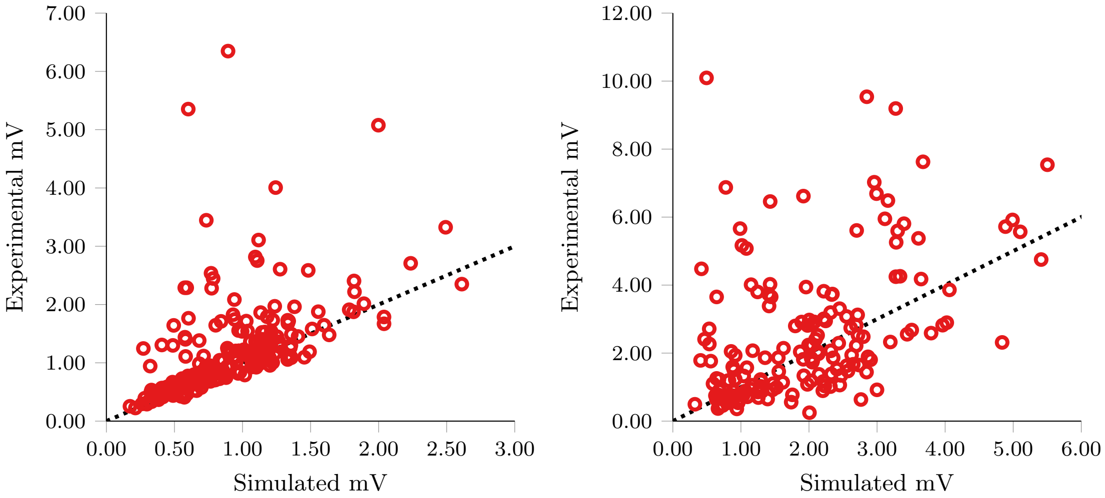

(a) *No skull* **(b)** *With Skull*

Figure 1.10: *Comparison of simulated and measured voltages in UCL head tank [74]*

1.3 EIT of brain pathologies

There are four main applications of brain imaging with EIT: stroke [7], [48], [80], epilepsy [28], [30], evoked responses [81], and fast neural activity [46]. Each of these techniques aim to exploit impedance changes in the brain caused by different underlying physiological effects. EIT of brain function has been the focus of the UCL group for several decades, with particular emphasis on stroke and fast neural applications in recent years.

1.3.1 Bioimpedance of stroke

Although there have been TD recordings made in stroke models, the difficulty in collecting accurate *in-vivo* measurements has precluded any single exhaustive study examining the impedance changes during acute stroke. However, a review of the literature by Horesh [82] enables predictions of the changes that will occur. A comparison of the conductivity spectra of the relevant tissues is given in fig. 1.11 from the results of this review [82]. The conductivity of normal brain is approximately 0.1 S/m at frequencies below 100 Hz, where current passes predominantly through the extracellular space. This increases to 0.18 S/m at 1 MHz as current flows through the cell membranes into the intracellular space. In contrast to healthy brain, the ischaemic tissue has a conductivity 0.07 S/m less at 10 Hz, and this difference reduces to around 0.02 S/m by 100 Hz with this difference maintained up to 1 MHz. Blood has a substantially higher conductivity of 0.7 S/m below 100 kHz, and this increases up to 0.82 S/m at 1 MHz.

The change in conductivity spectra between normal and ischaemic brain tissue is caused by a reduction in extracellular space due to cell swelling as a result of hypoxia caused by the

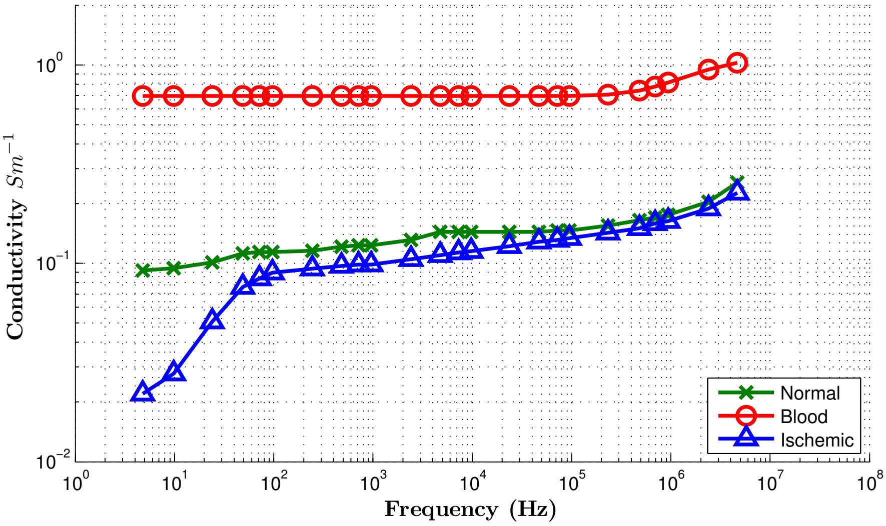

Figure 1.11: *Change in conductivity over frequency of normal brain tissue, ischaemic brain tissue and blood, adapted from [82]*

ischaemic event [83]. At low frequencies, the current cannot pass through the cell membrane, and must pass through the extracellular space. So this reduction caused by ischaemia results in a conductivity decrease of approximately 10-20 % at low frequencies (< 100 Hz). In contrast, a haemorrhage produces an area of high conductivity which is approximately flat across frequencies below 1 MHz [39]. It is these spectral differences which EIT of stroke attempts to exploit. Whilst there are differences in all three spectra up to approximately 1 MHz, the focus of stroke EIT is on frequencies below 2 kHz, where the difference is greatest. Therefore the possibility of distinguishing an ischaemic stroke is maximised.

1.3.2 Bioimpedance of intracranial bleeding

Tissue	Conductivity (S/m)
Skull	0.018
Scalp	0.44
CSF	1.79
Dura matter	0.44
Grey matter	0.3
White matter	0.15
Air	0.001
Blood	0.7

Table 1.1: *Summary of approximate head tissue conductivities below 1 MHz from Horesh [82]*

The conductivity changes arising from intracranial bleeding are similar to those expected from haemorrhagic stroke as they both involve blood entering the skull. However, depending upon which type of injury, the blood may replace different tissues within the skull, and thus present a different contrast. For example, in the case of a subdural haematoma (SDH), blood would replace both the CSF between the brain and the dura, and also compress the brain. Whereas with a interventricular haemorrhage (IVH), the blood enters the ventricles which are primarily filled with CSF. As the summary by Horesh [82] table 1.1 demonstrates, blood has a substantially different conductivity to most head tissues, representing an increase of 60 to 130 % increase compared to brain tissues, or a 150 % decrease compared to CSF. It is difficult to estimate the contrast between tissue from in vivo measurements, as the point spread function of the EIT reconstructions themselves, distrubuted the real conductivity changes over a wider region. Manwaring, Moodie, Hartov, *et al.* [14] found a mean conductivity difference of 19.5 ± 11.5 mS/m during injection of 1 ml of blood in a piglet brain, an order of magnitude less than would be expected from the values in table 1.1. It is possible the injected blood diffused over a larger area than intended, or cell ischaemia secondary to the introduction of blood into the white matter may have caused an impedance change in the opposite direction, cancelling out some of the change as a result of the blood. Therefore, care must be taken when conducting experiments into EIT of intracranial bleeding, not to overestimate the contrast blood represents in the brain.

1.3.3 Bioimpedance of epilepsy

It is well-established that the impedance of brain tissue increases abruptly during seizure activity. Animal experiments in the 1960s demonstrated that the impedance of cerebral tissue increases by 1-12 % during induced and spontaneous epileptic activity [84], [85]. Rao [86] measured local cortical impedance changes arising from electrically induced seizures of 9.5 % at 47 kHz. The increase in impedance has been attributed to cell swelling [87], [88], as intense neuronal activity creates an osmotic gradient which leads to movement of water inside the cells, causing the extracellular space to shrink. As with ischaemic stroke, at low frequencies (< 50 kHz), the injected current flows mostly around the extracellular fluid and consequently a reduction in the extracellular space causes an increase in the measured tissue resistivity and impedance [89]. Cell swelling develops soon after the onset of ictal and inter-ictal events and, according to some sources, may even precede electrographic changes [87], [90].

Besides its secondary effect through cell swelling, seizures also cause a direct, transient change in impedance. Highly synchronous neural activity causes a fast drop in impedance lasting a few ms due to the opening of ion channels, which allow current to flow through the intracellular space. These fast impedance shifts have been described in anaesthetised animals during evoked responses [46], [91]. Recent developments in the UCL group have demonstrated this fast neural signal is present during seizures [92], with a transient change of approximately 0.1 % lasting 2 ms.

1.3.4 Data collection and electrode localisation

The current procedure for collecting data in stroke patients in clinical studies within the UCL group is based on that described in [7]. 32 EEG electrodes are placed on the scalp of the patient by hand after preparation of the electrode sites with abrasive paste to reduce the contact impedance. The hardware used in these trials - UCL Mk2.5 - measures the contact impedance at 10 kHz and a threshold of 2.5 kΩ per electrode is set. The electrodes are held in place during recording by the paste and by elasticated material. The electrodes are localised by a procedure called photogrammetry. Targets are placed at the positions of the electrodes and multiple photographs are taken of the patient's head. The three dimensional locations of these electrodes can be reconstructed from the two dimensional images based on their scale, rotation and relative positions. The accuracy of this localisation has been found to be approximately 0.5 - 2 mm. An example of the data collection from an unpublished clinical study is shown in figure 1.12. The shape of the finite element model can give rise to significant errors in EIT images if it is not representative of the geometry of the volume under examination [73]. To minimise these errors in stroke EIT, FEMs specific to the patient generated from CT or MRI scans, are used in the image reconstruction [93]. The electrode coordinates obtained via photogrammetry are then rotated and scaled manually in the reconstruction software to bring them into alignment with the mesh geometry. In the stroke application of EIT in the ambulance, it will not be possible to have these accurate meshes before the patient arrives in the stroke unit as they would not have had a CT or MRI. Therefore, it is important that the electrode localisation is as accurate as possible to infer the geometry of the patients scalp from these measurements. Using these measurements it would be possible to warp a generic head mesh to match the measured geometry, thereby better representing the actual measurement conditions and improving reconstructed images. The measurement accuracy required is currently unknown, thus the aim of this project is to at least match the existing technique of photogrammetry.

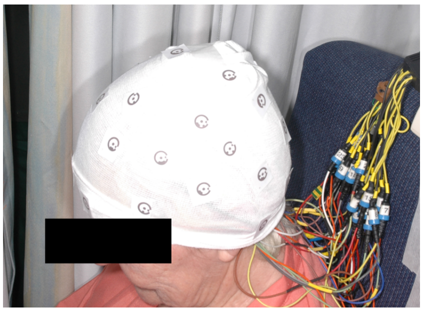

[redacted]

Figure 1.12: *Example of data collection for stroke EIT, photogrammetry markers are visible above elastic cap*

1.3.5 Summary of previous studies

Prompted by the encouraging results from Bagshaw, Liston, Bayford, *et al.* [64] which showed a measurable change on the scalp during seizures, an attempt to image epilepsy in human subjects was undertaken by Fabrizi, Sparkes, Horesh, *et al.* [30]. The UCLH Mark 1b system was used which utilized a single impedance four-terminal measuring circuit multiplexed to up to 31 electrodes [94] on the scalp of patients undergoing pre-surgical EEG-telemetry. Unfortunately no reproducible impedance changes were found during seizures, as the comparatively small boundary voltage changes were masked by large baseline drifts and movement artefacts from the electrodes. Another limitation highlighted by the authors was the lack of accurate patient FEM and electrode localisation.

A pilot clinical MFEIT pilot study was performed by Romsauerova et al. [7] which considered 7 patients with pathologies which mimic the impedance characteristics of a haemorrhage. Data were collected at 16 and 64 kHz and images reconstructed in a 30,000 element FEM generated from patient MRI data. No reproducible changes between patients were found in the raw data or the images. Since the publication of this study, work has been undertaken within the UCL group to improve the instrumentation, the measurement protocol [76], the FEM [93], the reconstruction algorithm and data rejection [68]. Although the results are unpublished, these improvements have not resulted in reproducible changes across patients in subsequent studies. Two of the issues that have yet to be tackled successfully are the drift in standing potentials over time caused by changes in contact impedance over time (section 1.4), and correct electrode localisation with respect to patient geometry.

1.4 Biomedical electrodes

1.4.1 Electrode - tissue interface and contact impedance

Properties of the electrodes and the electrode-skin interface have an impact in any biopotential recordings, and can be an accuracy limiting factor when performing EIT. The interface between the electrode and the skin resists the flow of current, which is termed the contact impedance. Large contact impedances can give rise to large potential drops at the electrode-skin interface which can mask those caused by the underlying tissues, therefore making impedance measurements difficult [95]. Reactive components of the contact impedance can also generate phase shifts leading to misleading measurements [96]. In principle, the four-electrode measurement system should cancel out the effects of contact impedance. However this is only the case if the impedances are exactly matched at all four electrode sites. In reality, variations in skin impedance and stray capacitance between channels cause significant errors in recorded impedance values [38] [97]. The mismatch of contact impedances in the current drive circuit develop a common mode voltage on the body, while those found in the voltage measurement circuit effectively reduce the common-mode rejection ratio (CMRR) of the differential amplifiers, and thus reduce the elimination of common-mode voltages [98]. Mismatches in contact impedance as small as 20 % have been shown to render EIT images “almost meaningless” [73], [99]. Results from the UCL MFEIT study show that contact impedances variations of this order can be expected on scalp recordings in the ward [100]. Therefore reducing the contact impedance mismatch is of primary concern in EIT of acute stroke.

Traditionally, gel is placed between the electrode and the skin which has a number of benefits (described below). Therefore the contact impedance represents the electrode-gel-skin interface which can be simplistically modelled as a resistor-capacitor network shown in figure 1.13 [95]. Contact impedances are dominated by the impedances of the outer layers of the skin, and are largest at low frequencies. It is at these frequencies (≈20 Hz) where the contrast between healthy and unhealthy brain tissues is greatest, see section 1.3.1, so contact impedance causes particular difficulties in MFEIT of acute stroke.

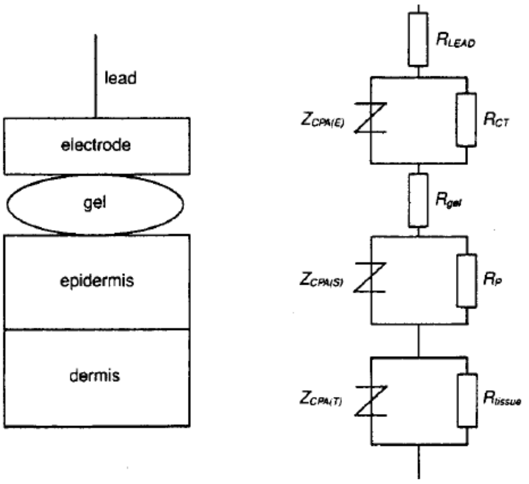

Figure 1.13: *Simple equivalent circuit model of electrode-gel-skin interface from [95]*

Skin impedance and abrasion

The skin impedance is dominated by the impedance in the epidermis - R_p and C_p in parallel, which can be further divided into two sub layers: the Stratum Corneum, the outer keratinised layer and deeper tissues including the stratum gerninativum. The Stratum Corneum is the outer skin layer consisting of dead cells, it acts as a fluid barrier and this has electrical isolation characteristics [101]. The equivalent circuit is now given in figure 1.14, with by far the greatest contribution from R_1, the resistance of the Stratum Corneum [102]. Removal of layers of the Stratum Corneum therefore results in a significant decrease in R_1 and thus R_p (and hence overall contact impedance). A study using adhesive tape to progressively remove layers of the epidermis of approximately the same thickness demonstrates dramatic reduction in R_p as shown in figure 1.15 [102]. The outer layers of the Stratum Corneum are the most resistive, so the most dramatic decreases are found after the first few strippings.

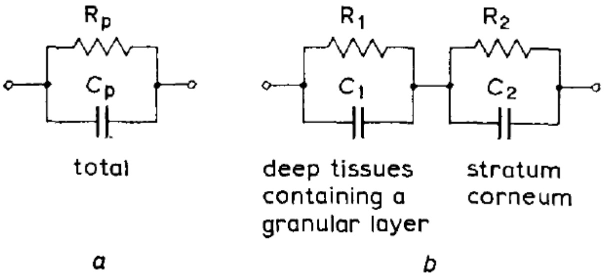

Figure 1.14: *Equivalent electrical circuit of the epidermis from [102]*

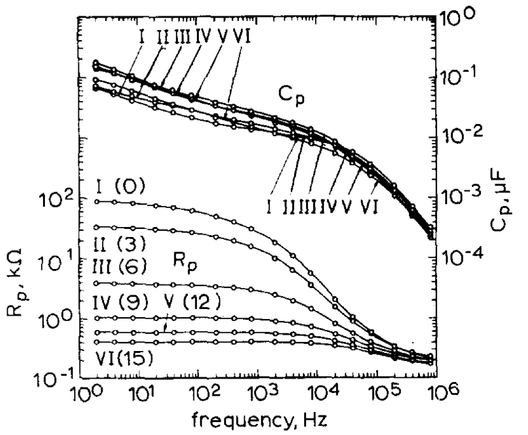

Figure 1.15: *Frequency characteristics of skin impedance from from [102] represented as values for the equivalent circuit in figure 1.14. Number of tape strippings given by numbers in parenthesis, Roman numerals denote corresponding data in R_p and C_p*

Due to these effects it is standard clinical practice to perform abrasion of the electrode contact site before taking measurements. This abrasion is typically performed by hand by a clinician using a cotton bud with abrasive paste, or by rubbing with sandpaper as shown in figure 1.16.

It is important to consider the inter and intra human variations of skin properties as they dictate the potential decrease is overall contact impedance. The thickness of the Stratum Corneum has been found to vary from as little as 10 μm to well over 100 μm in a single patient depending upon the area of the body measured [95]. Skin hydration greatly affects the value of R_p and considerable daily variations have been shown, as well as long term changes over seasons [103]. These issues coupled with the expected inter patient variations may explain why there is little agreement in the literature on the exact values of the impedance of human skin [104]. Therefore it is difficult to create any rules as to the amount of abrasion

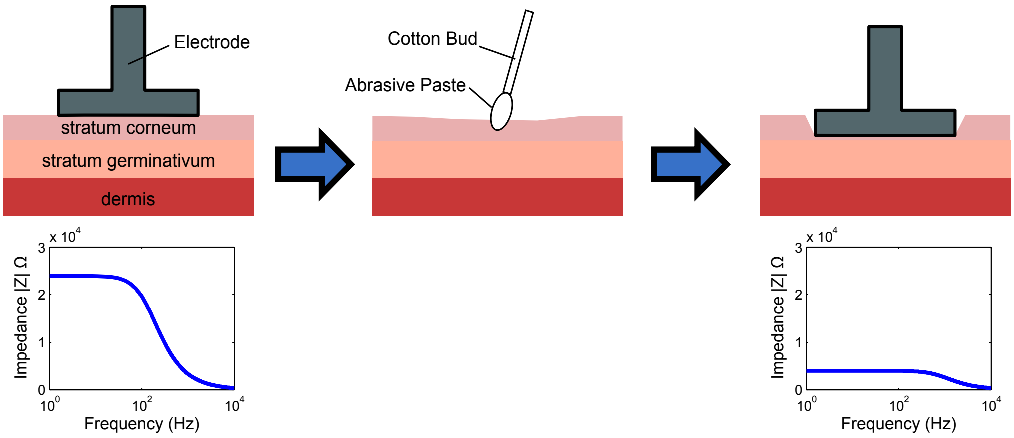

Figure 1.16: *Effect of abrasion of electrode site on the resultant contact impedance. Impedance values taken from [102] for zero and 9 strippings*

that is required to reach a low contact impedance as the impedance before abrasion, and the amount of tissue which can be safely removed vary to such a large extent, and depend upon the frequency of interest. However, as the impedance of the underlying tissues (R_2 and C_2 in figure 1.14) is relatively small, variations in thickness or characteristics will have less of an effect on the overall contact impedance. Hence, if the Stratum Corneum is largely removed, it would be expected that the variation in contact impedance across electrode sites and between subjects would decrease. This assumption allows for the use of general guidelines of acceptable contact impedances in clinical settings. For example, a value of 1 kΩ at 10 kHz per electrode is deemed acceptable for use in the UCL stroke trials [7]. The removal of the Stratum Corneum is not controlled or repeatable with manual abrasion. Instead the contact impedance is checked after electrode preparation, and the process is repeated for electrodes with contact impedances above the threshold. However, as has been described previously, impedances mismatches of as little as 20% are unacceptable for imaging and performing abrasion by hand does not allow for accurate control of the impedance.

Gel impedance

Electrode gels decrease the contact impedance by ensuring optimal electrical contact between the electrode and the skin. The gel rapidly fills up the pores and wrinkles in the skin, providing the maximum possible contact area. To ensure electrical conductivity electrode gels also contain ionic salts which are biocompatible, usually NaCL and KCL. A high concentration of electrolyte is used to decrease the charge transfer resistance R_{ct} and the skin impedance, therefore reducing the overall contact impedance [95]. However, biological tissues cannot tolerate long-term exposure to salt concentrations which differ from physiological levels. Therefore, high electrolyte concentration gels are not suitable for long term monitoring.

Electrode impedance

Theoretically an electrode can be made of any conductive material, and often practical considerations such as re-usability and corrosion resistance take priority over electrical characteristics. However in EIT, the electrical characteristics, particularly the contact impedance, are vital. The electrical properties generally considered desirable for an electrode-electrolyte interface are given in [95] as:

- low, stable offset potentials
- low, matched interface impedances
- low polarisation

An electrode which meets all of these criteria is the silver-silver chloride (Ag-AgCl) electrode. The offset potential of this electrode is determined by the activity of the Cl ion and hence is small and stable when the electrode is in contact with an electrolyte containing Cl^- ions. This is true for both fluids in human tissue and electrolyte gels [105]. Ag-AgCl electrodes also have low interface impedances due to the roughness of the electrode surface caused by the deposited layer which effectively increases the contact surface area. A simplistic model of this decrease in impedance has been proposed, in which the interface impedance of a rough surface is proportional to the square root of that of the smooth surface [97]. Electrode polarisation describes the additional voltage or "over potential" caused by the current flowing through the charge transfer resistance which gives rise to an additional voltage [106]. Ideally the electrode would be entirely non-polarisable, with no voltage being dropped across the interface. However, all electrodes are polarisable to a certain extent as charge transfer resistances (R_{ct}) are unavoidable. Ag-AgCl have low values of R_{ct} and thus are relatively non-polarisable. All noble metals have low polarisation (as well as low corrosion) properties, and as such electrodes are often made from these materials such as gold [107], platinum [46], [108] and iridium [109]. However, as they are considered to be inert, they do not react chemically with tissue, and thus do not gain the benefits offered by chloriding silver to produce Ag-AgCl. It is possible however to "platinise" a platinum electrode which deposits a fine layer of platinum on the surface, greatly increasing its roughness and decreasing the interface impedance [95].

1.4.2 Measurement Drift

Another significant source of error present in scalp recordings is baseline drift, *i.e.* slow changes in the standing potentials. Linear drifts of as little as 2 % have shown to create significant distortions in images, with the artefacts at 5 % almost completely masking any other impedance changes [99]. Drifts in measurements arise from two sources: changes in absolute error of the EIT hardware, and gradual changes in contact impedance either through motion artefact or other physiological effects [95].

To a certain extent, the drift in hardware performance can be minimised through frequent calibration and improvements in output impedance in the current source and input impedance in voltmeters to decrease the sensitivity of the measurements to changes in contact impedance. The burden on correct calibration increases with system complexity, Wi, Sohal, McEwan, *et al.* [110] recommend daily calibration of the KHU Mk 2.5 system to ensure optimal SNR and minimal error between channels. However, this cannot prevent small changes in absolute error during recordings. These errors have been reported as comparatively small over a short period of time ≈ 5 mins [111], but are worse soon after application of the electrodes.

Fabrizi, Sparkes, Horesh, *et al.* [30] found that drift in boundary voltages on the scalp entirely masked any potential signals arising from epileptic seizures. Drifts over 20 % were observed over the course of several minutes, far exceeding that expected from hardware errors. The primary source of error identified by the authors was movement artefact. If the electrodes were to shift on the scalp to an area insufficiently abraded, the resulting change in contact impedance could explain these large drifts. Additionally, even if the electrodes were correctly located, the pressure exerted on the scalp may alter as the patient moves and strains the electrode cabling.

Recently, work by Nir Goren [112] in the UCL group has shown that the addition of real baseline drifts recorded on the scalp over a time period of three hours can produce significant distortions in simulated reconstructions of intracranial haemorrhages fig. 1.17. In many cases the drift prohibited the reconstruction of any meaningful images, despite the comparatively larger signal size, blood representing a 60 to 130 % contrast compared to maximum of 12 % expected from seizures.

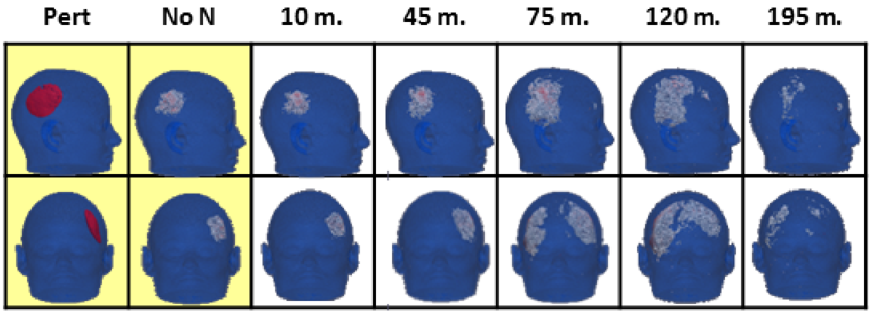

Figure 1.17: *Simulated reconstruction of Extradural Haematoma,* ***pert*** *is ideal reconstruction,* ***No N*** *is the reconstruction without any noise, the remaining columns correspond to the images with realistic measurement drift added*

Careful selection of the baseline reference voltages, and simple high pass filtering could mitigate these effects, particularly in the case of short duration signals such as seizures. However, intracranial haemorrhages may slowly develop over the course of hours or even days, in which case, filtering the drifts would also suppress signal resulting from the bleeding. As these post processing techniques are insufficient, there is a need for controlling the measurement drift over time during recordings.

1.4.3 Electrodes and electrode placement

The threshold for acceptable contact impedance is heavily dependent upon the application. For comparison, a threshold of 2.5 kΩ per electrode at 10 kHz is used in the UCL Mk2.5 system used in the UCL group stroke trials [7], compared to a threshold of 25 kΩ for commercial EEG systems (www.micromed.eu). The reasons for this more stringent requirement are related to the relative size of the signals and the addition of current injection electronics necessary for EIT. EEG signals are in the order of 100 μ V [97] whereas the signal changes in EIT are approximately 0.1% of the 1 mV standing potentials, or 1 μ V [7]. EEG amplifiers such as the AD8224 (www.analog.com) have input impedances in the order of T Ω, and thus should largely be protected against voltage divider effects due to contact impedances ($\approx$ 50 kΩ for unabraded skin). Similar components are used in modern EIT systems and can thus measure voltages reliably, as long as the mismatch between the contact impedances is not too great (section 1.2.2). Contact impedances prove a greater problem when considering current injection instrumentation. The output impedance of current generation EIT hardware is of the order of 1 M Ω [49], a million times smaller than the input impedance of the voltmeters, and are thus much more sensitive to current divider effects caused by large contact impedances (1.2.2). Thus it is possible to collect quality EEG data without abrasion, but it remains necessary for EIT.

Typical EEG electrodes

The electrodes used in the clinical studies performed in the UCL group, are Ag-AgCl cup and paste EEG electrodes (figure 1.18). They are approximately 1 cm in diameter and are reusable if washed and sterilised between uses. The electrode site is prepared through abrasion as described in figure 1.16 and a combined conductive and abrasive paste which has the same ingredients as the gel described in the previous section with the addition of an abrasive material such as pumice. This enables rapid abrasion of the skin under the electrode site through the use of an applicator. The electrode is then filled with paste and placed onto the abraded site. The contact impedance is measured by the EIT or EEG system, and if the impedance is above a certain threshold the clinician repeats the process. This technique, despite producing good results, is labour intensive and is generally used in situations where application time is not a primary concern. As a benchmark, experienced clinicians in the UCL group who have performed electrode placement on patients in the stroke ward require 20 to 30 minutes to apply 32 electrodes. This application is not feasible in the ambulance as it requires too much time and intervention from highly trained personnel.

Figure 1.18: *Example of traditional cup and paste EEG electrodes*

Self abrading electrodes

Self abrading electrodes are systems where the abrasion is performed *in-situ* by an electrode with an abrasive surface. One such system was proposed by Holder where the tissue was held against the electrode, which had a serrated surface, which was then rotated thus abrading the skin [113]. A schematic of this system is shown in figure 1.19. The tissue was held in place either by a spring or a pneumatic system was used should further force be required. The electrode was rotated by an electrical screwdriver operated by the clinician, who observed the contact impedance measured at 10 Hz by a battery powered impedance analyser. The abrasion was performed in this fashion until an impedance of 5 kΩ was recorded. A multitude of these electrodes were included in a ring array for breast imaging, with each electrode being abraded in turn. With this system it was possible to reduce the contact impedance to approximately the same values as achieved with traditional abrasion and Ag-AgCl electrodes.

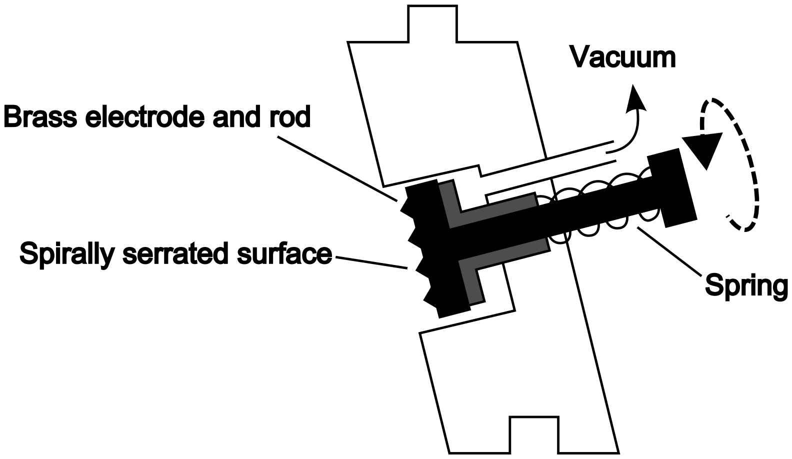

Figure 1.19: *Self abrading electrode from [113]*

However, the design still requires a substantial amount of intervention from the clinician.

One such commercial system is the QUINTON Quik-Prep Automated Patient Prep System for ECG electrodes (figure 1.20) [114]. Similar to the Holder array, the spring loaded electrode is held in place by the clinician who triggers the rotation of the electrode *in situ*. The electrode has a tined surface, which abrades the skin when rotated. The system has a built in impedance measurement circuit and indicates when good contact is made. This system does not use any paste or gels. However, this system is designed for ECG, which has far less stringent requirements for contact impedance than EIT or even EEG due to the relatively large signal size.

Figure 1.20: *Quinton Quik-prep system for ECG electrodes [114]*

Microspike Electrodes

Microspike electrode have been presented by a variety of researchers [115]–[119] as offering benefits compared to other "dry" electrodes (*i.e.* without paste) or even Ag-AgCl electrodes with paste. The principle (figure 1.21) is that the need for skin preparation is removed by bypassing the Stratum Corneum altogether with spikes directly in contact with the deeper tissues. Theoretically this removes the need for abrasion which can be time consuming and potentially uncomfortable to the patient. The other benefit of these electrodes is that the resultant contact impedance is less dependent upon the properties of the Stratum Corneum, which potentially offers much more consistent impedances across electrodes as well as stability over time [104]. This could offer significant benefits to EIT instrumentation by reducing the errors caused by impedance mismatch. However, the drawback with these electrodes is that the contact impedances tend to be much larger than is acceptable for EIT [116], [118]. There are also significant issues with motion artefacts as the contact impedance is heavily dependent on the number of spikes penetrating the Stratum Corneum and the depth of penetration. Therefore small lateral movement from the patient could result in some of the spikes no longer being in contact with the deeper tissues, drastically increasing the contact impedance [104]. These are likely to be the reason why these electrodes have not being used in clinical practice.

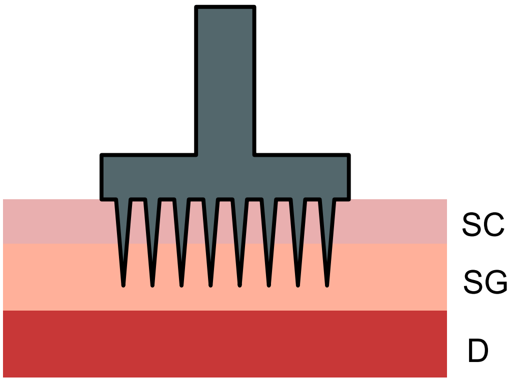

Figure 1.21: *Principle of dry microsprike electrode*

EEG/EIT head electrode systems

One solution to reduce the application time of electrode, whilst still taking advantage of the benefits of tradition EEG Ag-AgCl electrodes are headnets. This are caps or helmets which incorporate the electrodes into the material, thus allowing all electrodes to be placed on the scalp at once. Example commercial EEG headnets are shown in figure 1.22. Many of these headnets are designed for use with EEG systems with high input impedance amplifiers which compensate for electrode impedances up to 20 kΩ, so no method of abrasion is incorporated into the designs. A systematic review of these headnets found that it is possible to obtain contact impedances that match or in some cases improve upon the gold standard EEG electrodes, provided abrasion is still performed manually in the same manner [78]. This did allow for some reduction in the preparation time for the whole array but not to the extent at which it would be feasible in the ambulance. These systems also do not offer any benefit to electrode localisation or measuring patient geometry, so photogrammetry would be necessary as with conventional electrodes.

Figure 1.22: *Example EEG headnets. Clockwise from top left: Easycap, EEG electrodes, geodesic headnet and Physiometrix headcap from [78]*

1.5 Rationale

Successful EIT imaging of stroke from scalp electrodes in an ambulance requires an improved electrode application method which correctly locates electrodes in known positions with low contact impedance. The solution proposed in this thesis automates the electrode application process through a design of a novel electrode helmet bearing a multitude of servo-controlled self abrading electrodes. The design is an extension of existing self abrading electrodes, section 1.4.3, whereby the abrasion is performed by a servo motor with a contact impedance feedback loop. If successful, this design would enable rapid electrode application without significant intervention from skilled personnel. This design also offers a solution to the problem of modelling errors through electrode mis-location and unrepresentative mesh geometry, sections 1.2.6 and 1.3.4, by incorporating position sensors within each servo-electrode.

The helmet offers potential benefits in a broader range of EIT applications in the head, namely time difference imaging of epilepsy and intracranial haemorrhage. Whilst, time difference imaging is more robust, high contact impedance and intra-electrode variations in abrasion still limit the performance of hardware and must be mitigated for successful images. Crucially, control of the contact impedance with a servo mechanism not only allows the contact impedance to be minimised upon initial application, but also maintained throughout recordings. Thus the servo-electrode helmet is a possible solution to the measurement drift problems, section 1.4.2, which prevented successful images of epileptic seizures.

1.5.1 Intended application

The primary application for the helmet is imaging acute stroke in an ambulance where it is not possible to apply electrodes in the conventional manner, section 1.3.4, due to time constraints and lack of specialised expertise. Therefore the goal of the helmet is to as close as possible replicate the best practices of electrode application on the EEG telemetry ward. The secondary application for the helmet is to improve upon traditional cup and paste electrodes, section 1.4.3, particularly in reduction of electrode movement artefact and measurement drift.

Ambulance and patient considerations

Ambulance environment To design a system to apply electrodes to the scalp of a patient in an ambulance that is robust, consideration must be given to the conditions in which it will be used. While great care is taken when designing ambulances, the mechanical vibration experienced by the patient and the paramedics is often significant. One study found that peak acceleration at the patient head position was approximately 20 ms^2 or approximately 2 g [120], while another more recent study found significantly larger peaks greater than 3 g both in the front-to-back and side-to-side directions [121]. Both of these trials were conducted in non-emergency transports, which may underestimate the vibrations and impulses expected in an emergency situation such as with a patient with expected stroke. Therefore the system designed in this project must be shown to be robust against impulses of at least this magnitude.

Journey Time An understanding of how quickly the helmet should apply the electrodes ready to collect EIT data can be derived by considering the ambulance journey time and the time required for imaging. The NHS prioritises 999 calls based on the nature of the emergency. Stroke belongs to "Category A", which, per the targets set by the Department of Health, must receive an ambulance within 19 minutes in 95% of cases [122]. As previously mentioned in section 1.1.1, another target from the DoH is that 65% of stroke patients must reach a stroke unit within an hour **DeptartmentofHealth2012** Taking these values as a guideline, a fair assumption for the time for EIT data collection would be 20 minutes. Currently, in order to produce good quality tank images data must be averaged over a period of at least 20 minutes [68]. Therefore there is little margin of error so the electrodes should be correctly placed as soon as is possible. A first target of 10 seconds per electrode was chosen for the first preliminary experiments.

Patient safety The abrasion should not cause pain or damage to the patient beyond removal of the outer layers of skin. There are also numerous medical safety standards which the system will have to comply with before clinical trials could be performed. One desirable characteristic in particular is that the device is back-drivable, so that the electrode is sensitive to opposing forces caused by patient movement. Additionally, consideration to the weight of the helmet is necessary. If the helmet is too heavy it could be uncomfortable or even dangerous, especially given the size of the expected impulses. A review of head and neck injuries suggested a maximum weight of 2 kg for adult [123]. Other benchmarks are motorcycle helmets which are often in the range of 1.5 to 2 kg [124]. Therefore if the helmet exceeds this 2 kg value then some compensation for the forces on the patients neck will likely be necessary. Given the potential weight of the helmet, the centre of mass should be aligned with the neck such that the helmet balances evenly on the head to prevent uncomfortable straining.

1.5.2 Helmet specification

Using these considerations, coupled with the issues discussed within the literature review in this chapter, the following specifications for the helmet have been identified:

- 32 electrodes arranged according to the EEG 10-20 system
- Automated electrode placement and contact impedance reduction through abrasion to less than 5 kΩ at frequencies below 100 Hz
- Stable electrode placement below this threshold must be achieved as quickly as possible, with an initial target of 10 seconds

- The electrode locations must be returned with an accuracy of at least 2 mm, preferably 0.5 mm in X, Y and Z axes
- Components which come in contact with the skin must be sterilisable or disposable
- Electrical interference from the control hardware should be minimised (or removed through filtering) such that the SNR of the EIT signals is unaffected
- The electrodes must remain in contact without over-pressure on the scalp when subjected to 3 g acceleration impulses and the resultant patient motion
- Safety considerations: a target helmet weight of 2 kg or less, mechanical fail-safe to prevent dangerous forces being exerted, electrical isolation

Additional specifications for the secondary application of time difference imaging of epilepsy are:

- Contact impedance mismatch of less than 20 %
- The contact impedance must be monitored and automatically controlled over time course of at least an hour
- Reactivation of abrasion routine after large patient movement

1.6 Purpose

The overall purpose of this thesis was to improve the experimental methodology of imaging brain function using EIT, with a particular focus on improving electrode application through the design of a novel servo electrode bearing helmet. Previous work, outlined in this chapter, indicates that imaging of acute stroke and focal epilepsy is feasible with EIT, but a multitude of technical limitations have precluded successful imaging from scalp recordings. The electrode helmet was designed primarily to enable imaging of acute stroke through EIT in an acute setting through rapid application of electrodes. The secondary purpose of the helmet was to address the significant problem of movement artefact and measurement drift in long term scalp recordings for the epilepsy and TBI applications of EIT. Validation of the helmet necessitated testing as representative a scenario as possible, collecting real EIT data on the scalp. The results on previous studies on the stroke ward, section 1.3.5, highlighted significant limitations in the measurement strategy, namely the SNR and modelling errors, which would mask any potential advantages conferred by the helmet design. Therefore the first two chapters of this thesis address these more fundamental limitations in EIT imaging of the head before reassessing the feasibility of imaging brain function in the subsequent chapter. With the feasibility established, the remaining two chapters focus on the design and testing of the helmet.

In chapter 2 the issue of modelling errors in tank studies was addressed through the design of novel anatomically realistic 3D printed head tanks. Previous work by Packham, Koo, Romsauerova, *et al.* [68] demonstrated significant distortions in MFEIT images of a tank without a skull present, and modelling errors introduced by mismatch between tank and mesh geometry was identified as an key limitation. To address these problems novel 3D printed tanks of both the adult and neonatal head were created based on a CT and MRI segmentation, which reproduced the spatial variations of the skull conductivity. Additionally, advances in meshing and imaging by Aristovich, Santos, Packham, *et al.* [61] and Jehl, Dedner, Betcke, *et al.* [63], previously limited to simulation and recordings in the anaesthetised rat, were adapted for head tank experiments.

Chapter 3 addressed the hardware limitations identified during previous clinical and tank experiments. Drift and SNR were described as key limitations during MFEIT experiments both in tanks [68] and on the ward [7] and in TD measurements of seizures in the EEG telemetry unit [30]. Since these studies, there has been significant focus on improved EIT systems both within the group at UCL [125] and the IIRC group at Kyung Hee University, South Korea [45], [110]. However, these EIT systems had yet to be assessed with regards to brain imaging from scalp measurements, so it was not understood if the limitations identified in previous hardware had yet been overcome. To this end a comparison study was performed of the UCL ScouseTom system [125] and the KHU Mk 2.5 32 Channel system [110], in order to select the most suitable system for future experiments. The noise dependence on frequency, current amplitude and load was investigated, as well as precision and noise in tank and scalp measurements.

The work by Fabrizi, McEwan, Oh, *et al.* [58] demonstrated that imaging conductivity perturbations similar to that expected from seizures in a head shaped tank was possible, but with the SNR of the systems available at the time, the number of averages required made clinical recordings infeasible. The culmination of the work in the two previous chapters and the advances by Aristovich, Santos, Packham, *et al.* [61] and Jehl, Dedner, Betcke, *et al.* [63] provided an opportunity to reassess the feasibility of imaging brain function. A tank study using a similar methodology to that employed by Fabrizi, McEwan, Oh, *et al.* [58] was conducted in the newly constructed adult head tank, using the UCL ScouseTom system. As had been identified by Gibson, Bayford, and Holder [33], the neonatal anatomy may be more conducive to imaging with EIT, therefore a study using the same methodology was also conducted in parallel to that in the adult tank. 10 % conductivity perturbations were reconstructed in three positions inside the adult head, and five positions in the neonatal head and the images compared in terms of localisation error, resolution and image distortion. A simulation study was also performed to estimate the localisation error of perturbations throughout the head with and without realistic noise. The final test of the feasibility was to investigate the median signal size in μV arising from these perturbations, which provided a minimum noise level which must be achieved for successful clinical images.

Finally, the final two chapters concern the main focus of the methodological improvements in this thesis: the design of the electrode bearing helmet. Despite the prevalence of abrasion during the application of electrodes for EEG and EIT, there is a paucity of objective information regarding the mechanical characteristics of the abrasion performed. Therefore, chapter five describes the investigation into the electromechanical requirements of the self abrading electrodes. To this end, the force applied during manual abrasion was characterised and a large scale test rig was designed in which the applied force, speed and torque of rotation could be independently controlled. The final chapter describes the design of a miniature self abrading electrode unit which meets the specifications outlined in chapter five, and a 32 channel electrode controller system. A prototype helmet which incorporated the self abrading electrodes was designed based on a reference head model scaled to the average head size. Finally, the helmet was then tested in scalp recordings and the extent to which the helmet met the requirements outlined in this chapter, as well as the clinical feasibility of such a system was assessed.

1.7 Statement of originality

The material presented in this thesis is my own work and has not been previously submitted for a degree in any University. The intellectual content of this thesis is the product of my own undertaking, yet research such as this is inherently interdisciplinary and collaborative, particularly when conducted by a group as cooperative and gregarious as the UCL EIT group. I received assistance regarding experimental design, style and presentation as duly acknowledged in the acknowledgements of this thesis.

Within chapter 2, I used a method of reproducing conductivity with surface perforations initially proposed and validated by Tugba Doru. The code to position the cylinders in a uniform grid on the surface of the skull was written by Dr. Kirill Aristovich. The forward solver PEITS was written by Markus Jehl who assisted me in its correct use.

The work in chapter 3 is indebted to Dr. Thomas Dowrick who developed the UCL ScouseTom system, and the members of the IIRC group in Kyung Hee University, South Korea, particularly Dr. Tong In Oh and Bishal Karki, who designed and built the 32 channel KHU EIT system. The improved power supply regulator was designed by Bishal Karki, in collaboration with myself and Tim Perkins. Scalp recordings were collected by myself in cooperation with Nir Goren.

The analysis of tank images in chapters 3 and 4 were based on code written by Dr. Brett Packham and Dr. Emma Malone. I received advice on the correct procedure for tank experiments by Dr. Packham throughout. The implementations of zeroth and first order Tikhonov regularisation were written by Dr. Kirill Aristovich and Markus Jehl respectively.

The data describing the performance of the linear potentiometer and servo motors in chapter 6 was collected by Jevgenij Dmitrijev, an MSc. student under my supervision. All subsequent processing and analysis was undertaken by myself.

Chapter 2

Novel anatomically realistic head tanks for EIT

2.1 Introduction

Phantom experiments are an important experimental tool for testing during the development of new hardware or software in medical imaging. Studies in phantoms represent a bridge between idealised simulation experiments and clinical measurements, in which the errors from the hardware and realistic noise can be added to measurements on a test object with properties known to match those used in simulations. Thus it is possible to investigate the errors arising from the hardware, the robustness of the imaging to these errors and gain an objective measure of the quality of the resultant images. Previous studies have successfully reconstructed realistic perturbations in a head phantom without the inclusion of a skull [58], [68]. However, reconstructions with the inclusion of a skull have only been successful with either non-biological perturbations [53], [78] or with large biological perturbations in the most superficial areas of the head [58], [126]. A recent simulation study demonstrated the feasibility of stroke EIT with smaller contrast perturbations [59], which suggested limitations with the head phantom existent in the UCL lab. Traditionally the conductivity of the skull has been represented as homogeneous across the surface [78], [127], however more recent studies showed the conductivity varies as much as 400 % across the surface [128]. Thus there was the potential for significant improvement in the phantoms used in head EIT experiments. This chapter describes the novel method of phantom construction in which the geometry obtained from a CT/MRI segmentation was replicated with high precision using rapid prototyping technology. Two phantoms were created using this method; an adult head phantom with spatially varying conductivity and a neonatal head tank with fontanelles.

2.1.1 Skull conductivity

The low conductivity of the skull is a problem unique to brain applications of EIT, and has been considered the most important factor limiting successful imaging [30]. Therefore it is essential for accurate simulations and phantoms experiments that the conductivity of the skull is modelled correctly.

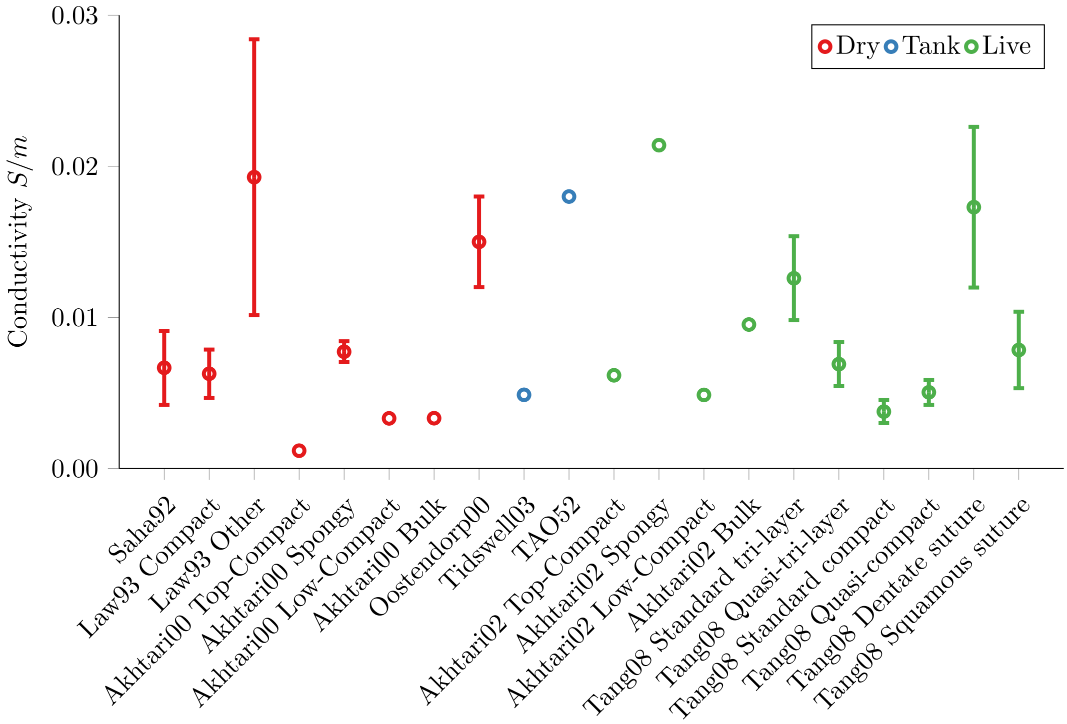

Figure 2.1: *various skull conductivities*

The conductivity of the skull is inhomogeneous due to variations in the tissue structure throughout [129]. Despite this, in EIT and other inverse source modelling applications it is common to consider the skull as having uniform conductivity and thickness [78], [127]. There have been numerous investigations into the conductivity of the skull and its variations with position, using either "dry" tissue from cadavers or "live" tissue measured soon after excision. A summary of these studies is shown in fig. 2.1.

The first detailed investigations into the variations of the skull conductivity were performed by Law [129] based on measurements of dry cadaver skull soaked in saline. The results demonstrated that conductivity varied with thickness as well as structure, and suggested a value of 0.006 S/m for the areas of the skull aside from sutures. However, this study and others based on a cadaver skull soaked in saline all suffer from an element of circular reasoning - the saline concentration used is based on assumed values of the conductivity of the interstitial tissue between the hard layers of bone [129], [130]. Studies on living tissue freshly obtained from patients undergoing surgery give generally lower estimates of the resistivity of the skull, and furthermore demonstrate that the skull could be divided into distinct layers as shown in fig. 2.2. The three primary layers are an inner and outer layer of compact bone and an internal layer of diploe - a spongey structure with its pores and cavities filled with tissues with a high fluid content [128], [131]. The ratio of diploe to compact bone has been shown to be highly correlated with the effective conductivity of skull in that region, and better explains the regional conductivity variations than the thickness, as shown in fig. 2.3 [128].

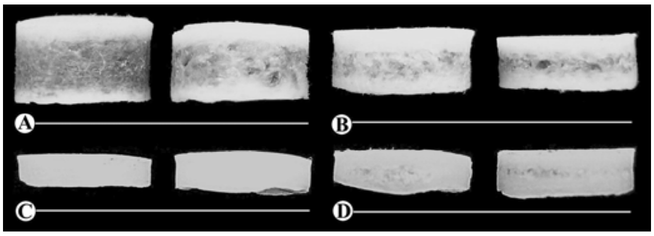

Figure 2.2: *Skull samples demonstrating tri-layered structure, with two outer "compact" bone layers and a inner spongey layer of diploe, from Tang, You, Cheng,* et al. *[128]*

These results from Tang, You, Cheng, *et al.* [128] represent the most systematic study of skull conductivity to date, and demonstrate a wide range in conductivities across the surface of the skull, from as low as 0.0037 S/m for the most compact bone to 0.0125 S/m for regions with the highest proportion of diploe. The sutures between the bone plates were shown to have a generally higher conductivity than the immediately surrounding bone [128]. The layered anatomy of the skull may also be the cause of the apparent anisotropy in its conductivity. A study by Sadleir and Argibay [132] demonstrated both in simulation and in phantom experiments that a high resolution FEM of three homogeneous layers can explain the anisotropy measured in skull plugs.

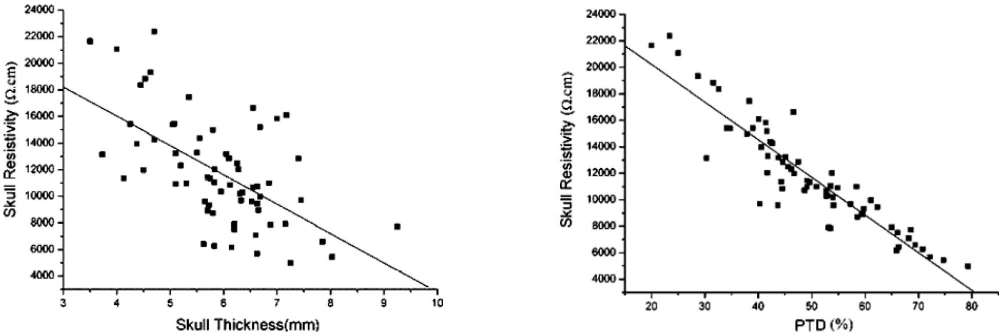

(a) *Thickness*

(b) *Diploe-skull ratio*

Figure 2.3: *Scatter plots demonstrating the correlation of skull resistivity with* ***(a)*** *thickness* $r = -0.596$ *and* ***(b)*** *percentage of diploe* $r = -0.917$ *from Tang, You, Cheng,* et al. *[128]*

Previous brain EIT studies have traditionally used a single value of the conductivity [59], [78], [127] which, in the light of the results from Tang, You, Cheng, *et al.* [128] and Akhtari, Bryant, Mamelak, *et al.* [131] is a poor representation of the real tissue conductivity. As the conductivity correlates best with the ratio of diploe, merely representing the thickness of the skull with a material of fixed conductivity will not represent the conductivity distribution accurately. Further, the value commonly used in the UCL group of 0.0048 S/m was based upon the results of Akhtari, Bryant, Mamelak, *et al.* [130] and Law [129] which, when compared to the literature in general, somewhat underestimates the real conductivity. Thus there was a clear need for a more realistic representation of the skull conductivity, both in simulations and in phantoms.

Neonate Skull conductivity

There has been less focus in the literature upon the conductivity of the neonatal and infant skull, with no in-vivo measurements in humans and the first mammalian conductivity values published as recently as 2011 by Pant, Te, Tucker, *et al.* [133]. The neonatal skull has a more complex structure than that of an adult skull, comprising of smaller bones connected by thin sutures and large openings known as fontanelles [134]. Moreover these smaller bones fuse together over a period of approximately two years, leaving behind the sutures seen in the adult skull [129]. This complexity and variability of the neonatal skull properties, coupled with the obvious difficulties in obtaining in-vivo measurements from skull plugs as conducted by Tang, You, Cheng, *et al.* [128], has necessitated the use of a range of conductivities when investigating neonatal brain function. One of the first impedance measurements of the neonatal head was performed by Murray [135] who suggested a range of conductivities between 0.033 to 0.2 S/m. These values present sensible upper limit based on the conductivity of most soft tissues in adults [136] and and a lower limit of the best estimate of adult skull at the time of writing. Despite a range encompassing the conductivities of nearly every human tissue, this estimate has persisted in the literature in the absence of a more detailed study [33], [137]–[140]. Thus it has been necessary for researchers to demonstrate the sensitivity of their chosen method to the potential conductivity of the skull by performing calculations with multiple models with varying conductivity. For example, Gibson, Bayford, and Holder [33] demonstrated that the size of the voltage changes for a realistic perturbation in the neonatal head varies by 15 % across the values suggested by Murray [135]. Tang, Oh, and Sadleir [140] created two separate models: “open skull”, where the fontanelles shared the same conductivity as scalp, and “closed skull” where they were set to the same value as the rest of the skull. The open skull demonstrated a 7-10 % increase in sensitivity in the centre of the brain.

To date the only in vivo estimate of a neonatal mammalian skull conductivity was performed by Pant, Te, Tucker, *et al.* [133] who measured the conductivity of skull plugs taken from a neonatal piglet model. The methodology was similar to that employed by Tang, You, Cheng, *et al.* [128], except measurements were only collected at single frequency of 1 kHz. Their results demonstrated that the conductivity was towards the lowest estimate of Murray [135], finding a value of 0.0358 S/m for frontal bones and 0.025 S/m for parietal bones. Similar to the conclusions of Tang, You, Cheng, *et al.* [128] it was noted the two bone types were of similar thickness, and the difference in conductivity was ascribed to differing fractions of the inner spongey layer. Pant, Te, Tucker, *et al.* [133] concluded a single value of 0.03 S/m for the overall conductivity, possibly increasing up to 0.04 S/m with consideration of the increase in conductivity with temperature.

Another factor unique to neonatal applications of head EIT is the changing structure of the developing skull. To date, no studies have investigated the age dependence of skull conductivity. Pant, Te, Tucker, *et al.* [133] showed there was no significant difference between the conductivity of full term and pre term piglet skulls, however the rate at which the conductivity reaches the adult values found by Tang, You, Cheng, *et al.* [128] is not descirbed in the literature. Additionally, the fontanelles, approximately 2.1 cm at birth, close over the course of several months, with 96 % closure rate at 24 months [134]. However, the median age of closure is 13.8 months, with 1 % of babies having closed fontanelles by as little as 3 months. This large variability not only in the tissue of the neonatal skull but also the geometry, presents a particularly difficult modelling challenge.

2.1.2 Head phantoms in EIT

The ideal phantom for EIT would accurately reflect the geometric and electrical properties of every tissue in the head, so as to simulate the current distribution in the head as realistically as possible. The irregular geometry of the head and the complexity of the internal tissues dictate that simplifications are often made. Cylindrical, hemispherical and spherical tanks are common as they are quick to achieve and do not require detailed FEMs [70], [127], [141], [142]. However, these shapes differ greatly from the real geometry and thus are of limited use when investigating the feasibility of brain EIT. Geometrically realistic head phantoms have been constructed for both EEG inverse source modelling [143] as well as for EIT specifically [78], [144], shown in fig. 2.4. Some simplifications are still necessary however. As the region of interest is the brain, the facial bones and structures like the ear canal and eyeballs are regularly not considered as they are difficult to model and their effect on EIT measurements still require investigation [78], [127], [141], [144], [145].

Modelling the electrical properties of the head tissues presents a more difficult challenge than mimicking the geometry, with the skull a particular challenge. As described in section 2.1.1 the skull has a high, spatially variable resistivity which cannot be represented with a single concentration of saline or gel [127], [141]. Anisotropy is traditionally considered negligible in EIT for the sake of simplicity, particularly in complex 3D geometry like the head [15], [53]. As the isotropic conductivity of the skull already presents a significant challenge in phantom creation, the anisotropy is commonly ignored. A new approach could be possible based on the results of Sadleir and Argibay [132], as the skull could be represented as three distinct homogeneous layers. However, the thin shell of the skull already presents a challenge when creating finite element models as there are large changes in voltage over a small volume, necessitating a large number of small elements. Moving to a three layer model would further exacerbate this problem, possibly resulting in a prohibitive number of elements in the FEM. The thinner shells, which in some places are less than a 1 mm thick [131] would also present a difficult challenge in phantom fabrication.

A simple spherical skull phantom, fig. 2.4a, was created by Liston, Bayford, and Holder [127] by casting plaster of Paris and soaking in calcium sulphate $CaSO_4$. Using this method it was possible to create a realistic conductivity of 0.012 S/m but it was difficult to control across the phantom, as the values were expressed only as a range of 0.008 to 0.013 S/m. A head tank formed of a clay model and employing a real human skull was produced by Tidswell, Bagshaw, Holder, *et al.* [78], shown in fig. 1.7b, and has been used successfully within the UCL group to image perturbations in time difference and frequency difference, under certain circumstances [54], [58], [68]. This tank was extended to also model the contact impedance with a skin of a marrow or giant zucchini in assessing electrode headnets. However, as described in section 2.1.1, it is the spongey diploe as opposed to the hard compact bone which defines the conductivity, and studies using dead tissue tend to underestimate the conductivity fig. 2.1. Further, the skull required soaking in saline for 48 hours before it was stable long enough to use for an experiment, and the resultant conductivity distribution was unknown [126]. Along with deterioration of the phantom, these are the likely sources of the error in simulated boundary voltages seen in fig. 1.10b.

(a) *Liston Spherical Tank* **(b)** *Sperandio Four Shell Tank*

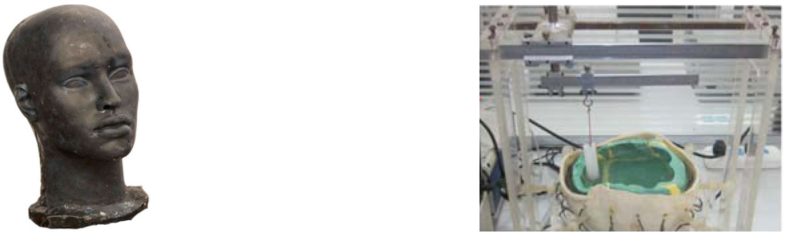

(c) *Collier Mannequin Tank* **(d)** *Li Resin Tank*

Figure 2.4: *3D head phantoms for EIT, **(a)** spherical tank from Liston, Bayford, and Holder [127], **(b)** four shell agar tank from Sperandio, Guermandi, and Guerrieri [141], **(c)** EEG phantom from Collier, Kynor, Bieszczad,* et al. *[143] and **(d)** anatomically realistic phantom from Li, Tang, Dai,* et al. *[144]*

Subsequently there have been efforts to create an improved head phantom with realistic, known conductivities. A hemispherical phantom was constructed by Sperandio, Guermandi, and Guerrieri [141], consisting of four concentric shells of agar gel thickened saline of differing concentrations. A volume conductive film (VCF) was placed between each shell to prevent diffusion between the differing concentrations in the regions. This material has an electrical conductivity similar to head tissues (0.2 S/m) but is impermeable, and thus prevents ion transfer. Unusually for head phantoms, this tank also included a layer representing CSF as well as those for skin, skull and brain. The phantom showed good agreement with simulated voltages at 100 kHz, accurately modelling the conductivity of the skull. However the VCF introduced a large reactance below 10 kHz, and thus would not be suitable for stroke studies as this is the frequency range of interest. To date, the most detailed work was performed by Li, Tang, Dai, *et al.* [144], who created an anatomically realistic head phantom, partially using rapid prototyping. The geometry was obtained from a CT segmentation, and resin molds created using selective-laser-sintering (SLS). The skull was divided into separate sections based upon the bone structure and resistivity values from Tang, You, Cheng, *et al.* [128]. Plaster soaked in calcium sulphate was used to mimic the conductivity of skull, a similar but more methodical technique to that of Liston, Bayford, and Holder [127]. The resistivity variations were replicated by varying the ratio of a mix of distilled water and dental-grade plaster. The problems in resistivity variation experienced by Liston, Bayford, and Holder [127] are not apparent. These were likely overcome through the use of an ultrasonic vibrator during the coagulation process and by allowing the resistivity to stabilise over 12 days during soaking. The results demonstrate the phantom resistivity was within approximately 3 % of the target value when measured directly. However it was difficult to assess the performance of the phantom fully, as only 2D simulations and reconstructions were performed, and only a subset of measurements were compared to simulations. Whilst both the four shell agar tank and the anatomically realistic tank produced accurate results when compared to the corresponding modelling, these methods were not capable of producing a continuously varying conductivity distribution. The resistivity in each section is defined by the plaster mixture, or by the saline concentration, and is uniform across that section [141], [144]. Thus in order for the conductivity to vary smoothly an impractical number of separate sections would be required to create the phantom. These phantoms also have practical disadvantages in that they are not suitable for sporadic use over the long term. The agar phantom created by Sperandio, Guermandi, and Guerrieri [141] required refrigeration between uses as well as thawing of five hours before data collection. The gypsum used in the phantom by Li, Tang, Dai, *et al.* [144] is moderately water soluble, and the solubility increases with saline concentration [146]. Thus repeated use may cause a drift in the resistivity.

Neonate head phantoms

To the authors knowledge, the only EIT phantoms created explicitly for neonatal brain imaging were manufactured by Tang, Oh, and Sadleir [140]. Initially a spherical design similar to those created by Liston, Bayford, and Holder [127] was built fig. 2.5a before construction of a simplified 3D printed head shaped tank the following year fig. 2.5b. The spherical tank consisted of two polycarbonate hemispheres containing stainless steel electrodes formed the outer layer, and saline of conductivity 1.2 S/m was used to match the CSF. Intraventricular haemorrhages were simulated using agar gel spheres of 0.67 S/m, placed in the centre of the phantom. The geometry used in the head shaped phantom was a smoothed reference model used in previous studies [36]. The model has to be adjusted to fit within the constraints of the printer used. As with the spherical tank, CSF was replicated as saline of conductivity 1.2 S/m. Unlike the models used in simulation in these studies, there was no skull present in either of these phantoms. With increased interest in neonatal applications of EIT, and only simple phantoms available in the literature, there was a clear need for a realistic phantom for neonatal EIT.

(a) *Spherical tank*

(b) *Smoothed head tank*

Figure 2.5: *Neonatal head phantoms.* ***(a)*** *spherical tank by Tang, Oh, and Sadleir [140],* ***(b)*** *smoothed head shaped tank by Tang and Sadleir [36]*

2.1.3 Modelling conductivity

A new method of reproducing the conductivity of skull using 3D printing has been proposed by [77], wherein an anatomically realistic skull model was printed directly out of insulating plastic. Cut into the surface of this skull are many small holes of a known cross-sectional area, which allow saline to pass through, and thus enable current to flow through the skull. The exact resistivity can be controlled by ratio of solid insulating plastic to saline within the holes, either by altering the density or diameter of these holes. This method provides a discontinuous resistivity on a microscopic scale, which is not representative of real skull tissue. However the method was been shown to be effective on the larger macroscopic scale at which EIT operates. The effective resistivity can be approximated through a simple estimation of the area ratio eq. (2.1).

$$\rho_{eff} \approx \frac{A_{tot}}{A_{saline}} \rho_{saline} \tag{2.1}$$

Experiments by Doru, Avery, Aristovich, *et al.* [77], fig. 2.6, demonstrated that in test phantoms, with sufficient density of holes, this calculation was sufficient to explain the effective conductivity to within 3 %. Moreover, errors from surface curvature and tortuosity effects - from the increased path length - are less than 2 % for the expected curvature of the head. These errors are of a similar order to those found by Li, Tang, Dai, *et al.* [144] for a plaster skull phantom. Therefore this method of surface perforation was suitably accurate to represent the conductivity of the skull. The other benefit of this method compared to those proposed by Li, Tang, Dai, *et al.* [144] and Sperandio, Guermandi, and Guerrieri [141], was that the conductivity can vary smoothly across the phantom, as opposed to a fixed value per segment.

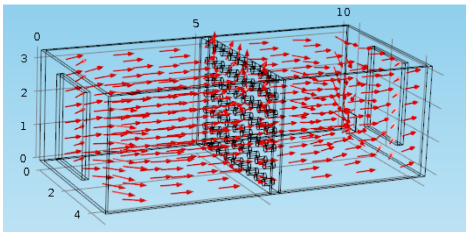

Figure 2.6: *Simulation of current flow through surface mimicking skull resistivity, from Doru, Avery, Aristovich,* et al. *[77]*

2.1.4 Reproducibility of tanks

There are a number of factors influencing brain EIT images relevant to phantom construction that are still under investigation in the community. Namely, mesh accuracy [61], [64], [93], minimum electrode number and ideal electrode positions [53], [58]. Altering the number of electrodes or their locations necessitates the construction of an entirely new phantom, which is often labour intensive and may not be reproducible as many phantoms are at least partially handmade, particularly for complex geometry [78], [127], [141]. Additionally, the extent of the dependence of localisation accuracy upon correct representation in the forward model is still a matter of interest, as the inclusion of erroneous prior information can lead to worse images than using a simple model [64], [140]. Thus a manufacturing method capable of rapid, repeatable iterations would be of particular benefit, enabling studies that would be prohibitively time consuming otherwise. A phantom created directly by rapid prototyping would meet this criteria as the results would be within the tolerances of devices (< .5 mm) and require little manufacturing expertise.

2.1.5 Purpose

The purpose of this study was to create head phantoms for EIT of both the adult and neonatal head with realistic geometry and skull conductivity, to improve the testing of algorithms and hardware for the imaging of brain pathologies. The solution proposed was the design and manufacture of phantoms based on an MRI or CT segmentation, and constructed using a 3D printer. The phantoms were constructed of insulating plastic for both the scalp and skull, which resulted in phantoms that were stable over time, and repeatable across phantoms. The conductivity variations of the skull were represented by the method proposed by Doru, Avery, Aristovich, *et al.* [77] in which holes are distributed across the surface of the purely resistive skull, enabling the effective volume of saline, and thus the conductivity to be controlled. The secondary purpose of this study was to investigate the extent to which the boundary voltages collected experimentally match simulation. Successfully validated, these phantoms had the potential to be the first standardised tanks for head EIT, easily reproducible by other researchers in other institutions.

2.1.6 Experimental Design

A novel method of creating head phantoms in EIT was developed, in which 3D printed tank and skull could, for a given concentration of saline, represent the geometry and spatially variable skull conductivity. Two head tanks were created, one of the adult head based on an MRI segmentation performed by Markus Jehl [63] and one of a neonatal head based on a separate CT segmentation. These segmentations were first converted into STL meshes, which were smoothed and extraneous features removed before being converted into CAD models for use in tank construction. The desired conductivities of each skull were determined from the literature review in section 2.1.1, and a series of perforations were cut into the models so as to mimic the conductive properties of the skull. The phantoms were then constructed by 3D printing the models using a consumer grade desktop 3D printer.

To the validate the manufacturing method, the geometric accuracy was tested through a deviation analysis comparison of the final 3D model to be printed, and a high resolution 3D scan of the adult tank. Further validation was performed by a comparison of boundary voltages simulated using a high resolution mesh of the solid models, and those obtained experimentally. The final validation was a comparison of simulated and experimental voltages with the skulls included in the phantom.

2.2 Methods

2.2.1 Segmentation to Solid Model

The geometry for the phantoms were obtained from segmentations of an MRI in the case of the adult head, and a CT scan for the neonatal head. The resolution of these scans were 1 mm or less in all 3 dimensions, which provided sufficient resolution to obtain segmentations of the scalp, skull, dura, grey and white matter and CSF in the adult MRI [63], and the scalp and skull in the CT. Creating tanks from these segmentations required the geometry to be represented as a parametric model used in CAD. This was performed in two stages: first the segmentation was saved as a surface triangulation mesh, in doing so the quantisation artefacts from the resolution of the MRI were clearly visible, fig. 2.7. As the quoted accuracy of the 3D printer used to create these phantoms was 0.2 mm, and would add unnecessary computational overheads when creating a solid model, these artefacts required smoothing before continuing to a solid model. Smoothing was first performed in Mesh Lab before trimming of extraneous features and further artefact removal in FreeCAD. FreeCAD was also used to convert this smoothed geometry to a parametric model ready to create a model ready to print. An overview of this process in shown in fig. 2.7.

Adult Tank

The segmentation used for the adult tank included 7 separate layers for different tissues in the head, of which only the scalp and skull layers were of interest for the adult tank. The structure of particular interest was the cranial cavity, and the areas of the scalp were electrodes were commonly attached. Therefore the segmentation was simplified by combining the scalp with the ear canal, nasal cavity and eyeballs to provide a single layer encasing the skull, shown in fig. 2.7. Similarly, the internal space within the skull was simplified by combining all dura, csf, grey and white matter layers into a single cavity, which will be represented as a single layer of saline in the final tank. Further geometric simplifications common to other head tanks were also performed, the ears, neck and face were trimmed from the scalp layer, similarly the jaw, nose and face were trimmed from the skull layer so as to leave only the bone which envelops the brain. The creation of the final scalp and skull models are described in fig. 2.7.

Neonatal Tank

A segmentation of CT was performed to obtain the geometry for the neonatal skull, as with the adult tank, only the scalp and skull layers were of interest. The tissue within the fontanelles was combined with the brain and scalp layers in order to fully isolate the skull. The geometrical simplifications performed for the adult tank were repeated for the neonatal segmentations. Additionally, the smoothing of the CT artefacts was constrained to the areas of skull away

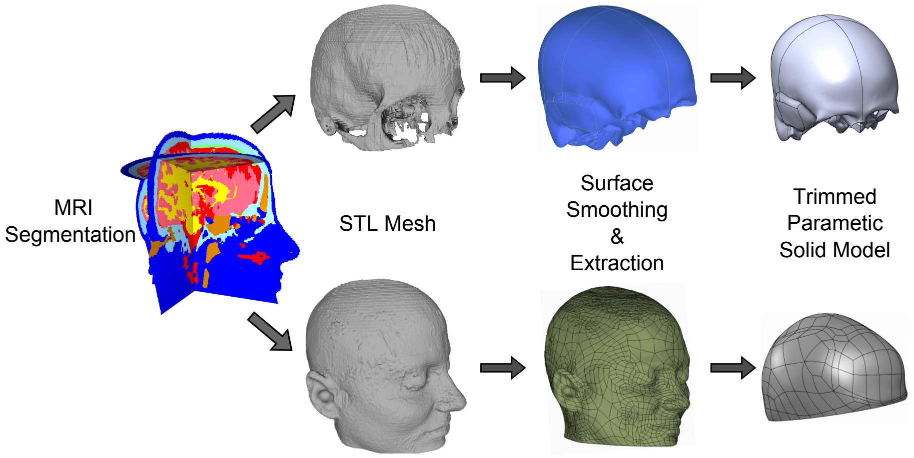

Figure 2.7: *Workflow to create solid models from an MRI segmentation for the design of the adult tank*

from the fontanelles so as to ensure the more complex geometry was preserved. To facilitate the surface extraction of the skull the frontal, occipital and parietal bones were isolated and modelled independently. These models were then recombined during the creation of the CAD solid model. The creation of the final scalp and skull models are demonstrated in fig. 2.8.

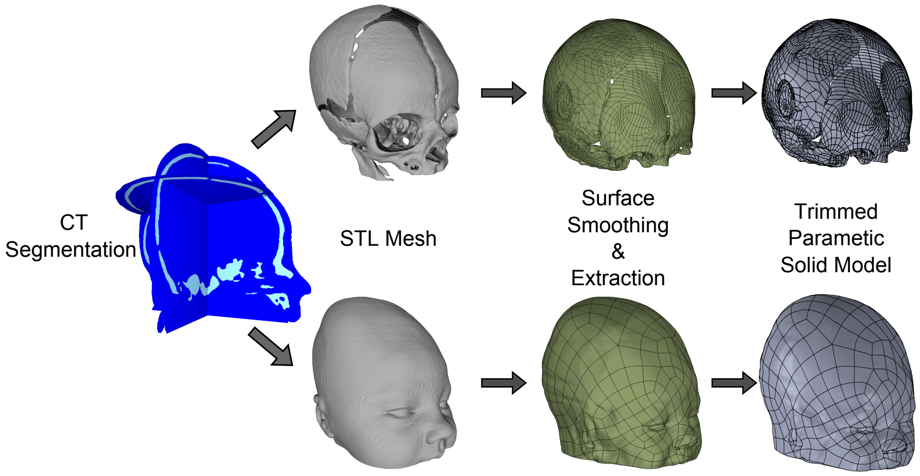

Figure 2.8: *Workflow to create solid models from a CT segmentation for the design of the neonatal tank*

2.2.2 Electrode Positioning

In both tanks 32 electrodes and a ground electrode were positioned on the respective scalp model based on the distributions proposed by Tidswell, Gibson, Bayford, *et al.* [53], which includes 21 positions from the EEG 10-20 system [56], eight from the extended 20-20 and five additional positions. These additional positions include modified positions from Tidswell, Gibson, Bayford, *et al.* [53] which places two electrodes above the mastoid bones behind each ear and two above the occiput at the back of the head. These were instead slightly repositioned to match points in the 10-10 extension [147], the electrodes behind the ear were moved to TP9 TP10, and the occiput electrodes were moved to posisions I1 and I2. The additional electrode was placed in the last remaining gap, position P0z at the back of the head, to provide even coverage of the head and a greater number of possible injections through the skull.

In the case of the neonatal head the electrodes at the back of the head were deemed too close together with the above configuration for the adult head. In this instance the two electrodes at the traditional 10-20 system locations of P3 and P4 were moved to locations P1 and P2 from the 10-10 extension, and two electrodes at the occiput were instead located at locations PP07h and PP08h from the 10-5 extension proposed by Oostenveld and Praamstra [147]. This provided an even coverage of electrodes across the scalp, whilst maintaining a configuration compatible with electrodes used clinically. It was noted that during placement in the model it would be possible to adjust the positions of several electrodes to be in line with the fontanelles, potentially improving the SNR by decreasing the amount of current diverted by the skull. However, the clinical EEG 10-20 locations were maintained as clinical compatibility was deemed more important for use in subsequent feasibility studies, and the location and size of the fontanelles may not be known *a priori* in clinical experiments.

The electrodes could be located precisely on the model mimicking the method used in clinical EEG practice by measuring by defining certain points and measure along the circumference. Therefore these positions reflect the "ideal" locations which could be obtained in practice.

2.2.3 Tank design

The design of the tank is detailed in fig. 2.9 using the neonatal tank as an example. First, the solid model of the scalp was duplicated and scaled by 10 % with respect to the centroid. A boolean subtract operation was then performed to create a hollow scalp with the internal cavity equivalent to that of the original scalp model. The shell was then cut along a plane which was parallel to the plane described by the inion-nasion line, the height of this plane was chosen so as to include the entirety of the brain cavity yet remove as much of the neck and facial structures as possible. This plane also defines the height of the saline within the tank, and thus the perimeter of the model used for mesh generation in 2.2.5. The walls of the tank were then extended to create a lip to prevent spillage of the saline when used in experiments. The locations of the electrodes were then imported from the model described in 2.2.2 and used to define axes normal to surface at each point. Models of the electrodes were then placed at each point and aligned with the axis normal to the surface, which is the closest possible approximation to how such electrodes would be applied in practice. Another boolean subtraction was performed for each of these electrode models, resulting in the complete geometry for the tank. The electrode models used to create the recesses was 0.2 mm larger in diameter to account for errors in printing, and 1 cm thick at the face to ensure all material was cleared away and all of the electrode surface was in contact with the saline. Finally support legs and a flat base were added to the scalp to create the finished tank model, fig. 2.10.

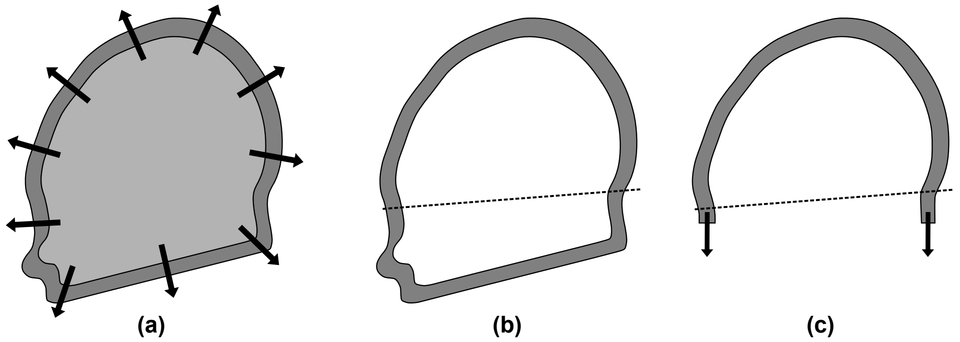

(a)
Scalp duplicated and scaled

(b)
Inner space removed
and model cut below
inion-nasion line

(c)
Tank walls extended

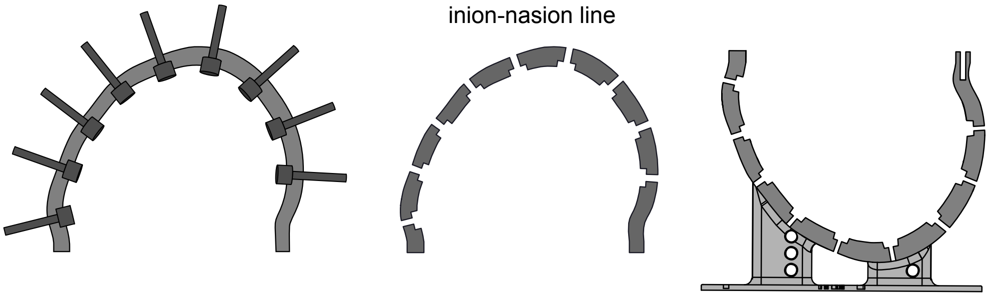

(d)
Electrode placement

(e)
Tank with electrode spacers

(f)
Final tank model

Figure 2.9: *Design of tank models.* ***(a)*** *the scalp model is duplicated and scaled by 10%,* ***(b)*** *the inner scalp surface is removed and the shell split below in inion-nasion line,* ***(c)*** *the model is trimmed and the walls vertically extended 1cm,* ***(d)*** *models of the electrodes with clearance are positioned according to 2.2.2,* ***(e)****, the clearance electrodes are removed from the tank volume,* ***(f)*** *Supports add and model is finalised*

2.2.4 Anatomically realistic skull design

The methodology to create the skull phantoms was similar to that used to create the scalp tanks, this process is outlined in fig. 2.11, again using the neonatal skull as an example. The solid model of the skull was cut along the same plane parallel to the inion - nasion line to leave only the bone encasing the brain and the resultant flat surfaces were extended vertically to match the height of the tank walls. A boolean subtraction was used to create the holes in the skull, by removing cylinders the described in section 2.2.4. The supporting structures were added which enable the skull to be suspended in place inside the tank. Localisation error was minimised by bolting the pieces together through corresponding concentric holes in the walls of the tank and the skull supports. In the case of the neonatal tank, the diameter of the skull meant it would not fit through the opening at the top of the tank. So the skull

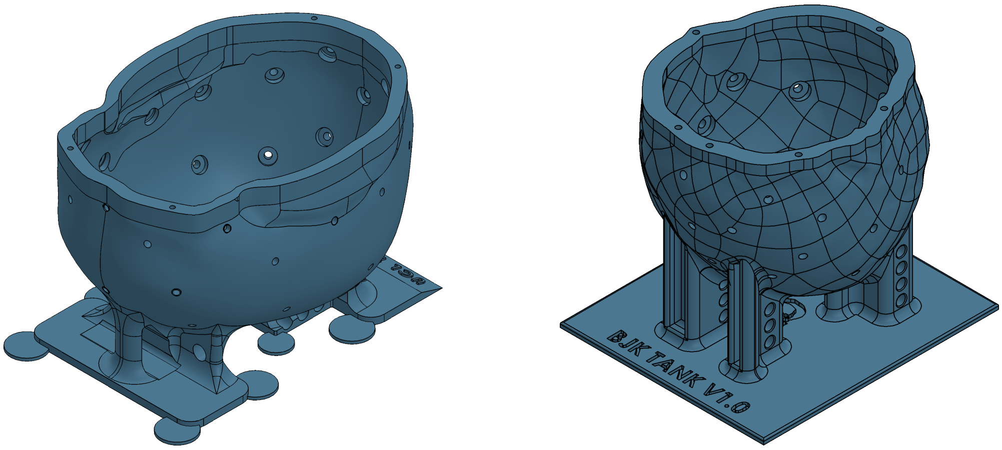

(a) *Adult tank*

(b) *Neonatal tank*

Figure 2.10: *Completed tank models for* ***(a)*** *adult head and* ***(b)*** *neonatal head*

was split into two parts along the lambdoid suture between the parietal and occipital bones, which could then be inserted sequentially into the tank.

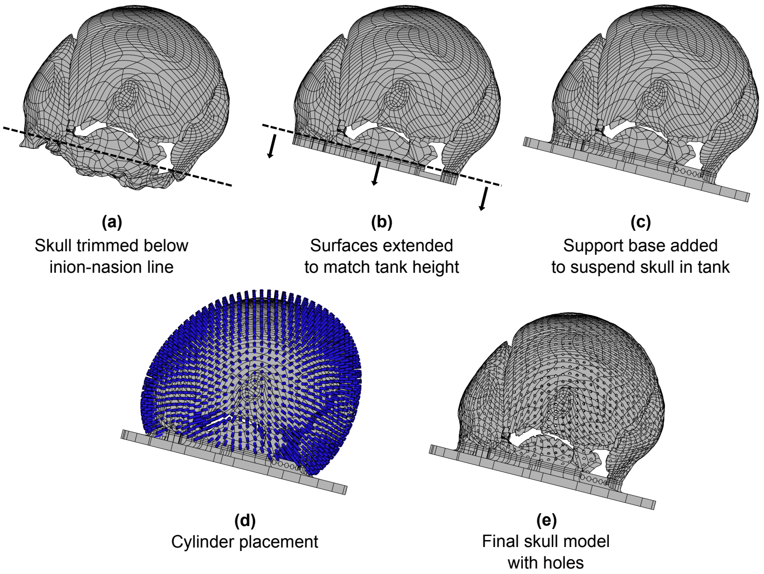

Figure 2.11: *Design of skull models.* ***(a)*** *the skull model is split below in inion-nasion line along the same plane as fig. 2.9,* ***(b)*** *the model is trimmed and the walls vertically extended 1cm to match the height of the tank walls,* ***(c)*** *a support base is added which is used to position the skull precisely in the tank,* ***(d)*** *cylinders are created centred around the points defined in 2.2.4 normal to the surface,* ***(e)****, the cylinders are removed from the tank volume giving the final skull model*

Conductivity distributions

The conductivity for the adult skull was taken from the results from Tang, You, Cheng, *et al.* [128] at 1kHz, described in 2.1.1. The spatial distribution of the different skull tissue types identified were not described until the publication of the anatomically realistic phantom by Li, Tang, Dai, *et al.* [144], outlined in section 2.2.4.

Position	Bone Type	Conductivity S/m
Frontal Bone, Occipital Bone	Standard Tri-Layer	0.0126
Parietal Bone	Quasi-tri-layer	0.0069
Sphenoid Bone, Temporal Bone	Quasi-compact	0.0050
Parietotemporal Suture	Squamous Suture	0.0078
Lamdoid, Coronal & Sagittal Suture	Dentate Suture	0.0173

Table 2.1: *Conductivities of human skull from Tang, You, Cheng,* et al. *[128] measured at 1 kHz*

The Sphenoid and Temporal bones at the side of the head are of the same “Quasi-compact” bone type. The Frontal and Occipital bones at the front and back of the head are both “Standard Tri-Layer”. The conductivity at the top of the head - the Parietal bone, is of the ”Quasi-tri-layer’ type. Thus, starting from the top of the head, the conductivity increases by 87 % towards the front and back of the head, and decreases by 32 % towards the sides. This distribution was modelled using eq. (2.2) as follows: the central point at the top of the skull was defined as the origin with a baseline conductivity $\sigma_0 = 0.0069\text{S/m}$. The conductivity at any point in the model was a linear combination of a linear increase in conductivity towards the front and back (x direction) of the skull and a linear decrease in conductivity towards the sides (y direction). The resultant distribution of conductivities is shown in fig. 2.12, and compared to the literature as shown fig. 2.15.

$$\sigma_{xy} = \sigma_0 \left(1 + 0.87\frac{x}{x_{max}} - 0.32\frac{y}{y_{max}} \right) \tag{2.2}$$

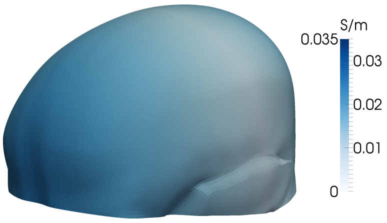

Figure 2.12: *Conductivity distribution of adult skull*

As the distribution is not well understood in the literature, the conductivity for the neonatal skull phantom was fixed at a value of 0.03 S/m as suggested by Pant, Te, Tucker, *et al.* [133] was chosen.

Hole Placement

To calculate the positions of the holes in the model an algorithm was written by Dr. Kirill Aristovich, which iteratively places holes based on an equispatial point distribution on the tetrahedral mesh of the skull model (section 2.2.5). An initial point p_0 was chosen in the geometric centre of the surface, and two new points p_{x1} and p_{y1} were placed along the orthogonal directions associated with the curved surface. This process is repeated with the constraint that the distance to all neighbouring points should be equal, until no new points can be added. The result of which is equidistant points distributed across the entire surface of the skull, shown in fig. 2.13a using the adult skull as an example.

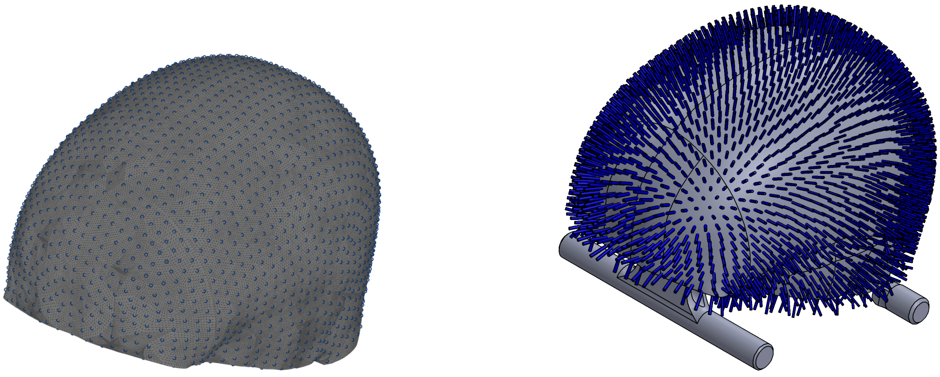

(a) *Hole locations* **(b)** *Cylinder placement*

Figure 2.13: *Calculation of hole location and size for the adult skull,* ***(a)*** *equispatial points,* ***(b)*** *cylinders aligned normal to model surface at each point*

The diameter of each hole was then calculated based upon the required σ from eq. (2.2), and the area calculated from eq. (2.1) assuming 0.2 % concentration of saline. Cylinders were then generated in FreeCAD, centred at each point, aligned to the normal of the surface and of the required diameter as shown in fig. 2.13b. The cylinders were then removed from the skull model using the same boolean subtraction to create the electrode recesses in section 2.2.3.

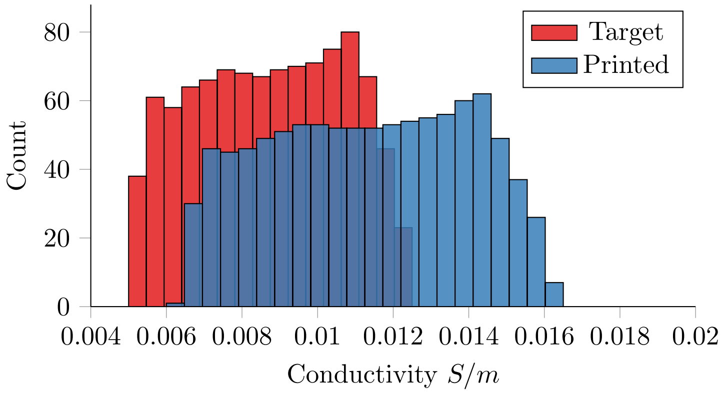

Figure 2.14: *Comparison of σ values for target and adjusted adult skull*

It became clear that during the printing of the skull that the hole size required at the sides of the skull to represent the conductivity of the temporal and sphenoid bones was too small to be printed correctly, due to the resolution of the printer. To compensate for these errors and ensure an equivalent spatial distribution, the conductivities were recalculated using a σ_0 value of 0.009, an increase of 30 %. The range of conductivities, shown in fig. 2.14, was thus increased from 0.005-0.0125 S/m to 0.006-0.0165 S/m. These new conductivity values are still within the range demonstrated in the literature, shown in fig. 2.15, but represent an above average distribution compared to the measurements by Tang, You, Cheng, *et al.* [128].

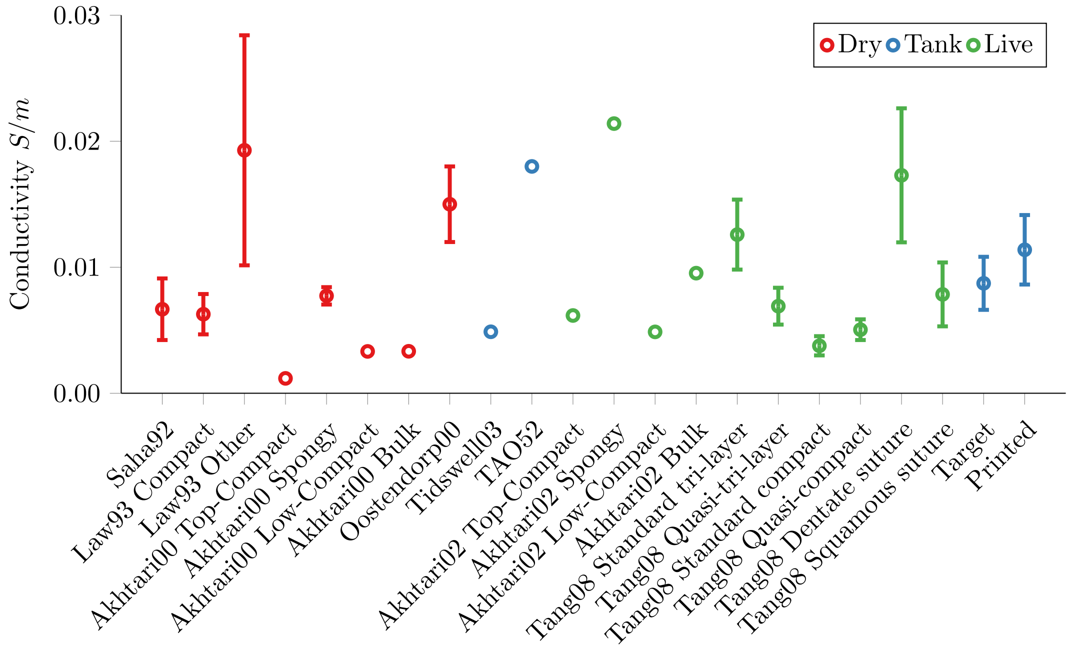

Figure 2.15: *Skull conductivities from the literature in comparison with target and adjusted adult skull conductivities*

Final Skull Models

The completed skull models are shown in fig. 2.16.

2.2.5 Construction

Printing

Rapid prototyping (also referred to as “3D printing” or “Additive Manufacturing”) is becoming increasingly common in medical applications for both education, surgical planning and research [148]. The most commonly used 3D printing technologies in medical applications are Selective Laser Sintering (SLS) wherein particles of thermoplastic or metal powders are fused together by a laser, or Stereolithography (SLA) where photopolymers are cured by UV light [149]–[151]. However, these are industrial standard technologies, which require handling by experienced technicians. SLS parts were investigated for this study, but the results were

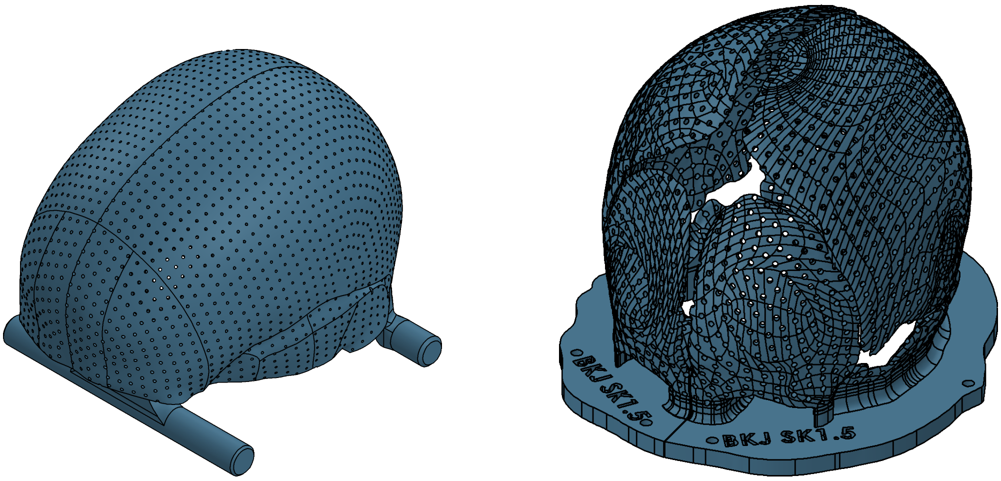

(a) *Adult skull* **(b)** *Neonatal skull*

Figure 2.16: *Completed skull models for **(a)** adult head and **(b)** neonatal head*

found to be porous, and as such not suitable for saline tanks. This study focused instead on Fused Deposition Modelling (FDM) printers, which create models by extruding small beads of thermoplastics which bond to the layer immediately underneath. These printers are less accurate than SLS or SLA, with layer heights typically 100 microns compared to 37 microns [152] or less for SLA printers Objet. However, FDM printers are more widely available due to their significantly lower cost, < £2000 [152] compared to > £25,000 for a standard SLS printer [153]. For this reason FDM printers are becoming increasingly common in many institutions, even in labs without other workshop facilities [154]. By designing the models to fit within the specifications of a common FDM printer, the phantoms could easily be replicated by other researchers, creating the potential for these phantoms to become a standard for head EIT.

The phantoms were created using a Makerbot Replicator 2 Desktop 3D printer (fig. 2.17), a common hobbyist-level FDM 3D printer. The models are printed in polylactic acid (PLA), a biodegradable thermoplastic with a build volume of 285 x 153 x 155 mm. The rated accuracy of the printer is 0.1 mm in the X and Y dimensions and user controlled within a range of 0.1 to 0.4 mm in the Z direction [152].

The limitations of the printing processes were such that a maximum 1 kg material could be used at one time and the maximum build volume was of 285 x 153 x 155 mm. Thus excess material in the supports and base were removed for both tanks to keep the model within these limits. The final adult tank model was just within these limits, requiring 998 g of material and within 3 mm of the maximum Y and Z dimensions of the build volume. To achieve this the supports for the skull, described in section 2.2.4 had to be separated and printed separately. The Z height limitations also required the supports to be shortened and the length of the electrode protruding from the tank to be cut by 1 cm. These modifications were performed

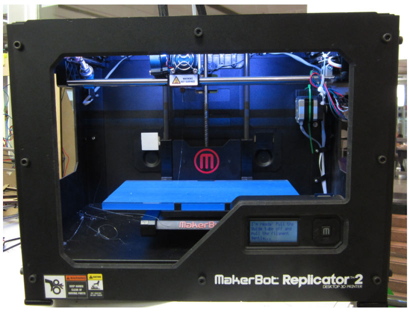

Figure 2.17: *The 3D printer used to create the tanks, The Makerbot Replicator 2 from Makerbot Ind.*

to ensure the tank could be printed as a single piece, thus minimising the risk of leaks or mis-alignment at the joins and limit the amount of work required after printing.

Of the myriad settings which could be altering during the printing the most significant were the Z layer height and the infill ratio, which determines how much of the internal structure of the model is filled in during each layer. For all models the infill ratio was set to 100 % to make the models entirely solid to prevent any leaks during use and the layer height was set to 0.2 mm to reduce the build time to less than 48 hours. Another important aspect to printing with FDM printers is the inclusion of supports. Overhangs in the model cause droop in the extruded material, and thus require a support scaffold, added automatically by the printer software. Supports prevent print failures but necessitate cleaning by hand where these scaffolds come into contact with the model.

Post Processing

Once the models were printed, they were post processed by hand to clean up the artefacts from the supports and from the surface of the build platform. The holes in the skull were individually cleared with a drill bit to ensure the holes were clear of any support material or printing artefacts. The PLA models were brushed with acetone to smooth the layering artefacts and ensure the binding of the outer layers, finally the models were rinsed in a jet wash and blasted with compressed air.

Electrodes

The electrodes used in both phantoms were 316 stainless steel, referred to as “marine grade" or “surgical steel". When choosing material electrodes for a tank there is a trade off between corrosion resistance and contact impedance (section 1.4). Stainless steel is commonly used due to its high corrosion resistance [127], [140], thus minimising the intra and inter measurement drift, whilst easily available and relatively inexpensive. However this comes at the expense of greater contact impedance compared to Ag/AgCl electrodes which are also commonly used [53], [144]. Silver electrodes are commonly thin discs stuck onto the side of the tank walls by hand, which makes localisation with sub mm precision difficult. Another reliability issue with Ag/AgCl electrodes is that the thin chloride layer is prone to removal through scratching or abrasion, which would alter their properties over time. These errors along with corrosion of the silicon seals could be a source of the errors in the voltages seen in fig. 1.10. Stainless steel electrodes are extremely robust and comparatively inexpensive, and can be made in a shape to fit the recesses described in section 2.2.3, and were thus chosen for these phantoms.

The electrodes were hammered into place to ensure a strong friction fit, and further sealed with silicon adhesive to prevent any leaks and to prevent saline entering into the space behind the electrode and changing the effective surface area. The contact impedance measured in all subsequent studies was found to be 224 ± 25 Ohm.

Completed Phantoms

The final constructed phantoms are shown in fig. 2.18

(a) **(b)**

Figure 2.18: *Completed phantoms for* ***(a)*** *adult head and* ***(b)*** *neonatal head*

Meshing

To create the tetrahedral meshes for each tank, a combined model of the skull inside the tank was created. The inner tank surface was extracted and capped with a planar surfaces flush with the electrode surfaces and one coincident with the saline level. This was then combined with a model of the skull which had also been trimmed along the saline level. Meshes of these models were then created in COMSOL with an element size of 2 mm and 1.4 mm for the adult and neonatal tank respectively. These values were chosen to provide meshes an equal number of elements, 4.2 million for the adult tank and 4.5 million for the neonatal head.

2.2.6 Geometry testing

Geometry analysis is important in assessing the precision of the resulting phantom, and, given the novelty of the construction of these tanks, in the validation of the feasibility of the manufacturing method.

Quantification of the manufacturing precision is made difficult by the irregular morphology of the head. Collier, Kynor, Bieszczad, *et al.* [143] avoided quantification altogether and merely cite the nominal precision of the moulding technique used, which represents a best-case value. One solution proposed by Li, Tang, Dai, *et al.* [144] is "shape distortion", wherein distances between key points are measured by hand, and the error expressed as a percent of the original distance. The errors found ranged from 0.02 to 0.56 mm, or 0.02 to 2.01 %, with a mean of 0.18 mm or 0.75 %. However, these measurements were only in relation to the resin-casted model *after* printing, rather than in comparison to the desired CAD model. A similar approach is taken in assessing the error in skull models used to aid maxillofacial surgery. Wherein linear measurements between landmarks in the printed skull and either a CT image, or a dry skull are compared. Mean errors between 0.65 and 2.1 % have been reported [149], which is consistent with the results from Li, Tang, Dai, *et al.* [144].

The methods currently employed in the literature have two drawbacks: measurements are not compared to the CAD model which is to be used in simulations and they do not adequately capture the irregular morphology of the head. The method proposed in this study is "deviation analysis", a common reverse-engineering technique used in many industrial applications [155], in which the surfaces of the CAD model are compared to a high-precision laser-scanned model of the part. This provides a measure of the deviation of the manufactured tank to the surfaces in the CAD model across the entirety of the model.

Deviation analysis

The tank was scanned using a Creaform Go!Scan20 [156], a hand-held scanner used for reverse engineering components in the field. The result of which is a high resolution mesh of the tank surface, as seen in fig. 2.19, with an accuracy of < 0.2 mm and > 2 million elements. Scanning targets were placed upon the model to enable registration and alignment of the resulting mesh with the solid model created in section 2.2.3.

To simplify the analysis, only the inner surface of the tank was considered. Additionally, the reflective surfaces of the electrodes in the tank caused artefacts in the scanning process, and thus they were removed from the model before the deviation calculation.

Figure 2.19: *Mesh of adult tank produced by 3D scanning*

2.2.7 Comparison to simulation

Data collection

Data were collected in both tanks using the BioSemi-Keithley EIT system, a parallel record system described in further detail in chapter 3. The “optimal” protocol, proposed by Malone, Jehl, Arridge, *et al.* [59], designed to maximise the distance between the electrodes while acquiring the maximum number of independent measurements, was used for experiments in the adult head tank. An “offset” protocol with 32 injections was used for the neonatal tank measurements, where a fixed offset of 4 electrodes was used between each source and sink. This was chosen to give the highest possible number of opposite injections, and represents a protocol suitable for imaging in the head.

In all experiments, the current injected was 200 uA amplitude at 1 kHz, with 75 ms per injection and 20 averages. The tanks were filled with 0.2 % saline with a conductivity of 0.4 S/m, to represent the scalp. Experiments were performed first without the skull present, and then with the skull in place.

Data analysis

The boundary voltages collected in each experiment were compared to simulation using the Parallel EIT Solver (PEITS) created by Jehl, Dedner, Betcke, *et al.* [63]. Voltages were recorded on the injection channels but these were discarded. The error was calculated as the absolute difference between the experimental and simulated voltages for each measurement. The result is then displayed as a grid to highlight the electrodes or injections with the greatest error. The errors were summarised as a mean and standard deviation for each dataset in absolute voltage. The error was also calculated as a percentage of the simulated voltage. Measurement channels with a simulated voltage less than 0.1 mV were removed from this analysis, based on the threshold described by Packham, Koo, Romsauerova, *et al.* [68], to avoid over estimation of the noise.

2.3 Results

2.3.1 Geometry analysis

The mean deviation was 0.21 mm with a standard deviation of 0.101 mm. Largest deviation measured was 2.3 mm. The distribution of the geometrical errors are shown in fig. 2.20.

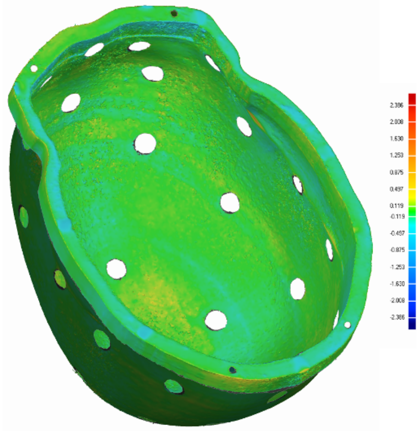

Figure 2.20: *Deviation analysis of head shaped tank*

2.3.2 Comparison to simulation

Adult Tank

The simulated and experimental voltages in the adult tank without skull using the optimal protocol are shown in fig. 2.21. The mean error across all measurements was 0.147 ± 0.099 mV. The largest errors were found in injection 2 and electrode 9, with a mean error of 0.251 and 0.233 mV respectively. The error across all recordings is shown in fig. 2.22.

Neonatal Tank

The simulated and experimental voltages in the neonatal tank without skull are shown in fig. 2.23. The mean error across all measurements was 0.079 ± 0.062 mV. The largest errors were found in injection 8 and electrode 28, with a mean error of 0.187 and 0.132 mV respectively. The error across all recordings is shown in fig. 2.24.

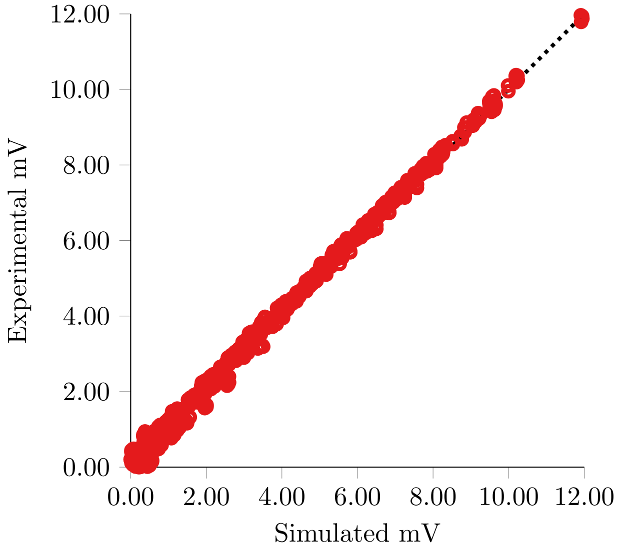

Figure 2.21: *Comparison of voltages in adult head tank with optimal protocol*

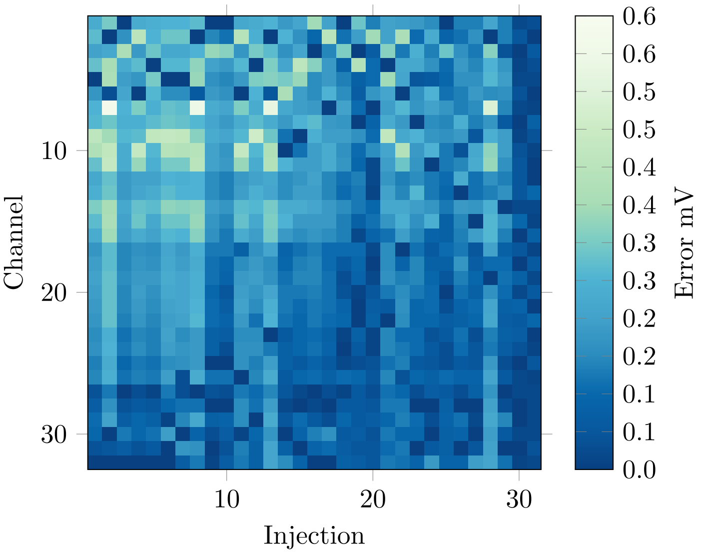

Figure 2.22: *Error Across injections in adult head tank with optimal protocol* $R = 0.9985$

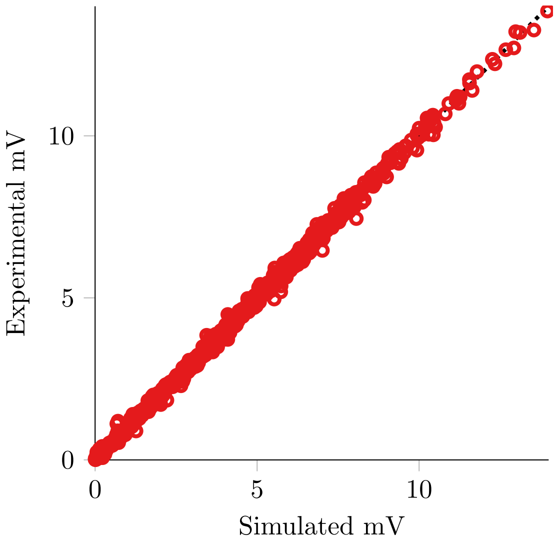

Figure 2.23: *Comparison of simulated and measured voltages in neonatal head tank* $R = 0.9992$

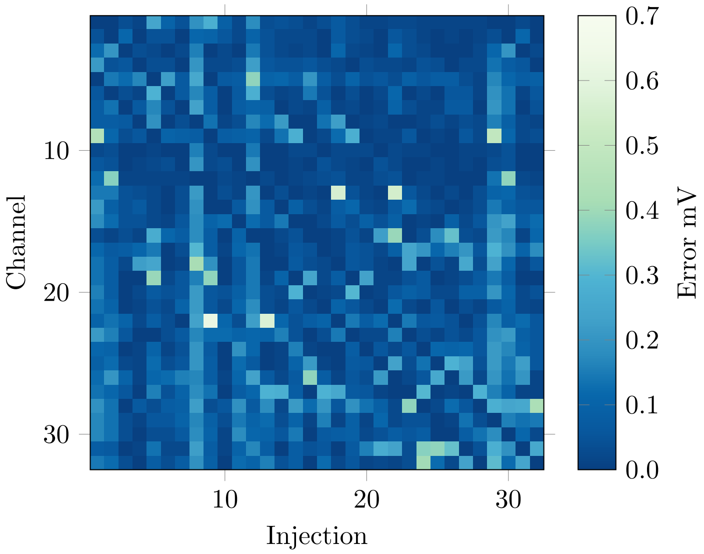

Figure 2.24: *Error in measured voltages across injections in neonatal head tank*

Adult Tank With Skull

The simulated and experimental voltages in the adult tank including skull using the optimal protocol are shown in fig. 2.25. The mean error across all measurements was 0.215 ± 0.229 mV. The largest errors were found in injection 3 and electrode 12, with a mean error of 0.513 and 0.439 mV respectively. The error across all recordings is shown in fig. 2.26.

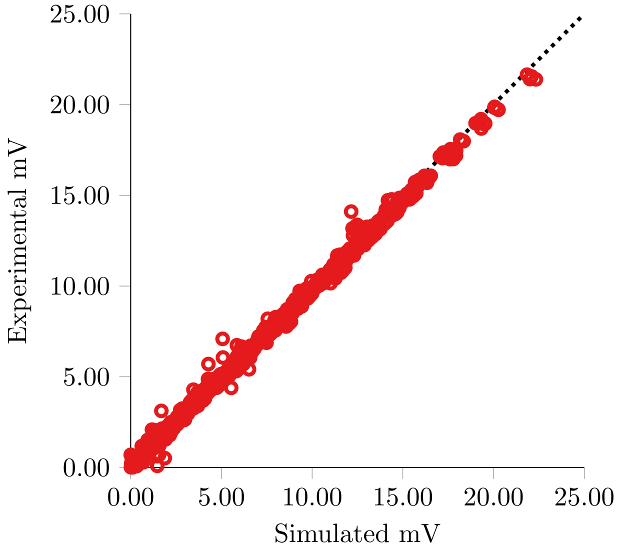

Figure 2.25: *Comparison of voltages in adult head tank with skull with optimal protocol* $R = 0.9985$

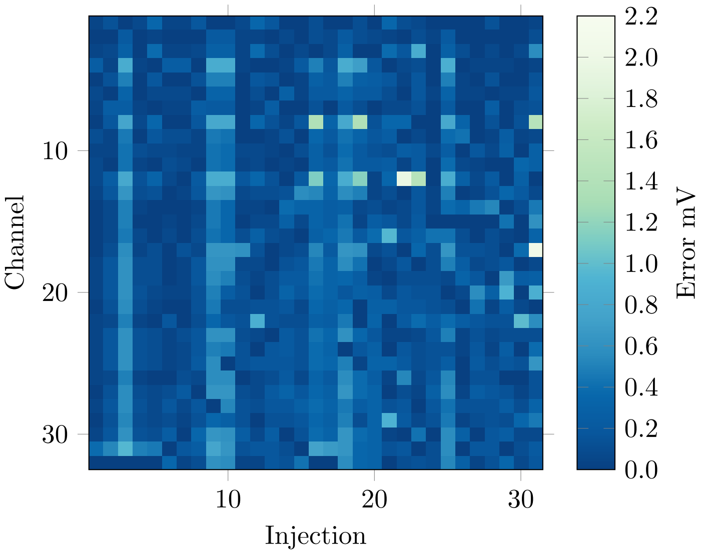

Figure 2.26: *Error Across injections in adult head tank and skull with optimal protocol*

Neonatal Tank with skull

The simulated and experimental voltages in the neonatal tank including skull are shown in fig. 2.23. The mean error across all measurements was 0.185 ± 0.198 mV. The largest errors were found in injection 29 and electrode 28, with a mean error of 0.569 and 0.254 mV respectively. The error across all recordings is shown in fig. 2.24.

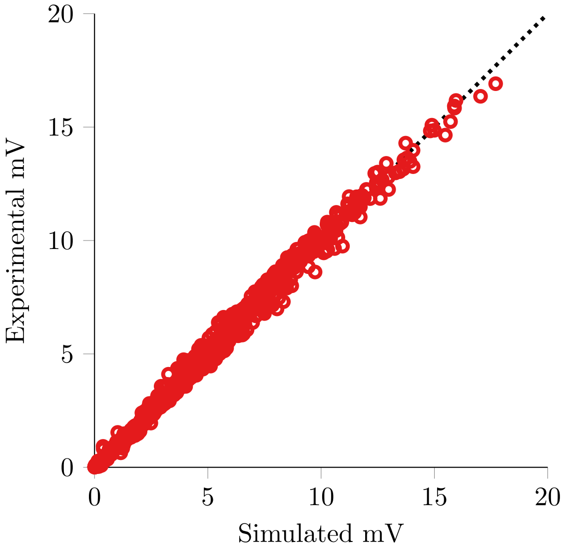

Figure 2.27: *Comparison of simulated and measured voltages in neonate head tank including skull phantom* $R = 0.9972$

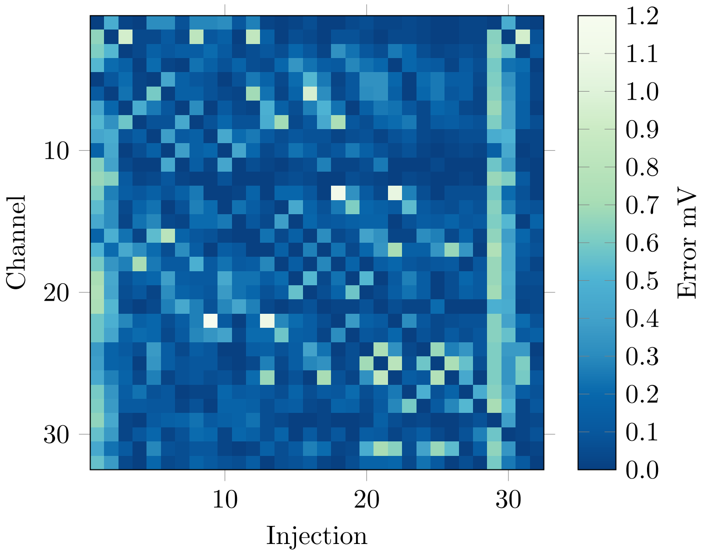

Figure 2.28: *Error in measured voltages across injections in neonate head tank including skull phantom*

Summary

The distribution of the errors expressed as a percentage of the simulated voltages for each recording are shown in fig. 2.29. The mean error for the adult tank was 4.87 % without the skull and 4.50 % including the skull. The error in the neonatal tank was 2.4 % and 5.14 % for measurements without and with the skull respectively. The inclusion of the skull decreased the mean error by 0.37 % for the adult tank, and increased error by 1.74 % for the neonatal tank. In both cases, the inclusion of the skull did not significantly increase the errors in the measurement, $P = 0.23$ and $P = 0.84$ for the adult and neonatal skull respectively.

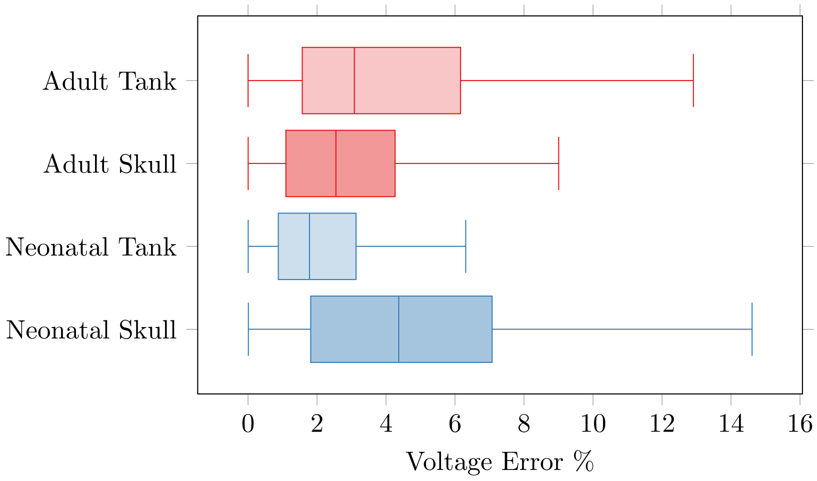

Figure 2.29: *Percentage errors in measured voltages*

2.4 Discussion

2.4.1 Geometry of phantoms

The deviation analysis in fig. 2.20 showed that the geometric error across the adult tank was approximately 0.2 mm. This is the the layer height (*i.e.* resolution) of the printed model, in the Z axis. This suggests that the printer as meeting its rated accuracy, and thus the other models have a similar error. A deviation of 0.2 mm is comparable to the error of 0.18 mm reported by Li, Tang, Dai, *et al.* [144] of calliper measurements in a phantom created from 3D printed moulds. By using a 3D scanner, these results show the error across the entire surface of the tank, rather than measurements between chosen landmarks, and thus gives a truer representation of the geometry. The mean error of 0.2 mm, is of the same order of magnitude as the shape error of the "ideal" cylindrical tank, indicates that geometry of the printed model is an accurate representation of the model used in the forward solution.

2.4.2 Comparison to simulation

Tank

The accuracy of the method is further displayed in the comparison of simulated and experimental voltages in fig. 2.21 and fig. 2.23. The voltages are in clear agreement for all injections, and appear to improve upon the correlation in the both the cylindrical tank (fig. 1.8) and the existing head phantom (fig. 1.10).

In the adult tank the mean error was 0.147 ± 0.099 mV across all measurements, nearly double the error of 0.079 ± 0.062 mV found in the neonatal skull. This greater average error is due to the positioning error of some of the electrodes in the adult tank. As fig. 2.22 shows, electrodes 9, 10, 14,15 and 16 have a consistently greater error across injections than the other electrodes. These electrodes are placed at sections of sharper curvature in the model, and the surface normal calculated in section 2.2.3 may result in the electrode not being aligned with, and not completely flush against, the tank wall. Another source of error occurs during meshing. The true surface of the electrodes are planar, however the surfaces used to create the tetrahedral mesh are the original scalp models which are still curved at the electrode positions. These effects were less pronounced in the neonatal tank, hence the reduced voltage error.

The error expressed as a percentage also demonstrates the same trend with 4.87 % and 2.4 % for the adult and neonatal tanks respectively. The median errors for the adult tank is 3.0 %, less than double then neonatal tank median of 1.78 %. The distribution of the errors, shown in fig. 2.29, demonstrate the effect of smaller boundary voltages on the error estimation. The larger percentage errors $> 10\%$, correspond to the channels with the lowest voltages which are not clearly visible in fig. 2.21. Even small differences between the geometry in the simulation and experiment would alter the isopotential lines. If electrodes are located on an isopotential line for a certain injection, small variations in the geometry could give relatively large changes in the voltage measured. Further, these smaller voltages are more susceptible to experimental error, as they are closer to the noise floor of the instrumentation. The adult tank has a greater proportion of channels with a low boundary potential, and subsequently the percentage error is overestimated. If only channels above 5 mV are considered, the percentage errors for both tanks are in stronger agreement, with 1.92 % and 1.85 % for the adult and neonatal tank respectively.

Studies in previous head tanks have required systematic rejection of small boundary voltage channels [68], so it is likely that the errors introduced from these channels would be mitigated.

Skull

The voltages with the inclusion of the skull as shown in figs. 2.25 and 2.27 demonstrate the same trend as the data with the tank only, with the experimental and simulated voltages in good agreement for all combinations. The voltages suggest much stronger correlation between the simulated and experimental phantom than in the 3D head tank previously used (fig. 1.10). The absolute error increased in both tanks with the inclusion of the skull, by 0.68 mV to 0.215 mV for the adult and 0.106 mV to 0.185 mV for the neonatal tank.

As fig. 2.26 demonstrates, injections 3, 9, 10, 18 and 25 have greater error than the other injections. These correspond to "polar" injections, *i.e.* source and sink on opposite sides of the head, specifically front to back, all with electrode 1 as a source or sink. The current path from electrode 1 to the back of the head passes around the support structure on the skull, which protrudes into the saline. The supports are modelled as a very low conductivity $\sigma = 0.01$ mS/m, to try and minimise these errors, but in reality the solid plastic is a number of orders of magnitudes less. This conductivity on a small area of the skull is the likely cause of these modelling errors. Measurements with electrodes 8 and 12 had the greatest error. These electrodes are located next to each other on the temporal side of the tank, level with the temporal suture in the skull. The curvature on the skull on the suture caused the cylinders used to create the holes to be mis-aligned. The increased current path length through the holes in this would increase the resistance, and result in larger measured voltages seen in fig. 2.26.

The same issue of misaligned holes is the cause of the greater error in injections 1,2,29 and 30 in the neonatal tank, seen in fig. 2.28. All four of these injections have the main current path through the frontal part of the skull, which, in the case of the neonatal a skull, contains a section of the orbital plate. The holes in the skull had to be located manually as it was not possible to place the holes automatically in this area of the skull using the algorithm described in section 2.2.4. Thus the hole density is not exactly equal with the rest of the skull, which would cause above average errors in this section of the skull. The more complex geometry in the neonatal skull is an another potential source of error. The discontinuities in the skull, gives rise to an uneven hole density at the edges of the bones and consequently an uneven conductivity distribution.

In both tanks the errors were greatest with injections through the frontal bones with electrodes near the top of the saline level. It is possible that the errors in the skull at this point are exacerbated by differences in the saline level in the tank compared to the simulation. Whilst level marks were added to the models of the tanks to minimise this error, even small deviations could result in a significant change the transimpedance, and consequently the voltages measured for these injection pairs.

Overall the percentage error for the adult tank actually improved with in the inclusion of the skull, decreasing from 4.87 % to 4.5 %. This is caused by the reduced number of small boundary voltage channels with the skull in place, and consequently a smaller number of high error channels. Whereas the error in the neonatal tank more than doubled from 2.4 % to 5.1 %. The smaller channels continue to overestimate the error, with the mean error decreasing to 2.65 % and 3.9 % for the adult and neonatal tanks respectively, if channels above 5 mV only are considered. However, given the variance of the errors without the tank, neither skull introduced statistically significant changes to errors, $P = 0.23$ and $P = 0.84$ for the adult and neonatal skull respectively. This suggests the errors are equal in the tank and skull models, and rather than originating from the surface perforation method, the errors are inherent to the fabrication method, or to the accuracy of the mesh.

2.4.3 Assessment of tanks

The modelling errors were approximately 0.2 mV or 5 % or less for both tanks. Both tanks demonstrate a strong correlation $R > 0.99$ with simulation and represent an improvement on currently available 3D phantoms in the UCL lab. Using widely available 3D printing technology it was possible to replicate the geometry of the head with an average error of 0.2 mm. It was difficult to compare these values to those described in the literature for other head tanks, as the results are not described in as rigorous a manner. An accuracy of 0.2 mm is feasible for a precision casting process used by Collier, Kynor, Bieszczad, *et al.* [143] and lower than the rapid prototyping technology used by Li, Tang, Dai, *et al.* [144] which has an expected accuracy of ≈0.1 mm. The linear measurements or "shape distortion" as measured by Li, Tang, Dai, *et al.* [144] was 0.18 mm which compares favourably with the tanks constructed in the chapter. Therefore these results demonstrate that it is possible to accurately replicate the morphology obtained through a CT or MRI segmentation using a affordable "hobbyist" 3D printer.

The error between simulated and experimental voltages is also difficult to compare to other tanks in the literature as they are often not expressed as a direct comparison to the simulated voltages. Li, Tang, Dai, *et al.* [144] demonstrated that plaster cylinders with the same concentrations used for the individual bone segments did not have a statistically significant difference in conductivity. However, comparison to simulations is limited to six measurements for two injections, expressed as a transimpedance $\frac{V}{A}$, plotted across frequency but not quantified. The graphs appear to show an error ranging from less than 1 % up to a maximum of 5 %. Sperandio, Guermandi, and Guerrieri [141] also represented the comparison to simulation as a graph of transimpedance, which demonstrates an error approximately $< 10\%$. The tanks created in this chapter compare favourably to these values, but without quantification of the errors in the other tanks, it is not possible to draw strong conclusions.

2.4.4 Reproducibility and limitations of method

The ideal for this method was that it could be easily adapted to either new head geometry, different electrode locations or skull conductivity distributions, and it would be easily reproduced by researchers. This has been achieved to a certain extent. The phantoms created in this chapter can be reproduced rapidly using a similar 3D printer. Printing time for all four models is approximately six days, but the required manual work of cleaning the models and placing the electrodes can be performed over the course of one day. Unfortunately, with the exception of the electrode positions, alterations to these models require access to, and expertise of specialist CAD software. Attempts were made during development to use freely available Open Source software such as FreeCAD or OpenSCAD, or Matlab packages, but they were not successful. Despite this, merely replicating the tanks or adjusting the electrode locations is still useful for a multitude of studies.

The method of perforating the skull with holes has been demonstrated to offer a good approximation of the target conductivity. As it is dependent upon the resistivity of the saline used, the effective conductivity is frequency independent. The true conductivity of the skull, shown by Tang, You, Cheng, *et al.* [128] is largely constant below 10 kHz and inversely proportional above, decreasing by 15 % at 100 kHz and over 100 % above 1 MHz. Each bone type also has a different frequency dependence. Therefore studies above 10 kHz necessitate the construction of a new phantom, as the conductivity and hole density require recalculation. However, the inter-subject variation at 1 kHz was shown to be 15-30 % at 1 kHz (section 2.2.4), so the frequency variations will not be significant until frequencies below 100 kHz. It was probably for this reason that the values quoted by Tang, You, Cheng, *et al.* [128] at 1 kHz were subsequently used by Li, Tang, Dai, *et al.* [144] for current injection at 50 kHz. Further, at higher frequencies (>100 kHz) even a remodelled skull would not provide a representation of the transimpedance, and it is not designed to match the permittivity of the skull at these frequencies.

The conductivity of the neonatal skull is not as well understood in the literature as the adult skull. The value of 0.03 S/m used for the neonatal phantom represents the current best estimation. The spatial variation of conductivity and how it varies with age still requires investigation. It is likely therefore, that the neonatal phantom created in this chapter is only one of a group of phantoms required to fully asses the feasibility of EIT in the neonatal head.

The finer structures of the skull, if they were present in the segmentation, were smoothed during the generation of the solid models. If a higher resolution MRI were to be used, it would be possible to keep much finer details (< 1mm) in the solid model, in which case the accuracy of the 3D printer is now the limitation. To improve upon the accuracy of the models printed in this chapter would require changing to a more precise, but more expensive technology such as SLS or SLA. These printers are less widely available, but are still an option for many research institutes.

The conductivity of the skull phantom relies on having a certain concentration of saline within the holes. This was achieved in these experiments by using a single saline concentration throughout the phantom. However, a side effect of this is that the scalp and brain are effectively modelled as the same conductivity, whereas the true conductivity of the scalp is at least double that of the brain [59].

2.4.5 Technical considerations

The 3D models for both tanks are at the limits of what is possible to print with our 3D printer. Successful printing of these parts required considerable iterations, modifications and debugging over the course of nearly a year. Theoretically, these tanks could be replicated by any researcher who has access to a similar printer will little expertise. However in reality, some familiarity with this technology was required to guarantee success.

2.4.6 Recommendations for Further Work

The experimental results in this phantom are encouraging, and suggest that they are suitable for future experiments in head EIT. The results show a good match to simulations with errors less than 5 % for both tanks. As there is no frequency dependence in the background, these results are only representative of a time difference application of EIT. The experiments would have to be repeated with a frequency dependent background such as carrot-saline mix [68] to explicitly test its suitability for stroke or other time difference applications. This could be achieved simply if the saline concentration was the same inside and outside the skull, or through the use of coating of volume conductive film (VCF).

Currently, the variation of the conductivity is linear across each bone. However, the estimation of the spatial distribution of the skull conductivity could be improved through a separate segmentation of the diploe in the MRI. Segmentation of the diploe is possible from MRI scans with higher resolution than those used to create this phantom [157]. Tang, You, Cheng, *et al.* [128] showed that the conductivity of the skull is highly correlated with the thickness of the diploe. Thus a segmentation of the diploe would enable an element by element estimation of the conductivity in the FEM, but could also be used to calculate the hole density or diameter at each point in the skull phantom.

Chapter 3

Comparison and modification of two parallel record EIT systems for EIT of the Head

3.1 Introduction

Instrumentation performance is a critical factor in determining the success of EIT reconstructions. EIT hardware has previously been a considerable focus within the UCL group, culminating in the design of the UCH Mark 2.5 MFEIT system [48]. This system has been used successfully in a multitude of studies within the UCL group [7], [68], [71], but the compromises necessary at the time to reduce the size of the device, to enable its use in a telemetry ward, have meant the success has been limited. One of the main limitations is the time to complete a scan due to its serial voltage measurement. For the most common protocols, a frame is completed in approximately 60 seconds which precludes imaging fast impedance changes such as those arising from fast neural activity [46] or epilepsy [158]. The 12 bit ADC is comparatively low resolution by modern standards, resulting in a typical noise of 200 μ uV or 0.3 % [79]. Large measurement drifts were identified as the critical limitation during clinical measurements in the EEG telemetry ward by Fabrizi, Sparkes, Horesh, *et al.* [30], and have been observed using the UCH system by Nir Goren in testing even in a healthy subject at complete rest fig. 3.1. Investigation with another system, particularly one with a faster scan speed, would help separate the errors arising from the EIT hardware and the physiological effects, as well as offering more detailed characterisation.

Since the last iteration of the UCH EIT system design, there have been advances in instrumentation for human recordings by other collaborating groups, as well as new systems for animal studies within the UCL group. The two systems of interest are the KHU Mark 2.5 [110] and the UCL ScouseTom [125]. These systems have potentially better performance than systems previously used within the group, however they have not been designed or validated

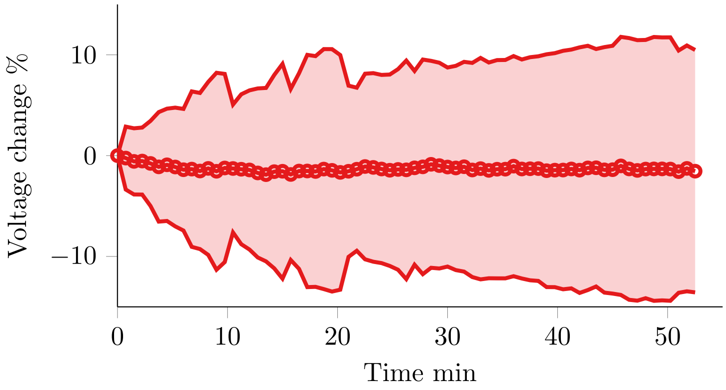

Figure 3.1: *Drift across an hour recording on the head with the UCH mk2.5, as percentage of baseline mean plus standard deviation*

for EIT of the head. This chapter first describes the modifications made to the two systems in order to meet the requirements for imaging stroke or epilepsy in the human head. Then the performance of both system is characterised and compared, to identify which system would yield best signal quality in subsequent studies in the tank or scalp.

3.1.1 EIT systems

KHU Mk2.5

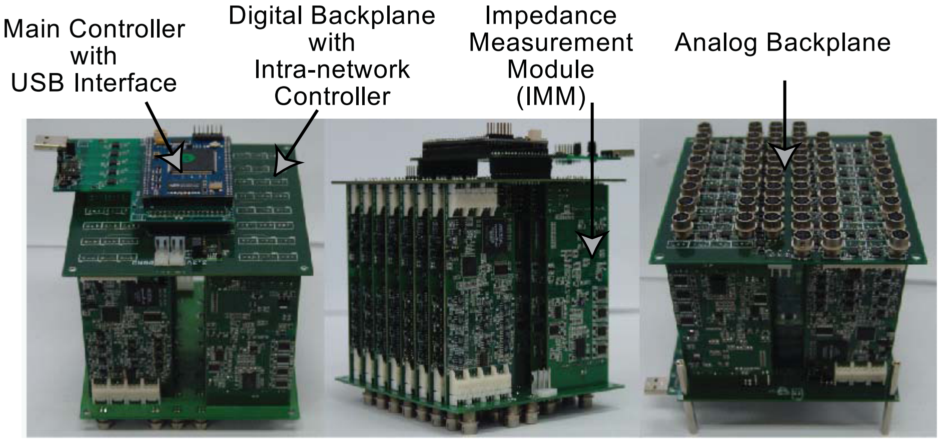

Figure 3.2: *Internal view of 16 channel KHU Mk 2 system, from which the 32 channel KHU Mk 2.5 system used in this study is descended, from Oh, Wi, Kim,* et al. *[49]*

The first device used in this study is the 32 Channel KHU Mark 2.5 (KHU), a multi-frequency fully parallel EIT system [110], [159]. The system operates at 10 frequencies between 10 Hz to 500 kHz, with a current injection range of 175 to 641 μA. The main body of the system (shown in fig. 3.2) is comprised of a main controller, intra-network controller, Impedance Measurement Modules (IMMs) and an analogue backplane to which the electrodes are connected. The

DSP controller communicates with a PC through an isolated USB connection, and transmits commands to the IMMs through the intra-network FPGA. Each of the IMMs, shown in fig. 3.3, contains an independent current source, differential voltmeter, current source calibrator and generalised impedance converter (GIC). The GIC serves to improve the output impedance of the current source by cancelling the effect of stray capacitance through a tunable inductance [110]. Differential voltages are recorded between neighbouring channels as determined by the wiring on the analogue backplane. Driven shields are used to minimise the stray capacitance in the cabling.

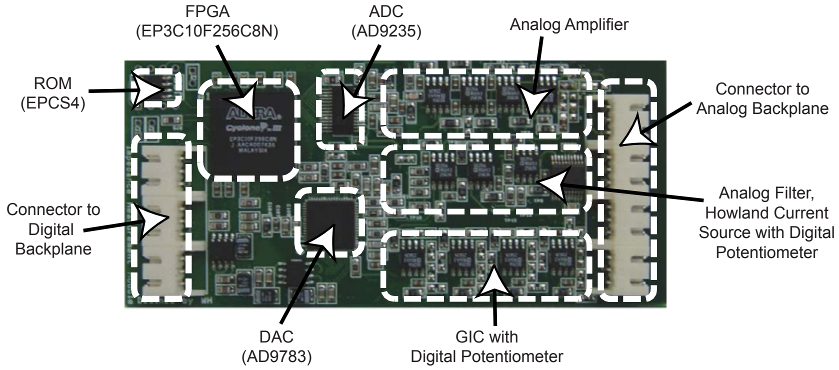

Figure 3.3: *Function blocks of the KHU Impedance Measurement Module (IMM), from Oh, Wi, Kim,* et al. *[49]*

Each IMM can be separately calibrated in four different ways automatically [110]:

1. DC offset: output of 10-bit DAC adjusted to add or subtract DC current to minimise offset of sinusoidal output current
2. Output Impedance: Circuit on IMM switches to include known resistance into test impedance. All permutations of values of digital potentiometers in GIC and Howland circuit are tested to find largest output impedance
3. Amplitude Calibration: All channels connected to resistor phantom. Current source pairs balanced by taking one channel as a reference, output of remaining channels adjusted to minimise current exiting through ground cable.
4. Voltmeter calibration: Zero phase expected on resistive phantom, so any phase measured is used as a calibration factor and subtracted from subsequent measurements. Magnitude correction factors calculated from comparison to SPICE simulation.

A 16 channel version of this system, provided it was correctly calibrated, was able to maintain SNR of 80 dB for frequencies below 250 kHz and reciprocity error of less than 0.5 % across a 24 hour recording [110]. The system used in this study is a newly designed 32-channel system which comprises of a new digital backplane, 32 IMMs and two 16 channel analogue backplanes.

ScouseTom

A custom EIT system is used within the UCL group for the development of EIT of fast neural activity and epileptic activity, known as the “ScouseTom” (ST) [125]. In which the two principle components - the current source and voltage measurement unit - are commercially available, off-the shelf-units: A Keithley 6221 current source, and a Biosemi ActiveTwo EEG amplifier (fig. 3.4). The benefits of this approach are a greater versatility, useful during methodological development, and ease of use, as a further layer of abstraction is added between the electronics and the end user. This system has been employed successfully to reconstruct images in the rat cortex, one of the more challenging EIT applications [61], [92], [158].

The disadvantages of this approach are a delay in imaging, as the data cannot be processed in real time, and a reduced frequency range as the bandwidth of EEG systems are typically $< 5kHz$ [160].

(a) *Biosemi ActiveTwo* **(b)** *Keithley 6221*

Figure 3.4: *Commercial components of the ScouseTo, EIT system,* ***(a)*** *BioSemi ActiveTwo EEG Amplifier and* ***(b)*** *Keithley 6221 Current Source*

Voltage measurements The voltage record side of the ST system is a BioSemi ActiveTwo EEG system [160]. The system is battery powered and fully isolated from the mains supply and earth ground by BF type isolation in IEC60601 and communicates with a PC via an optical fibre (ActiveTwo, BioSemi, Netherlands). The system can be configured to use 32, 64 or 128 channels with corresponding changes in signal bandwidth and sampling rate in its analogue-to-digital converter (ADC). The system specification is shown in table 3.1. Each individual channel is comprised of a DC-coupled preamplifier, filter and ADC. The measurement sensitivity of the system is 125 nV with a 24 bit resolution ADC. The sampling rate was 16 kHz, and the signal bandwidth was from DC to 3.2 kHz.

As the Biosemi only stores the unprocessed voltages on every channel, the demodulation, filtering and boundary voltage processing are performed after the data were collected. The bandwidth of the BioSemi is considerably less than that of the KHU, and is thus appropriate

Parameters	Specifications
Number of channels	128
Sampling rate	16,384 Hz
Bandwidth (-3dB)	DC-3200 Hz
Resolution (Sensitivity)	125 nV/bit in 24 bits
Total input noise (Z_e^* < 10 kΩ)	2 μV_{RMS} (12 μV_{pp})
Input impedance	$10^{12}\Omega$ in parallel with 11 pF
Input range	-1048 to +1048 mV

Z_e^*: Electrode impedance

Table 3.1: *BioSemi ActiveTwo, EEG system specifications*

for a limited number of applications.

Current Source The current source used in the ST system is a Keithley 6221 [161], designed primarily for characterising the AC response of semiconductors and for use in nanotechnology applications. It has a current range of 2 pA to 100 mA within a frequency range from 1 mHz to 100 kHz, and can be controlled from the front panel or programmed via Serial connection. The voltage limit or “compliance” is programmable up to 105 V, and in these experiments is set to the input range of the BioSemi - 1 V - to prevent saturation of the amplifiers or the BioSemi turning off as an over-voltage protection.

Parameters	Specifications
Frequency range	1 mHz to 100 kHz
Amplitude range	2 pA to 100 mA
Total output noise (10Hz to 20 MHz, 50 Ω load)	< 1 mV_{RMS} (5 mV_{pp})
Output impedance	$10^{14}\Omega$ in parallel with 10 pF

Table 3.2: *Keithley 6221 AC current source, system specifications*

The injection electrodes were then programmed using a custom switch network, designed by Dowrick, Blochet, Chaulet, *et al.* [125], comprising of daisy-chained ADG714 CMOS switches (Analog Devices Ltd., UK). These switches were programmed using an arduino nano as shown in fig. 3.5, and a 3-wire serial interface. The values on the `+CHN` and `−CHN` pins are passed down the shift register across the switches each cycle of `CLK`. The switches are updated when the `SYNC` is brought from low to high. The switches have a typical R_{ON} of 2.5 Ω with a maximum of 4.5 Ω, the resistance match between channels is 0.4 Ω. The current source injects continuously during recording, thus there are artefacts when the switches are updated due to the varying loads on the electrodes. These artefacts are trimmed before demodulation.

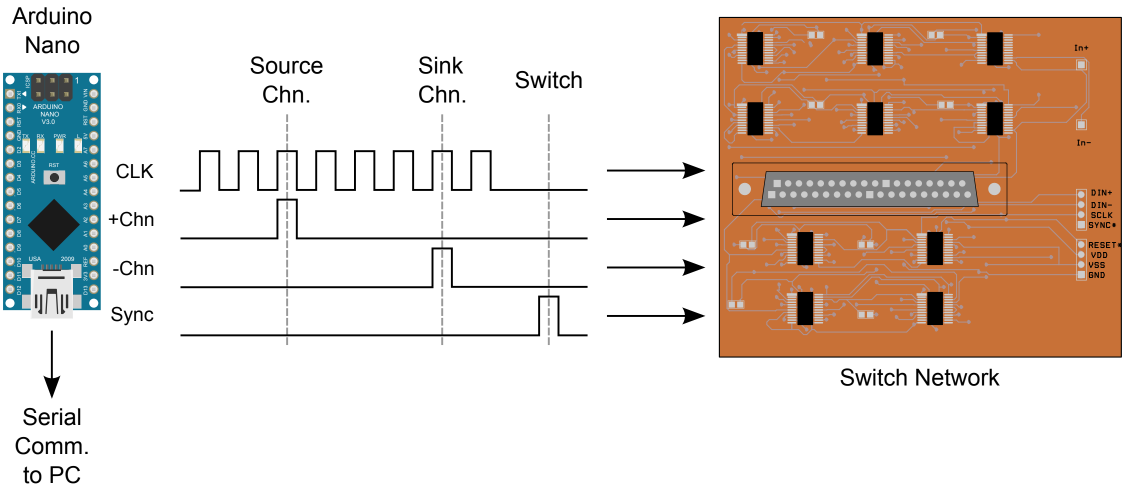

Figure 3.5: *Programming ST switch network. Source and sink channels set by pulses on +chn and -chn pins, injections pairs switched when sync pin set to high*

Comparison

A summary of the specifications of the two systems is given in table 3.3.

	ScouseTom	KHU
Channels	32	32
Design	Serial Inject Parallel Record	Fully Parallel
Measurement Configuration	Ref. Ground	Differential adjacent
Frequency range	1 mHz to 3.2 kHz	10 Hz to 500 kHz
Amplitude range	2 pA to 100 mA	175 to 641 μA
Max. Injection Time	< 1 hour	64 sine wave cycles
Calibration	Manufacturer (CS & EEG) Manual (Switch Network)	Automated

Table 3.3: *Comparison of EIT systems used in this study*

3.1.2 Purpose

The purpose of this study is to compare two parallel-record EIT systems: the KHU EIT MK2.5 32 Channel, and the UCL ScouseTom, for imaging brain function on the scalp. Modifications were necessary before both systems met the requirements for imaging in the human head. The KHU requiring a new power supply, cooling and reduced current amplitude, and the UCL ScouseTom requiring a new switching controller and boundary voltage processing. After these modifications were validated, the systems were compared in resistor phantom measurements, investigating the performance across frequency and load, as well as the noise and drift in measurements across time. Experiments were then performed in the adult head tank created in chapter 2 with a plastic perturbation, and the images with both systems compared. Finally, scalp recordings were made on two subjects to assess the clinical suitability of both systems.

3.1.3 Experimental Design

Modification of systems

These experiments focus on the newly designed 32 channel KHU EIT mk2.5 system, which is an adaptation of the more mature 16 channel system [110]. However, the new 32 channel system required some modifications before its performance matched expectations based on the 16 channel system. First a new power supply was designed to meet the increased specifications of the new system. Modifications to the FPGA firmware by the group at KHU allowed the current level to be reduced to <50 uA, within the requirements for Fast Neural EIT experiments on the rat cortex. The reduced current level necessarily reduced the SNR of the output current, so resistor phantom experiments were performed to ascertain if the reduced SNR was still acceptable. Finally software was written to assist the user in calibration, data collection and data processing.

The bespoke system [125], referred to as the UCL ScouseTom (ST), has been used successfully in experiments on the rat cortex investigating fast neural activity and cell swelling during epilepsy [61], [158] but required some adaptation before it was suitable for tank and human scalp recordings. A new controller for the switch network and current source was created on the Arduino [162] platform, controlled through a Matlab interface, which allowed the injection pairs to switch as often as every 3 μs, within an accuracy of 1 μs. Software was written to measure the contact impedance of the electrodes in the same manner as with the UCH Mk2.5 [100], which is necessary for experiments on human subjects. Coded pulses were sent to the digital trigger channels of the Biosemi EEG system [163] from the Arduino controller, which were used to partition the data during boundary voltage processing.

Resistor Phantom Recordings

Resistor phantoms are a common tool used in assessing the performance of EIT systems as they provide a load that is both known, frequency independent and easily varied [48], [164]. From these measurements it is possible to obtain the noise, load and frequency characteristics of the systems. Measurements were first collected with a single channel for six loads from 6.8 to 70.3 Ω for an injection current of 150 μA and 1.125 kHz. A resistor network was set up to mimic four-terminal measurements, as described in Fabrizi, McEwan, Woo, *et al.* [164], with the contact impedance modelled with 1 kΩ resistors between each channel and the load.

The interchannel variations were then measured using a 32 channel resistor phantom created by *Swisstom AG* [165], which is designed to replicate the resistance of a human thorax for use in lung ventilation EIT. The resistance of the phantom is equal for all electrodes, thus for a repeated injection pattern, an ideal system would measure identical voltages for each injection. These inter-channel variations are particularly important when comparing systems, as they highlight any advantages or disadvantages in the different system architecture, namely single multiplexed current source compared to separate current sources. Measurements were collected using this phantom for a fixed frequency of 1.125 kHz and a range of currents from 50 uA to 350 uA, and then for a fixed current of 150 uA for the full range of frequencies. Finally, the noise and baseline drift were measured over the course of an hour recording.

Tank Measurements

The two systems were next compared in experiments using the adult head phantom created in chapter 2. Initially, baseline measurements were compared to simulated voltages to compare the accuracy of the systems. Next, spherical perturbations were placed inside the skull in the positions defined by Malone, Jehl, Arridge, *et al.* [59] during a simulation study using the same head geometry. Time difference images were then reconstructed using first order Tikhonov reconstruction [63] and both systems. An objective comparison of the images was performed based upon the quantification algorithms by Malone, Jehl, Arridge, *et al.* [59] and Packham, Koo, Romsauerova, *et al.* [68]. The measurement protocol differs between the two systems as the ScouseTom measures with respect to the ground electrode, whereas the KHU measures the differential voltage between each electrode. These differences mean that the sensitivity matrix is different for each system. The differences of the sensitivity across the head was investigated, to give context to explanations of any potential differences in image quality between the two systems.

Scalp recordings

Scalp measurements on two subjects were collected over the course of 30 minutes, as part of a study in collaboration with Nir Goren in the UCL group, using 16 Ag/AgCl electrodes arranged in the configuration described by Fabrizi, McEwan, Oh, *et al.* [54]. These experiments are the closest scenario to real clinical measurements. This enables investigation into the effects of increased magnitude and mismatch of contact impedance, additional physiological noise sources such as muscle artefact, blood vessels and temperature variations.

3.2 Methods

3.2.1 KHU Modifications

The modifications to KHU EIT system served to reduce the noise and measurement drift over time through an improved power supply design, and a reduced current range to enable its use in animal studies. First a new power supply was designed to with improved heat dissipation, cooling was then improved through a new case design for power supply and system. Finally firmware changes by KHU to reduce the current amplitude were validated.

Power Supply and Case

Preliminary testing the with new 32 channel KHU mk 2.5 system was performed on a simple resistor phantom as outlined in fig. 3.6. Current was injected at 1 kHz at 100 μA across two 1.1 k Ω resistors, over the course of half an hour. The resultant voltages, shown in fig. 3.7, are considerably noisier than expected for such a stable test phantom. The noise is approximately 5 mV or 7.25 % of the amplitude, over an order of magnitude greater than the the 0.1 % measured by Oh, Wi, Kim, *et al.* [49].

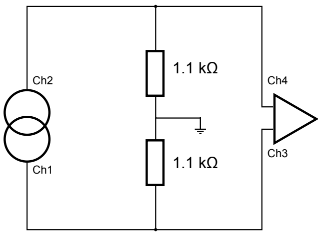

Figure 3.6: *Resistor set up for preliminary testing of the 32 channel KHU Mk 2.5 EIT system*

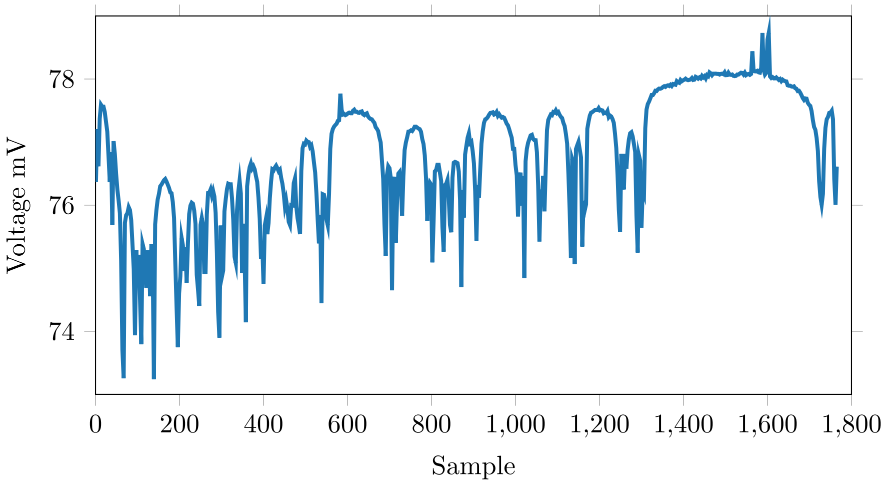

Figure 3.7: *Noise in voltages recorded on 1.1 kΩ resistor during preliminary testing of the 32 channel KHU Mk 2.5 EIT system*

To identify the cause of the noise, the voltages across the resistors were measured simultaneously with a NI 6211 USB-DAQ, and a separate estimate of the magnitude was calculated as the RMS value of each group of sine waves. It is clear from comparison of these voltages, shown in fig. 3.8, that the noise is correlated in both voltage measurements, which leads to the conclusion that the noise is present in the current injected across the electrodes. Test points were included into the design of the IMMs, which, by probing with an oscilloscope, it was possible to determine that the noise was not present in the output signal from the DAC, rather it occured after the Howland current pump. The op-amps in this circuit are powered by the ±5 V "Analogue" supply, which was not performing to expectations.

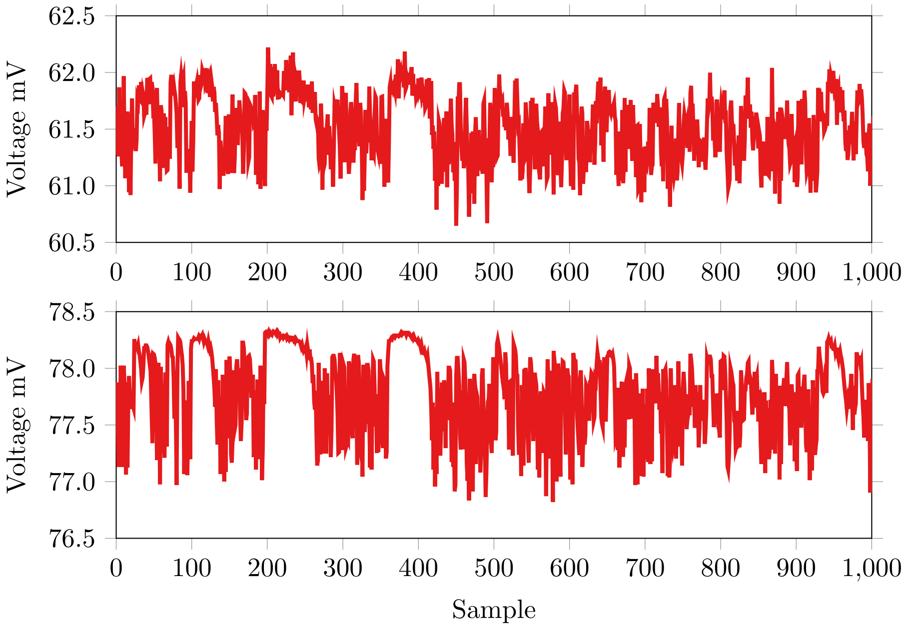

Figure 3.8: *Comparison of the amplitude of the sine wave across 1.1 kΩ resistors, top: as calculated from the rms of voltage collected with a NI USB DAQ, bottom: the output from the KHU system*

The analogue ±5 V, as with the "digital" 3.3 V supply, consists of an AC-DC switched mode power supply, and a precision regulator board, where a shunt regulator IC supplies a stable 5 V reference to a power transistor. Overheating of the transistors was determined to be the cause of this noise, arising from inadequate cooling. The area surrounding the transistor was visibly charred, it became clear from probing with an oscilloscope that the *TL431* reference has been damaged. The regulator had been designed for the 16 channel KHU system [49], [110], which has nearly half the current supply requirements of the 32 channel used in these experiments, and as such was unable to dissipate the excess heat generated.

A new power regulator based on the existing circuit was designed in collaboration with Bishal Karki, shown in fig. 3.9. The single transistor was replaced by three transistors in a cascaded darlington pair arrangement which provided a notional DC Current gain h_{FE} of 62500. These components were then spaced far apart to allow for large heat sinks to be connected, and the reference IC was moved into the middle of the board, to prevent any de-rating or damage from the heat generated by the transistors. The circuit was then tuned for 3.3 and ± 5V and separate boards created for each, using the same switching mode AC/DC converters as used previously. A finished regulator board is shown in fig. 3.9b.

A new case, shown in fig. 3.10, was designed to house the new power supply, in which

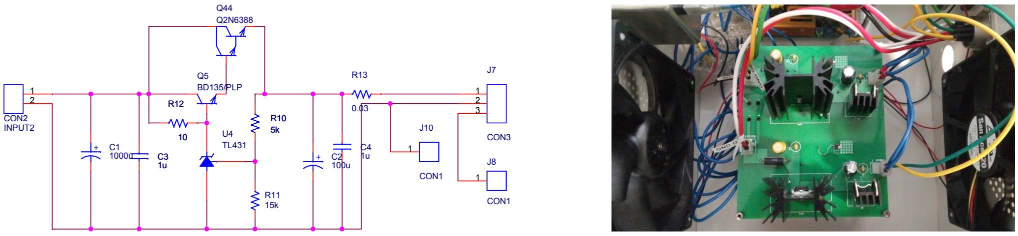

(a) *Circuit Diagram* **(b)** *Finished Board*

Figure 3.9: *Updated regulator board for 32 Channel KHU Mk. 2.5,* ***(a)*** *circuit diagram*

each regulator has a pair of fans in "push-pull" configuration to maximise the airflow across the heat sinks, and improve the heat dissipation. The additional cooling served to maintain a stable low temperature inside the case with the system under load, and thus would help reduce drift in performance caused by increases in temperature. The walls of the case were drawn in SolidWorks and cut from ABS using an CNC machine. All external parts were constructed out of non-conductive materials.

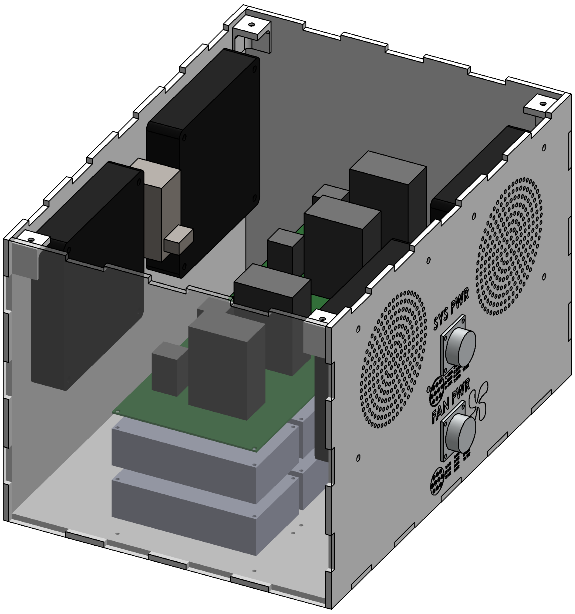

Figure 3.10: *Improved power supply design for KHU 32 channel system*

The power supply noise was measured with a NI 6211 USB-DAQ, with the 32 channel system connected in idle and scan mode. The 5V results in fig. 3.11 show a dramatic improvement with the new regulator design, with the noise decreasing between 20 and 60 dB with the system in idle mode. Overall the noise was 265 μV. These results compare favourably with those described by Wi, Sohal, McEwan, *et al.* [110], who found a switching noise less than -90 dB at 70 kHz and noise of 295 μV, when using the original regulators with the 16 channel system. The results with the system in scanning mode show a similar 30-60 dB decrease above 5 kHz, but the new regulator has 10 to 20 dB greater noise than with the system in idle mode. There is an artefact of less than 10 mV visible in the voltages synchronised with the start of each injection, caused by the change of load when the front panel switches open. This may have occurred with the original voltage regulator, but it would have been masked by the other noise. This artefact would contaminate the output from the Howland current pump in the IMM, but the effect would be negligible. The artefact is transient, less than 1 ms, and represents a change of 0.2 % in voltage. This artefact is approximately constant for each injection and would therefore be cancelled out during difference imaging.

Aside from these artefacts, the noise with the new regulator still demonstrated the same significant decrease compared to the original design. Further the variations in the DC voltage, taken as an average of a minute recording, were also reduced by almost a factor of 100, from 8.2 mV to 0.085 mV or 0.0017% over the course of half an hour. This stabilisation of the supplied voltage to the Howland current pumps should reduce the drift in the measurements, and is investigated in section 3.2.3.

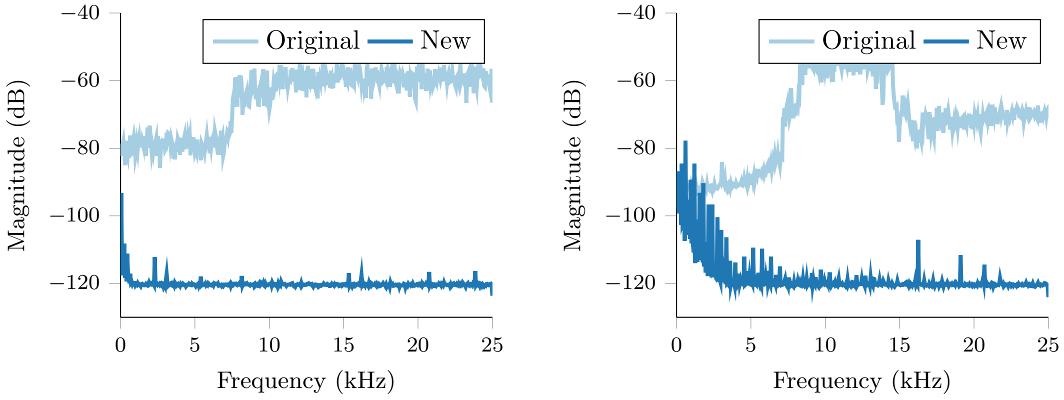

(a) *PSD System Idle*

(b) *PSD System Scanning*

Figure 3.11: *PSD of the voltage from KHU +5V regulator for original and new design,* ***(a)*** *with system idle* ***(b)*** *with system in scan mode*

Whilst the ±5V regulators, which power the Howland current pump, are the most critical for the performance of the system, the new 3.3 V power supply was also validated. The current requirement of 10 A necessary to power all of the FPGAs placed significant strain on the original 3.3V regulator, which resulted in a decrease in the power output. This lead to system instability as the FPGAs were not supplied with sufficient voltage. Thus it was prudent to design and validate a new 3.3 V regulator, despite its minimal impact on the SNR. The Power Spectral Density of the voltage recorded from the output of the regulator is shown in fig. 3.12, with the system idle and scanning respectively. With the new regulator, the noise decreased by an average of 17.3 dB across all frequencies, and variation in the DC level decreased from 0.42 mV to 0.039 mV or 0.0002 %.

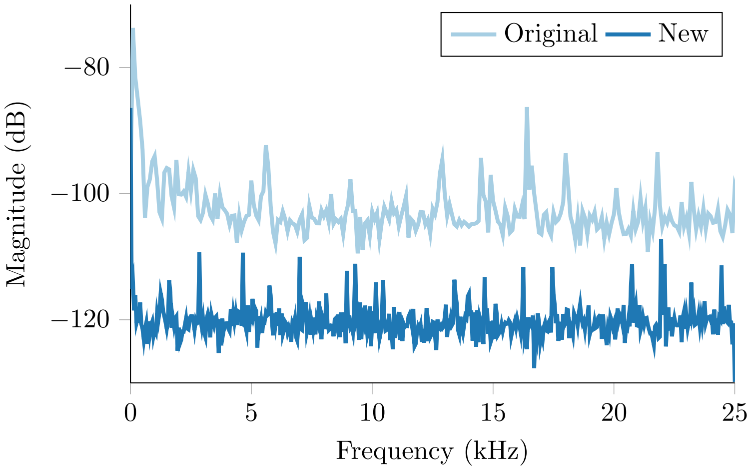

Figure 3.12: *PSD of the voltage from KHU 3.3 V regulator for original and new design with system in scan mode*

System Case

The 32 Channel system itself also required the design of a new case to improve the cooling. Preliminary testing, even with the new power supply design, showed that over the course of an hour long experiment the performance of the system deteriorated to the extent that the data collected was no longer meaningful. These results clearly did not meet with expectations, as the 16 channel KHU Mark2 system had demonstrated a drift in amplitude of 0.1 % or less [49]. As with the power supply, doubling the number of channels had a consequent increase in other requirements that were not considered. The close proximity of the IMMs means there is little airflow between them, especially for those at the centre of the bottom row. Natural convection may have been sufficient to cool the circuit boards in the centre of the 16 channel system, but the deterioration in performance demonstrated that additional cooling was necessary for the larger system. An overview of the new system case is shown in fig. 3.13a. Fans were positioned directly above the and below the IMMs, fig. 3.13b, to maximise airflow across the FPGAs. This arrangement aided the natural convection cooling of the IMMs and reduced the thermal equilibrium temperature inside the case. In preliminary tests, the system could now be used over the course of an entire day without experiencing the overheating problems previously encountered. Detailed testing of the drift is investigated in section 3.2.3.

Modification of current level

The current which may be injected into the patient during EIT measurements is limited by the IEC 60601 regulations [166], specifically the maximum patient auxiliary current. In normal operation, from 0.1 to 1 kHz the limit is $100uA_{RMS}$, above 1 kHz, the RMS current is restricted

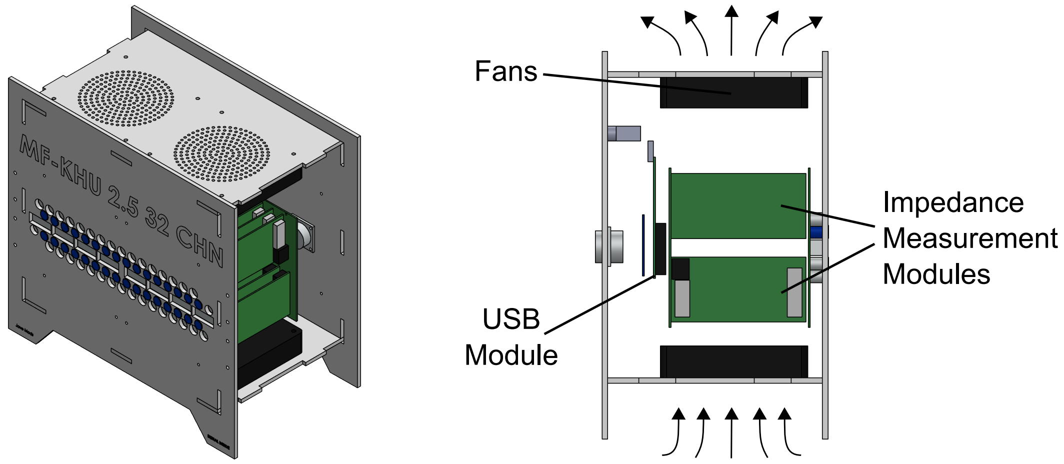

(a) *KHU System Case* **(b)** *Fan alignment*

Figure 3.13: ***(a)*** *Improved case for KHU Mk 2.5 system,* ***(b)*** *section view demonstrating fan alignment*

to $100uA_{RMS} \times f$ where f is the frequency in kHz. The current amplitude used in previous epicortical recordings was below 50 uA or 35.4 μA RMS, [46], [61]. The current amplitude range of the KHU system was 124 to 453 μA RMS, which is greater than the maximum allowable current below 1.2 kHz for human studies, and exceeds the limit for epicortical experiments for all frequencies. A solution to this problem was implemented by the KHU IIRC group to reduce the output current without the need to redesign the IMM. Originally, the amplitude of the voltage signal from the DAC was fixed, and the current amplitude was controlled only by the gain in the Howland current pump circuit. An additional parameter `current level` was added which controlled the number of bits used to define the sine wave sent to the DAC. By default, a 16 bit word is used to define each value in the sine wave, but choosing a `current level` of 1 removes 1 bit from the definition, and consequently reduces the amplitude of the sine wave by half. Therefore, using the same Howland current pump circuit, the range of current amplitudes decreased to 62 to 226.7 μA RMS with a current level of 1, and 31 to 113.4 μA with a `current level` of 2, and so on. This modification widens the range of possible output currents to meet the requirements for low frequency measurements in the human head, as well as epicortical experiments.

However, decreasing the number of bits used to define the sine wave necessarily decreases the SNR of the output. The signal to quantisation noise ratio (SQNR) for an ideal DAC is equal to $SQNR = 20\log 2^{Q} dB \approx 6.02 \cdot Q dB$ where Q is the number of bits. Thus removing 1 bit and decreasing the amplitude by half would have a consequent decrease of $\approx 6dB$ in SNR of the voltage signal input to the howland current pump. To quantify the resultant decrease in the SNR of the output current, voltages were collected with a NI USB DAQ USB 6211 during current injection across a 1 k OHM resistor. Current was injected at a single frequency of 1.125 kHz for a range of amplitudes chosen to cover the values expected for human and animal studies. Where possible, the same current amplitude was set using different `current level` settings, which will demonstrate the effects of the increased quantisation noise in the voltage signal. Voltages with the USB DAQ were sampled at 40 kHz, and the data for 100 repetitions combined for subsequent spectral analysis. The SNR was defined as ratio of the power at the carrier frequency to the power in the remaining frequencies, expressed in decibels. The measured decrease in SNR, shown in fig. 3.14, for a signal with the same amplitude but a higher current level setting, is less than 1 dB in all cases, which is less than that expected from the decreased SQNR alone. The quantisation noise floor has considerably less influence on the overall SNR than the harmonic distortion, demonstrated in section 3.3.1.

The SNR at the minimum amplitude of 50 μA, is 16.7 dB, approximately 2 dB less than 140 uA, the minimum amplitude for scalp recordings. This is not a substantial decrease in SNR compared to the 20 dB measured at 200 uA and a `current level` of 0. Thus these results suggest that with these modifications,the system is suitable for epicortical recordings of fast neural EIT [46], [61], and low frequency scalp recordings for stroke [48].

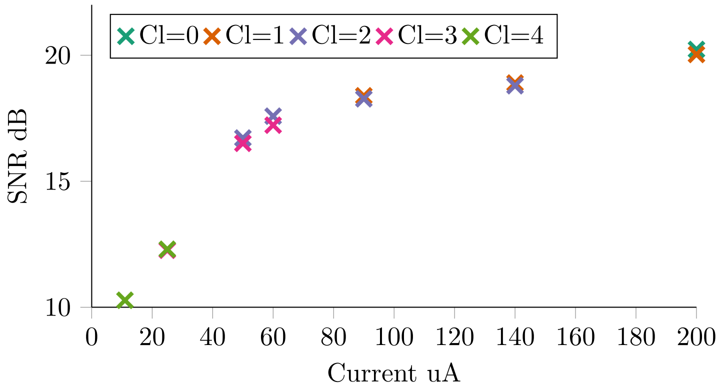

Figure 3.14: *Comparison of signal to noise ratio of injected current for the KHU mk2.5 with increasing current level setting*

Software

The `script` and `projection` files used to define the current injection protocol, require a number of different settings to be entered in a specific manner as there is limited error checking in the KHU software. Further The gain and current settings in the `projection` files are the 10 bit values used to define the wiper position of digital potentiometers on the respective circuits, rather than the target values. These issues often lead to mistakes when iterating the protocol parameters. So Matlab scripts were written which would convert target values of gain and current level in μA into the potentiometer settings, and also ensure the correct formatting of the files. The minimum interval T_{proj} between each injection pair or "projection" is calculated using eq. (3.1).

$$T_{proj} = InjDelay + \left[\frac{3 + AvgNum + DMDelay + 1}{f_{wave}} \right] \times S_{clk} \tag{3.1}$$

Where $AvgNum$ is the number of cycles to be averaged, f_{wave} is the injection frequency, $DMDelay$ is the number of addional cycles injected before demodulation starts (default 0) and S_{clk} is the system clock frequency 45 MHz. The software calculates the minimum interval for the settings the user has specified and sets the correct values `TimeInfoHigh`, `TimeInfoMid` and `TimeInfoLow` in the script file.

Alongside this new software to generate new protocols, software was written to convert the output data into voltages. The KHU software writes `Scan#` files for each repeated protocol (refereed to as both a "Scan" or a "frame"), in which the real and imaginary components of the voltages are written in 15bit values (unless Voltmeter calibration is used). Therefore in order to recover the voltages correctly, the ADC values must be converted to voltage and divided by the gain for each channel. The settings sent to the FPGAs on each IMM are stored in a textfile `CCSTableDownSendLog`, from which it was possible to obtain the injection channels, current, frequency and gain settings for every injection pair and for every measurement channel. The KHU software was modified by Bishal Karki to create an additional text file `EITSettings`, which sorted the `current level` parameter, the number of cycles averaged, and additional information regarding the timing of injections. A Matlab script was written to convert the data into the correct voltages, and to recover the protocol, current and frequency used from the combined information of these two files.

The protocol generation and data conversion scripts, in combination with the increased mechanical stability from the improved case design made the KHU suitable for use by non expert users.

3.2.2 ScouseTom Modifications

The ST system required some modifications before it was suitable for traditional EIT experiments in tanks and scalp recordings. The switch network controller was redesigned to switch with $< 1\mu$V precision and to send coded pulses to the trigger channels of the BioSemi EGG amplifier. Software was written to process the data using these pulses, and to output the data in the format used in the image reconstruction software within the UCL group.

Controller and user interface

The ScouseTom system has been used successfully in the rat epicortical experiments performed within the UCL group [92], [158]. However, the experimental paradigm, described by Oh, Gilad, Ghosh, *et al.* [46] differs from the traditional EIT methods used in tank and scalp recordings [7], [30]. Standard EIT measurements, such as those performed by the KHU system, involve short injection times (64 cycles) on each pair of injection electrodes in order to obtain complete protocols as quickly as possible, often giving a frame rate of 1 or more per second. Whereas the relatively small magnitude of the fast neural signal necessitates a large number of repeated stimuli per injection pair to achieve sufficient SNR [46], generally 60 s or greater [79], [92]. These long injection times place less demand on the precision of the switching controller, particularly as the data processing was gated by the stimulation trigger, rather than the switching time. The accuracy of the existing switch controller was ≈10 ms, with a minimum usable switching time of 100 ms. This is sufficient when compared to the 60 s injections used in the EP studies, it is not sufficiently fast or precise enough for traditional EIT measurements, which typically have switching times of 20 to 100 ms or less, dependent upon carrier frequency.

A new switch controller was designed using an Arduino Uno and PCB or "shield" based on the Arduino Nano prototype by Dr. Tom Dowrick. The daisy chained ADG714 switches were programmed using the 3-wire Serial Peripheral Interface (SPI) library on the Arduino. This reduced the programming time to less than 2 μs, increasing the range of potential injection times to include all those which are experimentally feasible. The switch timing was performed using the Arduino library function `DelayMicroSeconds`, which has an accuracy of 1 μs, which should minimise any observed jitter given the 61 μs sampling period of the BioSemi EEG system. The completed switch network controller is shown in fig. 3.15, inside a 3D printed housing. The housing was designed to fit on top of the BioSemi system, to reduce the length of ribbon cable needed, and to reduce clutter during experiments.

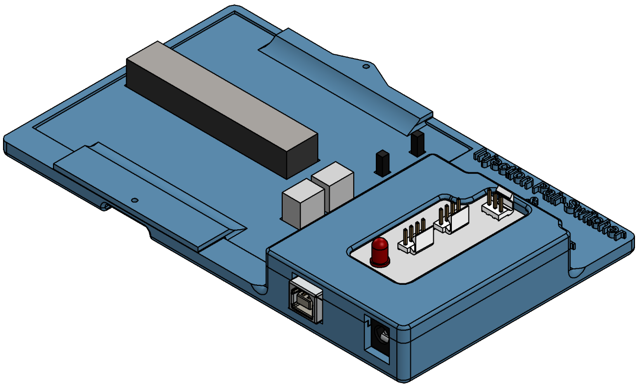

Figure 3.15: *Switch Network Controller for ST EIT system: Switch network PCB and Arduino Uno with shield in 3D printed housing*

Coded pulses were sent to one of the digital trigger channels on the BioSemi to indicate the start of injection, a switch of injection pairs, and the end of injection. Additionally, a separate stimulation trigger of variable pulse width was added so the controller could be used in EP studies [92].

A Matlab user interface was written to communicate with both the Switch Network controller and the Keithley current source. As it was not possible to write data to the headers of the BioSemi .bdf files or write any additional files using the BioSemi software, it was important to store as much information regarding the experiment as possible for future data processing. A file structure in the Matlab software was imposed such that, if the user stored the EEG files in the correct place, the context of the data collected could be understood. An overview of the modified ST system is shown in fig. 3.16.

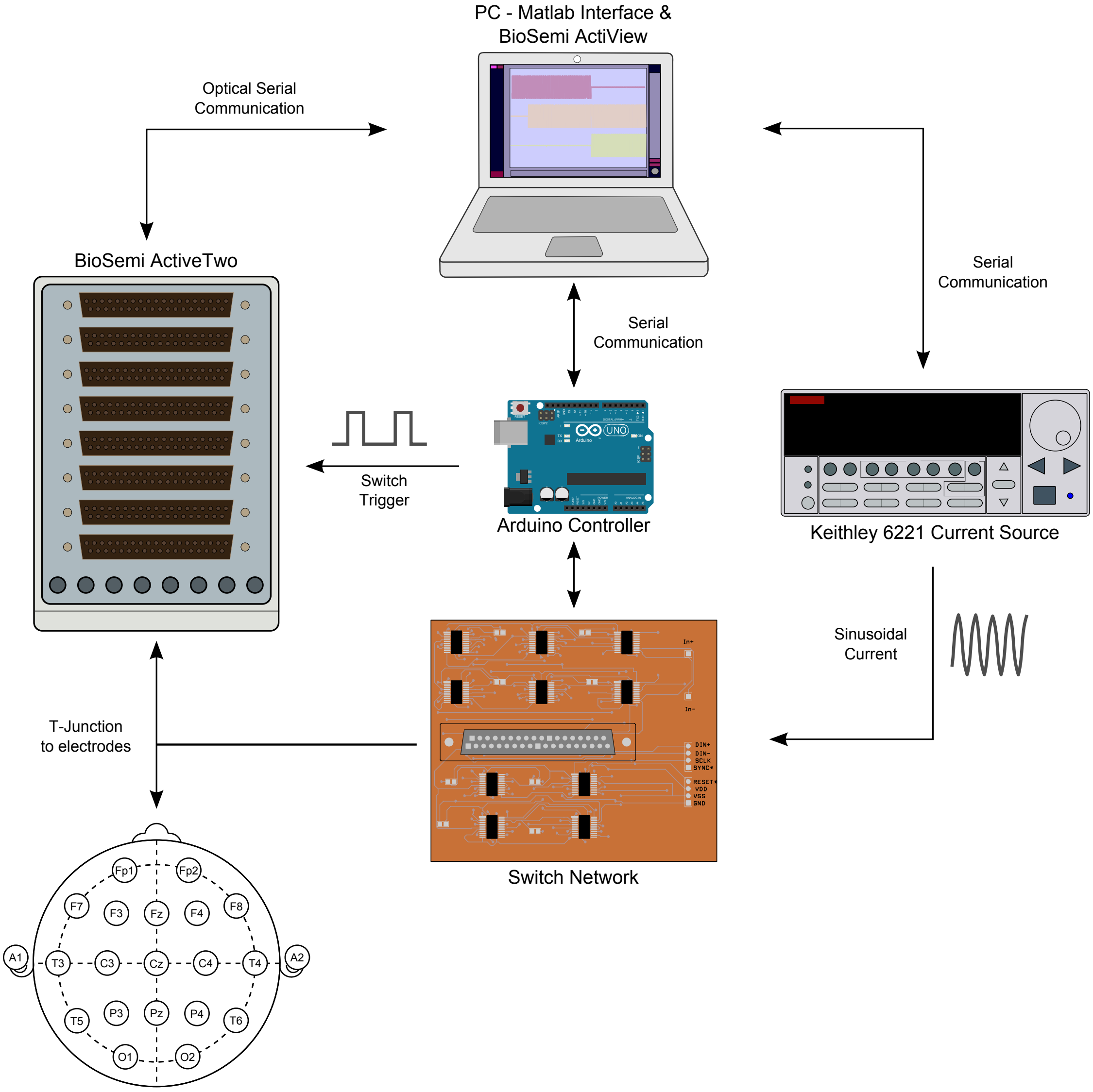

Figure 3.16: *Overview of ScouseTom EIT system. Current source and switch network controlled via Serial communication and Matlab interface. Switching indicators sent to BioSemi Digital Input channels*

An important function available on the UCL Mk2.5 was the ability to quickly check the contact impedance on all the electrodes before collecting data. An extra routine was added to the Arduino controller to replicate this feature, by injecting current between each neighbouring pair of electrodes for 200 ms at 1 kHz at 100 uA for a single protocol. The voltage between each electrode was then used to calculate the two-terminal resistance, and thus give an estimate of the contact impedance. The BioSemi ActiView software also gives an indication of the quality of the electrode contact by displaying the DC offset of the voltage on each channel. This data is displayed in real time, and is a useful tool for checking electrode contact during electrode application.

Data processing

The data processing used in the fast neural experiments differ slightly from traditional EIT boundary voltage estimation [46], [158]. Commonly, amplitude and phase across a short burst of ≈ 64 sine waves are averaged to give the boundary voltage at a given time point. However, the fast neural experiments require a continuous impedance (dZ) signal which is averaged across repeated evoked potentials, due to the short duration of the impedance changes (≈ 3 ms). This is achieved by first band pass filtering around the carrier with a Zero-phase forward and reverse filtering operation. A wide bandwidth of $BW = 1000$ Hz, is used to give a time resolution of 1 ms. The Hilbert transform is then used to provide the instantaneous amplitude, and thus the envelope of the amplitude modulated signal.

The boundary voltage in the format output by the KHU, can be obtained by simply averaging this Hilbert transform of the signal. However, some modifications to the bandpass filtering were necessary to ensure optimal SNR during demodulation. The measurements of the BioSemi are DC-Coupled, and thus the voltages used in processing have a significant non-zero mean. This discontinuity introduces a ringing artefact due to the impulse response of the IIR filter, shown in fig. 3.17 for an example measurement collected on the human scalp. This ringing artefact is trimmed during processing of fast neural data [158], as the duration at which the artefact is non-negligible (<150 ms) is insignificant compared to the overall length of injection ($\approx$60s). However, the target for scalp recordings is to switch much more frequently ($<$ 100ms) and thus this truncation of the measured signal is no longer negligible.

To reduce the duration of filtering short switch times, a comparison of the SNR of demodulated signals with different filtering characteristics was performed. The third order Butterworth filter used in previous studies, was compared to a fifth order Butterworth filter and FIR filter with a Blackmann-Harris window. The Blackmann-Harris window was chosen as it is designed to minimise the sidelobe level, and thus minimise the energy in the stop band of the filter [167]. The bandwidth of all filters was set to 50 Hz, or 25 Hz either side of the carrier, as a trade off between maintaining the amplitude at the carrier frequency and improved noise rejection through an increased stop band.

Using these three filters, with a fixed bandwidth of 50 Hz around the carrier, the effect of increasing the number of truncated samples was investigated on a single channel scalp

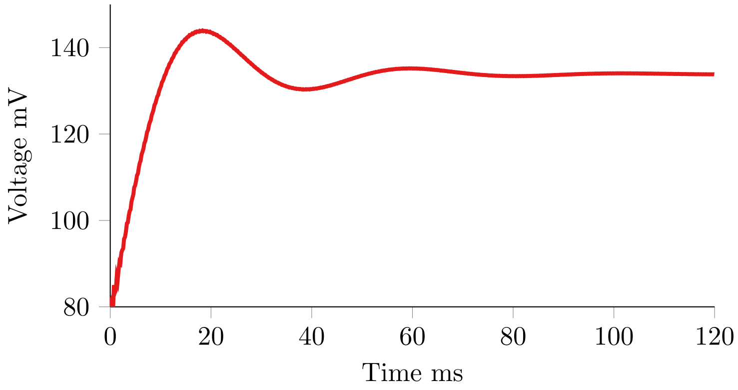

Figure 3.17: *Ringing artefact in ScouseTom demodulation*

recording. The SNR of a measurement was defined as $SNR = \frac{P_{sig}}{P_{noise}}$ the ratio of power of the truncated signal V_{sig} to the power of the truncated signal with the mean subtracted V_{noise}. For a given number of samples to be truncated s_{trunc}, a FIR filter of order $N = s_{trunc}$ was applied, along with the 3-rd and 5-th order IIR filters. The effect of increasing s_{trunc} is shown in fig. 3.18. All three filters converge to the same SNR of 63.5 dB which is the inherent noise in the measurement. However, the FIR filter converges after only 100 samples, when $N = 100$. Below this value, the FIR filter order is not sufficient to filter the noise to the same extent as the 3rd and 5th order filters, and thus the SNR decreases. Above $N = 110$ there is no significant increase in SNR. The 3rd and 5th order IIR filters require 1100 and 1700 samples to be truncated to give the true SNR. In this case the higher order IIR filter confers no additional noise rejection benefits, as the maximum SNR is the same as that with the 3rd order filter.

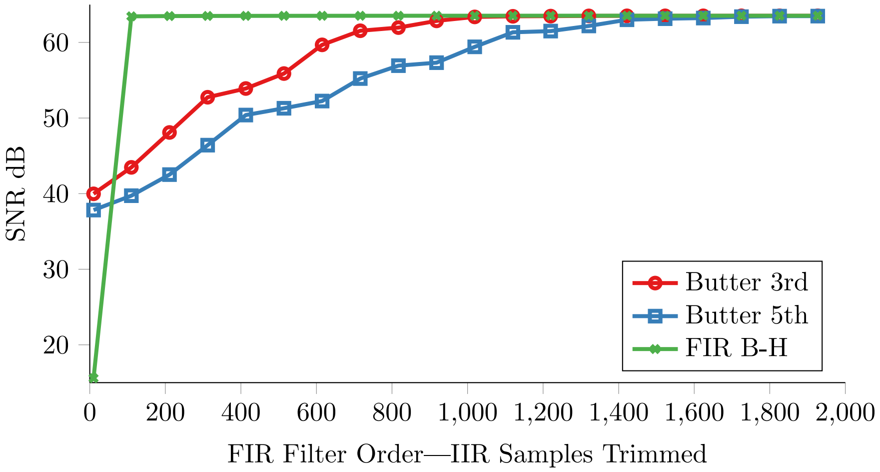

Figure 3.18: *Effect of increasing truncation samples for 3rd and 5th order IIR filters and increasing N*

The conclusion of these tests are that for shorter injection times an FIR filter is more suitable, as only 110 samples (<6ms) need to be truncated before averaging. The disadvantage of such a high order FIR filter is the extra computation time. Thus during data processing the filtering is set dynamically for each data set based on the length of injection. Assuming at least 50 % of the signal is required for a sufficient average, the maximum number of samples to trim are $s_{trmax} = \frac{s_{tot}}{4}$. If $s_{trmax} > 1200$ the 3rd order Butterworth filter is used, with $s_{tr} = 1200$, otherwise the FIR filter is used with $N = s_{tr} = 110$. Thus the minimum suggested injection time is now 440 samples or 27 ms.

3.2.3 Resistor Phantom Measurements

Resistor Arrangement

Four-terminal measurements were performed in the same resistor set-up used by Fabrizi, McEwan, Woo, *et al.* [164] (fig. 3.19), using 1 kΩ resistors as contact impedance. The range of R_{load} was chosen based on the expected four-terminal impedances of 5.3-73 Ω during scalp recordings, from McEwan, Romsauerova, Yerworth, *et al.* [48], which in turn was based on modelling by Horesh, Gilad, Romsauerova, *et al.* [168]. These values were subsequently used by Fabrizi, McEwan, Woo, *et al.* [164] in comparison of three EIT systems. The majority of the loads measured on the two tanks in chapter 2 also fall into this range, with a range of 0.01 to 57.9 Ω for the adult tank, and 0.038 to 67.7 Ω for the neonatal tank. The smaller minimum loads are likely due to differences in protocol between the tank experiments and those used in the modelling by Horesh, Gilad, Romsauerova, *et al.* [168]. Six approximately linearly spaced loads were chosen between 7 and 70 Ω, and validated using an Hewlett Packard 4284A Impedance Analyser.

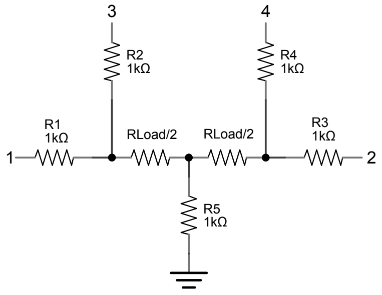

Figure 3.19: *Four terminal measurement set-up. Injecting electrodes connected to terminals 1 and 2, measurement electrodes connected to terminals 3 and 4*

Similar to the comparison study by Fabrizi, McEwan, Woo, *et al.* [164], a symmetrical resistor network was used to assess inter-channel variations. The resistor phantom used in these experiments was the "Swisstom EIT Resistor Mesh Phantom 32-HG" (fig. 3.20), a simplified version of the design proposed by Gagnon, Cousineau, Adler, *et al.* [169]. The phantom was designed for testing EIT systems for lung ventilation imaging, and therefore has a load towards the lower end of the range expected on the scalp, ≈ 15Ω. Current was injected between all 32 neighbouring pairs, and voltages recorded on all 32 channels for both systems. The subsequent data analysis focussed on the measurements closest to the injection channels with the largest impedances 5-15 Ω, as these were within the range suggested by Horesh, Gilad, Romsauerova, *et al.* [168].

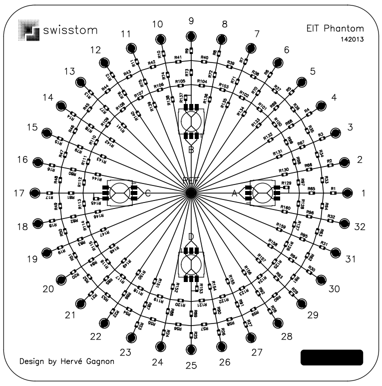

Figure 3.20: *Circuit diagram of SwissTom Resistor Phantom [165]*

System Set-up

The length of each current injection was 64 cycles for the KHU system, with the exception of 10 and 100 Hz, where 2 and 8 cycles were used due to FPGA memory limitations. In each case, the switching time for the ScouseTom was chosen such that, after removal of switching artefact, the resultant signal used in averaging was the same length as that used by the KHU. Additionally, the frequency of injection with the ScouseTom were set to match those of the KHU when in direct comparison, i.e. 1.125 kHz rather than 1 kHz. The KHU system was calibrated on the same day as each test. For the KHU, the differential voltage was recorded directly, whereas the ScouseTom recorded the absolute voltages at each terminal. In order to allow direct comparison between systems the differential voltage was calculated during data processing.

It became apparent that, for the same settings, the amplitude of the injected current by the KHU varied significantly at 1 kHz or below, see fig. 3.28. Therefore, in all experiments except the frequency response test, the amplitude settings were adjusted to match the output of the ST.

Variations with load

A four terminal measurement, fig. 3.19, using a single channel was performed on six loads: 6.8, 19.8, 31.8, 47.3, 59.9 and 70.3 Ω. Current was injected between terminals 1 and 2 using channels 1 and 2 on both systems, and voltages were measured across terminals 3 and 4. For both systems, the other 28 channels were connected to ground.

Originally 1024 repetitions were intended to be recorded for both systems, however consecutive use of the same IMM caused an overheating problem during recording with the KHU. As fig. 3.21 shows, after 220 repeated injections using the same IMM the data becomes excessively noisy in a manner similar to that seen before the redesigned case and power supply in fig. 3.7. The data returned to normal after a cooling period of 30 minutes. Thus the repeats used in the load variation experiments were limited to 200, with half an hour between each recording. This issue was only present when an single IMM was used consecutively, and was not observed in subsequent 32 channel tests.

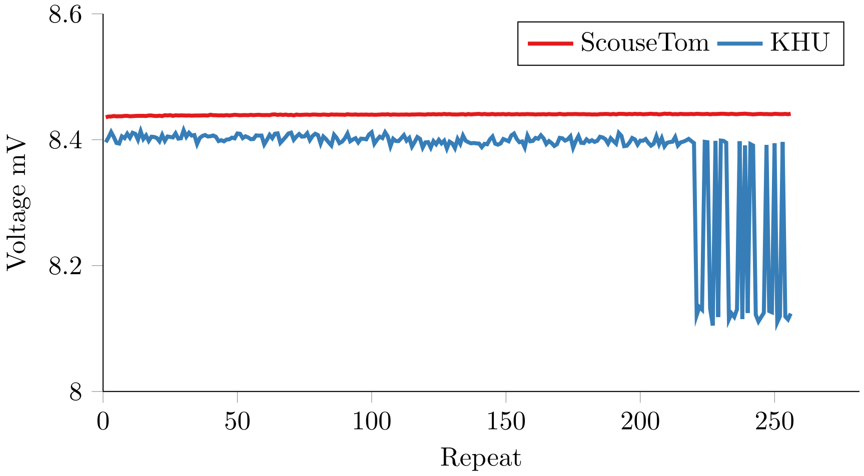

Figure 3.21: *Example four terminal recording with both systems. KHU begins to overheat after 220 repeats*

Both systems were allowed two hours to warm up before recording and the order of the loads was randomised for each system. The noise was expressed as the standard deviation across the whole recording in μV.

Amplitude Accuracy

Current was injected between all 32 neighbouring channel pairs on the SwissTom resistor phantom at 1.125 kHz, for currents ranging from 25 to 300 μA, repeated 50 times for each, with a randomised current order. The measurement corresponding to the largest voltage on a non-injection electrode, for each of the 32 injections, was used in subsequent analysis. The effective trans-resistance was calculated in each case and the average compared to the ideal value given by SwissTom. The variation across all 32 injections was then expressed as a standard deviation for each current amplitude.

Amplitude across Frequency

Recordings were taken with each system on the resistor phantom for six different carrier frequencies at 100 μA amplitude. For the KHU the first six carrier frequencies were chosen: 11.25 Hz, 112.5 Hz, 1.125 kHz, 5.625 kHz, 11.25 kHz and 56.25 kHz. The overlap of the frequency range of the two systems is small, as the KHU only has three possible carrier frequencies below the filter cut-off 3.2 kHz of the BioSemi EEG system used in the ScouseTom system. Therefore three other frequencies were included in the ScouseTom recordings, to give the complete list of 11.25 Hz, 112.5 Hz, 500 Hz, 1.125 kHz, 1.5 kHz and 2 kHz. The injection was repeated 50 times for each frequency, and the frequency order randomised. The average of the largest voltage on a non-injecting channel was calculated and used for comparison.

Signal-to-Noise Ratio

The distortion of the injected sine wave was measured for both systems by recording the voltages using the BioSemi EEG system for injection with a single injection pair. The measurement was repeated 50 times and the data was windowed such that the same number of samples were used in the calculation of the PSD for both systems. The signal to noise ratio was calculated as $SNR = \frac{P_{f_c}}{P_f}$, the ratio of the power at the carrier frequency f_c to the power at all remaining frequencies. Due to the limitations of the sampling rate of the BioSemi, only three frequencies were considered: 10 Hz, 100 Hz and 1 kHz.

Long term drift and noise

Measurements were collected on the SwissTom phantom over the course of an hour, with an injected current of 150 uA and 1 kHz. The drift in each measurement was defined as the percentage change relative to V_{T0}, the initial voltage, for the voltage averaged over two minutes. The noise on each channel was expressed as the standard deviation of the voltage after removal of any linear trend.

This data was also used to investigate the inter channel variations of the two systems. The relative standard deviation $RSD = \frac{s}{\bar{x}} \times 100$ of equivalent measurements with each injection pair was calculated for both systems. Two pairs of measurements on two impedances (four in total) fell within the expected load range from McEwan, Romsauerova, Yerworth, *et al.* [48], and were thus the focus of subsequent analysis.

Reciprocity is a key indicator to assess EIT measurement quality [38]. Reciprocity implies that the same impedance signal will be found if voltages are applied and currents measured, or if currents are applied and voltages measured, using the same electrodes. The metric commonly used is reciprocity error (RE), which is the ratio of the impedance measured with the voltage and current electrode pairs swapped, in a four terminal measurement [49], [110].

This was also calculated from the measurement on the resistor phantom for both systems and averaged across the whole protocol.

3.2.4 Tank Measurements

Adult head tank

The adult head tank created in chapter 2 was used for the system comparison. The experimental set up was identical to that described in section 2.2 with 0.2 % saline and skull present.

System settings

In all experiments, the current injection protocol used for both systems was the "optimal" protocol, proposed by Malone, Jehl, Arridge, *et al.* [59], described in section 2.2. The current amplitude was 150 uA at 1.125 kHz, with the same injection settings as in section 3.2.3. Each recording was repeated 20 times over the course of approximately one minute, to replicate a more realistic clinical scenario which precludes extensive time for averaging. A fixed gain setting of 51 (setting = 1000) was set for every measurement channel on the KHU, as this was found to be the maximum possible without any saturation.

Simulation

The same 4 million element FEM described in section 2.2.5 was used in this study, and the Parallel EIT Solver (PEITS) created by Jehl, Dedner, Betcke, *et al.* [63] was again employed to calculate the forward solution. The measurement protocol differs between the two systems as the ScouseTom measures the voltage on each electrode with respect to the ground electrode, whereas the KHU measures the differential voltage between each electrode, therefore the sensitivity matrix is different for each system. The differences of the sensitivity across the head was investigated, through summing of the protocol lines of the Jacobian J, to give context to explanations of any potential differences in image quality between the two systems. To further separate the effects of the differing protocols or system noise, perturbations were simulated for both protocols without noise, and the results compared to the "ideal" reconstructions, an example of which is shown in fig. 3.22b.

Data Collection

Initially, measurements were collected with a saline background and skull and compared to simulated voltages to compare the accuracy of the systems. The error analysis described in section 2.2.7 was then repeated for both datasets. Then a spherical plastic perturbation 3 cm diameter, was placed in three positions within the tank: posterior, central and lateral, which

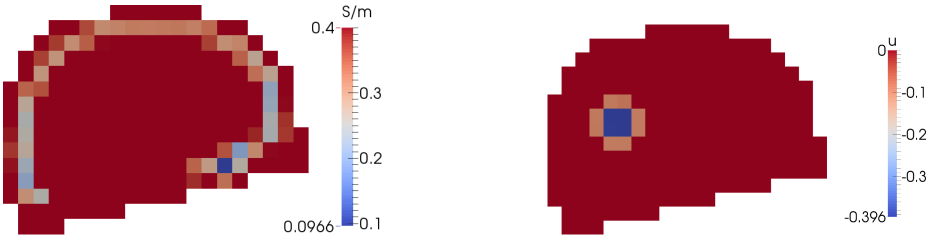

(a) *Baseline* **(b)** *Perturbation*

Figure 3.22: *Section view of conductivities in hexahedral mesh of head tank.* ***(a)*** *baseline conductivity of saline and skull,* ***(b)*** *"ideal" perturbation in posterior location*

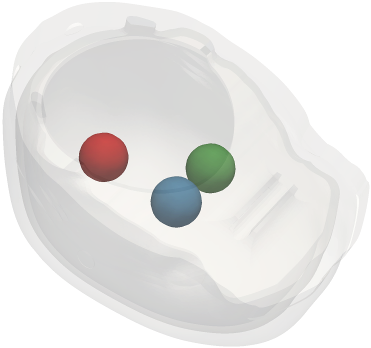

Figure 3.23: *Three locations of perturbations used in tank study, based on positions from Malone, Jehl, Arridge,* et al. *[59]*

correspond to the positions used in a simulation study by Malone, Jehl, Arridge, *et al.* [59] using the same head geometry shown in fig. 3.23.

Data were then collected with both systems for all positions for subsequent image reconstruction. A baseline was taken between each perturbation, and care was taken to keep the saline level constant by removing the excess saline with a syringe.

Image Reconstruction

Time difference images were reconstructed using a first order Tikhonov regularisation implementation by Markus Jehl in the UCL group [63]. The perturbations used both in simulation and tank experiments are meant to represent brain pathologies such as stroke, haemorrhage or epileptic foci, which are often approximated as small isolated perturbations [54], [68]. Therefore it is possible to introduce prior information into the reconstruction by using first order Tikhonov regularisation to bias the algorithm towards finding small connected perturbations. The image reconstruction problem in EIT, can be described by the minimisation of the cost functional

$$\mathbf{\Phi}\left(\mathbf{x}(\sigma)\right) = \frac{1}{2}\left(\mathbf{F}(\mathbf{x}) - \mathbf{v}\right)^{\top}\left(\mathbf{F}(\mathbf{x}) - \mathbf{v}\right) + \frac{1}{2}\lambda^2 \mathbf{x}^{\top}\mathbf{D}^{\top}\mathbf{D}\mathbf{x} \tag{3.2}$$

where **x** the change in conductivity, **v** the voltage difference between the two measurements, $\mathbf{F}(\mathbf{x})$ a non-linear function relating conductivity to voltage changes. Linearising $\mathbf{F}(\mathbf{x})$ around the model values of **x** then gives

$$\boldsymbol{\Phi}(x) = \frac{1}{2}(\mathbf{Jx}-\mathbf{v})^\top(\mathbf{Jx}-\mathbf{v}) + \frac{1}{2}\lambda^2\mathbf{x}^\top\mathbf{D}^\top\mathbf{Dx} \tag{3.3}$$

and the minimum can be found by setting the derivative to zero

$$\boldsymbol{\Phi}'(x) = 0 = \mathbf{J}^\top(\mathbf{Jx}-\mathbf{v}) + \lambda^2\mathbf{D}^\top\mathbf{Dx}. \tag{3.4}$$

Using the generalised singular value decomposition (gSVD) of the scaled Jacobian **J** and regularisation **D** this equation can be solved for **x**

$$\mathbf{x} = \left(\mathbf{J}^\top\mathbf{J} + \lambda^2\mathbf{D}^\top\mathbf{D}\right)^{-1}\mathbf{J}^\top\mathbf{v} = \left(\boldsymbol{\Lambda}^\top\boldsymbol{\Lambda} + \lambda^2\mathbf{M}^\top\mathbf{M}\right)^{-1}\mathbf{X}\boldsymbol{\Lambda}^\top\mathbf{U}^\top\mathbf{v}, \tag{3.5}$$

where we used $\mathbf{J}_x = \mathbf{U}\boldsymbol{\Lambda}\mathbf{X}^\top$ and $\mathbf{D} = \mathbf{VMX}^\top$. Since both $\boldsymbol{\Lambda}$ and **M** are diagonal matrices with a limited number of generalised singular values [72], they can easily be inverted and **x** is obtained by

$$\mathbf{x} = \mathbf{X}\left(\boldsymbol{\Lambda}^\top\boldsymbol{\Lambda} + \lambda^2\mathbf{M}^\top\mathbf{M}\right)^{-1}\boldsymbol{\Lambda}^\top\mathbf{U}^\top\mathbf{v}. \tag{3.6}$$

To reduce the computational cost of calculating the gSVD and to prevent the 'inverse crime' [170], a hexahedral mesh with a considerably smaller number of elements (2526 elements of $[1 \times 1 \times 1]cm$ size) were used for image reconstructions (fig. 3.22a). The Jacobian matrix $\mathbf{J}_\sigma$ as computed on the fine mesh is summed into geometrically regular cubes $\mathbf{J}_{hex}$ and the Laplacian **L** matrix for the first order Tikhonov regularisation is computed on this hexahedral mesh.

The regularisation factor was kept constant at $\lambda = 4.6 \cdot 10^{-4}$ for all reconstructed images. The value was chosen based on the shape of the L-curve [72] by Markus Jehl, as the L-curve was not pronounced enough to choose λ automatically. The solution norm $||\mathbf{x}||_2$ for the chosen λ was generally around 0.1 and the residual norm $||\mathbf{Jx}-\mathbf{v}||_2$ around $1.0 \cdot 10^{-4}$. The colour bar of all images was scaled according to the largest reconstructed change in the whole mesh. Therefore images of slices sometimes do not contain the maximum value of the colour bar.

The perturbation was defined as the mean of the *reconstructed perturbation* conductivity changes, with the *reconstructed perturbation* being the largest group of connected hexahedra with conductivity changes above half the maximum conductivity change. The background was defined as the mean of all the conductivity changes not belonging to the *reconstructed perturbation*.

Image Quantification

An objective comparison of the images was performed based upon the quantification algorithms by Malone, Jehl, Arridge, *et al.* [59] and Packham, Koo, Romsauerova, *et al.* [68], modified for use with hexahedral meshes. Each image was analysed by first identifying the *reconstructed perturbation*, and then using three metrics defined as follows:

1. Localisation error: the vector displacement of the *centre of mass* of the *reconstructed perturbation* with respect to its real position, as a percentage of the tank's diameter.
2. Shape error: the mean of the difference in each axis of the *reconstructed perturbation* to the perturbation's actual width, expressed as a percentage of the tank's diameter.
3. Image noise: the standard deviation of all conductivity changes not belonging to the *reconstructed perturbation* expressed as a percentage of the mean of the *reconstructed perturbation*'s conductivity changes.

All of these metrics are calculated with respect to a background or comparison image. For the simulated reconstructions, an "ideal" conductivity distribution, fig. 3.22b was used. The experimental images were compared to these simulated reconstructions to separate the effects of the protocol and the system noise.

3.2.5 Scalp Recordings

Scalp recordings were taken in collaboration with Nir Goren in the UCL group as part of a study into long term drift in EIT recordings. 17 Ag/AgCl EEG electrodes, 16 EIT and one ground were applied to the scalp of a single subject in the `spiral_16` configuration (fig. 3.24) as proposed by Fabrizi, McEwan, Oh, *et al.* [58], based on the EEG 10-20 system [56]. Each electrode site was prepared through abrasion with an abrasive paste (NuPrep, Weaver and company, USA, www.weaverandcompany.com), before application with conductive EEG gel (Elefix, Nihon Kohden, Japan). A current of 150 uA at 1 kHz and 1.125 kHz was used for the ST and KHU respectively, with the injection time set for both systems to provide 64 sinewave periods for both carrier frequencies. As the protocol used in this study only addresses 16 of the 32 channels on both systems, the remaining channels were all connected together to ground during recording. The `spiral_16` protocol has 34 current injections, which made for a complete protocol every 3.4 sec. The first 20 minutes ($\approx$ 350 frames) were used in subsequent analysis as this represents the longest feasible time for recording for a stroke recording as described in section 1.5.1. Recordings were collected on two subjects for both systems, and the data combined into a single data set for analysis.

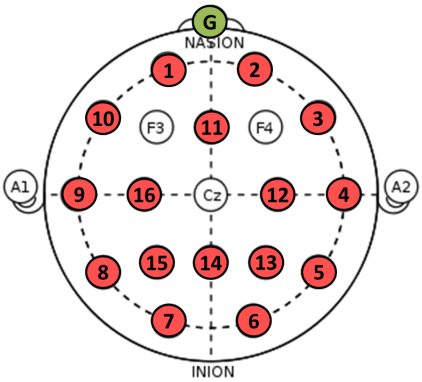

Figure 3.24: *Scalp electrode locations, based on the* `spiral_16` *protocol by Fabrizi, McEwan, Oh,* et al. *[58]*

3.2.6 Test object complexity

The data for all three test objects were compared by considering the *proportional noise* as a percentage of the mean. This was used previously by Fabrizi, McEwan, Woo, *et al.* [164] in a comparison of three EIT systems, using three four-terminal measurements on each test object. To take advantage of the parallel voltage measurements, and to give a more representative sample, all combinations meeting the boundary voltage criteria for imaging were included.

In the resistor phantom, the measurements meeting the criteria were the same four measurements described in section 3.2.3. For the tank and scalp recordings, the voltage rejection criteria used were those proposed by Packham, Koo, Romsauerova, *et al.* [68], who recommend removal of combinations with voltages less than 0.1mV. These criteria resulted in 128, 847 and 280 total combinations in the resistor, tank and head experiments respectively.

3.3 Results

3.3.1 Resistor Phantom Measurements

Variations with load

The standard deviation of the single channel measurements across the six loads are shown in fig. 3.25. The noise in the ST system was less than 0.8 μV for all resistances and was weakly correlated with load ($R^2 = 0.54$). The KHU demonstrated much greater variation across the load range. Between 20 and 50 Ω the noise was less than 1 μV, similar to that of the ST. However at the extremes of the load range the noise was significantly larger, 9.87 μV at 5 Ω and >4.5 μV above 50 Ω.

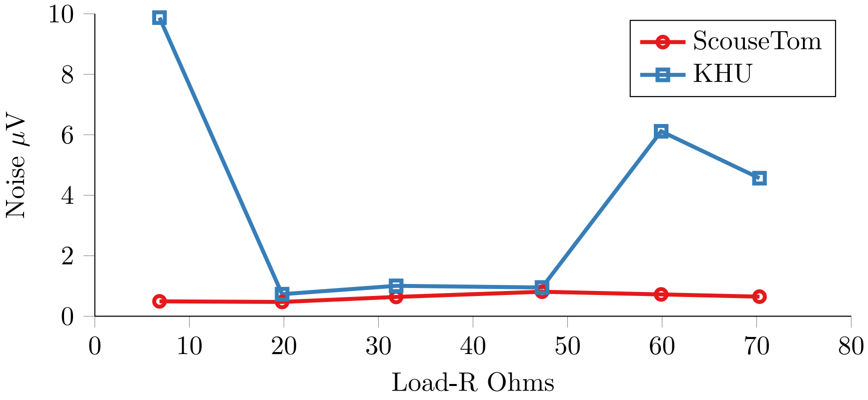

Figure 3.25: *Noise in four-terminal measurements across expected load range, comparison of ST and KHU systems*

Amplitude Accuracy

The transimpedance $\frac{V}{A}$ measured with the ST was stable across the current amplitude range, varying 0.037 Ω or 0.23 %, shown in fig. 3.26. The KHU demonstrated an order of magnitude greater variation with injected current, 0.37 Ω or 2.37 %. Overall the inter channel variation was considerably smaller in the measurements with the ST system compared to the KHU. The mean inter channel variation across current was 0.01±0.003 Ω with the ST system and 0.19±0.17 Ω with the KHU. The maximum variation occurred at 25 μA for both systems, with a varation of 0.013 Ω and 0.41 Ω for the ST and KHU systems respectively.

SNR

A comparison of the PSD of the voltages measured with the two systems is shown in fig. 3.27 for 1 kHz and 1.125 kHz injection with the ST and KHU respectively. The voltages measured with the KHU contain clear harmonics of the carrier frequency, which were not visible with the ST. Aside from the carrier frequency and harmonics thereof, the noise floor of the ST measurements are approximately 6 dB less than those with the KHU system. The SNR of these measurements, defined as ($SNR = \frac{P_{f_c}}{P_f}$), for 10, 100 and 1000 kHz or equivalent and given in table 3.4. On average the SNR of the ST was 12 dB greater than with the KHU.

Amplitude across frequency

The amplitude of the voltages measured with the ST show minor variation with frequency below 1 kHz, after which the voltage decreases from 1.37 mV to 1.08 mV at 2 kHz. The KHU demonstrates much stronger frequency dependence, with the voltage at 10 Hz as little as 0.02 mV.

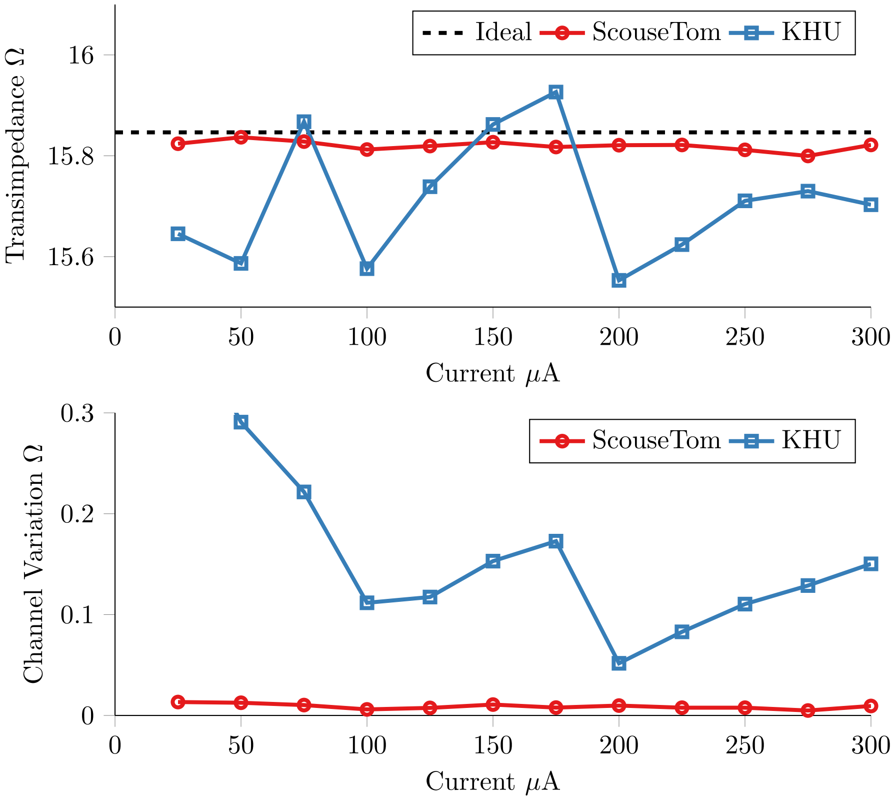

Figure 3.26: *Variation across current of transimpedance $\frac{V}{A}$ recorded on SwissTom resistor phantom with the ST and KHU EIT systems. Top: average transimpedance across all channels, bottom : standard deviation transimpedance across channels*

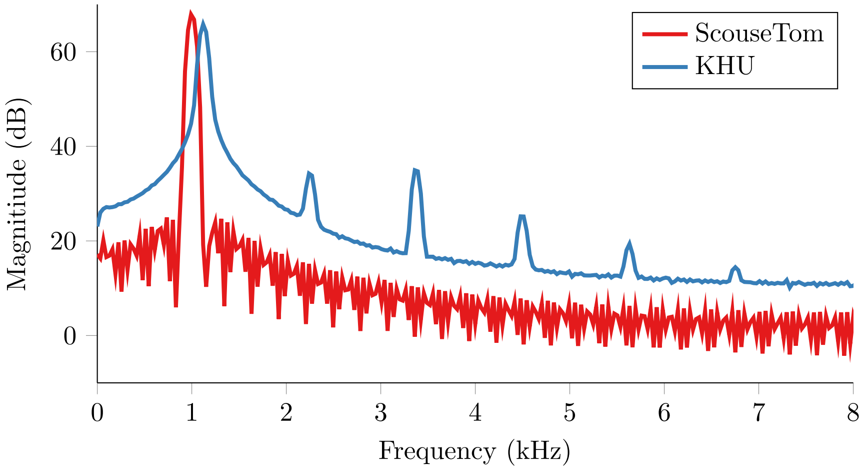

Figure 3.27: *PSD of ScouseTom and KHU EIT systems with 1kHz and 1.125 kHz current injection respectively*

	SNR (dB)	
Freq (Hz)	ScouseTom	KHU
10	30.9	17.8
100	28.0	21.0
1000	34.5	15.9
mean	30.8	18.3

Table 3.4: *SNR of injected current on the SwissTom resistor phantom as measured with the BioSemi EEG system*

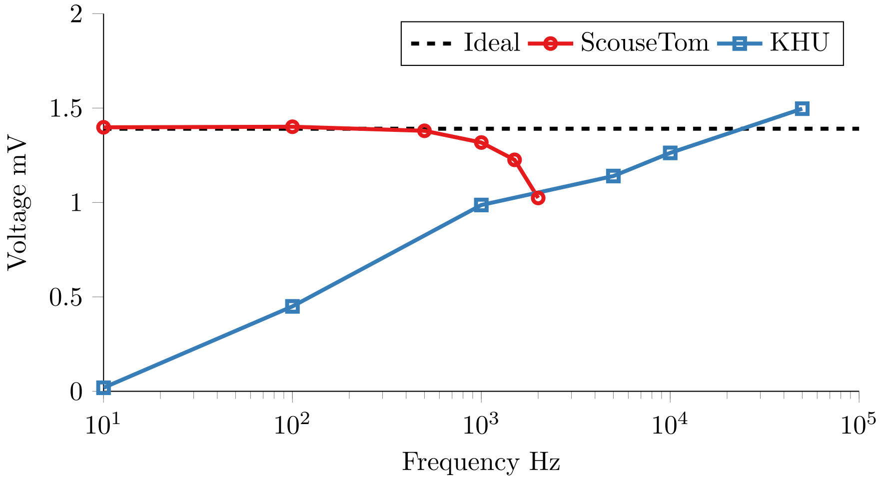

Figure 3.28: *Variations of the voltages measured on the SwissTom resistor phantom across frequency with the ST and KHU EIT system*

Drift and Noise

A histogram of the standard deviation of the voltages recorded over the course of an hour with both the ST and KHU systems is shown in fig. 3.29. The ST has, on average, approximately two-thirds of the noise as the KHU system, with 0.34±0.034 μV, and 0.55±0.16 μV for the ST and KHU systems respectively. The majority of the voltages with both systems have noise below 0.5 μV.

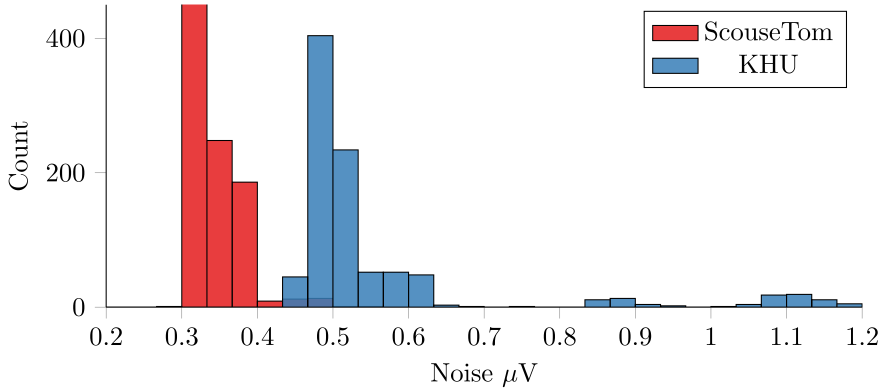

Figure 3.29: *Noise in hour long recording on resistor phantom*

The mean and standard deviation of the measurements as a percentage change from t_0 is shown in fig. 3.30. There is a clear positive linear drift ($R^2 = 0.989$) in the measured voltages with the ST, with a mean increase of 0.58 % at the end of the hour recording. The measurements with the KHU have a far less consistent change over the course of the hour recording. The maximum change of 0.014 % occurs at the end of the hour recording, but the linear trend is far less clear ($R^2 = 0.261$).

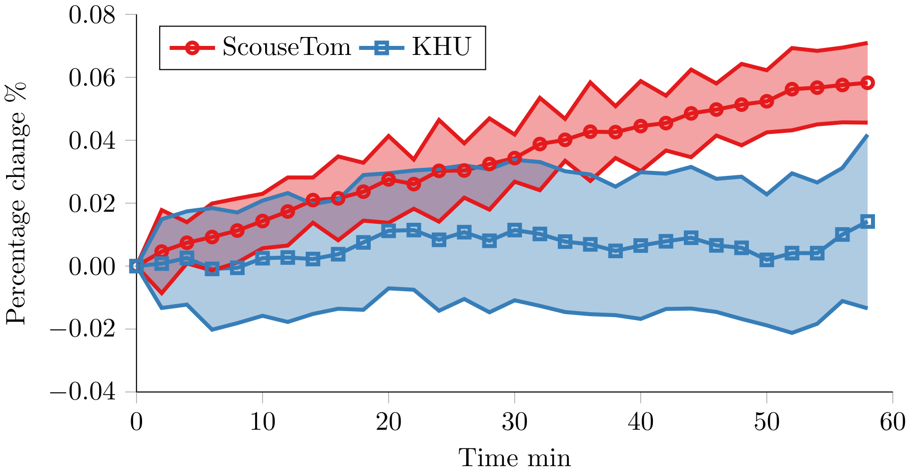

Figure 3.30: *Mean and standard deviation of drift across channels over one hour recording on SwissTom phantom with ST and KHU systems*

The interchannel variations for both systems, expressed as a relative standard deviation, as measured on four separate protocol combinations on the resistor phantom are compared in fig. 3.31. The transimpedance for combinations 1 and 2 was 4.48 Ω, and 15.8 Ω for combinations 3 and 4. The variation between channels was close to an order of magnitude greater with the KHU system than with the ST. The maximum variation with the ST was 0.33 %, whereas the maximum variation was 3.6 % for the KHU. For both systems, the variation between channels was greater for the smaller transimpedance (combinations 1 and 2). The mean reciprocity error was 0.42 % and 0.80 % for the ST and KHU systems respectively.

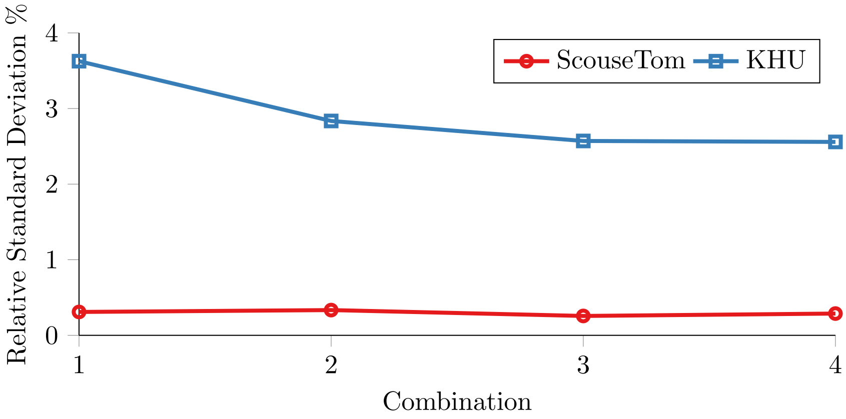

Figure 3.31: *Inter channel variations in one hour long recording on four separate protocol combinations, expressed as relative standard deviation.* $R_{load} = 4.48$ *for combination 1 and 2,* $R_{load} = 15.8$ *for combinations 3 and 4*

3.3.2 Head Tank

Baseline Accuracy

Both systems show strong correlation with simulated voltages $R = 0.999$ and $R = 0.993$ for the ST and KHU systems respectively, shown in fig. 3.32. The mean error across all combinations was 0.215±0.22 mV and 0.239±0.28 mV for the ST and KHU respectively. The KHU measurement protocol produces a greater proportion of smaller boundary voltages (< 1 mV) than the ST measurement scheme, 43 % and 11 % respectively . The percentage errors of the two datasets are shown in fig. 3.33. The error in the KHU is a median error of 11.1 %, over four times greater than that of the ST.

Noise

The average noise across all 6 recordings for each system was 0.99±0.71 μV and 1.73±1.57 μV for the ST and KHU respectively as shown in fig. 3.34. The performance of the two systems are

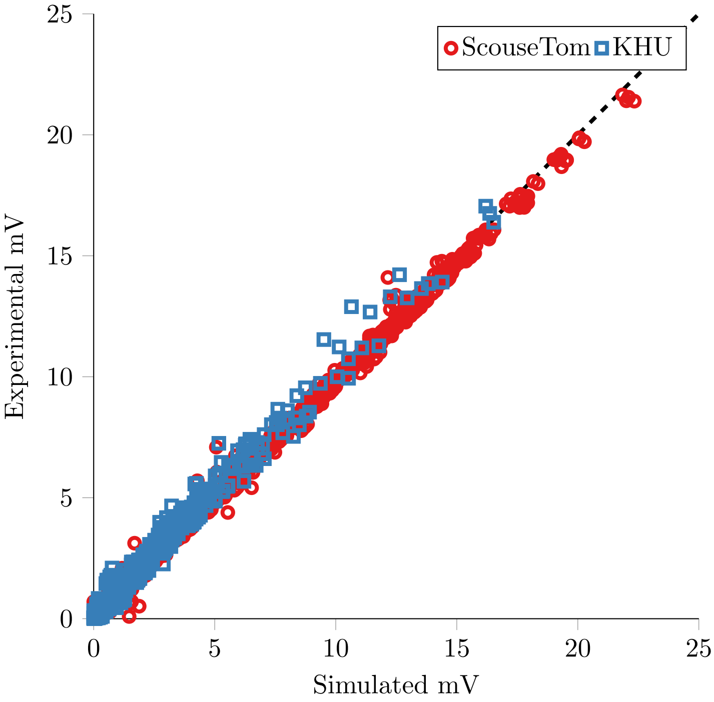

Figure 3.32: *Comparison of baseline voltages measured in adult head tank with ST and KHU systems to respective simulations*

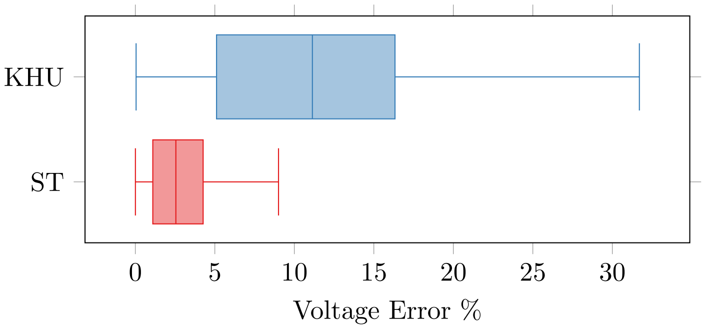

Figure 3.33: *Percentage errors of measurements from ST and KHU systems in comparison to simulation*

qualitatively more similar in this than than was found in the resistor phantom in section 3.3.1. In both cases, the mean noise trebled compared to the resistor measurements.

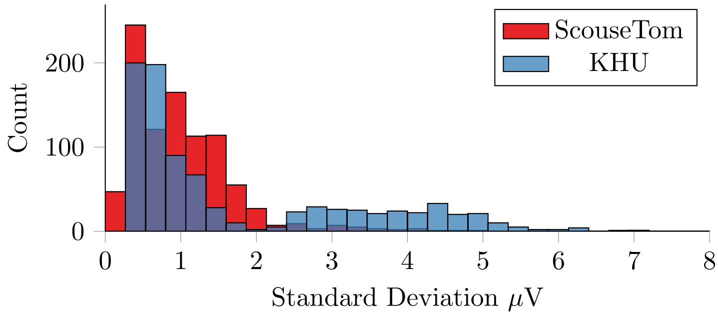

Figure 3.34: *Standard deviation of recordings in adult head phantom*

Sensitivity

The differences in sensitivity for each measurement protocol are shown in fig. 3.35. The mean sensitivity was 3.2 $\times 10^{-4}$ Vm/S and 2.9×10^{-4} Vm/S for the ST and KHU measurement schemes respectively. The ST measurement scheme has a higher overall sensitivity inside the skull (40-80 % increase), whereas the adjacent measurements by the KHU are comparatively more sensitive (≈ 40 %) in the scalp and skull. The exception to this is the nasion, the area surrounding the ground electrode at very front of the head. In this area the sensitivity is much greater in the ST measurement scheme, over 100 % change or >0.02 Vm/S inside the skull.

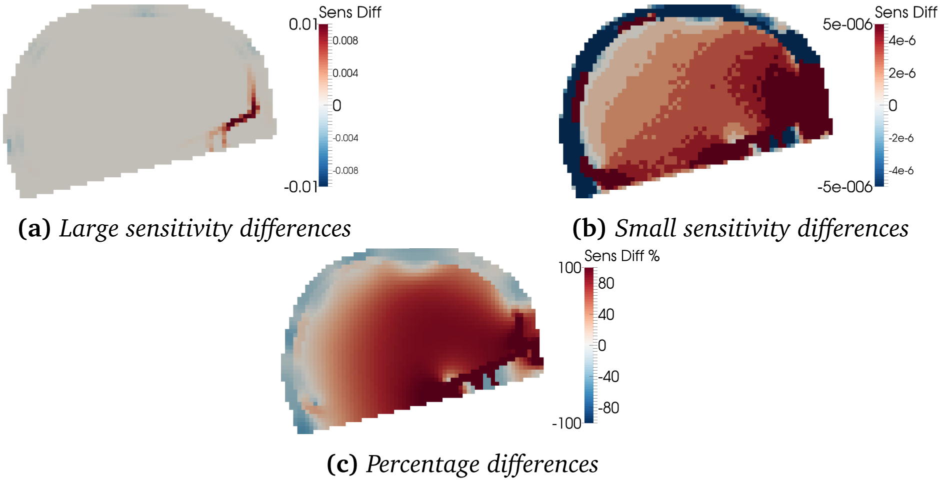

(a) *Large sensitivity differences*

(b) *Small sensitivity differences*

(c) *Percentage differences*

Figure 3.35: *Differences in sensitivity with ST and KHU measurement protocol, positive changes correspond to greater sensitivity with ST, negative to greater sensitivity with KHU.* ***(a)*** *full range highlighting skull sensitivity with ST,* ***(b)*** *narrower range displaying differences inside skull and* ***(c)*** *expressed as a percentage change*

Simulated Reconstructions

The simulated reconstructions for both measurement protocols are shown in comparison to the “ideal” perturbation first as all hexahedra above half max in fig. 3.36, and then as a slices through the complete image in figs. 3.37 to 3.39.

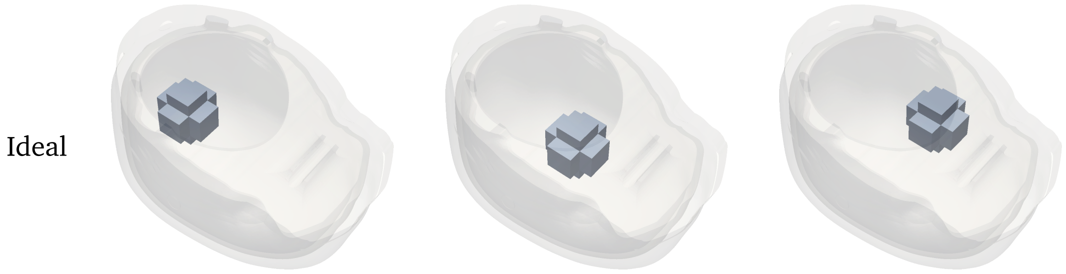

(a) *Posterior* **(b)** *Central* **(c)** *Lateral*

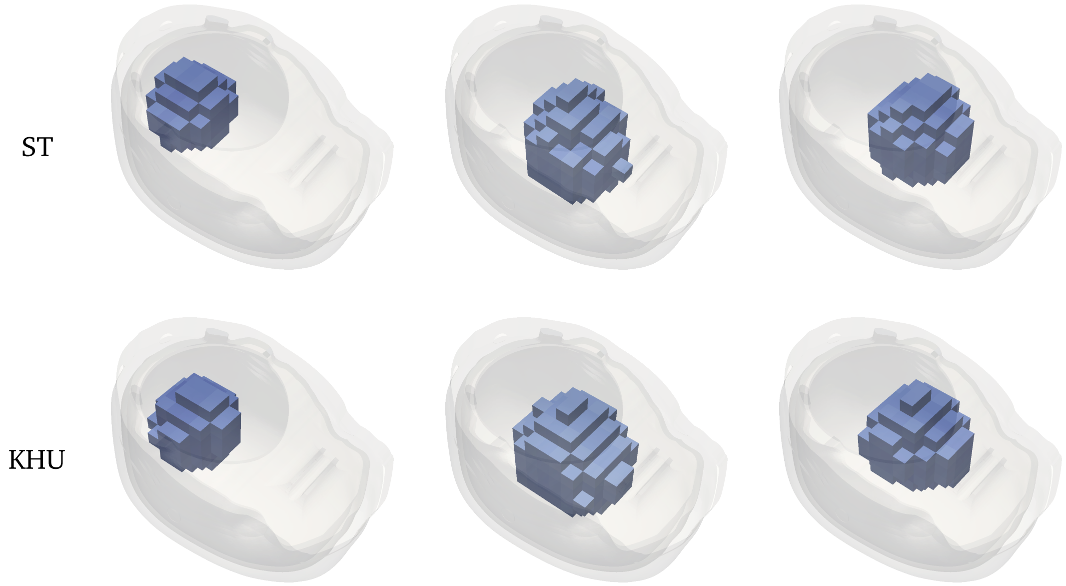

Figure 3.36: *Simulated reconstructed perturbations for corresponding measurement protocol in comparison to ideal perturbation*

Overall there is no substantial difference in image quality between the two systems. All perturbations were reconstructed close to the correct locations, with a single localised perturbation. Each perturbation was broader than real target diameter. Qualitatively, the the posterior and central perturbations are correctly located, whereas the lateral perturbation has been drawn further into the centre for both systems (fig. 3.39). The spread of the posterior perturbation (fig. 3.37) is smaller with the KHU measurements, whereas for the central and lateral positions(figs. 3.38 and 3.39), the ST protocol produces qualitatively better results.

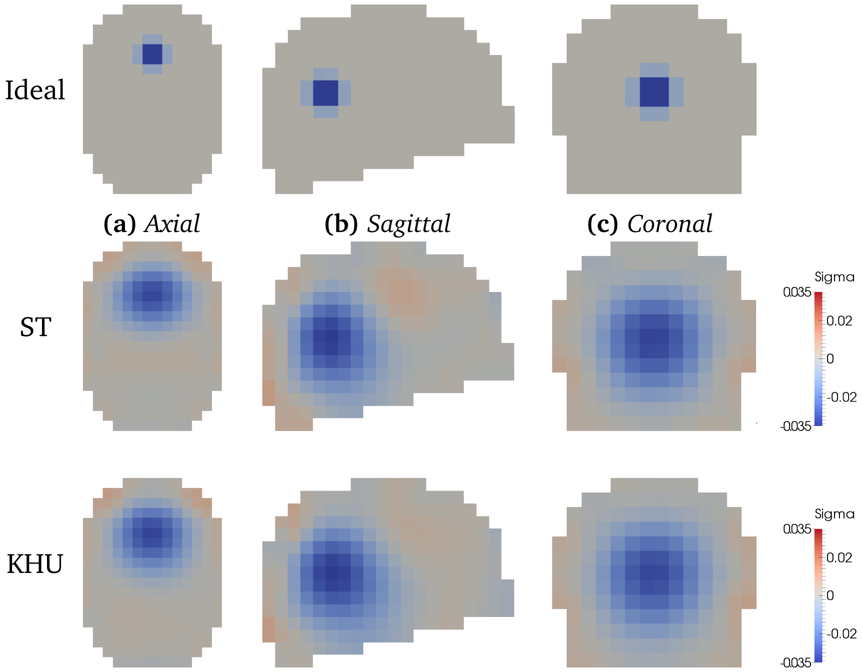

(a) *Axial* **(b)** *Sagittal* **(c)** *Coronal*

Figure 3.37: *Section views of image of simulated reconstruction with* **posterior** *perturbation for ST and KHU measurement protocols*

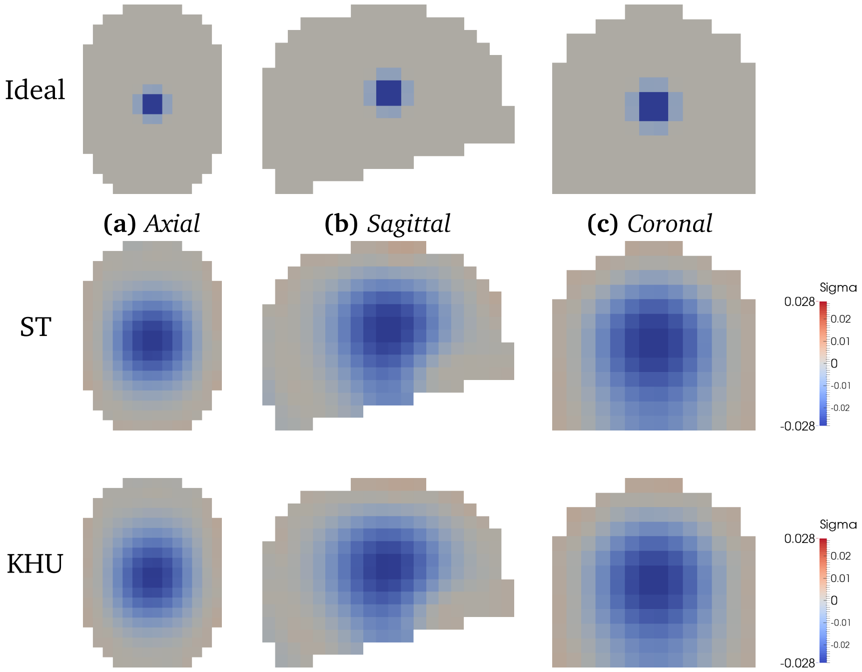

(a) *Axial* **(b)** *Sagittal* **(c)** *Coronal*

Figure 3.38: *Section views of image of simulated reconstruction with* **central** *perturbation for ST and KHU measurement protocols*

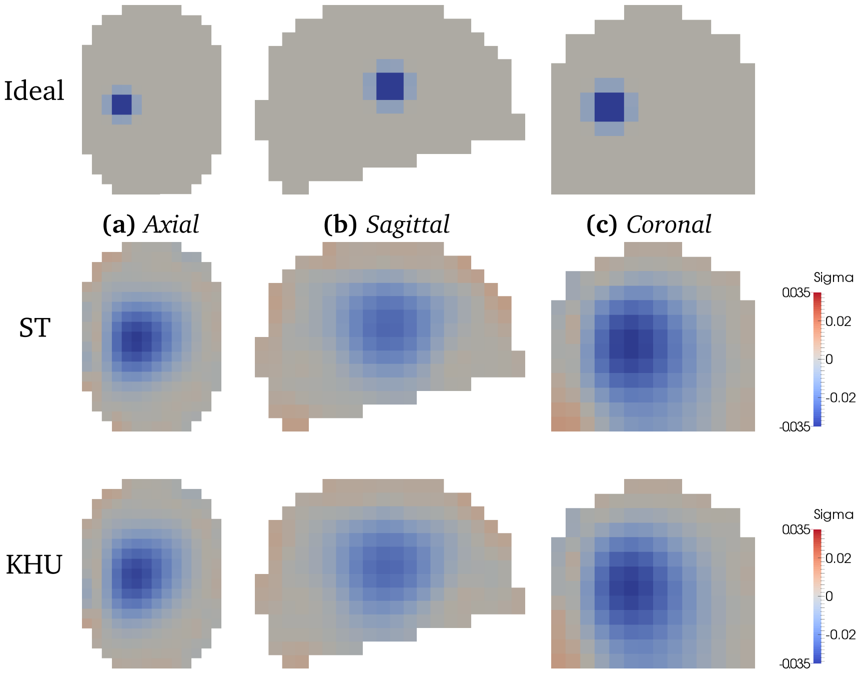

(a) *Axial* **(b)** *Sagittal* **(c)** *Coronal*

Figure 3.39: *Section views of image of simulated reconstruction with* ***lateral*** *perturbation for ST and KHU measurement protocols*

Quantification of Simulated Images

The image quantification results for the simulated perturbations, fig. 3.40, show the same pattern as the previous qualitative analysis. The largest error for all positions was the shape error, with a maximum of 6 % for the central perturbation. The error with both measurement protocols is similar, with less than 1 % difference across the three perturbations. For each metric, and for all locations the ST protocol had less image error than the KHU. The largest difference was in the noise error at the posterior location, with 8.76 % and 9.62 % total error for the ST and KHU respectively.

Reconstructed Images

The experimental reconstructions for both measurement protocols are shown in comparison to the “ideal” perturbation first as all hexahedra above half max in fig. 3.41, and then as a slices through the complete image in figs. 3.42 to 3.44.

Each experimental image is qualitatively similar to the simulated reconstructions in section 3.3.2. The artefactual positive conductivity changes are larger in the experimental images, particularly on the edges of the tank. Overall there is no substantial difference in image quality between the two systems. The artefacts on the edges of the tank appear greater in the KHU images, fig. 3.44, whereas the ST posterior image has the clearest artefact inside the skull

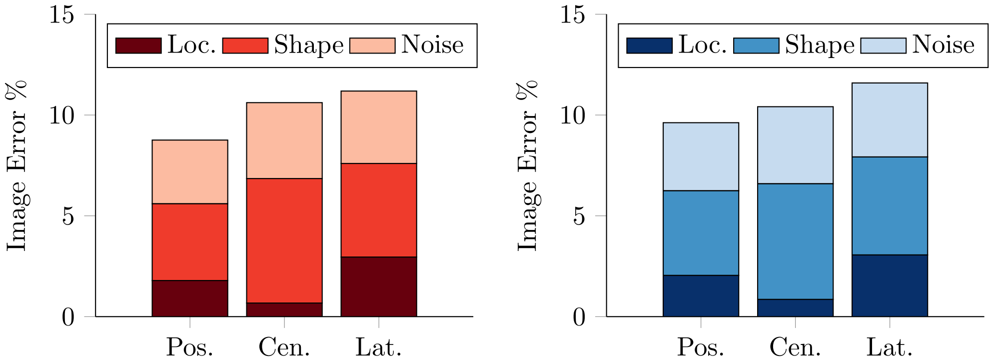

(a) *ST simulation error* **(b)** *KHU simulation error*

Figure 3.40: *Image error metrics for simulated reconstructions compared to "ideal" perturbations, for* ***(a)*** *ScouseTom Protocol and* ***(b)*** *KHU protocol*

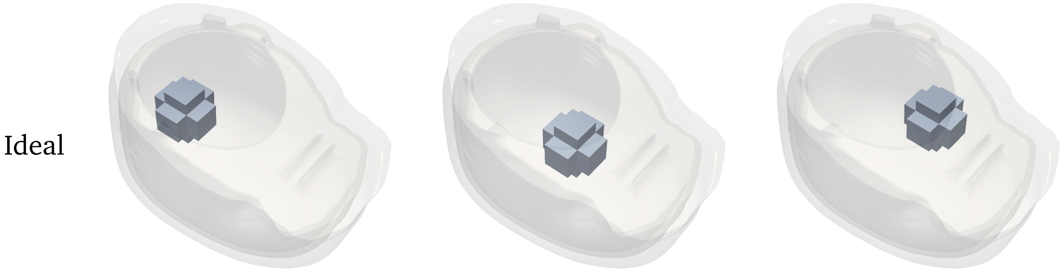

(a) *Posterior* **(b)** *Central* **(c)** *Lateral*

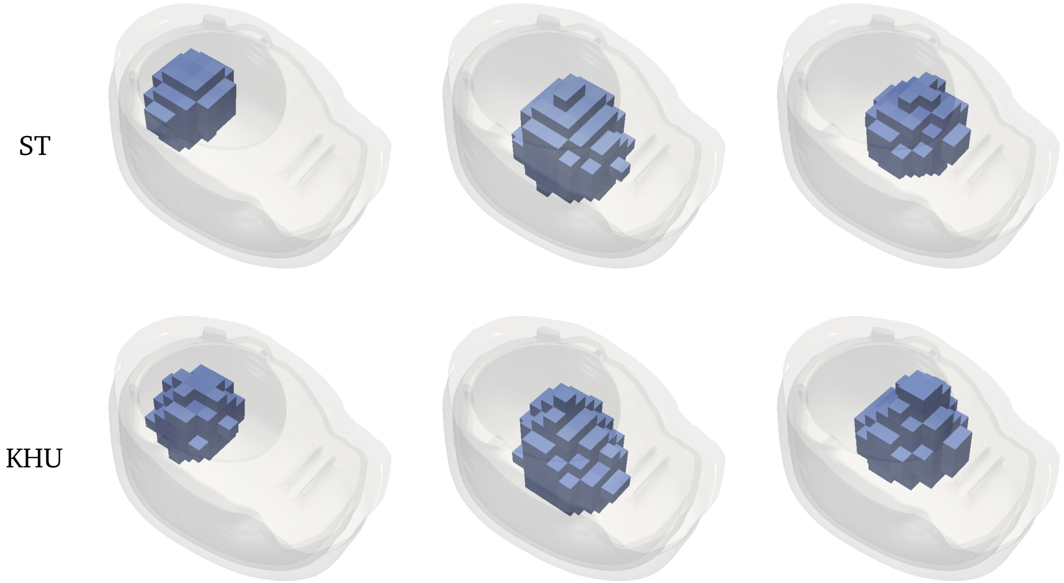

Figure 3.41: *Reconstructed perturbations in adult tank with both ST and KHU systems, in comparison to ideal reconstructions*

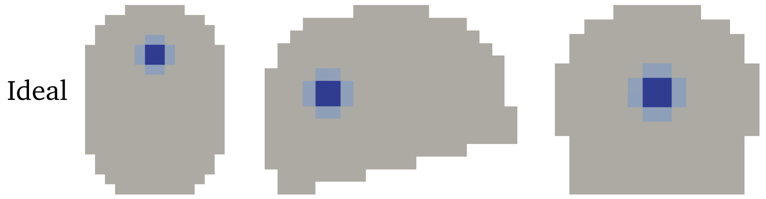

(a) *Axial* **(b)** *Sagittal* **(c)** *Coronal*

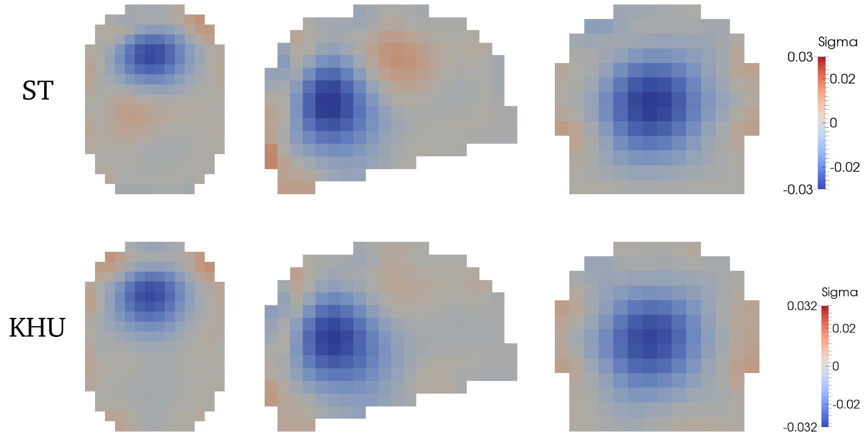

Figure 3.42: *Section views of image of experimental reconstructions with* ***posterior*** *perturbation for ST and KHU measurement protocols*

fig. 3.42.

Quantification of Experimental Images

The experimental image error compared to simulated images is approximately half that of the simulations in comparison the ideal reconstructions, fig. 3.45. The noise error metric was more than five times greater than either the location or shape errors in all positions. The difference between the error with the two systems was less clear, with the KHU having on average 0.45 % greater error than the ST.

3.3.3 Scalp Recordings

The average noise including all combinations across both recordings was 5.95±8.9 μV and 10.13±9.1 μV for the ST and KHU respectively. In both cases, the mean noise increased five fold compared to the tank measurements. Whilst the noise range for both systems is similar 0-40 μV, the ST has a much greater number of channels with <5 μV, fig. 3.46.

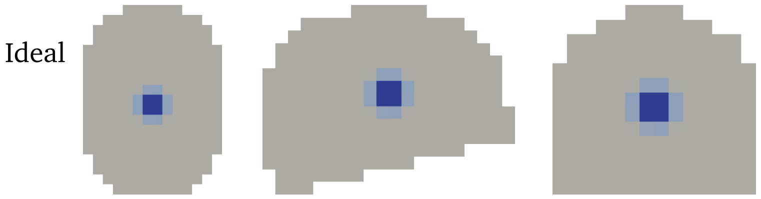

(a) *Axial* **(b)** *Sagittal* **(c)** *Coronal*

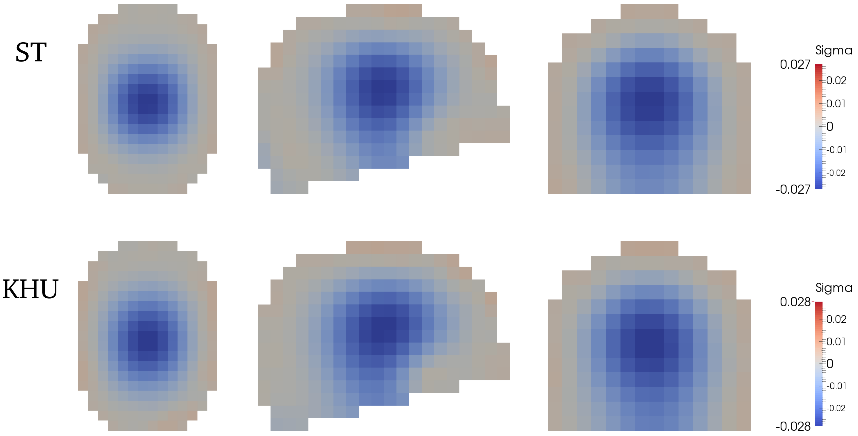

Figure 3.43: *Section views of image of experimental reconstruction with* ***central*** *perturbation for ST and KHU measurement protocols*

3.3.4 Test Object Complexity

The distribution of the percentage noise for increasing test object complexity for all relevant combinations as described in section 3.2.6 is shown in fig. 3.47. For the the resistor and tank experiments, the proportional noise was significantly smaller with the ST than the KHU ($p < 0.05$). The median noise increased with increasing complexity with the KHU, increasing from 0.53 to 0.54 and 1.34 % respectively. Whereas the noise decreased from 0.026 to 0.0139 % between resistor and tank with the ST, with the largest noise measured in the scalp of median 0.65 %. The scalp recordings for both systems represent the largest noise, over an order of magnitude greater than in the tank measurements, and are not significantly different ($p > 0.05$).

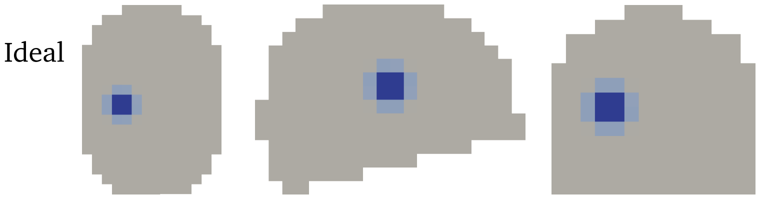

(a) *Axial* **(b)** *Sagittal* **(c)** *Coronal*

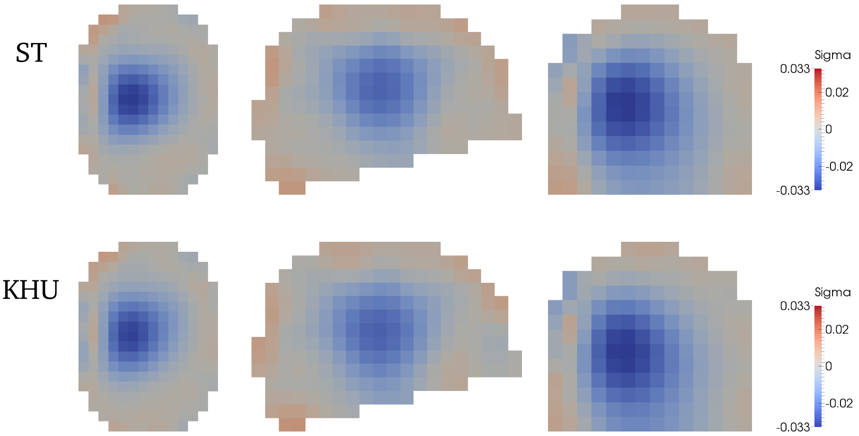

Figure 3.44: *Section views of image of experimental reconstruction with* ***lateral*** *perturbation for ST and KHU measurement protocols*

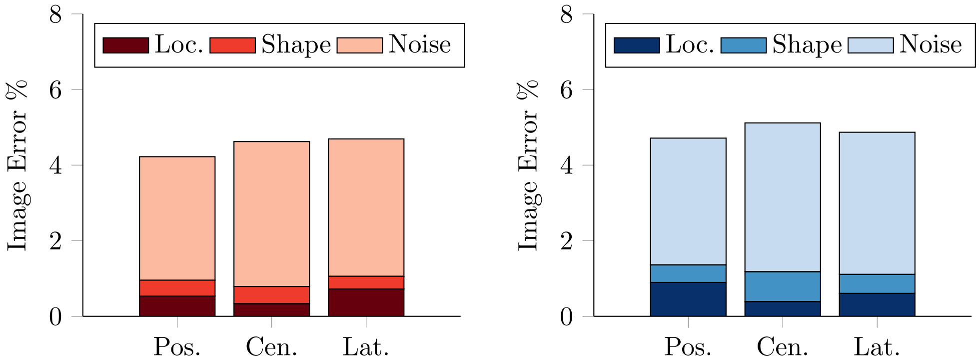

(a) *ST simulation error* **(b)** *KHU simulation error*

Figure 3.45: *Image error metrics for experiments compared to simulated perturbations for* ***(a)*** *ScouseTom Protocol and* ***(b)*** *KHU protocol*

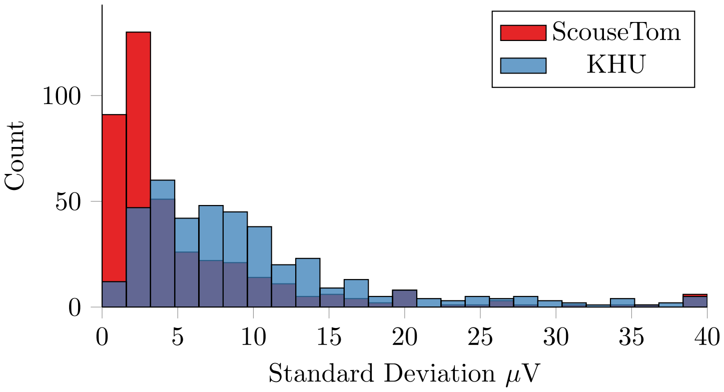

Figure 3.46: *Standard deviation of recordings in adult head phantom*

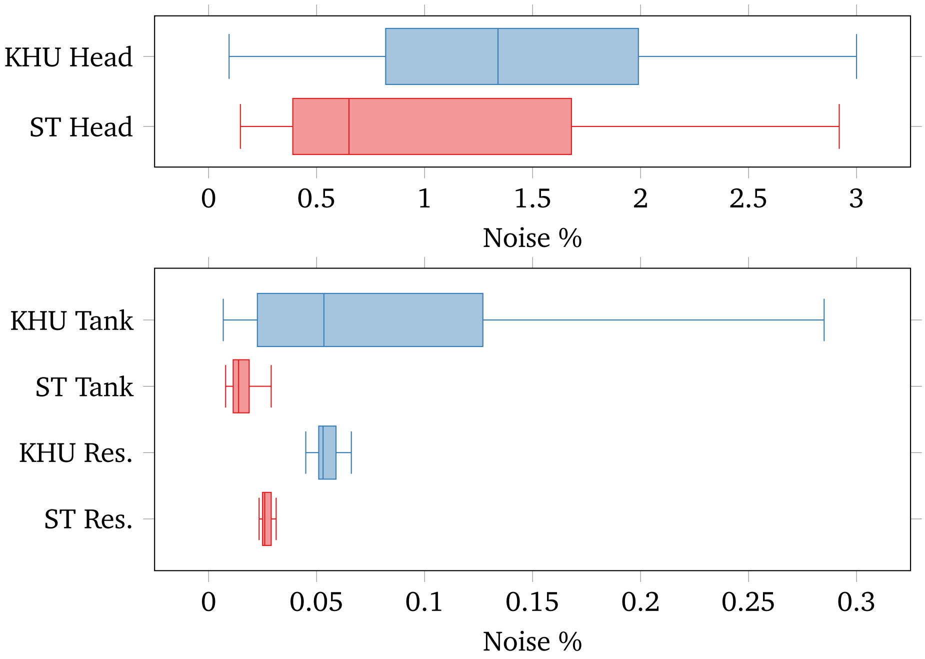

Figure 3.47: *Proportional noise as % of mean across all experiments, resistor phantom, saline tank and scalp*

3.4 Discussion

3.4.1 System Comparison

Resistor Phantom

Overall the ST performed better across all resistor phantom experiments, with the exception of the drift across an hour recording fig. 3.30. The noise across loads was less then 0.8 μV for the ST whereas the KHU had a noise of 1 μV between 20 and 50 Ω and > 4.5 μV otherwise. The noise across all channels was consistently less with the ST than the KHU in the long term measurement fig. 3.29, which follows from the results in the single channel.

The measurement drift was significantly greater with the ST system, fig. 3.30, which is likely due to heating of the passively cooled Keithley 6221 Current Source. This cooling is less effective compared to the substantial cooling added to the KHU system in section 3.2.1, which would suggest that the ST would benefit from additional cooling. It is important to note that the Keithley 6221 was in constant use being the only current source in the ST system, and a single IMM overheated after 220 measurements (fig. 3.21) when used in this manner even with this additional cooling.

Whilst the noise measured with the KHU matched that of the ST for 19.8 to 47.3 Ω (fig. 3.25) and 75 and 150 μA (fig. 3.26), significantly, the ST performed much more consistently across the parameter range in every experiment. The variation over current with the KHU was ten times larger than that measured with the ST. The variations across frequency were much greater with the KHU, particularly below 1 kHz, shown in fig. 3.28. Despite the 3.2 kHz cutoff (-3 dB) of the anti aliasing filter of the BioSemi, the measured voltages decreased above 1 kHz. This is due to the large transition band in the anti aliasing filter, and thus limits the usable frequency range to within 2 kHz. The KHU demonstrates a strong frequency dependence, with the output at lower frequencies significantly attenuated by the band pass filter between the DAC and the iHCP on the IMM.

Further, the inter-channel variations were close to an order of magnitude greater with the KHU system in both the amplitude test fig. 3.26, and the long term measurements fig. 3.31. These variations were significantly greater at lower currents (<100 μA) (fig. 3.26), where the `current level` setting described in section 3.2.1 was 1 or greater. The calibration steps described in section 3.2.1 can only be performed successfully for a `current level` setting of 0, and the steps to correct the DC offset are too coarse for the lower current amplitudes. Therefore the calibration settings are not optimal for the lower current levels, which results in a greater variation between IMMs.

The distortion of the sinusoidal current, described in section 3.3.1, was also greater with the KHU, with harmonics clearly visible in the spectra. These are negligible when considering the amount of current injected with regards to patient safety, but may cause problems during multi-frequency recordings as the harmonics are in band with other potential injection frequencies.

Head Tank

Both systems were able to replicate the simulated tank voltages with a similar degree of accuracy, with a mean absolute error of 0.215 and 0.24 mV, for the ST and KHU respectively. However the adjacent measurement protocol made for a higher proportion of small (< 1 mV) channels which contributed to an almost four-fold increase in the mean percentage error. The noise distribution in fig. 3.34 in both datasets were closer than that measured on the resistor phantom, with the exception of some higher noise outliers with the KHU. The noise for a both systems increased by 300 % on average from the resistor measurements. These results suggest that the noise inherent in the tank measurements is large enough to obscure the difference in performance of the two systems visible on the resistor phantom.

The 150 μA and 1.125 kHz current used in the tank experiments were amongst the parameters providing the highest performance for the KHU in the resistor phantom experiments. Additionally, the majority of the transimpedances in the tank correspond to the range of loads in section 3.3.1 with the lowest noise with the KHU. Therefore these measurements represent the ideal scenario for achieving the best possible results with this system. It is clear that outside these settings, especially considering the increased noise for lower boundary voltages, the performance of the system could degrade.

There was little difference between the simulated perturbations with the two measurement protocols despite the 40-80 % increase in sensitivity inside the head, as the image quantification in section 3.3.2 shows. All perturbations could be reconstructed experimentally with both systems, with minimal additional error from the system noise. For both systems the largest additional error metric was the noise error, section 3.3.2, due to the increased artefacts in the scalp and skull. As with the simulated images, the ST had the least total across all perturbations, albeit only 0.45 % less. These results suggest that both systems have the SNR capable of replicating simulated images.

The similarity of the reconstructed images in section 3.3.2 highlights the benefits of error cancellation during time difference EIT. The recordings with the KHU had on average two thirds greater absolute noise (section 3.3.2), and over four times greater proportional error (section 3.3.2), but the effects upon the image quality was negligible. It is likely that the noise of both systems persisting after time difference cancellation were insufficient to mask voltage differences as a result of the high contrast perturbation. Repeating the experiment with a smaller perturbation with a lower contrast may reveal further differences in the reconstructed images with the two systems.

No boundary voltage processing or rejection was performed before image reconstruction in this study, which is common in previous head tank studies [54], [68]. It is possible the reconstructions could have been improved by employing these methods. However, the broad shape of the reconstructed perturbations, even in simulation (fig. 3.37) suggest that the imaging is still the major limiting factor in the accuracy of EIT of the brain. This should be taken into consideration in any future studies, alongside optimised boundary voltage rejection, if more precise reconstructions are desired.

Scalp Recordings

The noise in the scalp recordings was considerably larger than in tank experiments, with both systems showing a similar noise distribution (fig. 3.46) albeit with the ST having a greater concentration of channels with <5 μV noise. The mean noise across all channels with the ST was close to half that of the KHU however, as the KHU has a greater number of considerably higher noise channels > 30 μV. As with the tank studies, it is likely that the additional noise inherent in scalp recordings is masking the differences in performance of the two systems clearly visible in the resistor phantom. These findings appear to confirm the findings of Fabrizi, Sparkes, Horesh, *et al.* [30], who found the thermal, quantisation and amplifier noise were only responsible for ≈5 % of that observed in scalp recordings.

Test Object Complexity

Overall, the percentage noise increased with increasing test object complexity as shown in fig. 3.47. With the exception of the scalp recordings, the ST had significantly smaller percentage noise than the KHU. The tank recordings showed a smaller percentage noise overall for the ST and close to half of the measurements with the KHU also had less noise than the corresponding resistor phantom measurements. However, there was a much wider range of percentage errors with the KHU recordings, compared to the ST. There are a number of contributing factors to this result. Firstly, unlike the ST, there is a clear optimum load range for the KHU (section 3.3.1), so when the transimpedance fall inside this range, the performance is similar to that of the ST. The adjacent measurement protocol of the KHU results in a higher percentage of channels with the lowest transimpedances, which fall outside the optimum range for the KHU and thus have a higher percentage noise.

The proportional noise was an order of magnitude larger in the scalp recordings and no longer significantly different between systems. The implication of this result is that the physiological noise introduced by measuring with electrodes on skin has a stronger influence upon the resultant SNR than the system noise.

3.4.2 Technical considerations

The limited frequency range of the ST coupled with the limited injection frequencies of the KHU meant dictated that the tank and scalp experiments had to be performed at 1.125 kHz.

This limited the output current based on the IEC 60601 regulations [166] to a 159 μA. This is close to the lower range of injection currents for the KHU, and as such does not represent the optimum performance parameters. Further, the GIC circuit is not active for frequencies below 5 kHz, so it is not possible to obtain any conclusions regarding the benefits this confers. It was also at 1 kHz that Wi, Sohal, McEwan, *et al.* [110] found the largest variation in Output Impedance across the 16 channel KHU Mk. 2.5. It is possible that for a higher current or a higher frequency the benefits of the complexity in the design of the IMM and the driven shields would become clearer.

3.4.3 Implications for future experiments

Both systems offer significant improvement on previous EIT systems used in the group [68], and go some way to meeting the requirement of 0.1 % baseline variability outlined by Fabrizi, Sparkes, Horesh, *et al.* [30] for imaging epilepsy in the adult head. The largest contributors to the baseline variability appear to arise from the introduction of the electrodes in the tank and human recordings, as well as other physiological sources of error.

The limited frequency range of the ST severely limits the amount of current which can be injected, due to the IEC 60601 regulations [166], which is one of the simpler ways of improving SNR. Due to the modular nature of the system, the BioSemi ActiveTwo voltage record side could easily be replaced by another EEG system with a higher sample rate. Preliminary testing within the UCL group has been successful with two such systems: the “g.tec g.HIamp” [171] and the “Brain Vision actiCHamp” [172], which offer much higher bandwidth (> 40 kHz). However, the noise with the ST even with the limited current injection outperforms the KHU on all tests with the exception of the long term drift in section 3.3.1. The reduced frequency range of the ST system may preclude its use in many applications in EIT, but it remains suitable for the major focuses within the UCL group of EIT of stroke [59], epilepsy [158] and TBI [173]. The KHU system is currently best suited for the time difference applications in the head as there are insufficient carrier frequencies within the 5 Hz to 5 kHz frequency range for stroke [59]. Further carrier frequencies could be added, but this is not trivial given the complexity of the system.

Possibly the most important benefit to the use of the Keithley 6221 is its consistency across current amplitude, frequency and load. The KHU did match the performance of the ST in certain situations, but it not as consistent. Wi, Sohal, McEwan, *et al.* [110] demonstrated how critical detail and frequent calibration was to maintain the SNR of the 16 channel system. Doubling the number of channels only increases the complexity further, increasing the reliance on proper calibration. It is possible that for a given application, with fixed amplitude, frequency, and transimpedance the KHU calibration procedure could be optimised and the SNR maximised. However, the majority of these parameters have not been optimised, for any brain EIT applications, thus the versatility of the ST is particularly useful in future research.

Measuring the voltages with an EEG amplifier, whilst having the disadvantage of increased processing time, offers other benefits. The noise and DC offset on each channel is visible in real-time, which is useful during electrode application on the scalp, before checking with the contact impedance measurement routine. Recording the raw voltages, as opposed to merely the demodulated amplitude allows for correlation with other signals such as EEG. This is already standard practice in the animal work within the group [79], [158], and may be beneficial in human scalp recordings, particularly in epilepsy.

3.4.4 Recommendations for future work

Both systems will require further modifications before any clinical data is collected, particularly for users who are not engineers familiar with the underlying electronics. Both systems would require updated user interfaces with robust input validation. Custom drivers have been written for the BioSemi ActiveTwo system [174] to process EEG data in real time. These could be adapted to form the basis of a real time demodulation software package to give simplified reconstructions in real time.

Chapter 4

Revaluation of the feasibility of imaging epileptic seizures with EIT

4.1 Introduction

Time difference imaging of epileptic activity in adult patients has previously been the focus of the UCL group with measurements taken on patients in an EEG telemetry ward [30]. No reproducible impedance changes were found during these recordings, which were attributed to low SNR and movement artefacts. Work was performed subsequently by the authors to solve the problems identified, but the conclusion was the SNR was still too low with the systems available at the time [58]. The improvements in the realistic head phantoms in chapter 2, and the increased SNR of the UCL ScouseTom (chapter 3), coupled with the improvements in imaging by Jehl, Dedner, Betcke, *et al.* [63] and Aristovich, Santos, Packham, *et al.* [61] present an opportune moment to reassess the feasibility of imaging epileptic foci with EIT. This chapter represents a revaluation of the problem of imaging epileptic seizures in the head through a combined tank and simulation study, using the latest hardware and imaging algorithms developed in the UCL group. Alongside a comparison to the previous work in the adult head, images were also reconstructed in the neonatal head, the morphology of which is conducive to impedance imaging and is relatively unexplored in the literature.

4.1.1 Previous tank experiments

Saline tank experiments are traditionally used in EIT to test new hardware or reconstruction algorithms as well as assess the feasibility of subsequent clinical measurements. As described in chapter 2, creating a realistic saline phantom of the head provides a particular challenge in and of its itself, and much of the testing in previous head tanks has focussed on testing the phantom themselves, often with non biological perturbations [64], [78], [127], [144].

The variations in tank geometry, background medium, perturbation size, location and conductivity, as well as system settings such as current amplitude, carrier frequency and number of averages, renders comparisons between studies problematic. Fabrizi, McEwan, Oh, *et al.* [58] performed the first direct test of the feasibility of imaging brain pathologies in an anatomically realistic head tank [53] which considered the localisation of a realistic perturbation in three dimensions. The centre of mass of a perturbation of 30 % contrast was reconstructed within 10 - 13.5 % of the tank width fig. 4.1a, with a total error (including shape deformation and artefacts) of ≈ 35.5 %. Subsequent work within the UCL group into multi-frequency EIT for potential stroke diagnosis also included time difference reconstructions for reference. Packham, Koo, Romsauerova, *et al.* [68] imaged a high contrast (≈ 90 %) potato perturbation without skull within 1-2 % of the same tank diameter, with a total error of 4.2 %, fig. 4.1b. Continuing on from this work Doru, Avery, Aristovich, *et al.* [77] repeated the experiment with the skull used by Tidswell, Gibson, Bayford, *et al.* [53] in place. The localisation error increased to 3.4 % and the total error was approximately 8-17 % across four perturbation positions, fig. 4.1c. Data were collected in all three of these studies using the UCH Mk.2.5 system and post processed to reject channels with high noise enabling images to be reconstructed using Truncated SVD.

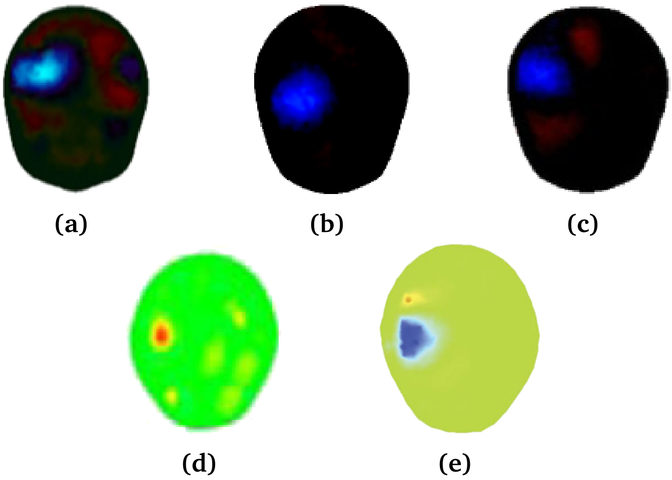

Figure 4.1: *Lateral perturbation reconstructions in anatomically realistic head tanks. True 3D reconstructions, **(a)** 30 % contrast Fabrizi, McEwan, Oh,* et al. *[58], **(b)** 90 % contrast without skull Packham, Koo, Romsauerova,* et al. *[68] and **(c)** 90 % contrast with skull. 2D reconstructions, **(d)** 176 % contrast Li, Tang, Dai,* et al. *[144] and **(e)** 2000 % contrast Dai, Li, Hu,* et al. *[16]*

Outside of the UCL group, the most directly comparable work was performed by Li, Tang, Dai, *et al.* [144], who created an anatomically realistic head tank described in section 2.1.2. In testing the tank, 2D reconstructions were produced with an agar rod perturbation of 176 % contrast fig. 4.1d. However, no objective analysis was given of the image quality, and the output from the weighted minimum norm method (WMNM) reconstructions are in "Arbitrary units", which makes a direct comparison to results from the UCL group difficult. Finally, using this same phantom and WMNM method, Dai, Wang, Xu, *et al.* [15] produced images of a substantially higher contrast perturbation of 2000 % change fig. 4.1e, designed to replicate the increased resistivity of irrigating 5 % dextrose solution used in treatment of subdural haematoma. These changes are 200 times greater than the less conservative estimates of the changes during seizures, and thus serve as an upper bound of potential image quality.

4.1.2 Neonatal Tank Studies

Neonatal applications of head EIT have been the subject of less focus within the literature despite being proposed early in the development of the technique [13]. A 2D finite element modelling study by Gibson, Bayford, and Holder [33] demonstrated the higher skull conductivity and presence of the fontanelle apertures increased the sensitivity to impedance changes inside the neonatal brain, and suggested that it represented the ideal first clinical test of EIT in the head. Subsequently reproducible images were reconstructed of evoked responses in neonates in a spherical [175] and head shaped mesh [176]. Recently there has been interest in imaging intraventricular haemorrhage in neonates by Tang and Sadleir [36] culminating in, to the author's knowledge, the first 3D EIT images of an anatomically shaped neonatal head tank, fig. 4.2. Anomalies were located within 17 % relative diameter, using only 16 electrodes arranged in a configuration similar to EEG 10-20 and the KHU Mk.1 system [45].

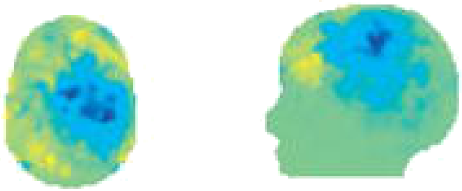

Figure 4.2: *Time difference image of 50 % contrast representing intraventricular haemorrhage in neonatal head tank without skull Tang and Sadleir [36]*

Whilst demonstrating the principle, this study does have important limitations, the most significant of which is that the skull was not included in the tank images. Previous work by the same authors have shown the importance of correctly modelling the skull and the fontanelles [142]. Therefore there is a requirement for a more stringent test of the feasibility of imaging physiological perturbations in the neonatal brain.

4.1.3 Purpose

The purpose of this study is to evaluate the feasibility of imaging epileptically induced impedance changes through EIT measurements on the human scalp. The work represents a revaluation of the feasibility in the adult head, based on the work by Fabrizi, McEwan, Oh, *et al.* [58], taking advantage of the advances in hardware, imaging and experimental methodology both within the UCL group and as part of this thesis. The study also comprises the first investigation into imaging epileptic foci in the neonatal head using modern EIT methods, with the last simulation study within the group performed in 2D simulation by Gibson, Bayford, and Holder [33]. To achieve this, images of biologically representative perturbations were reconstructed in both the adult and neonatal tanks constructed in chapter 2, subsequently quantified and compared to results in the literature. The second half of the chapter consists of a simulation study wherein the quality of reconstructed images across the entire volume of the head was considered. The error in localisation was calculated for > 1000 reconstructed perturbations placed inside both tanks to give an estimation of the potential resolution if used in clinical practice. Finally, the average signal size *i.e.* the change in boundary voltage resulting from the perturbations, was calculated to form the basis of an estimation of the minimum noise level which must be achieved for successful clinical images.

4.1.4 Experimental Design

Experiments were performed using both the adult and neonatal tanks designed and built in chapter 2, with the skulls present in all cases. Time difference images of sponge perturbations designed to replicate the ≈ 10 % impedance changed expected during a seizure [53] were reconstructed in three positions in the adult tank and five positions in the neonatal tank. Data were collected using the UCL ScouseTom system with higher current and carrier frequency than that used in section 2.2.7. The results of the tank study in chapter 3 showed that the error in simulated perturbations was greater than the contribution of the hardware errors, so an additional regularisation algorithm was used to potentially improve the reconstructed images. Along with the first order Tikhonov regularisation described in section 3.2.4, cross-validated zeroth order Tikhonov with noise-based scaling developed by Aristovich, Santos, Packham, *et al.* [61] within the UCL group, was also implemented. The assumptions implicit within zeroth order are weaker than those of first order, and as such do not bias the result towards smaller contiguous conductivity changes, rather to the smallest global conductivity change. Agreement between the images with both of these regularisation schemes would suggest a high data quality and a robustness of the technique.

One of the limitations of a tank study is that it is prohibitively time consuming to test perturbations in every location inside the tank, instead several representative positions must be chosen. This is sufficient to demonstrate the feasibility of an EIT application, or to investigate the influence of instrumentation noise and other non-idealities. However it is not possible to draw strong conclusions regarding the spatial distribution of the accuracy of reconstructions, or the required instrumentation sensitivity from such a small sample. Therefore a simulation study was also performed wherein perturbations were placed in a dense grid throughout the head, and the resulting localisation error and voltage change calculated for each one, with and without realistic noise. From these results it was possible to draw conclusions regarding the accuracy of reconstructions throughout the head, as well as the hardware sensitivity necessary to measure changes on a sufficient number of channels to successfully reconstruct these impedance changes.

4.2 Methods

4.2.1 Tank Study

Tank

Both the adult and neonatal head tanks created in chapter 2 were used in this study. The methodology used first in section 2.2 and expended upon in section 3.2.4 was once again employed in these experiments with 0.2 % saline and skull present in all cases.

Perturbations

The three perturbation locations, *Posterior*, *Lateral* and *Central* described in section 3.2.4, as proposed by Malone, Jehl, Arridge, *et al.* [59], were again used during the adult tank recordings. Two locations were added in the neonatal study, as spatial variations arising from the neonatal skull are less understood in the literature. To investigate the effects of the frontal or metopic suture between the two frontal bones, a perturbation was added in the *Anterior* position. The *Central* perturbation was shifted upwards by 20 mm towards the corona capitis, and a new *Caudal* position was added in the centre of the head level with the temporal fontanelles. This new perturbation is located at a point the furthest possible distance away from the electrodes, and thus represents the "worst case" scenario for reconstructing images.

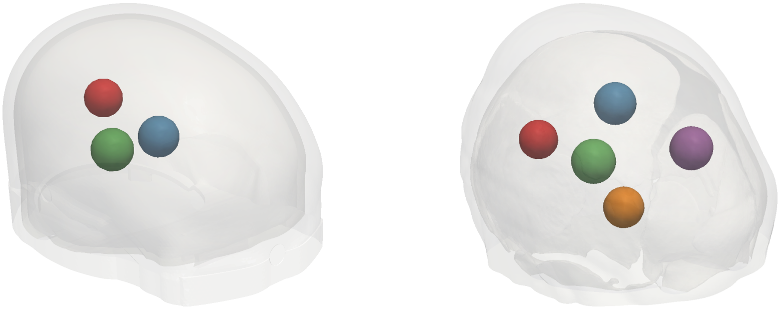

(a) *Adult Tank* **(b)** *Neonatal Tank*

Figure 4.3: *Perturbation locations used in tank study,* ***(a)*** *adult tank based on positions from Malone, Jehl, Arridge,* et al. *[59] and* ***(b)*** *neonatal tank with two additional locations*

The perturbations used in this study were spheres of polyurethane sponge (5 % density), chosen to match those used by Tidswell, Gibson, Bayford, *et al.* [74] to provide an impedance change of ≈ 12 %, similar to those found during epileptic seizures by Rao, Gibson, and Holder [28] and Elazar, Kado, and Adey [84].

For the adult tank the perturbations were 25 mm in diameter, whereas for the neonatal experiments the volume of the perturbation was scaled based on the relative volume of the skull cavity, giving a perturbation of 19 mm diameter. The air was removed from within the sponge through repeated compression in saline, and was kept submerged in saline between recordings. A baseline was recorded between each perturbation.

EIT System Settings

The ScouseTom system, described in section 3.1.1, was used for all recordings as it was found to have the best performance in the tank study in chapter 3. The “optimal” and “offset” injection protocols described in section 2.2.7 were used in this study for the adult and neonatal tanks respectively. The current injection was increased to 250 μA which, due to IEC 60601 regulations, necessitated an increase of carrier frequency to 1.76 kHz. The injection time of 75 ms was maintained, resulting in a scan time of $\approx$ 2 s for both the “optimal” and “offset” protocols. The protocol was repeated 20 times for each background and perturbation recording, the same number used by Fabrizi, McEwan, Oh, *et al.* [58].

Image Reconstruction

Images were generated using two separate reconstruction methods in this study. First the implementation of first order Tikhonov regularisation by Markus Jehl [63], described in section 3.2.4 was used. Secondly a zeroth order Tikhonov regularisation noise-based correction developed by Aristovich, Santos, Packham, *et al.* [61] was used to reconstruct images. Unlike first order Tikhonov regularisation, zeroth order does not bias the solution towards finding small connected perturbations, and thus does not include prior information regarding the expected changes. Zeroth-order Tikhonov minimises the L2 norm magnitude of the conductivity changes:

$$\hat{\delta\boldsymbol{\sigma}} = \mathrm{argmin}_{\delta\sigma} \, ||\delta\mathbf{v} - \mathbf{J}\delta\boldsymbol{\sigma}||^2 + \lambda||\delta\boldsymbol{\sigma}||^2 \tag{4.1}$$

where $\hat{\delta\sigma}$ is the estimated conductivity change, $\delta\mathbf{v}$ is the boundary voltage change and λ is a hyper-parameter set using cross validation.

The optimal value for λ was the one which minimised the cross validated error, and was found using leave-one-out cross validation using a range of 3000 logarithmically spaced λs between $\times 10^{-20}$ and $\times 10^{-2}$ [61]. Once the optimal λ was found, the Jacobian matrix was inverted using:

$$\mathbf{J}_\lambda^{-1} = \left(\mathbf{J}^T\mathbf{J} + \lambda\mathbf{I}\right)^{-1}\mathbf{J}^T \tag{4.2}$$

These images were post processed using a noise based correction approach developed by Aristovich, Santos, Packham, *et al.* [61]. The standard deviation of the conductivity change in each hexahedron in the inverted Jacobian $\mathbf{J}_\lambda^{-1}$ was calculated for random Gaussian Noise in the voltage measurements:

$$\delta \boldsymbol{\sigma}_n = \mathbf{J}_\lambda^{-1} \delta \boldsymbol{v}_n \tag{4.3}$$

where $\delta \boldsymbol{v}_n$ is normal distribution of mean 0 and standard deviation equal to that of the noise in the measured voltages. $\delta \boldsymbol{\sigma}_n$ is the conductivity change matrix of size m (number of elements) by k (number of samples) caused by the noise in the voltage change $\delta \boldsymbol{v}_n$ on the electrodes. For the actual conductivity change in each element a t-score can be computed:

$$t_i = \frac{\delta \sigma^i}{\langle \delta \sigma_n^i - \delta \bar{\sigma}_n^i \rangle} \tag{4.4}$$

The values in the reconstructions with this algorithm therefore represent the noise based-scaled values, which are unitless and do not reflect the absolute conductivity in S/m.

The ≈ 4 million element “fine” meshes, described in section 2.2.5 were used to compute the forward solution and generate the Jacobian matrices using PEITS [63]. For both the adult and neonatal head meshes, the Jacobian matrix $\mathbf{J}_\sigma$ computed on the fine mesh was summed into geometrically regular cubes $\mathbf{J}_{hex}$, as was performed in section 2.2.5.

Separate hexahedral meshes were generated for use with zeroth and first order Tikhonov. One of the benefits of the simpler regularisation of zeroth-order Tikhonov is that it does not require the use of the memory-intensive gSVD (section 3.2.4), which limits the number of elements in the hexahedral mesh. Thus the number of elements in the meshes used for zeroth order reconstructions are significantly greater than the corresponding meshed for first order. For the adult head, the 2526 10 mm element mesh created in section 3.2.4, and a 76996 3 mm element mesh were used for first order and zeroth order reconstructions respectively. For the neonatal head a 4012 6 mm element mesh was used for the first order reconstructions, and a 83839 mesh of 1.5 mm elements was used in the zeroth order reconstructions.

The hyper-parameter λ was found using cross validation as previously described for zero order Tikhonov. A constant $\lambda = 4.6 \cdot 10^{-4}$ as described in section 3.2.4 was used for the first-order reconstructions in the adult head tank. As with the adult tank, the L-curve was not pronounced enough to find the value automatically for each neonatal tank reconstruction. Thus the lambda was again fixed, at a value of $\lambda = 2.5 \cdot 10^{-4}$, giving similar solution norm $||\mathbf{x}||_2$ and residual norm $||\mathbf{Jx}-\mathbf{v}||_2$ similar to those in the adult tank of around 0.1 and $1.0 \cdot 10^{-4}$ respectively.

Image Quantification

Images were quantified using the same algorithms written in section 3.2.4. The *reconstructed perturbation* was first identified before the *Localisation Error*, *Shape Error* and *Image Noise* metrics were calculated with respect to the “ideal” reconstructed perturbations. Additionally, the localisation error was expressed as the norm of the displacement of the centre of mass in mm, to give a more intuitive understanding of the error.

Boundary Voltage Preprocessing

As this study does not have many commonalities with previous tank experiments within the group, with different geometry, hardware, mesh, forward and inversion, it was unclear the extent to which the conclusions previously drawn regarding boundary voltage preprocessing were relevant. Therefore the processing was kept to a minimum. Occasionally during measurements, a change in the DC offset across all channels would occur, which would corrupt all measurements for a single injection. These were removed from the calculation of the average boundary voltage by removing measurements six times above the median for that channel. This was largely unused throughout the experiments, being invoked a total of three times across 16 measurements.

4.2.2 Simulation Study

Localisation Accuracy

Simulated perturbations of 10 % conductivity change of radius r were placed inside the skull cavity of both meshes in an overlapping grid of points p_{ijk} spaced $r/2$ distance apart in x and y dimensions. The elements in the "fine" tetrahedral mesh with a centre less than r from each point p_{ijk} each were set to 0.04 S/m. These conductivity changes were then projected onto the hexahedral mesh by averaging the conductivity changes of the corresponding tetrahedra, to give $\delta\sigma_{hex}$. Any perturbations with less than 90 % scalp tetrahedra were removed for the analysis to prevent artefacts arising from perturbations inside the skull or on the edge of the mesh. The radius r was 14 mm and 9.5 mm , which resulted in 1139 and 2433 perturbations for the adult and neonatal heads respectively.

The corresponding voltage changes δv were calculated by multiplying the conductivity changes $\delta\sigma_{hex}$ by the Jacobian $\mathbf{J}_{hex}$. Images were then reconstructed for each perturbation using both zeroth and first order Tikhonov as described in section 4.2.1. Further, each reconstruction was performed without noise to show the maximum achievable resolution, and the effects of measurement errors. Noise was added to δv corresponding to 5 μV additive based on the results from section 3.3.3 on the scalp and 1 % multiplicative errors based on the percentage error in the tank from section 3.3.2, averaged over 10 recordings.

Finally, the image quantification described in section 4.2.1 was applied for all reconstructed perturbations, yielding an error score for every perturbation point p_{ijk}. The results were projected back onto the original hexahedral mesh by summing the scores across all points p_{ijk} inside each hexahedron. The result is a map of the spatial variation of the image quality across for each of the eight permutations of mesh, regularisation and noise.

Signal size

The boundary voltage changes simulated in section 4.2.2 are used as the basis of an analysis of the size of expected changes in the head. Only the voltages generated using the higher resolution Jacobian $\mathbf{J}_{hex}$ used for the zeroth order reconstructions were considered as the smaller hexahedra provide a more accurate representation of the shape of the perturbation. Using the same technique described in section 4.2.2 for the image error, the spatial distribution of the median voltage change in μV was projected onto the hexahedral mesh. The median was chosen as opposed to the mean as successful image reconstruction requires at least ≈ 50 % measured channels [68], [77].

To provide an estimate of the measurement sensitivity required, voltage changes for each perturbation were then thresholded for a range of minimum voltages v_{min} in increments of 0.5 μV, to provide a percentage of measurable channels, *i.e.* the number of channels with a voltage change above a given v_{min}, for each perturbation p_{ijk}. As the percentage of usable channels varied significantly with perturbation location, the results are given as a median with 5th, 25th, 75th and 95th percentiles to show the distribution across all positions. From this data, it is possible to estimate a minimum SNR required to ensure a given percentage of channels have a measurable signal for 95 % of perturbations.

4.3 Results

4.3.1 Adult Head Tank

The reconstructed perturbations with both regularisations are shown in comparison to the "ideal" perturbation, first as all hexahedra above half max in fig. 4.4, and then as a slices through the complete image in figs. 4.5 to 4.7.

In all cases the reconstructed centre of mass was close to that of the target position, but the conductivity changes were spread over a much wider region of the skull. Qualitatively, the reconstructions using zeroth order Tikhonov were less successful in all positions, than those with first order. The full width half maximum perturbations in fig. 4.4 are larger with zeroth order and in the posterior and central locations, the perturbation has been drawn vertically towards the top and bottom of the mesh. This is demonstrated clearly in the slices through the complete image, *e.g.* fig. 4.5, which show the negative (correct direction) conductivity changes have been spread across the majority of the Sagittal and Coronal cross sections, whilst having a clearer foci in the axial plane. Whereas the reconstructions with first order Tikhonov show a more regional conductivity change. Artefactual positive conductivity changes were present in all images, particularly for the central perturbation, located primarily in the anterior and posterior regions closest to the skull. The greatest artefacts inside the skull were found with zeroth order.

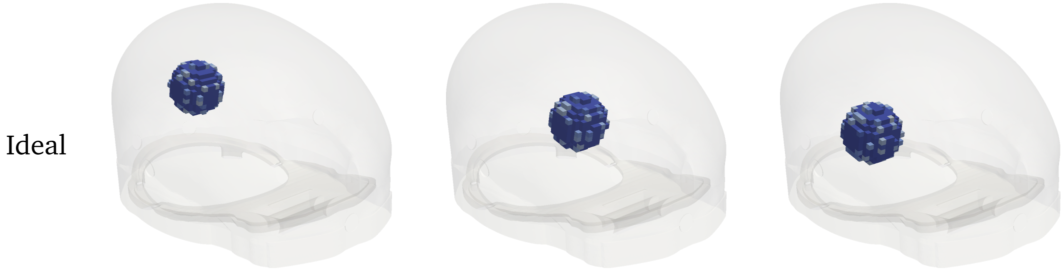

(a) *Posterior* **(b)** *Central* **(c)** *Lateral*

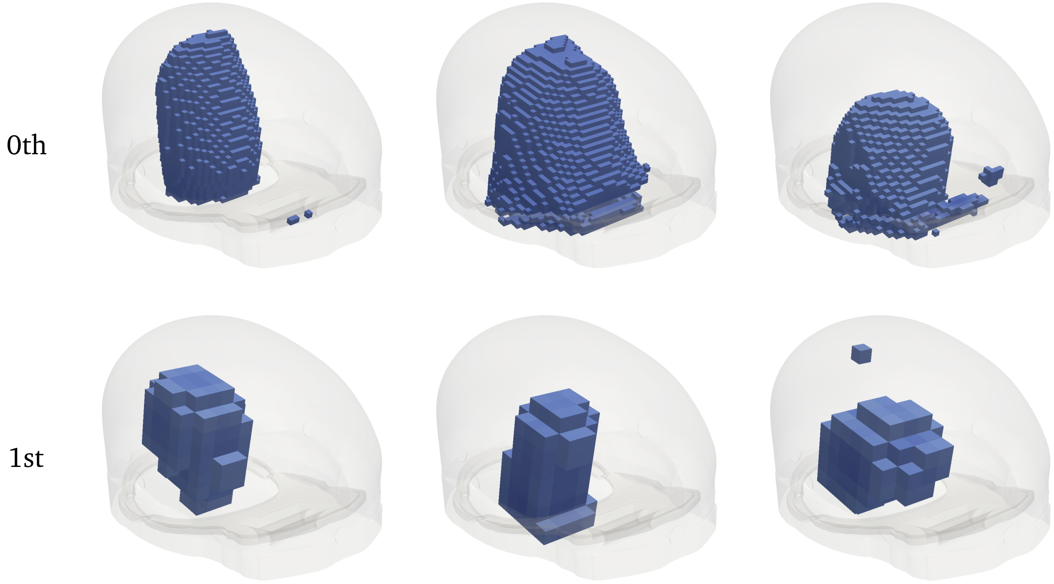

Figure 4.4: *Perturbations in adult tank, reconstructed with both zeroth and first order Tikhonov, in comparison to ideal reconstructions*

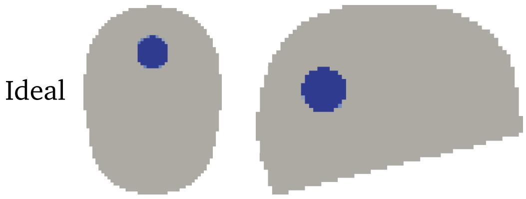

(a) *Axial* **(b)** *Sagittal* **(c)** *Coronal*

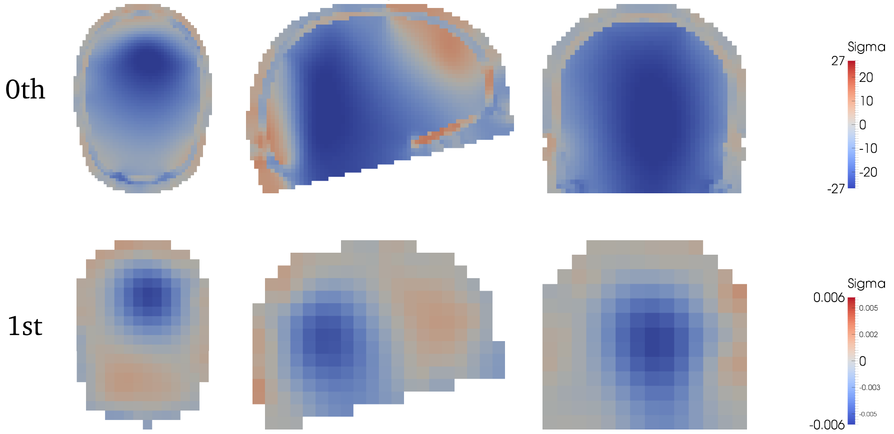

Figure 4.5: *Section views of image of experimental reconstructions with* **posterior** *perturbation with both zeroth and first order Tikhonov regularisation*

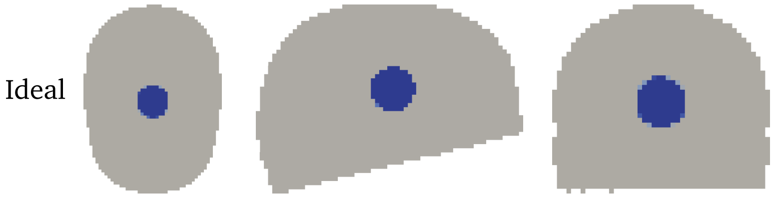

(a) *Axial* **(b)** *Sagittal* **(c)** *Coronal*

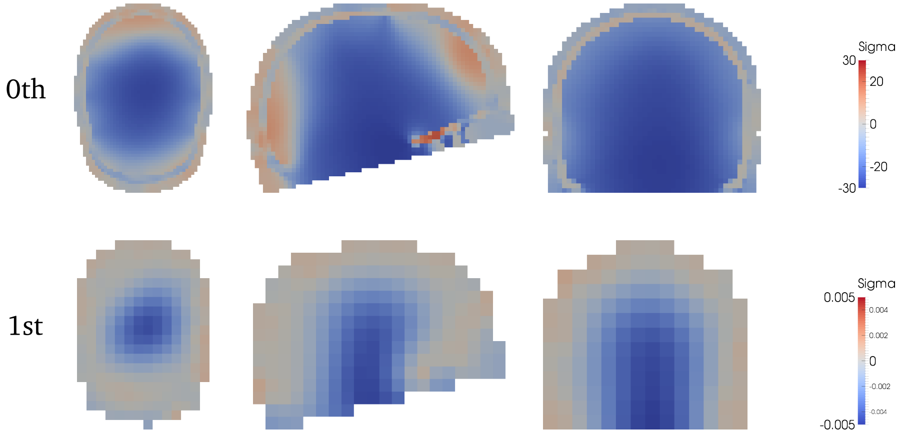

Figure 4.6: *Section views of image of experimental reconstructions with* **central** *perturbation with both zeroth and first order Tikhonov regularisation*

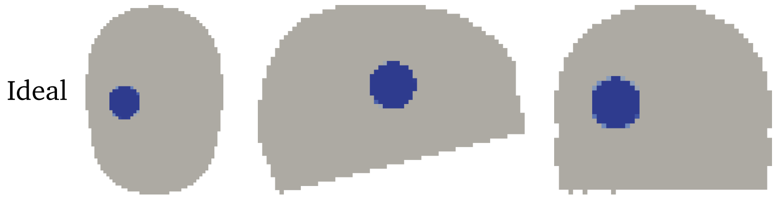

(a) *Axial* **(b)** *Sagittal* **(c)** *Coronal*

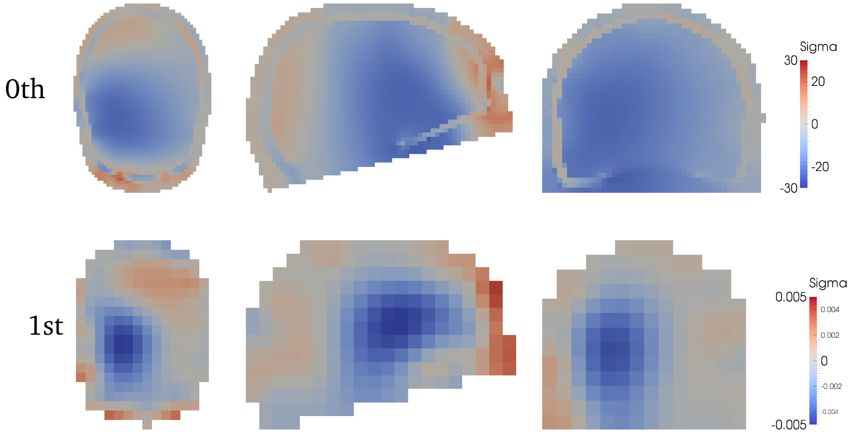

Figure 4.7: *Section views of image of experimental reconstructions with* ***lateral*** *perturbation with both zeroth and first order Tikhonov regularisation*

Image Quantification

The lowest error was achieved using first order Tikhonov, for all positions and error metrics (fig. 4.8), with a global mean of 7.55 % compared to 12.8 % with zeroth order. The largest differences between regularisations is found in the shape and localisation errors. The localisation errors with zeroth order range from 3.1 to 5.9 %, whilst the first order results are more consistent: 1.76 to 2.1 %. The lowest error was obtained in the central location for both regularisations, although this was the position with the largest localisation error with first order.

4.3.2 Neonatal Head Tank

The perturbations were reconstructed successfully in all five locations including the “worst case” Caudal position. Qualitatively, the perturbations were correctly located yet broader compared to the target position fig. 4.9. The deformation of the perturbation shape is less pronounced than that seen in the adult head tank fig. 4.4. Overall, the performance of the two regularisations schemes is similar across all perturbations. However there were a greater occurrence of artefactual positive conductivity changes with zeroth order, particularly in the anterior and posterior locations, figs. 4.10 and 4.11.

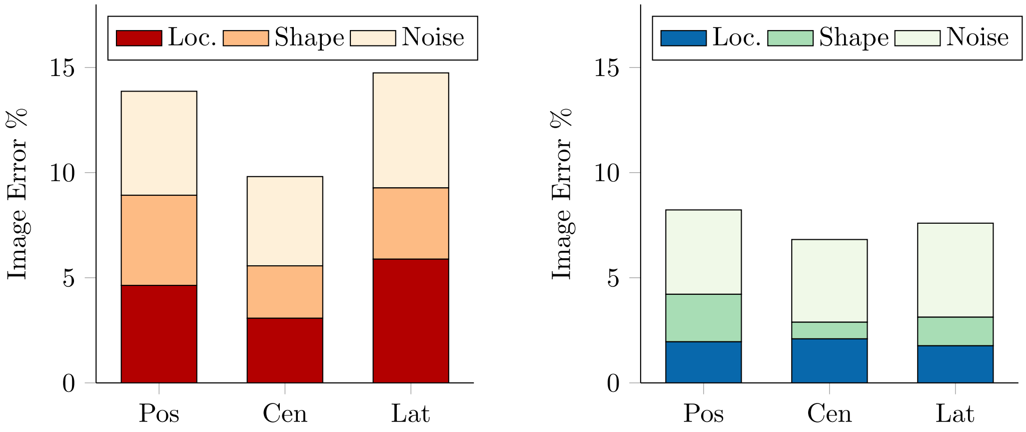

(a) *0th order* **(b)** *1st order*

Figure 4.8: *Image quantification results in adult tank,* ***(a)*** *zeroth order and* ***(b)*** *first order Tikhonov regularisation*

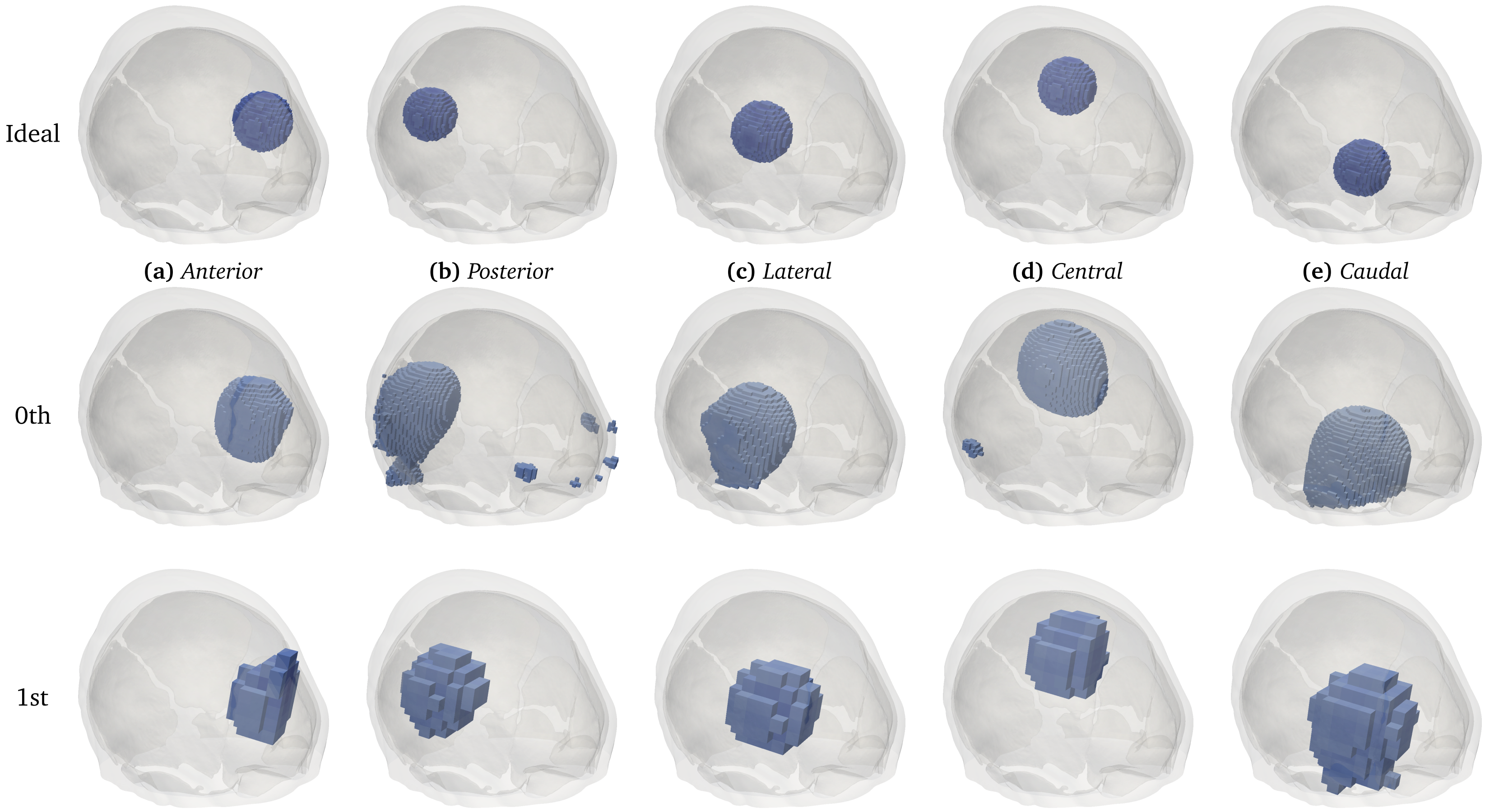

(a) *Anterior* **(b)** *Posterior* **(c)** *Lateral* **(d)** *Central* **(e)** *Caudal*

Figure 4.9: *Perturbations in neontal tank, reconstructed with both zeroth and first order Tikhonov, in comparison to ideal reconstructions*

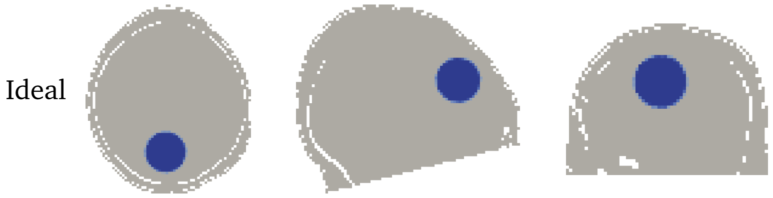

(a) *Axial* **(b)** *Sagittal* **(c)** *Coronal*

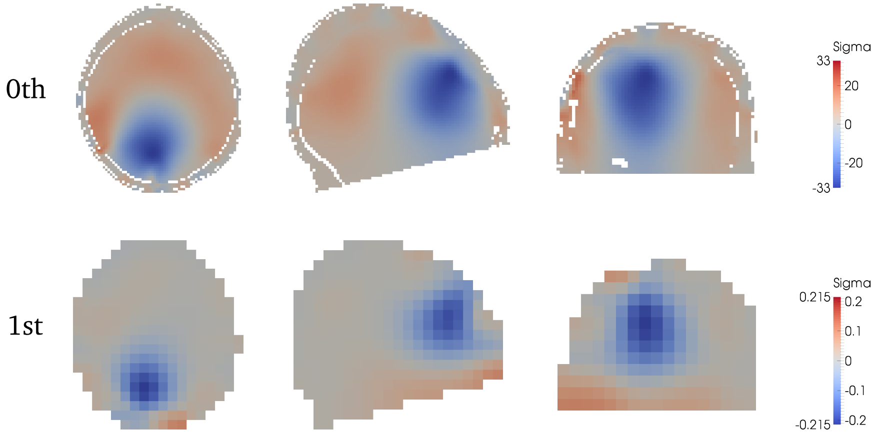

Figure 4.10: *Section views of image of experimental reconstructions with* ***anterior*** *perturbation with both zeroth and first order Tikhonov regularisation*

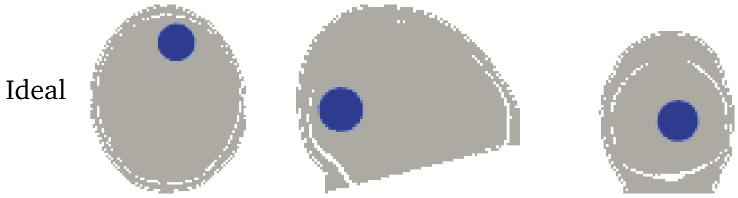

(a) *Axial* **(b)** *Sagittal* **(c)** *Coronal*

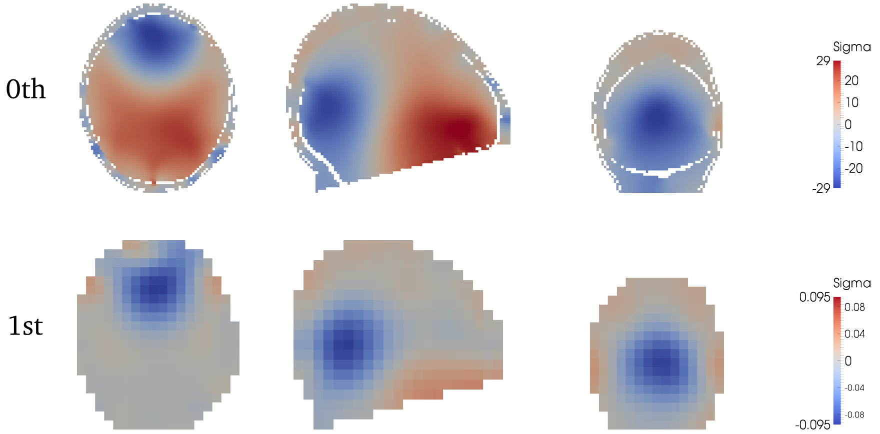

Figure 4.11: *Section views of image of experimental reconstructions with* ***posterior*** *perturbation with both zeroth and first order Tikhonov regularisation*

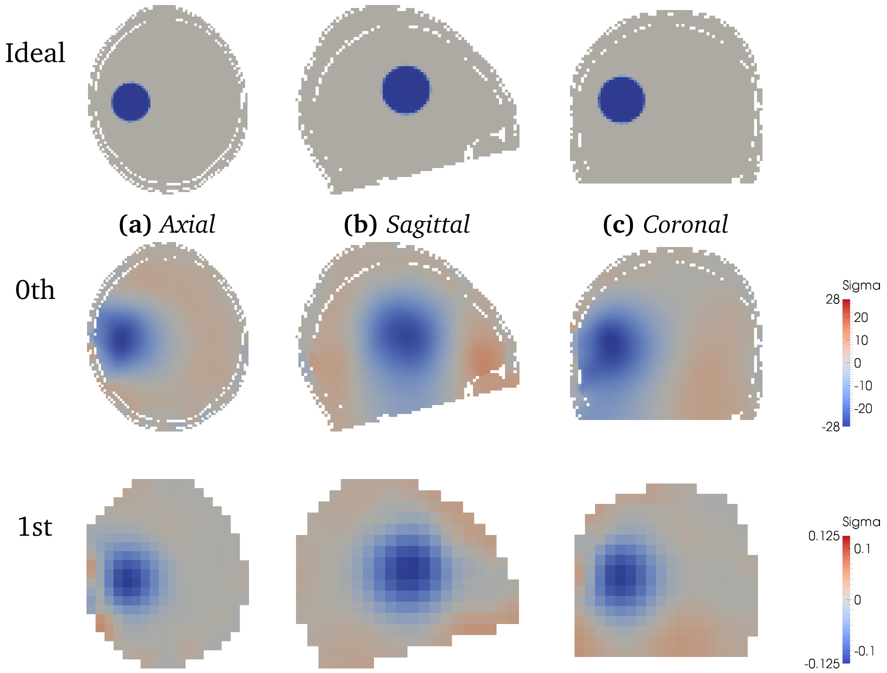

Figure 4.12: *Section views of image of experimental reconstructions with* ***lateral*** *perturbation with both zeroth and first order Tikhonov regularisation*

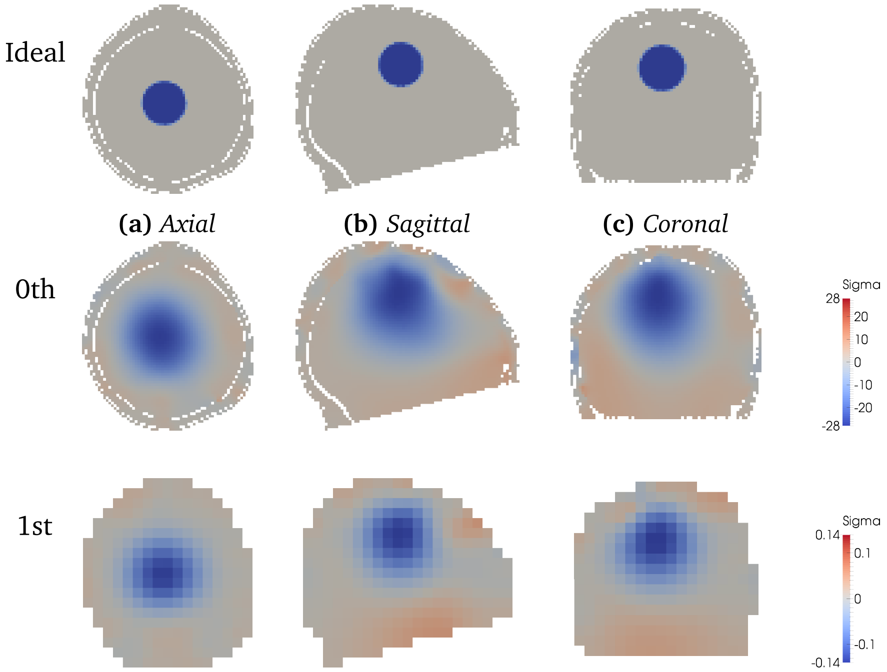

Figure 4.13: *Section views of image of experimental reconstructions with* ***central*** *perturbation with both zeroth and first order Tikhonov regularisation*

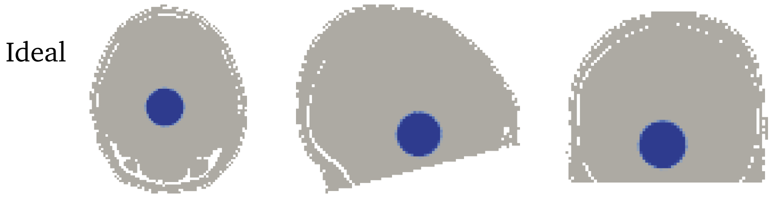

(a) *Axial* **(b)** *Sagittal* **(c)** *Coronal*

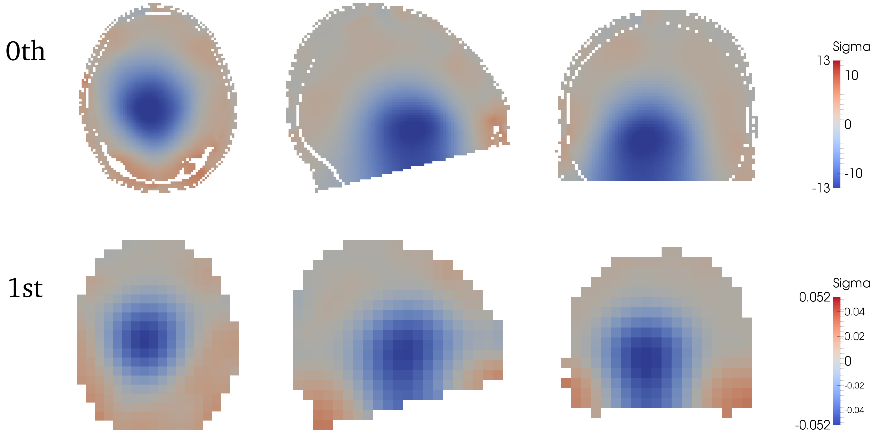

Figure 4.14: *Section views of image of experimental reconstructions with* ***caudal*** *perturbation with both zeroth and first order Tikhonov regularisation*

Image Quantification

The image error, fig. 4.15, with both regularisation methods was generally 8 % or lower across the neonatal head with the exception of the posterior location. The artefacts in these positions were considerably larger than other locations, giving rise to significantly larger noise errors of 8 % and 6% for zeroth and first order respectively, compared to ≈3 % elsewhere. The shape error with first order was 2 % greater than any other position. The performance of the two regularisations was similar, with a total mean error of 8.54 and 8.72 % for zeroth and first order respectively. The localisation error was less than 2.5 % across all perturbations and regularisations. Zeroth order reconstructions had ≈ 0.3 % greater localisation error than the first order for the anterior, posterior and lateral positions but 1 % less in the central and caudal positions. Generally, the localisation error was greater towards the surface of the skull, with the central position having the least error.

4.3.3 Localisation Accuracy

The mean localisation accuracy in the adult tank was 18.1 and 12.9 mm or 11.7 and 8.4 % with zeroth and first order respectively. Without noise added, the accuracy with first order regularisation was significantly greater than zeroth order ($p < 0.05$). The range of errors was also relatively larger using zeroth order, with a standard deviation of 8.5 mm compared to 5.0

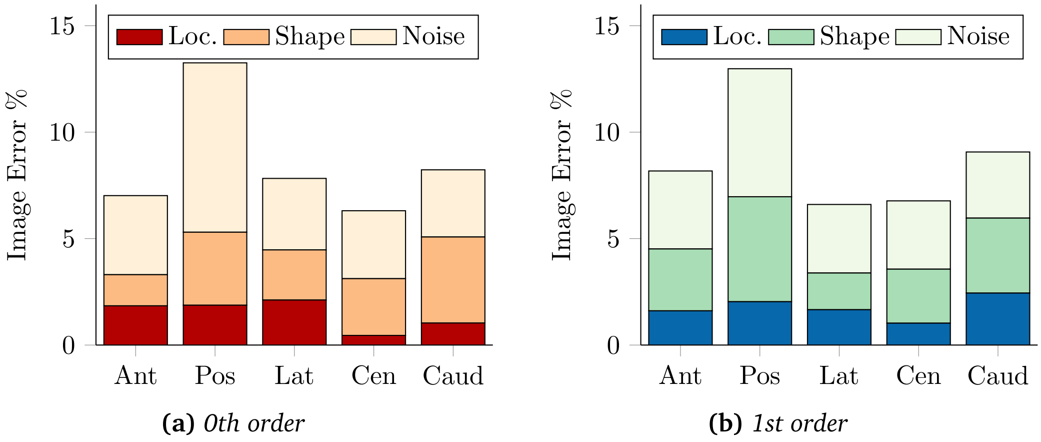

(a) *0th order*

(b) *1st order*

Figure 4.15: *Image quantification results in neonatal tank,* ***(a)*** *zeroth order and* ***(b)*** *first order Tikhonov regularisation*

mm for first order. For both regularisations, the addition of noise significantly increased the localisation error ($p < 0.05$), to 23.1 mm or 15.0 % for zeroth order and 18.0 mm or 11.72 % with first order.

The location error in the neonatal head was approximately half that of the adult head, with both mean errors less than 5% without noise. Unlike the adult head, the two regularisation algorithms had a similar performance in the neonatal head, with less than 2 % difference. Also contrary to the results in the adult, zeroth order Tikhonov gave the greater accuracy: 3.3 mm or 2.96 % compared to 5.5 mm or 4.95 % with first order. As was found in the adult head, the addition of the noise significantly increases the localisation error ($p < 0.05$), to a mean of 4.87 mm or 4.35 % with zeroth order, and 7.4 mm or 6.6 % with first order.

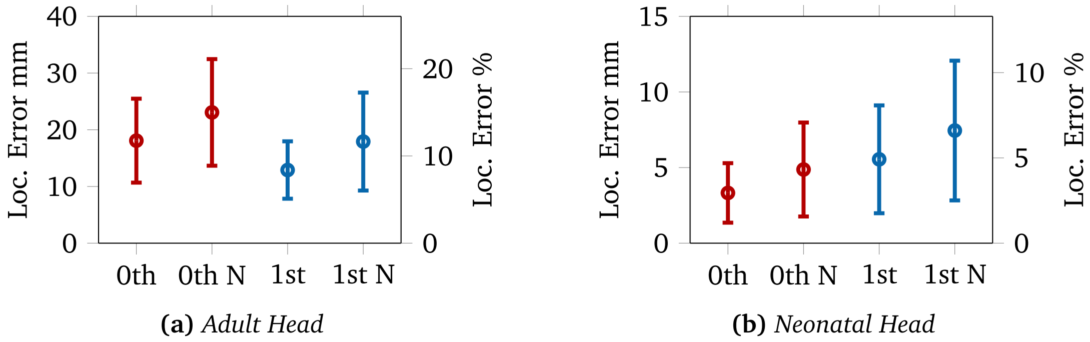

(a) *Adult Head*

(b) *Neonatal Head*

Figure 4.16: *Localisation error (mean±std) of the simulated perturbations in* ***(a)*** *adult and* ***(b)*** *neonatal head, with and without noise present, for both regularisations, expressed as norm of vector distance in mm, and as a percentage of mesh dimensions*

The greatest localisation errors with zeroth order regularisation were found towards the edges of the adult tank, particularly in the posterior and coronal regions, where the location error is ≈ 40 mm. The localisation error is lowest in the centre of the head, approximately 10 mm, which correlates with the experimental results in section 4.3.1. The localisation error is more evenly distributed in the simulations with first order Tikhonov, with an accuracy close to 10 mm across the entirety of the adult head. However there is still a significantly higher region of 20-30 mm error in the coronal region of the head closest to the skull. The addition of realistic noise results results in a greater error across the head, with the the largest increases found in the posterior region of the head. The spatial distribution of the error with zeroth order is largely unchanged with the addition of noise, whereas with first order, small region of higher error are now found towards the centre of the skull.

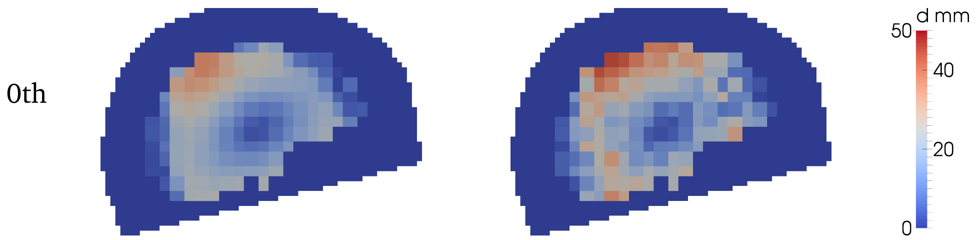

(a) *Clean* **(b)** *Noise*

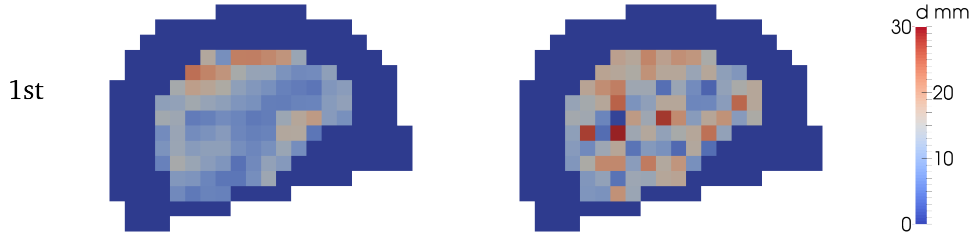

Figure 4.17: *Spatial distribution of localisation error in mm in adult head for both zeroth and first order Tikhonov regularisations, for simulated perturbations with and without realistic noise added*

The spatial distribution of the localisation error is more complicated in the neonatal head compared to the adult head, figs. 4.17 and 4.18. Broadly, the localisation error is lower, approximately 5mm, in the upper half of the head above the axial plane compared to the lower region of the skull where the error is approximately 10 mm. There is less variation with depth than was observed in the adult head. The error at the most caudal areas at the base of the mesh, level with the temporal fontanelles is lower than the error in the immediate surroundings. The addition of realistic noise has a similar effect to that observed in the adult skull in that the error is larger and more evenly distributed across the head. Further, for perturbations close to the inion fig. 4.17, the artefacts present in zeroth order reconstructions, *e.g.* fig. 4.11, were large enough to be incorrectly identified as the perturbation in the image. Thus in this location the localisation error is close to 100 % of the mesh diameter.

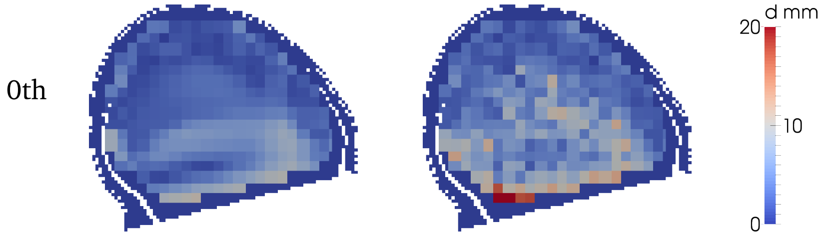

(a) *Clean* **(b)** *Noise*

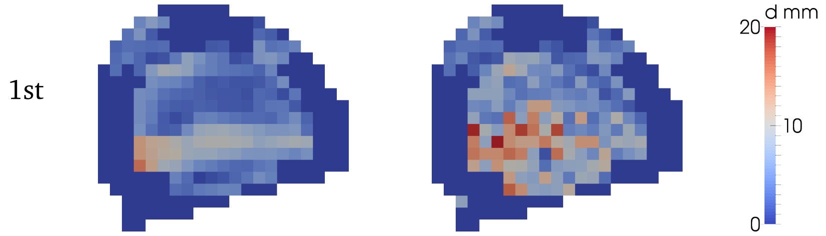

Figure 4.18: *Spatial distribution of localisation error in mm in neonatal head for both zeroth and first order Tikhonov regularisations, for simulated perturbations with and without realistic noise added*

4.3.4 Signal Size

Adult Head

The spatial distribution of the median voltage change in the adult head in shown in fig. 4.19. The largest changes, approximately 6 μV are found in the anterior of the head, close to the ground electrode. The median change decreases as the perturbations move towards the posterior of the skull, to a minimum value of approximately 0.5 μ V.

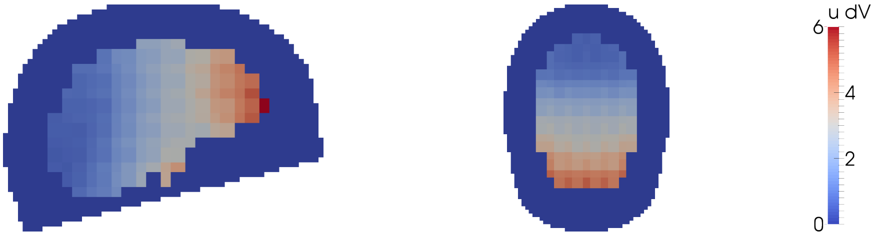

(a) *Side* **(b)** *Top*

Figure 4.19: *Median voltage change μV for 10 % contrast perturbations across the adult head,* ***(a)*** *sagittal section and* ***(b)*** *axial section*

The potential number of measurable voltages for a given minimum signal is shown in fig. 4.20. The minimum voltage which yields 50 % potential combinations in 50 % of the perturbations is 1.85 μV, however this decreases to 0.5 μV to ensure 50 % potential combinations in 95 % of the perturbations.

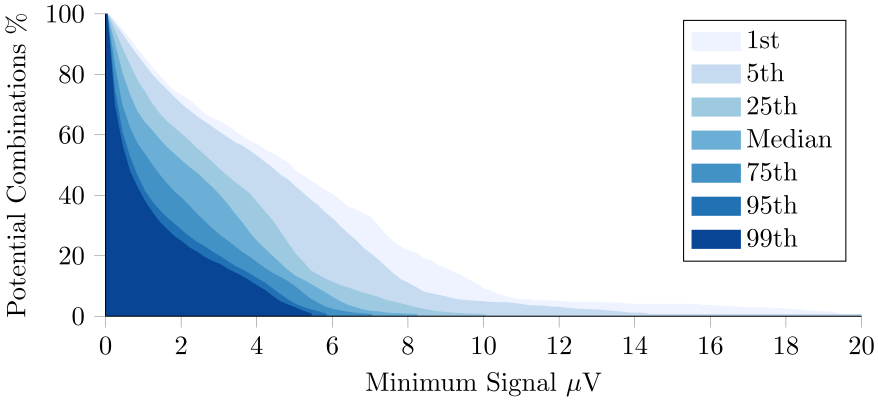

Figure 4.20: *Percentage of measurable voltages for a given minimum signal size in μV across all perturbations p_{ijk} in adult head, expressed as percentiles of the perturbation distribution*

Neonatal Head

The spatial distribution of the median voltage change in the neonatal head in shown in fig. 4.21. As was found in the adult skull, the largest changes, approximately 8-9 μV occur in the anterior of the head, close to the ground electrode. The median change decreases as the perturbations move towards the posterior of the skull, to a minimum value of approximately 0.5 μ V.

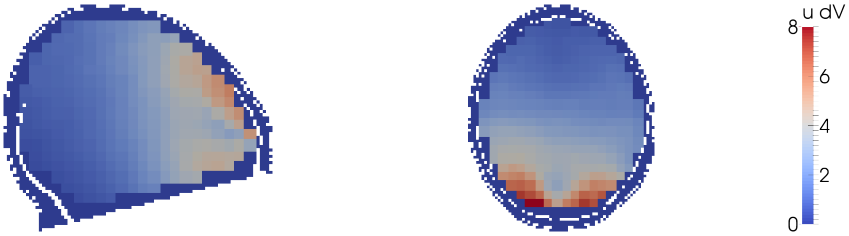

(a) *Side* **(b)** *Top*

Figure 4.21: *Median voltage change μV for 10 % contrast perturbations across the neonatal head,* ***(a)*** *sagittal section and* ***(b)*** *axial section*

The potential number of measurable voltages for a given minimum signal is shown in fig. 4.22. Similar to the adult tank, the minimum voltage which yields 50 % potential combinations in 50 % of the perturbations is approximately 2 μV, however this decreases to 0.68 μV to ensure 50 % potential combinations in 95 % of the perturbations.

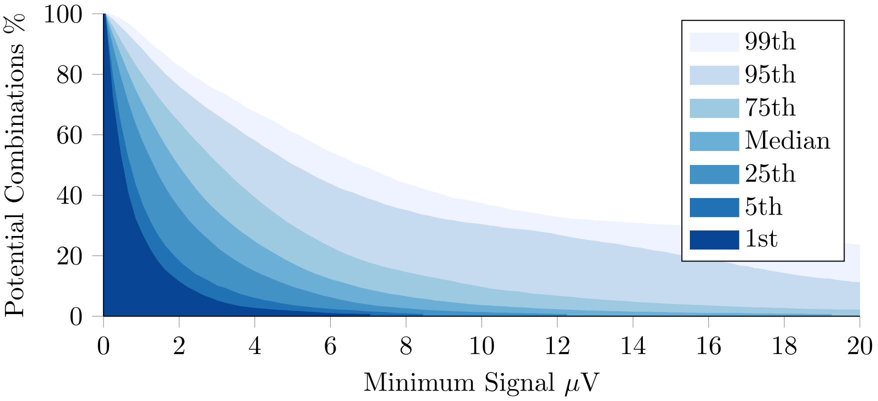

Figure 4.22: *Percentage of measurable voltages for a given minimum signal size in μV across all perturbations p_{ijk} in neonatal head, expressed as percentiles of the perturbation distribution*

4.4 Discussion

4.4.1 Summary of results

In this study, localised impedance changes of approximately 10 % were reconstructed reliably in both an adult and neonatal phantom, using both zeroth and first order regularisation schemes. In the adult tank the global image error was 7.55 and 12.8 % for zeroth and first order respectively. For both regularisations, the localisation of the centre of mass of the perturbation was approximately 5 % or less of the mesh diameter, which equates to approximately 8 mm or less. The reconstructed images in the neonatal head tank were qualitatively better with conductivity changes appearing more localised. The image error in the neonatal tank on average was 8.5 % for all five positions and reconstructions, the centre of mass of the perturbations was reconstructed with 2.5 % or less error, corresponding to 3 mm or less.

The simulation results indicate that 10 % contrast perturbations, such as those arising from focal epilepsy, could be imaged inside the adult head with a mean accuracy of less than 12 % using first order Tikhonov regularisation, 250 μA current and the "optimal" protocol. The estimated accuracy in the neonatal head was double that of the adult head with a mean localisation error less than 6 % or 5 mm for both regularisation schemes.

The changes in the standing voltages from these 10 % perturbations were found to range from 0.5 - 6 μV on average in the adult head and 0.5 to 8 μV in the neonatal head. A noise level of 2 μV was shown to provide a measurable change on 50 % of the combinations within each injection protocol for 50 % of the perturbations.

4.4.2 Tank study

The results in this study compare favourably to the previous images reconstructed in a head shaped phantom with skull in section 4.1.1 by Fabrizi, McEwan, Oh, *et al.* [58], with less than half the localisation error. These images were produced without the post-processing necessary in other studies, including PCA and boundary voltage rejection [58], [79], which is likely due to the increased accuracy of the tank and forward model described in section 2.3.2 and lower noise in the measurements with the ScouseTom system. The three perturbation locations used in the adult tank correspond to the areas with the lowest median signal change as calculated in the simulation study section 4.3.4, and thus do not represent the optimal locations for imaging. Qualitatively, the reconstructions with first order Tikhonov *e.g.* fig. 4.5, are not dissimilar to those obtained in section 3.3.2 with a high contrast plastic perturbation, with the exception of increased artefacts inside the skull cavity.

To the author's knowledge, these images represent the first reconstructions of a biologically realistic perturbation in a geometrically realistic neonatal head tank with skull. The reconstructions show localised impedance changes across the neonatal head, including the caudal position at the furthest point from the electrodes fig. 4.14. The reconstructed images were both a qualitative and quantitative improvement over the images in the adult head, with clearer localised impedance changes and half the image error. The likely reason for this improvement is the increased sensitivity in the brain due to the increase in skull conductivity and the presence of the fontanelles reducing the shunting of current around the skull. These images suggest that there is a strong cases for clinical success in imaging within the neonatal patients compared to the adult head.

4.4.3 Simulation study

The simulation study shows a clear spatial dependence in the localisation accuracy of perturbations across the head, particularly with zeroth order regularisation. The localisation error was greater towards the centre of the skull in the adult tank, which is in agreement with the results from Fabrizi, McEwan, Oh, *et al.* [58]. The broadness of the perturbation using zeroth order regularisation, figs. 4.4 and 4.5, draws the centre of mass towards the centre of the tank, despite the correctly located maxima. The bias towards the centre of the tank is the likely cause for the counter-intuitive increase in localisation accuracy for perturbations in this region, where the sensitivity is lowest.

The benefits conferred onto the localisation error by the fontanelles is further evinced in the results of the simulation results fig. 4.18. The error is significantly lower in the upper region of the skull where current is injected between electrodes located close to the anterior and posterior fontanelles. The sphenoid and mastoid fontanelles also improve the localisation in the deeper structures, compared to perturbations in the axial plane above the temporal bone. This dependence upon the fontanelles may prove a challenge in clinical experiments as discrepancies between the actual morphology and the forward model could give rise to greater modelling errors compared to those experienced with the solid skull in the adult skull.

The addition of noise had the greatest influence upon the localisation accuracy in the adult head and in the posterior of the neonatal head, which correlates with the median signal size in figs. 4.19 and 4.21. The less conductive skull in the adult head reduces the signal size by ≈ 2 μV, which consequently reduces the SNR in comparison to the neonatal head with equivalent noise. The change in voltages are substantially greater in the anterior region of the brain

The additive noise added to the simulated voltages was based on scalp recordings from section 3.3.3 which correlates with the sensitivity map of the optimal protocol with the fig. 3.35. This uneven sensitivity and, consequently, signal size, could potentially be alleviated through repositioning of the ground electrode and recalculation of the "optimal" protocol using a 'seed" electrode placed on the posterior of the head. The noise added to the simulations was equivalent to 1.54 μV, when averaged over 20 recordings. The minimum signal size in figs. 4.20 and 4.22, suggests that a median number of perturbations had 55 % of combinations with an SNR above 1, and 99 % of the perturbations had at least 30 % measurable channels. The majority of the perturbations were still localised within 30 mm and 10 mm in the adult and neonatal heads respectively, even without rejection of these noisy channels. Improvements to SNR through improved hardware or higher current, given the sharp increase in the number of percentage channels at 1 μV should bring the localisation error closer to the ideal simulated case.

4.4.4 Assessment of regularisation algorithms

Generally, the images reconstructed with zeroth and first order Tikhonov regularisation are in good agreement throughout the experiments. The clearest differences are found in the adult head reconstructions, where the zeroth order reconstructions are substantially blurred across the whole of the head, which belies the accuracy of the focal point of the change. In the neonatal head the results are objectively similar with the exception of increased artefact in zeroth order reconstructions. The size of the hexahedra in the zeroth and first order meshes was chosen to maintain the same ratio between adult and neonatal head, this resulted in a zeroth order neonatal mesh with five times the number of elements than the adult tank. The benefits of a higher number of hexahedra for zeroth order is made clear when comparing the images in the adult and neonatal tank. Therefore it is likely that the images could be improved in the adult head with a finer element mesh.

This highlights the main benefit of first order regularisation over zeroth order in this case, its consistency and stability over positions, perturbations and meshes. The result is sufficiently stable across λ not to require careful, data specific selection. Despite the L-curve [72] not being sufficiently pronounced to chose the hyper-parameter λ automatically, a single fixed value was sufficient for all reconstructions. This is in contrast to zeroth order, which requires careful selection of λ through cross validation, within which there is a further variable of the number of sub-samples (folds) k of the data chosen, post processing with noise based scaling and as the results show, is more dependent upon the mesh quality.

Caution must be taken when drawing conclusions from these results, as the assumption of a small connected perturbation is known to be valid *a priori* in these experiments, which may not be the case during clinical measurements. As the zeroth order reconstructions generally produce a single connected perturbation without being biased towards such a solution, a combined approach could be used in practice. If the zeroth order reconstructions indicate localised impedance changes inside the head, as they do in the result in this study, then first order regularisation could be subsequently employed to improve the resultant image.

4.4.5 Study limitations

Whilst this study represents an encouraging demonstration of the improvements in methodology within the UCL group, there are a number of limitations which prevent strong conclusions being drawn from the results. The most important element missing from this feasibility study is realistic physiological noise and measurement drift observed during scalp recordings, as described in section 1.4.2. Images were still successfully reconstructed in the simulation study with additive noise of 5μV on every channel based on scalp recordings taken with the ScouseTom system, which in most cases is an overestimation compared to the results in section 3.3.3. However, the multiplicative noise, in the absence of a scalp recording comparison, was based upon the percentage errors measured in the tank. Unexplained measurement drift of up to 20 % was the primary source of error found by Fabrizi, Sparkes, Horesh, *et al.* [30] during measurements on a telemetry ward, and until either the method is shown to be robust to those errors, or that these drifts have been minimised, it is not possible to make any claims regarding feasibility.

The SNR was sufficient to successfully image perturbations throughout both the adult and neonatal head. However the estimates were based upon averaging over 10 frames, or approximately 20 seconds. This is more than sufficient for imaging slow changes such as those arising from intra-cranial bleeding, which have a time course ranging from minutes to hours [177]. Currently, the time course of the impedance changes resulting from an epileptic activity is still unclear, and much of the early work showed impedance changes lasting the order of 10 s of seconds [84], [178]. Although, results results within the group have shown changes in impedance lasting less than a second after interictal spikes [92], time enough for only a single frame. Therefore, with the SNR of the current set up, it is unlikely that this activity would be reliably imaged.

As mentioned in chapter 2, the 32 electrodes used in the neonatal scalp is likely an overestimation of the amount feasible in practice, particularly in proof of principle studies using existing EEG montages. Additionally, the neonatal skull used in this study represents a somewhat idealised model from the perspective of successful imaging. The conductivity of the fontanelles is set to the same value as the brain tissue in this study, whereas in reality is likely closer to the full skull conductivity [140]. Further the fontanelles present in the model used those of a new born infant, and thus represent that largest possible aperture for current flow. As the fontanelles close, the benefits to the signal size seen in the simulation study will decrease.

4.4.6 Recommendations for future work

As the number of electrodes used in the neonatal study may not be representative of the amount feasible in initial clinical measurements, it is important to repeat the experiment with fewer electrodes in the positions commonly used in neonatal EEG, and find the optimal injection pattern for that set up. In doing so it would be possible to reduce the number of injections and thus decrease the time for each frame. Concurrent to the investigation into the minimum number of injections, experiments should be carried out to determine the sensitivity of the image reconstruction to the fontanelle size and conductivity. Construction of a model with closed fontanelles would be relatively simple with the existing CT segmentation, as would assigning a separate conductivity to the region.

The simulated voltages were generated through multiplication of the hexahedral Jacobian $\mathbf{J}_{hex}$ for simplicity which constitutes an “inverse crime” [170]. At the time of writing, running the forward solver for the ≈ 8000 different perturbations would have been prohibitively time consuming, but recent refinements to the PEITS solver [63], means this is now feasible. Any future feasibility studies should calculate the voltages in this manner for more accurate voltages. Much of the edge artefact which resulted in mislocation of the centre of mass with first order Tikhonov was found in the hexahedra at the very edge of the mesh. Optimisation of the hexahedral mesh to remove hexahedra on the edges of the mesh which correspond to a small number of tetrahedra in the fine mesh could thus improve image localisation.

For brevity, only the localisation error was considered in the simulation study as the correct centre of mass was deemed important for imaging epileptic foci or TBI. However, the SNR of the majority of the measurements would be less than 1, which are not likely to result in satisfactory images without data rejection. It is likely that the shape error of many of these reconstructions would be much larger than those measured in the tank in this study. Therefore consideration of the global error, and each error individually would be necessary for a complete feasibility study.

If, as described in chapter 3, the BioSemi EEG system were to be replaced with another system with a higher sampling rate, the SNR could be readily increased through the use of a higher carrier frequency. The maximum allowable current is proportional to the carrier frequency as per IEC 60101 [166], doubling the frequency would allow for twice as much current to be injected, with corresponding benefits to SNR. A higher carrier would also allow for faster switching times, and thus a higher frame rate, which could allow for imaging the faster impedance changes recorded by Vongerichten [92].

Chapter 5

Reducing skin impedance through abrasion: preliminary characterisation of the effects of rotation and force

5.1 Introduction

To enable imaging of acute stroke with Electrical Impedance Tomography an electrode-bearing helmet was proposed in chapter 1, which comprises multiple individually advancing and abrading electrodes. This chapter considers the design of a single self abrading electrode unit, built for assessment in-vitro, without the spatial limitations that would apply to a head-mounted device. This prototype was used to demonstrate the principle in a controlled test environment before testing in a more representative situation with a human test subject.

The literature regarding minimising contact impedance through abrasion, whilst clearly demonstrating the benefits is often vague as to the extent of the abrasion required. In most clinical studies, the contact impedance is measured after electrode application, and the abrasion process is repeated until a satisfactory impedance is reached [78] [7]. Some studies have aimed at quantifying abrasion, however the results are often specific to the technique or device used, or in the case of human controlled abrasion are not transferable to other investigators. For example, a study by Tam and Webster [179] quantified the reduction of motion artefact with increasing sandpaper abrasion strokes. However, they did not quantify either the force applied during an abrasive stroke or the thickness of the skin removed per stroke. A study using a dental burr to abrade a circular area of skin showed repeatable results with the same operator, but without quantification of the torque output of the burr, nor the number of rotations or force applied it is not possible to repeat these results [180]. One proposed system punctured the skin to a repeatable depth of 0.5 mm, and 4 punctures were found to significantly reduced motion artefact [181]. However the focus of this study was not the quantification of the contact impedance, and the damage to the Stratum Corneum from puncture is not readily transferred to an equivalent thickness of a layer removed. Microdermabrasion is a technique designed to remove the Stratum Corneum for cosmetic-dermatologic conditions. Studies have shown that it is possible to remove the Stratum Corneum without damage to the underlying tissues using a commercial microdermabrasion device [182]. However the problem still remains of transferring the results of this study to the acute stroke application, as the mechanical specifications and quantification of the devices are not described.

There are limitations on the design of the helmet in terms of the size and weight of the components, particularly as multiple units are required. It is important therefore that the electrode unit design be optimised to meet the mechanical requirements with a minimal size and weight. As these mechanical requirements are not described clearly in the literature, investigation was required. To achieve this, the prototype was designed to be flexible in terms of the force, torque and number of rotations applied to the surface. This enabled experiments to be performed to describe the effect of variations in force and torque on abrasion. These results will inform the design of the subsequent miniature prototype.

5.1.1 Purpose

The main purpose of the work described in this chapter was to construct a prototype self-advancing and abrading electrode, and to characterise its performance. The goal was that the electrode should meet the specifications set out in chapter 1 (1.5), by reaching an acceptable contact impedance (<5 kΩ) within 10 seconds. To achieve this, a test rig was constructed using orange skin as a test object. The target impedance was modified to 6 kΩ based on the differences between human and orange skin (section 5.2.7).

The specific questions to be answered were:

1. Does the prototype meet the specifications?
2. What are the optimum settings for:
    (a) The applied force
    (b) The speed of rotation
    (c) The total angle rotated
3. What control strategy is needed? Open or closed loop, if closed which variables?
4. Is the finished design ready for use testing on human subjects? Or are there changes necessary?

5.1.2 Experimental Design

Design, validation and characterisation of prototype

Initially, a prototype self abrading electrode and test rig were constructed. The accuracy of the measurements of force, impedance and torque were evaluated using known test objects before subsequent charactisation of abrasion.. Details are given in section 5.2.7. Based on the goals set out in section 5.1.1, the criteria for determining the success of the prototype were as follows: reduce contact impedance at 20 Hz to <5 kΩ in 10 seconds or less.

Characterisation of Manual Abrasion

A comparison study with the current “gold standard” abrasion technique, wherein abrasive paste in rubbed on the surface with an applicator. Contact impedance was measured before and after abrasion, and the force exerted was recorded throughout. The experimental set up is described in section 5.2.8.

Contact impedance as a function of applied force

The impedance decrease as a result of increasing pressure on the test object was measured. The measurement set-up is described in detail in section 5.2.8. The results from this experiment were used to determine the range of forces in the subsequent studies.

Impedance during abrasion over a range of applied forces

The impedance was recorded during abrasion of the test object for a range of applied forces. In each case the impedance was expressed as a function of the angle rotated by the electrode. The experiment is described in detail in section 5.2.8.

Impedance during abrasion for minimum and maximum applied torque

Abrasion was performed as with the previous experiment with the exception that the torque output of the rotation was reduced to the minimum possible value. This minimum value was determined experimentally as described in section 5.2.7.

Proof of principle on human skin

Abrasion was performed on human skin for a single applied force. The experiment was repeated with and without the application of abrasive electrode paste.

5.2 Methods

A prototype single electrode device was designed and constructed with two independently controlled degrees of freedom: rotation, with open-loop control of torque; and linear position with closed-loop control of force. Linear refers to the direction normal to the skin surface, and rotation always refers to rotation about this axis. For the purposes of the initial testing and experiments, a human skin analogue made from orange skin was used. The test rig and prototype have numerous elements, each of which were individually validated before experiments were performed.

5.2.1 Test object: skin analogue

The test object in these experiments had to represent both the mechanical and electrical properties of human skin, which ruled out the use of traditional tissue phantom materials like agar gel. In previous work from the UCL group [78], fruit or vegetable skin was used to represent the impedance characteristics of human skin. These biological tissues are histologically and cytologically similar to human skin in that they have a highly resistive outer layer, analogous to the Stratum Corneum. Therefore abrasion of these tissues should reduce the contact impedance in a similar manner as human skin. However, the disadvantage of these tissues, is the variability between samples, both in terms of mechanical properties and impedance characteristics. It is important therefore to understand this variability before conclusions can be drawn from the results from the experiments. The biological object used in these experiments was orange skin, and an experiment to measure the variability of the test object was set up as shown in 5.1.

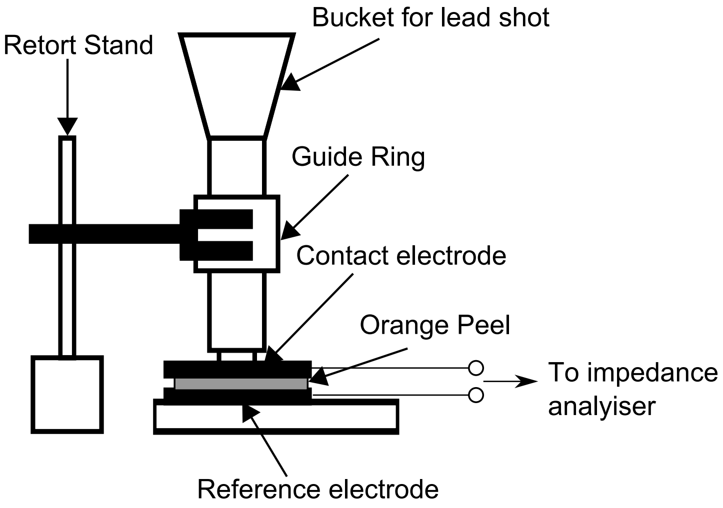

Figure 5.1: *Diagram of experimental set up to determine expected load impedances*

A 30x30 mm square of orange skin was clamped between two 30x25 mm silver electrodes and placed on a non-conductive surface. 400g weight of lead shot was applied in order to achieve contact, but with the aim to avoid excessive compression of the orange peel. The impedance between the two electrodes was recorded on the Hewlett Packard 4284A Impedance Analyser at frequencies from 20 to 10 kHz. The experiment was then repeated with a section of orange skin for which the outer layer had been removed. This was achieved by abrasion with sandpaper in a backwards and forwards motion repeated ten times per sample. Each recording was repeated with three different samples of orange skin, and the results given in figure 5.2 and table 5.1.

	Impedance kΩ + Standard Error			
Frequency	20 Hz	100 Hz	1 kHz	10 kHz
Non-abraded	20.9 ± 9.62	17.1 ± 7.11	10.9 ± 2.68	5.08 ± 0.77
Abraded	1.12 ± 0.10	0.98 ± 0.10	0.86 ± 0.09	0.65 ± 0.06

Table 5.1: *Orange Peel Impedances*

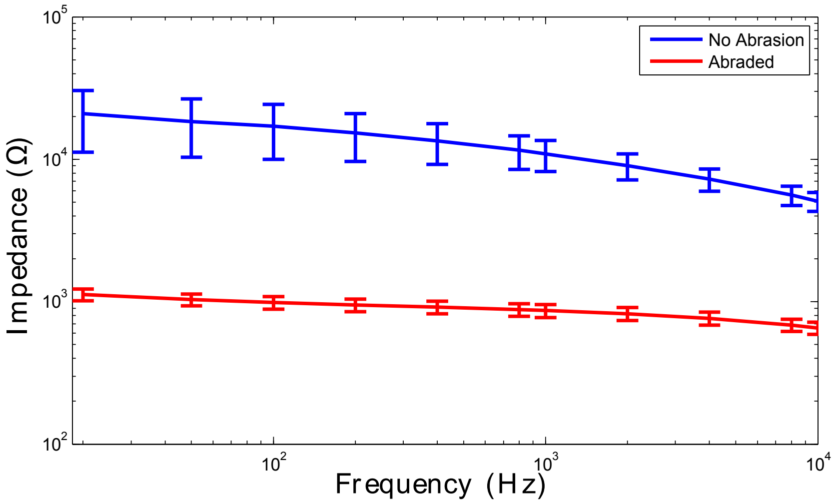

Figure 5.2: *Impedance of orange peel sections before and after abrasion*

The results show a much larger variation in the impedance values for unabraded orange skin, with standard errors at low frequencies approximately 50 % of the mean value. The shape of the impedance spectra is more consistent between samples, which all demonstrate a reduction in impedance at higher frequencies before abrasion. After abrasion the impedance is much more consistent across frequency, with variation between samples approximately 10 % of the mean. This variation is similar to that measured on the scalp with EEG electrodes section 1.4, and is thus an acceptable variation for test objects in these experiments.

Sample preparation

Each of the test object samples used in the experiments were cut to a size of 30x30 mm using a template. As an effort to minimise variation in thickness and skin toughness the samples where taken from the equatorial section of the orange skin. The time from dissection to testing was also limited to 20 minutes, to reduce loss of moisture from the orange skin.

5.2.2 Overview of prototype and test rig

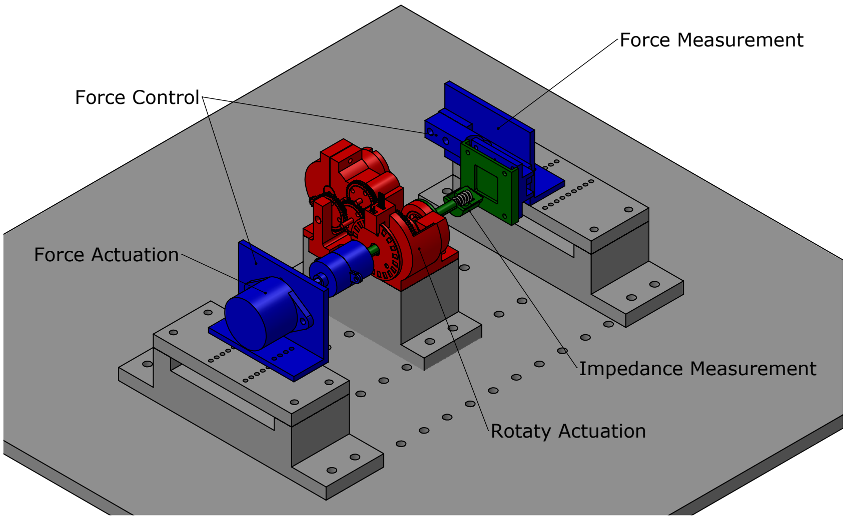

Figure 5.3: *Overview of test rig, highlighting force control, rotary actuation and impedance measurement components*

The electrode was connected to a spindle aligned normal to the test object surface. The linear actuator was positioned behind the spindle and the force applied was measured by a load cell positioned behind the test object. Feedback control was implemented to maintain the force applied during abrasion. The spindle was also independently rotated by a Direct Current (DC) motor, and this rotation was measured by a rotary encoder. The rotation was controlled using an open-loop controller. The impedance was measured throughout between the actuated electrode, and a reference electrode behind the test object.

The actuators and sensors were each mounted on a steel baseplate via aluminium mounting blocks. These were designed to house the components as rigidly as possible, whilst maximising the flexibility with regards to potential configurations. As each component was designed to be independent a more detailed description of each component can be given separately in turn.

5.2.3 Force control

The force applied by the electrode onto the test object during abrasion was controlled via a 4-phase unipolar linear actuator and attached spring. The force was measured by a load cell

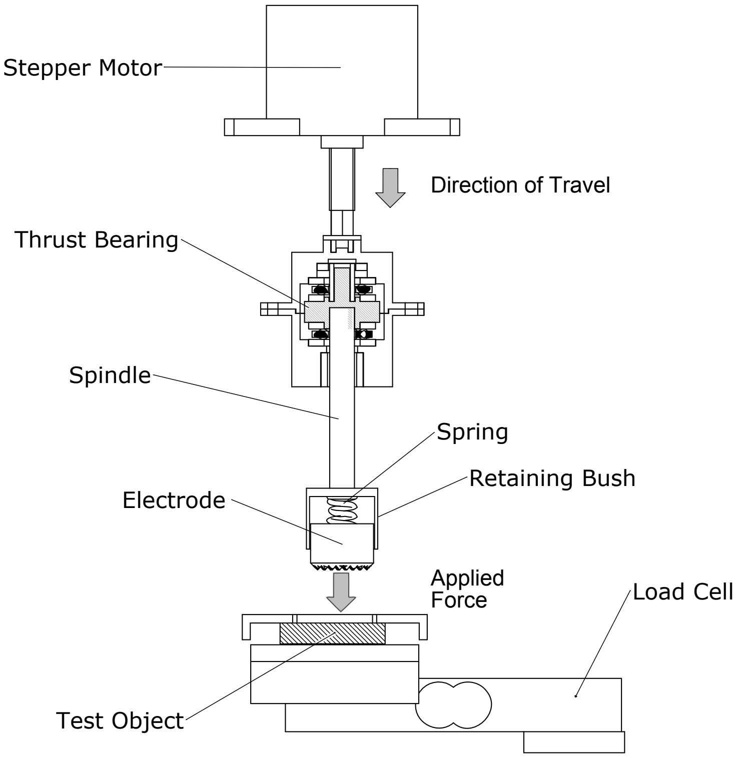

Figure 5.4: *Schematic of force control components in prototype*

placed behind the object under test, and the signal amplified by a custom made instrumentation amplifier circuit. A schematic of these components is shown in figure 5.4.

Stepper Motor

A linear stepper motor consists of a typical angular rotation stepper motor with a leadscrew nut inserted into the rotor, which converts its angular rotation to linear translation of the leadscrew spindle. The stepper motor used had a rated travel (*i.e.* the displacement of the spindle) of 10 mm with a linear step resolution of 0.033 mm. A stepper controller PCB was used and controlled via Labview, through which the speed and direction of travel could be controlled. The step type could also be switched from full-step to half-step, which doubles the step resolution at the cost of a decrease in the output torque.

Load Cell

A bending beam type load cell, rated up to five kg force with four strain gauges in full Wheatstone bridge arrangement was extracted from a domestic kitchen weighing scales: Salter 1029 WHDR. The electronics had to be discarded due to interference from the clock signal, and inbuilt calibration based on the scale's housing. Therefore a custom amplifier had to be designed and calibrated. The amplifier used was an Analogue Devices AD620 instrumentation amplifier, which requires a resistor to set the gain value which was chosen experimentally to maximise the dynamic range of the output. A maximum force of 10 N was chosen as an initial estimate, based on what was a comfortable pressure acting on a typical one cm disc eeg electrode. The resistor value was 24.7 Ω, corresponding to a gain of 2001, was chosen so that a 10N force resulted in an output voltage close to the maximum 5 V.

Calibration and repeatability error Calibration of the load cell was achieved through mounting the sensor on a rigid base, and applying 10 N weights in 1 N increments. This sequence was repeated 5 times in order to quantify the errors to ascertain if the sensor is sufficiently accurate for the needs of the test rig. A summary of the maximum error across load range is given in table 5.2.

Error	% of range
Linearity	0.2
Repeatability	0.11
Hysteresis	0.035
Peak to Peak noise	0.28

Table 5.2: *Load Cell Errors*

The sensor demonstrates good repeatability across the load range, with a maximum error of 0.11 % which corresponds to ±0.01 N. The implications for the test rig are that the force measurement, and thus the force control, have a theoretical limit of 0.01 N precision. The peak to peak noise was calculated based on data sampled at 100 Hz, thus the results may be an underestimate. The high gain of the amplifier coupled with a high sampling rate may further increase the peak to peak noise as mains hum and other noise sources are included in the signal. When a higher sampling rate was necessitated by the acquisition hardware, the sensor values were averaged to reduce this noise.

Mounting The load cell mounting (figure 5.4) was chosen to maximise deflection and thus the sensitivity of the sensor. The load cell is positioned so that the electrode exerts a force at the end furthest from the spacer.

Stepper motor as force actuator

Stepper motors are most often used as displacement actuators, in position control systems. However, for the electrode unit prototype the control variable is force, not position, so some adaptation is necessary. As long as the friction and inertia are not sufficient to prevent the motor stepping, the spindle will advance a fixed amount, compressing the target. Therefore, the force applied per “step” is dependent upon the compliance of the target object. This is only acceptable if an accurate model of this target compliance is known, or the force applied can be measured with a very high precision [183]. Another issue is the discrete nature of the stepper output means that only certain force levels can be achieved. Which, for a system with low compliance, could result in a very limited range of possible forces, thus making force control impossible.

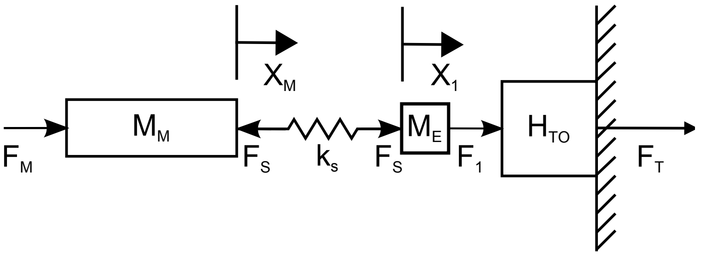

Figure 5.5: *Free body diagram of force control system, with generic test object*

It is clear, therefore, that the output from the motor must be converted so that a force is applied to the target, rather than a displacement. The simplest method is to place a compliant object i.e. a spring, between the motor spindle and the target as shown in figure 5.5. This converts the displacement from the spring's equilibrium position into a force via Hookes law $f = -kx$. The spring constant k_s in the prototype was chosen so to maximise the number of steps within the force range of interest. So for a rated travel of 10 mm and a maximum force of 20 N, the desired spring constant was 2000 N/m.

Force Measurement and Test Object

The controlled variable in this control-loop is the force directly applied onto the test object by the electrode. However, the experimental set up does not have an "in-line" load cell, *i.e.* one placed at the end of the motor spindle, which directly measures the force exerted onto the object (F_1 in fig. 5.5). Instead, the test rig load cell is mounted in an "external" configuration, which measures the force *after* the target object (F_T in fig. 5.5). The test object is left as a generic transfer function H_{to}, which is subject to change depending upon the model or object used. The electrode M_e is assumed to be a rigid body, which exerts a force F_1 upon the test object. The force measured by the load cell is F_t

This configuration is now no longer a direct measure of the exerted force on the object F_1, rather it is now recording the force *transmitted* through the object F_T. For non-rigid bodies $F_1 \neq F_T$. Instead the force transmitted is given as a ratio of the applied force $\left|\frac{F_T}{F_1}\right|$, known as the transmissibility TR. For a single degree of freedom mass-spring-damper system the force transmissibility is given by the equation

$$\left|\frac{F_T(\omega)}{F_1(\omega)}\right| = \sqrt{\frac{k_{TO}^2 + \omega^2 c_{TO}^2}{(k_{TO} - m_{TO}\omega^2)^2 + \omega^2 c_{TO}^2}} = \sqrt{\frac{1 + (2\zeta\omega/\omega_n)^2}{\left[1 - (\omega/\omega_n)^2\right] + \left[2\zeta\omega/\omega_n\right]^2}} \tag{5.1}$$

where ω is the frequency of excitation ω_n is the natural frequency of the material and ζ is the damping ratio [184]. Therefore it is now possible to approximate the amplitude of F_1 from the amplitude of F_T. A simulation of the transmissibility for various damping ratios is shown in Figure 5.6. Aside from the resonance at $\omega/\omega_n = 1$ the *TR* is below 1, which is to be expected as the force is absorbed by the object. At $\omega/\omega_n = 0$ or at zero frequency, the force is no longer dynamic, instead it is a static load on the object. As such the stiffness and damping have no effect, the TR from equation (5.1) is 1, so the force is transferred completely.

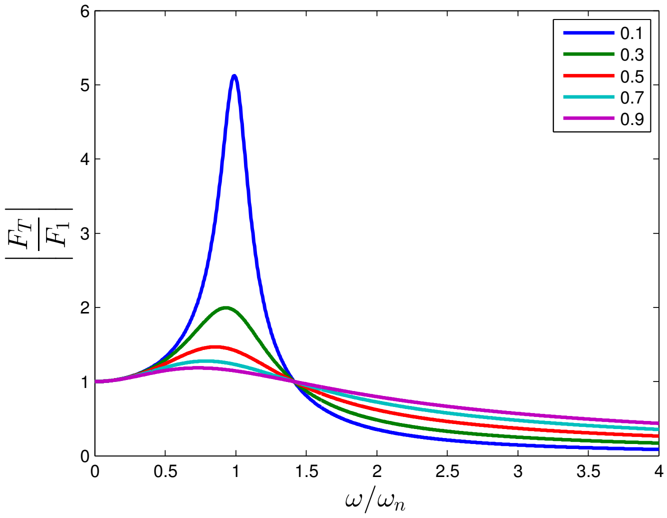

Figure 5.6: *Simulation of transmissibility for MSD model showing the change with increasing damping ratio ζ. Human skin has $\zeta \approx 0.8$*

This model can now be used to estimate errors introduced by measured F_T rather than F_1. It is clear from figure 5.6 that the damping ratio has a large bearing on the extent of error, with high ζ giving smaller errors. A study of the dynamic properties of the human skin found that, whilst frequency dependent, human skin has a damping ratio of approximately 0.8 for low frequencies **Potts** Therefore this high damping ratio would give a ratio of $\left|\frac{F_T}{F_1}\right|$ close to unity. Thus F_T is representative of the applied force F_1. Although not quantified in the literature, orange skin is also highly damped, and so would exhibit similar results to that of human skin in this regard. Therefore the forces measured by the load cell - F_T in the rest rig represent acceptable estimates for the force applied to the test sample surface.

It is also important to note that these differences in F_1 and F_T only occur in *dynamic* forces, as the system decays to the steady state, the forces become static, and $F_1 = F_T$. It is therefore important to investigate how quickly the steady state is reached to determine the validity of the experimental set up. This is investigated in section 5.2.7.

Control with stepper motor

Stepper motors are controlled by sending a digital pulse from the controller which advances the rotor by a fixed angle or "step". Unlike DC motors where the torque is controlled by controlling current and speed is controlled by controlling voltage, stepper motors are operated with a fixed voltage and current supply. Torque output *per step* is fixed, and output speed is controlled by the number of pulses sent from the controller per second. The output of the motor is thus discretised into certain positions based on the step resolution.

Linear control schemes such as Proportional-Integral-Derivative (PID) are traditionally employed with an analogue controlled variable. Whereas the discrete output of the stepper motor simplifies the control scheme. Position control of a stepper motor can be implemented as an on/off controller, based upon the sign of the error: positive error results in step forwards, negative error results in step backwards.

In reality, the discrete output of the stepper motor means that the error will never be exactly equal to zero, instead the error will exist between two steps. Therefore the positive error would cause the motor to advance beyond the set point, then the negative error would cause the motor to retreat past the step point. This pattern would repeat *ad infinitum* and is known as limit cycling. The amplitude and frequency of this oscillation is dependent upon the speed of the controller (*i.e.* the frequency at which control decisions are made), relative to the step speed. If the step speed is less than the loop speed the amplitude of oscillation is equal to a single step. A faster step speed than the controller speed would result in a larger overshoot before the controller recognises the error. An example of limit cycling with the force control hardware is shown in figure 5.7.

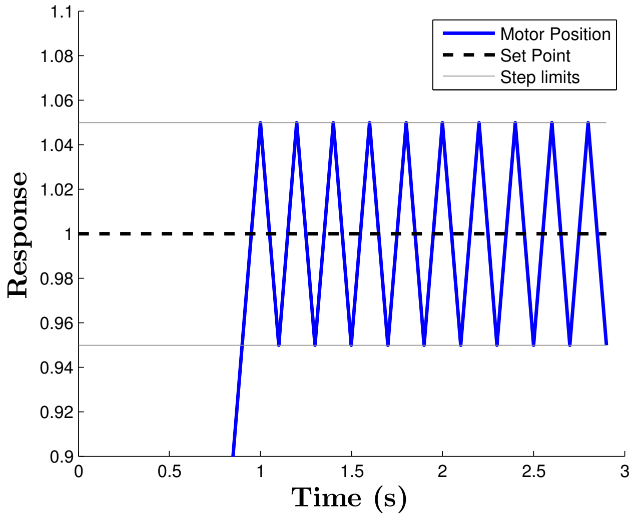

Figure 5.7: *Limit cycling example*

To prevent limit cycling a threshold can be included in the on/off controller, also known as a "dead band". The error has to be above a certain threshold before the motor will step in either direction. The threshold value should be set to the minimum acceptable value to minimise the loss in accuracy. The block diagram of the feedback control for a stepper motor with deadband is shown in Figure 5.8.

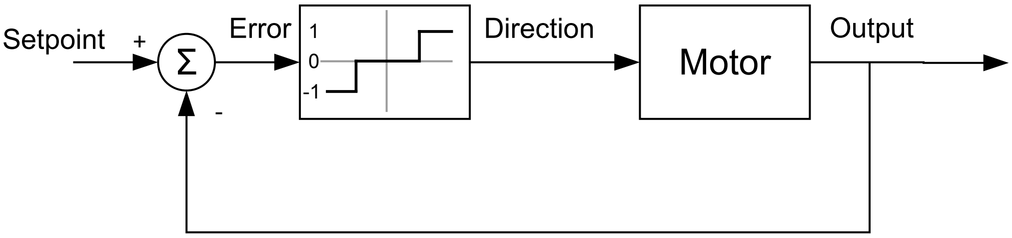

Figure 5.8: *Block Diagram of stepper feedback control, with dead band*

Minimum threshold to prevent limit cycling

Due to limitations in the control hardware setup, the minimum control loop rate was 50 Hz. The step speed was set at 100 Hz. The minimum threshold which prevented limit cycling was found to be 0.2 N. The result of this dead band can be seen in figure 5.9.

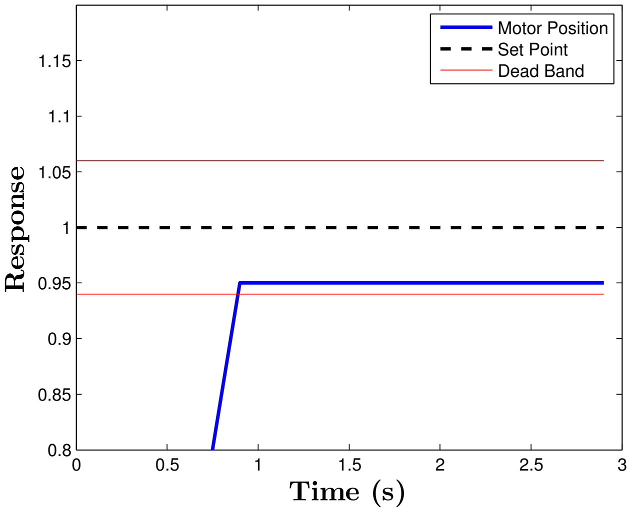

Figure 5.9: *Limit cycling example*

5.2.4 Rotary Actuation

Rotation of the electrode was achieved through a DC motor and a transmission system comprising of a gear train and a keyed joint. A schematic of the components is shown in 5.10. The target rotation speed was ≈ 1 Hz, based on what was found to be a comfortable speed of rotation for self abrading electrodes in the literature [113].

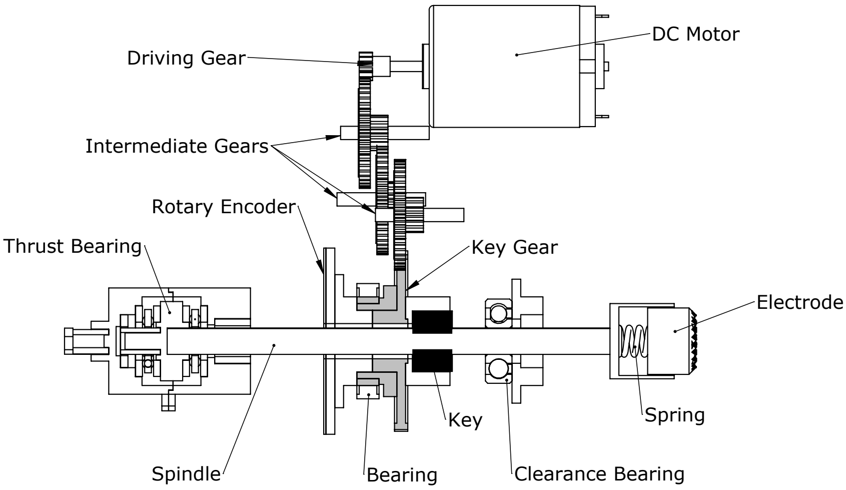

Figure 5.10: *Schematic of rotary actuation components*

Transmission

A cross section view of the transmission of the DC motor torque to the spindle is shown in figure 5.11. The gear ratios of the transmission were 4 : 1 for the intermediate gears and 10 : 6 for the key gear, resulting in a ratio of 106.67 : 1. The motion of the gears was transferred to the central electrode spindle through a keyed joint. The key gear was attached to the inner race of a clearance bearing, with the spindle passing through the central bore of both without any contact. Two keys were attached to the key gear and bearing arrangement so they protruded into the central bore. Matching slots were cut into the spindle so that the rotation of the keys was transferred to the spindle. Thus the spindle is free to translate axially as it is being rotated.

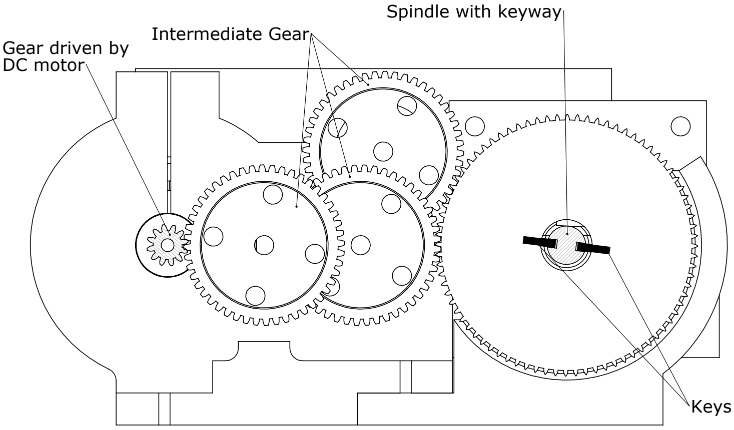

Figure 5.11: *Schematic of rotary actuation components, front view highlighting the transmission from DC motor to spindle*

Control of DC motor

The DC motor was controlled via Pulse Width Modulation (PWM), by changing the duty cycle (the ratio of high time to low time) of the input waveform. A higher duty cycle supplies a higher average power to the motor, thus increasing the speed and torque of the motor output. The extent at which the motor could be controlled was investigated and the results given in section 5.2.7. Higher frequency PWM signals give reduced fluctuation or "ripple" in the torque output of the motor. However there are limitations placed on the PWM frequency by the maximum switching frequency of the electronics. The frequency chosen was 10 kHz, which was chosen as it was below the maximum switching frequency of the power transistor so the square wave was amplified with good fidelity. The effect of changing the duty cycle on the speed and torque output was investigated, and the results given in section 5.2.7.

Rotary Encoder

An incremental encoder was used to measure the angle through which the electrode has rotated. An incremental encoder consists of a light-emitting diode (LED), a codewheel with a regular pattern of opaque and transparent sectors attached to the shaft, and a light detector. As the codewheel rotates, the light is blocked by the opaque sectors, which results in square wave pulses as output from the light detector. The number and frequency of pulses can then be converted into position or speed of rotation. A schematic of the encoder set up used in the prototype is shown in figure 5.12, a Infra Red LED was used, along with a quadrature encoder with an input wavelength which matched that of the IRLED. Quadrature encoders have two separate light sensors side-by-side, which allows *direction* to be measured by counting which channel changes output first.

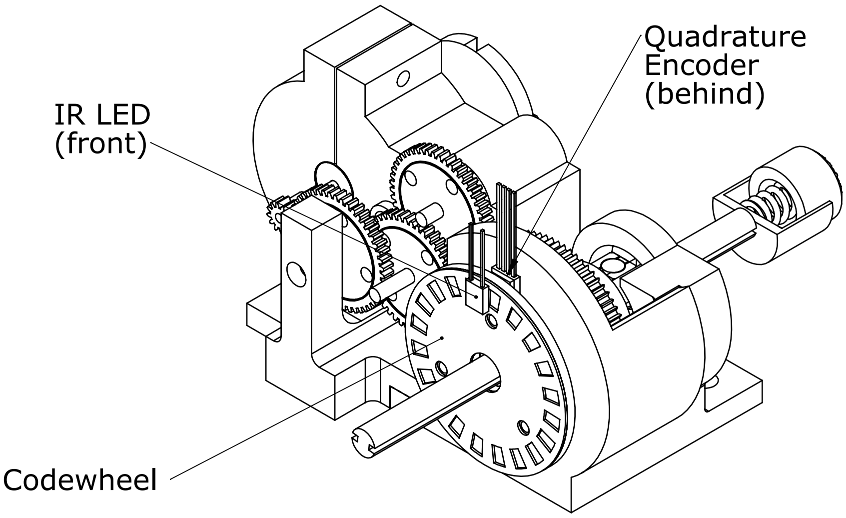

Figure 5.12: *Quadrature endcoder location, mounting hidden*

The codewheel with was laser cut out of aluminium foil, and held in place between two transparent perspex discs. The resolution of the position measurement is dependent upon the number of slots cut out of the foil disc. In order for the encoder to detect a change in position, the irradiance (power of incident light per unit area) must be below 15 % of the maximum to transition from high to low and 85 %. for low to high. If the codewheel tracks are too narrow, the change in irradiance insufficient as multiple tracks are within the encoders focal plane. The optimum track size for the geometry specific to this application was determined experimentally. Codewheels with 10, 20, 30 and 40 tracks were laser cut and the change in irradiance measured by a phototransistor as the wheel was rotated. The results are shown in figure 5.13. Codewheels with 10 and 20 tracks consistently decreased the irradiance below the threshold, whereas the 30 track codewheel gave intermittent results. Therefore the 20 track codewheel was chosen as it was below the threshold, and gave the higher position resolution.

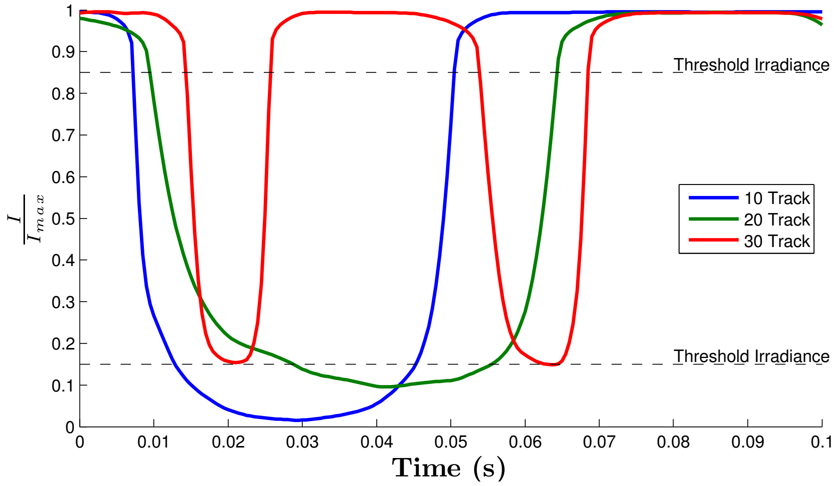

Figure 5.13: *Phototransistor output for different codewheel track numbers. 10 and 20 track codewheels reliably decreased irradiance below threshold*

5.2.5 Impedance Measurement

A simple two electrode impedance measuring circuit was designed and implemented on a PCB and National Instruments DAQ. The impedance was measured between an electrode placed on the motor spindle, and a reference electrode placed behind the test object. Thus impedance measured includes both the contact impedances and both electrode impedances. A large 30x25 mm silver reference electrode was used to minimise its contribution to the impedance measured. The impedances of both electrodes were calculated experimentally section 5.2.6.

The simplified block diagram of the impedance measurement circuit is shown in 5.14. A National Instruments USB 6221 DAQ was used to generate a sine wave at the desired frequency and amplitude - V_{in}. The two electrodes are then connected, the dashed box represents a simple resistor-capacitor model for the load based on the model for human skin in section 1.4. The current in the circuit was calculated from the voltage drop V_c across a resistor with a known resistance, R_{sense}. Similarly the differential voltage drop V_{load} across load impedance, Z_{load}, was also measured. These differential voltages are amplified by the op-amps I_1 and I_2 respectively, and then sent to the DAQ.

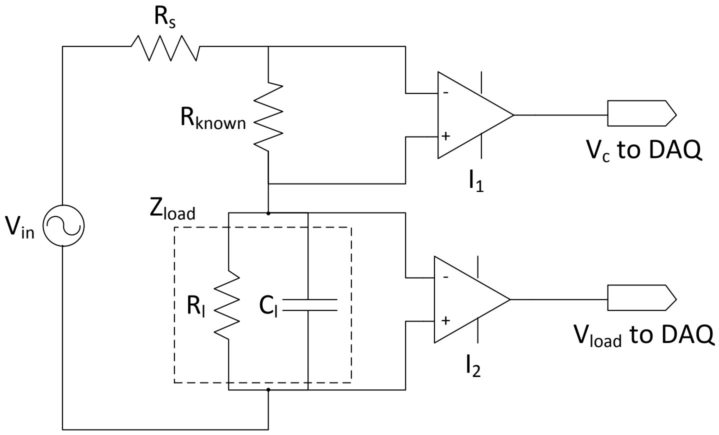

Figure 5.14: *Block diagram of impedance measurement circuit*

R_{sense} was matched to the required impedance measurement range, which was determined based on the results from the experiment in section 5.2.1. The range of impedances expected during test rig experiments at 20 Hz ranges from approximately 1.12 kΩ to 20 kΩ. The size of the electrode and area of abrasion were greater in this preliminary experiment, thus the impedances are expected to be larger in the test rig experiments. Thus a value of 10 kΩ was chosen for R_{sense}.

Frequency of interest

Impedance at low frequencies represents the most stringent test of the abrasion as skin impedance is largest at these frequencies, as described in section 1.4. The lowest frequency used in the UCL Mk2.5 stroke protocol is 20 Hz thus it was chosen for the frequency of V_{in}.

Impedance Calculation

Once the voltages from the circuit have been recorded by the USB DAQ, Z_{load} can be calculated from the following equation:

$$Z_{load} = \frac{V_{load}}{I} = \frac{V_{load}R_{sense}}{V_c} \tag{5.2}$$

The magnitude of V_{load} and V_c was calculated by a tone measurement program in LabView, which determines the amplitude of the largest frequency bin in the Fourier domain. Components of the signal other than 20 Hz were filtered before calculation, thus reducing the sensitivity to noise. The impedance measurement system was validated in section 5.2.7.

5.2.6 Electrode

The electrode was constructed out of a brass disc with a pyramidal pattern cut into the surface. The peripheral edge of the electrode was chamfered to remove sharp edges. The benefits of this pattern are that it increases the contact surface area, which decreases the contact impedance, and it helps wear away the skin surface in a manner similar to tools such as files and rasps. A schematic of the electrode is shown in figure 5.15. A retaining bush provides support in the transverse (radial) directions, while allowing motion in the axial direction. The electrode was attached to the spring with conductive silver epoxy to provide an electrical path from the electrode to the spindle.

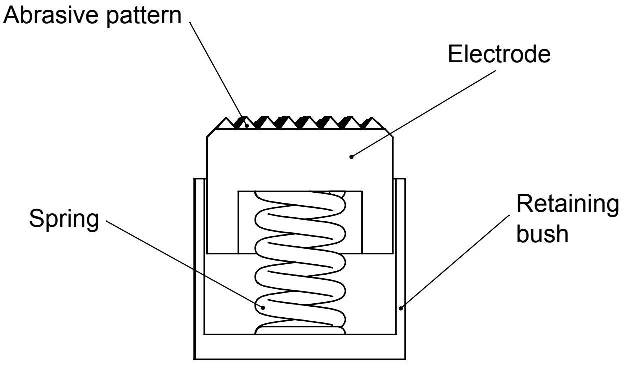

Figure 5.15: *Schematic of electrode design*

Surface roughness

A measure of the sharpness of an edge is its minimum radius. which describes the extent of the edge rounding. To measure the minimum radii of the textured electrode surface, pictures of a single pyramid were taken under a calibrated microscope. The point at which the edge was no longer straight was found for each edge of the pyramid silhouette. From these measurements a minimum radius of 0.06 mm was found.

Electrode Impedance

The impedances of the brass electrode and a silver reference electrode were measured experimentally. Electrodes were placed at either ends of saline filled tubes of varying lengths and the impedance measured with the Hewlett Packard 4284A Impedance Analyser. The combined electrode impedances were calculated by extrapolating the impedance for a tube of zero length. The experiment was performed twice: with two silver reference electrodes, and with a brass and single reference electrode. Values for the impedance of both electrodes were then calculated and the results given in figure 5.16.

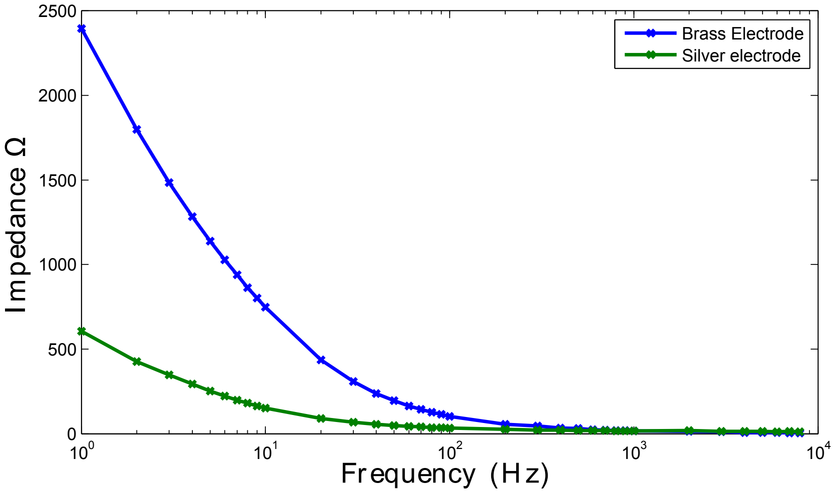

Figure 5.16: *Comparison of electrode impedances of brass electrode and silver reference electrode*

The most significant value is the impedance of 415 Ω at 20 Hz, as this is the frequency used in test rig experiments. This value must be taken into account when setting the impedance threshold for the abrasion, as the impedance recorded will be inclusive of this 415 Ω electrode impedance. The impedance of the reference electrode in the tube experiment is 90 Ω at 20 Hz, however the reference electrode in the test rig is approximately twice the area. Therefore the combined electrode impedance is approximately 450 Ω.

Electrode electrical contact

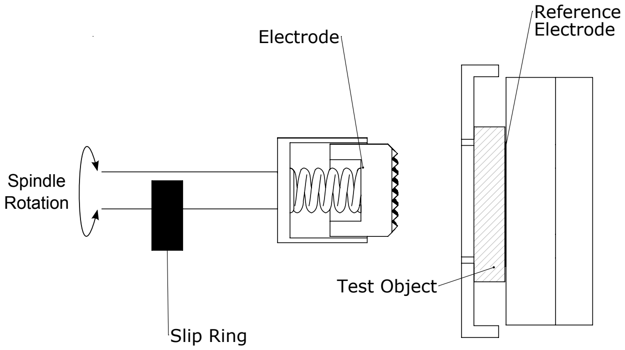

Figure 5.17: *Schematic of electrical connection of reference and actuated electrode, slip ring highlighted*

A slip ring (leaf spring) was constructed to maintain electrical contact with the actuated electrode during rotation. The spindle has two longitudinal grooves which would alter the area in contact with the leaf spring during rotation. This could potentially produce artefacts in the V_{load} signal used in the impedance calculation at twice the frequency of rotation (≈ 1 Hz). The frequency of interest in these experiments is 20 Hz, which could potentially contain harmonics of any noise at 2 Hz. To verify this, two slip rings were connected to the spindle and a 3 V DC signal was measured as it was rotated. The power spectral density of the signal is shown in figure 5.18. The majority of the noise in the signal is interference from the DC motor, for example the PWM switching frequency at 1 kHz and associated harmonics. There is also some significant interference at 325 Hz and 450 Hz present only when the spindle is rotating. However, there is no significant source of noise at 20 Hz, so this interference will not negatively impact the results of the experiments.

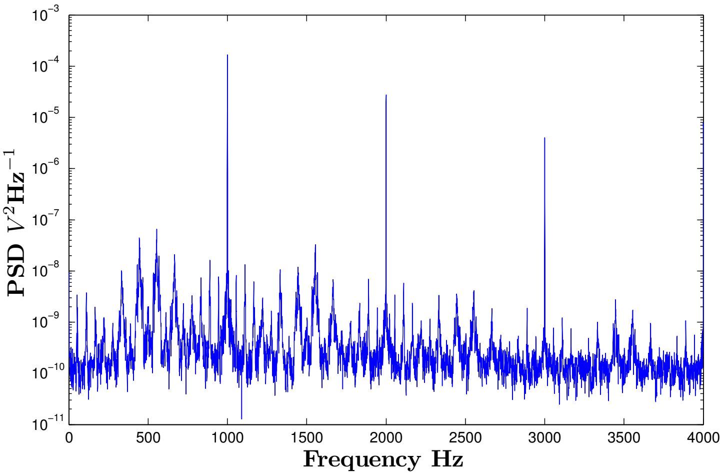

Figure 5.18: *Power spectral density of noise from spindle and slip ring*

5.2.7 Methods validation

Before collecting experimental data it was necessary to carry out further validation and characterisation studies of some components of the prototype. The focus of these studies was determining accuracy of the impedance measurements, understanding the limitations of the simple MSD model in the force transmissibility equations, and characterising the torque and speed output of the rotation stage.

Validation of Impedance Measurement Module

Accuracy across load range Measurements of R_{load} were performed for resistive loads, from 150 Ω to 100 kΩ at 20 Hz carrier frequency. The results were then compared to measurements from the Hewlett Packard 4284A Impedance Analyser. The percentage error, shown in figure 5.19 was less than 0.25% across the whole range. The error is greatest at the extremes of the

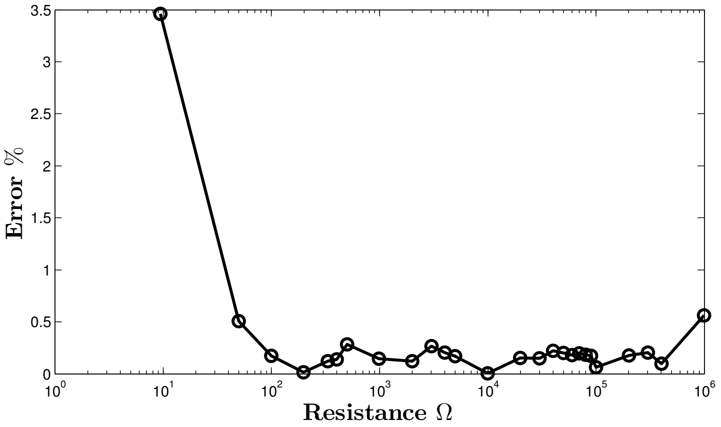

Figure 5.19: *Error in resistance measurements with impedance measurement module (R_{IMM}) and Hewlett Packard 4284A Impedance Analyser (R_{HP})*

measurement range, where the amplitude of either V_{load} or V_c are too small to be measured accurately.

Accuracy across frequency - Complex Test Circuit A parallel resistor capacitor circuit was created, based on the equivalent circuit of the Stratum Corneum from [102]. Values for the resistor and capacitor were chosen to approximate from the values of R_p and C_p at 20 Hz with no removal of the Stratum Corneum - 80 k Ω and 0.07 μF respectively. The actual values used were 82 kΩ and 0.047μF with a 1 % tolerance. A frequency sweep function was created which measured the modulus and phase of Z_{load} for a range of frequencies between 1 Hz and 8 kHz. The output sample rate of the DAQ used to generate the sine wave was 20 kHz, which limited the accuracy of the results of the sweep at higher frequencies, as is clear from the results in fig. 5.22.

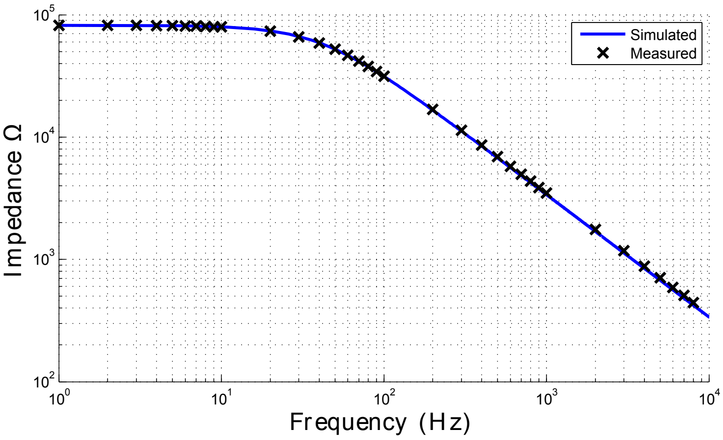

Figure 5.20: *Impedance of RC circuit, comparison of simulated and measured values*

A comparison of the measured and simulated impedance magnitude is shown in 5.20.

There is strong agreement between the simulated and experimental results across the frequency range, with a maximum error of 350 Ω. The resistive and reactive components were calculated using the modulus and phase, and the comparisons are shown in figures 5.21 and 5.22 respectively.

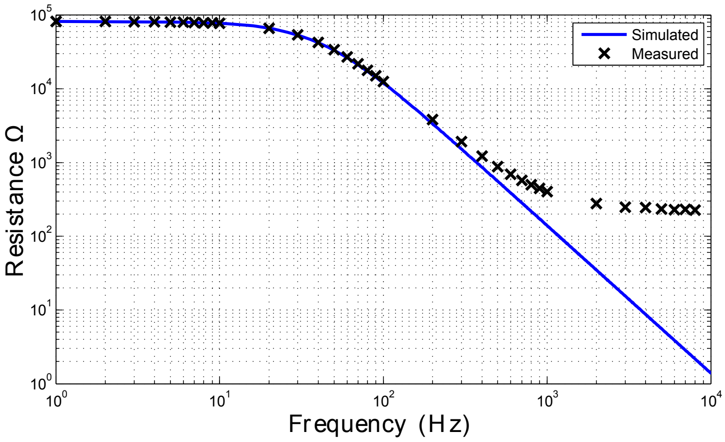

Figure 5.21: *Resistance of RC circuit, comparison of simulated and measured values*

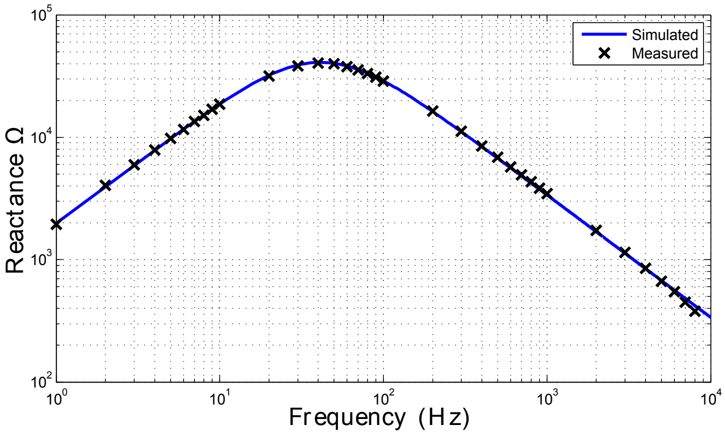

Figure 5.22: *Reactance of RC circuit, comparison of simulated and measured values*

This is a more stringent test of the measurement system as the results are now sensitive to errors in the phase measurements. There is significantly greater error in these calculations compared those of the magnitude. Lower than 300 Hz the resistance has an error less than 0.3 %, but this error increases exponentially as the overall impedance decreases. This is likely due to errors causes by the limitations of the National Instruments USB 6221 DAQ output sample rate, which is insufficient to represent V_{in} as a pure sine wave accurately at higher frequencies, resulting in errors in the tone measurement algorithm.

These results demonstrate that the impedance module is sufficiently accurate to measure the impedance of the test object within the frequencies of interest during the experiments, specifically 20 to 100 Hz. Errors in phase measurements result in large errors when decomposing the impedance into resistance and reactance at high frequencies, which must be taken into account when comparing impedance spectra with those from the literature.

Validation of force measurement - dynamic performance

As described in section 5.2.3 the force transmitted through the sample to the test object is only truly representative of the force applied to the surface of the sample in the steady state. To determine the extent of the errors introduced with these assumptions, the step response of the system was measured. The electrode was advanced onto the sample till a force of 5 N was recorded, at which point the motor advanced and retreated by a single step. The average of 50 forward steps is shown in figure 5.23.

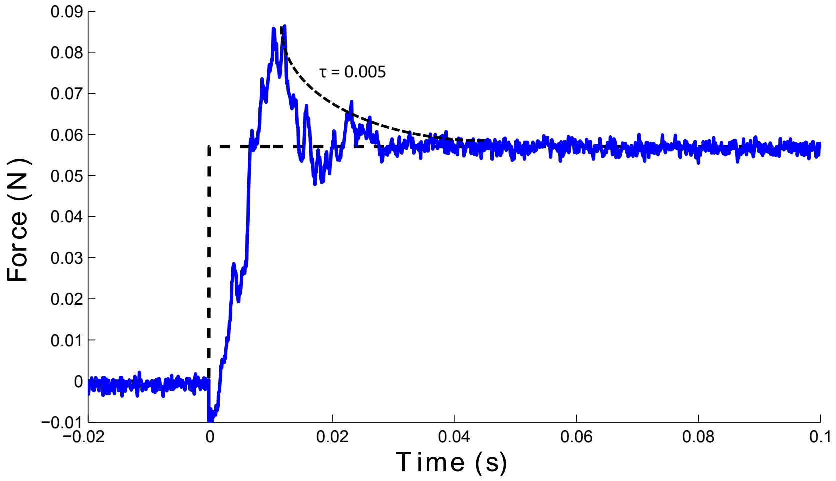

Figure 5.23: *Averaged step response of orange peel*

The steady state decay time is approximately 0.035 s, and the overshoot is 0.028 N which corresponds to a fractional overshoot of 0.49. The time constant of the overshoot was approximated by the time taken for the overshoot to decay by 63.2 %, and calculated to be 0.005 s. Therefore the errors in the force measurement will only be significant if they are recorded at a frequency greater than 200 Hz. Therefore the force controller must execute at a frequency less than this value. As the controller loop period has a minimum of 15 ms or 66.67 Hz, this overshoot is not significant. Additionally the force values were values averaged over 10ms, further reducing the effect of these errors.

Validation of orange skin as human skin analogue

In order to draw conclusions from the impedance data obtained in these experiments, the differences in the impedance of the orange skin samples and human skin were investigated. The spectra obtained in section 5.2.1 were compared to those from the literature [102] (see section 1.4 for details) as shown in figure 5.24. Stray capacitance limits the frequency range of the orange skin results to 10 kHz.

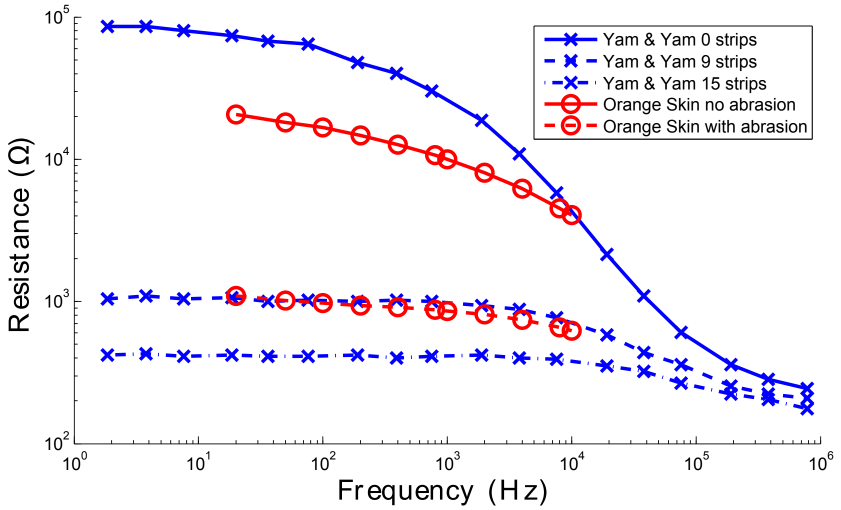

Figure 5.24: *Comparison of orange skin impedance before and after abrasion, and impedance of human skin with 0,9, and 15 strippings from [102]. Reduced frequency range in orange peel results due to limitations in measurement system*

The orange skin spectra demonstrates the same broad trend as the human skin spectra. The initial resistance of human skin is approximately 3 times larger at low frequencies but decrease more rapidly with frequency compared to orange skin. Abraded orange skin has a very similar spectra to that of human skin after 9 strippings or approximately 72 μm. However, in the Yamamoto & Yamamoto study, the stratum corneum was not fully removed until 15 strippings had been completed, for a depth of 120 μm. The final impedance was found to be approximately 400 Ω across the frequency range, whereas the orange skin was found to be approximately 1 kΩ. Therefore, the contact impedances with orange skin after abrasion will be greater than the equivalent with human skin. Provided this is taken into account when analysing the results, orange peel provides a sufficiently accurate representation of human skin for conclusions to be drawn from the following experiments.

Target impedance Given the large electrode impedance of 430 Ω as calculated in section 5.2.6 and that the impedance of abraded orange peel is 700 Ω greater than the human skin equivalent, the target of 5 kΩ contact impedance was increased to 6 kΩ. This value was used as the threshold for subsequent experiments.

Characterisation of rotary actuation

The zero-load speed for a range of duty cycles was calculated from the angle of rotation over 30 seconds. Given the coarse measurement of rotation - 18 degrees and the slow rotation speeds ≈1 Hz it was not possible to obtain an accurate profile of the speed of rotation over time. However, the average speed can be calculated from the total angle rotated during 30 seconds.

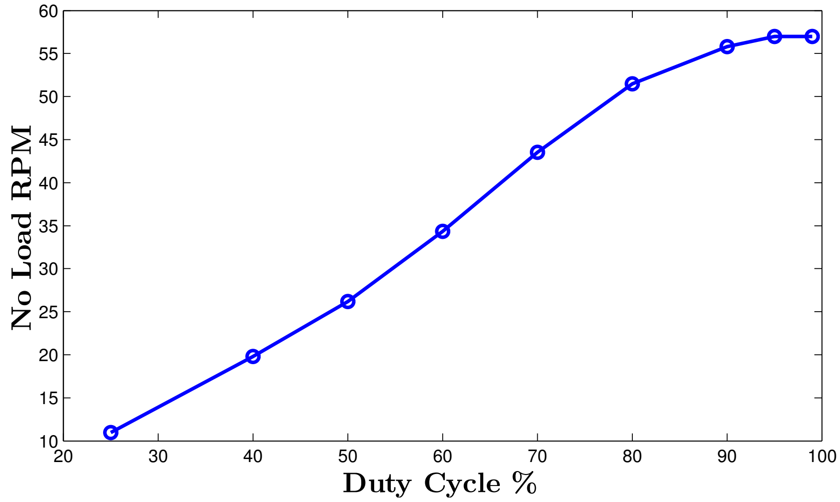

Figure 5.25: *Speed profile of electrode rotation*

The minimum duty cycle necessary to overcome the static friction in the transmission system was found to be 25 %. The speed was measured for a range of duty cycles between the minimum 25 % and 100 %, the averaged speeds are shown in figure 5.25. The results demonstrate an approximately linear relationship between duty cycle and speed between 25 and 80 % duty. Above this value, the output speed tends towards the maximum value of 57 RPM - just below the desired speed of 60 RPM or 1 Hz.

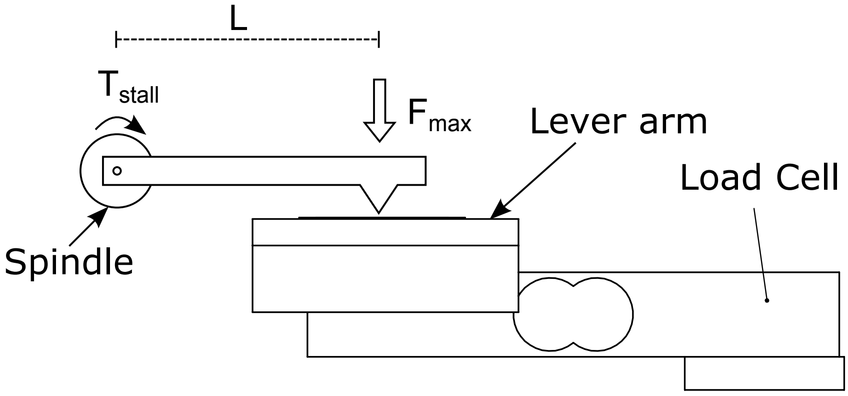

Figure 5.26: *Experimental setup to determine stall torque T_{stall} of motor from maximum force F_{max}*

The torque output was characterised by measuring the stall torque T_{stall} for each duty cycle using the experimental setup described in figure 5.26. The stall torque was determined from the maximum force F_{max} applied to the load cell. The results of the experiment are shown in figure 5.27. Overall the range of output torques is less than that of the output speed, with a particularly gradual increase with duty cycle above 40%. For example, decreasing the duty cycle from 90% to 50% reduces to speed to less than half, whereas the torque is decreased by a factor of 0.2 only. Using these results, it is now possible to estimate the torque output of any chosen duty cycle, which will give an indication of the torque necessary to abrade for a given applied force.

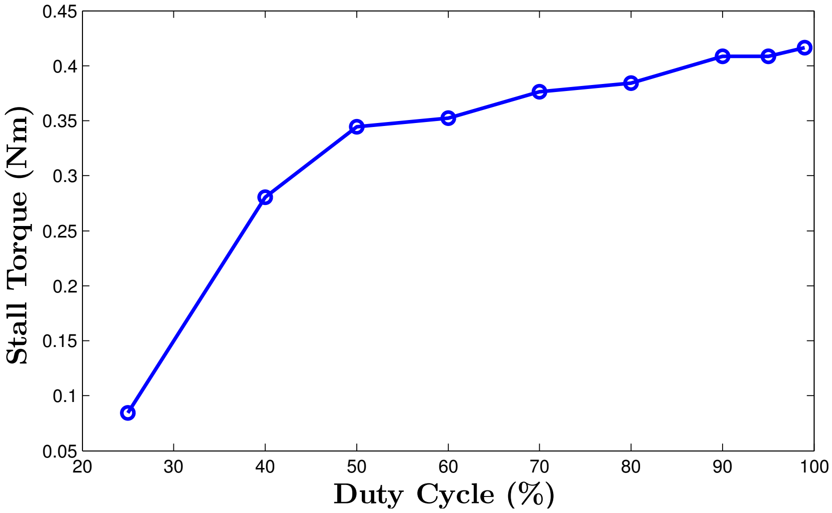

Figure 5.27: *Stall torque (maximum torque available) profile of electrode rotation as a function of duty cycle*

5.2.8 Test protocol

The experiments were performed as described below. The results were then averaged across measurements and are presented with error bars representing one standard error, unless stated otherwise.

Characterisation of manual abrasion

The aim of this experiment was to quantify the force (and thus pressure) applied to the skin surface by manual abrasion, and the resultant impedance decrease. The set up for the first experiment is shown in figure 5.28.

A test sample was abraded by a cotton bud with abrasive paste, and the force normal to the surface measured by the load cell. The abrasion was performed by a member of the UCL group experienced in applying electrodes to the scalp in clinical trials. These trials are currently unpublished but are based on the methods set out in previous UCL studies [185]. The surface area of the abrasive device was approximately 25 mm^2. The contact impedance spectra was measured between two silver reference electrodes, using the impedance module and frequency sweep function described in section 5.2.7. The sample was then abraded in the

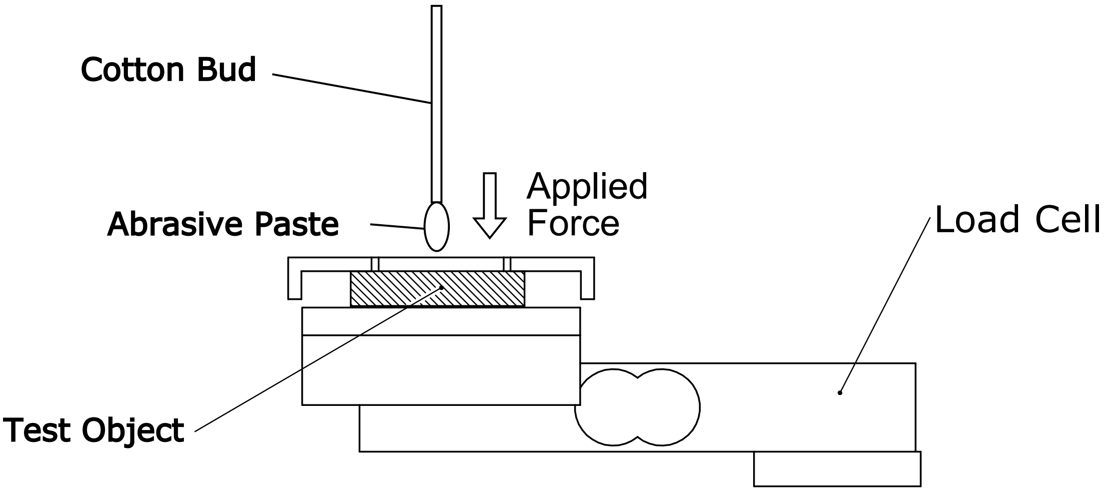

Figure 5.28: *Experimental setup to measure force applied during manual abrasion, and resultant impedance*

conventional manner, and the resultant impedance spectra was measured. The experiment was repeated for a total of three samples.

Contact impedance as a function of applied force

The aim of this experiment is to measure the change in contact impedance as a result on increased force. The contact impedance was measured at 20 Hz as the electrode advanced at a constant rate until a maximum of 20 N was measured. The experiment was repeated for a total of 9 samples.

Impedance during abrasion over a range of applied forces

The purpose of this experiment was to quantify the decrease in contact impedance caused by abrasion through rotation of the electrode. The electrode was advanced onto the test object until the desired force was reached. The electrode was then rotated for 30 seconds with a duty cycle of 90 %. The impedance at 20 Hz was recorded throughout the abrasion. The experiment was repeated with 3 samples for force levels of 2,3,5,7.5 and 10 N. The mean impedance decrease as a function of the number of rotations was calculated across test samples, for each force applied (2,3,5,7.5 and 10 N). The change in impedance per sixth of a rotation was also calculated for each of the mean impedances. The impedance spectra before and after abrasion was recorded for a single experiment with a set force of 10 N.

Impedance during abrasion for minimum and maximum applied torque

The aim of this experiment was to determine the minimum torque necessary to abrade for different applied forces. Differences in the decrease in impedance for rotation with the minimum and maximum torque available was also investigated. The procedure in the previous experiment was repeated for a single force of 5 N with the lowest duty cycle which allowed the electrode to rotate.

Proof of principle on human skin

The electrode was advanced onto the load cell until a force of 7.5 N was exerted. The load cell was then removed and replaced by the subject's arm, which compressed the spring by the same distance. Thus the force applied to the skin by the electrode was approximately maintained at 7.5 N. The electrode was then rotated 10 full rotations at 90% duty cycle. The impedance was recorded between the actuated electrode and a 50x70 mm silver reference electrode, which had been prepared with conductive abrasive paste. A diagram of the experimental set up can be seen in figure 5.29. The experiment was repeated with and without conductive abrasive paste on the actuated electrode. Impedance spectra were measured before and after the abrasion.

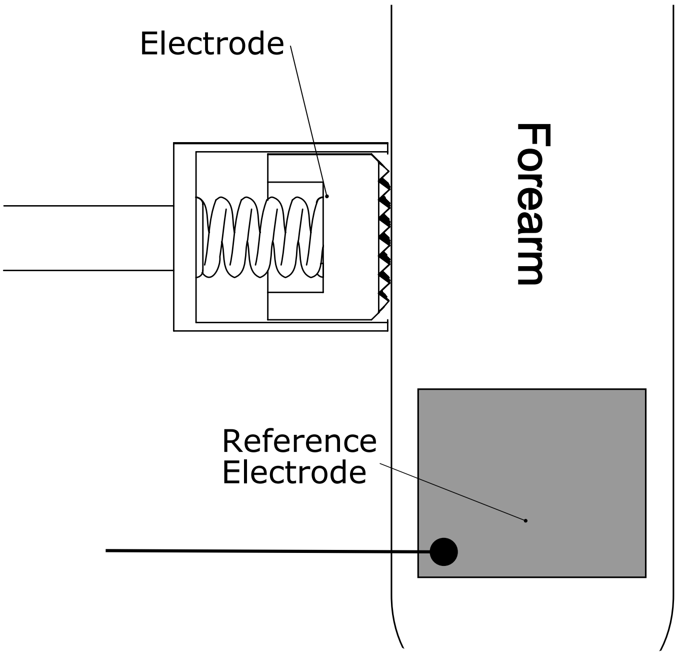

Figure 5.29: *Experimental setup to measure impedance decrease during abrasion of the human*

5.3 Results

5.3.1 Characterisation of manual abrasion

Force applied during manual abrasion

The average root-mean-square force applied normal to the sample surface was 0.62 N ±0.09, which equates to a pressure of 24.8 kPa, given an area of 25 mm^2 for the abrasive device. An example force profile during the abrasion procedure is shown in figure 5.30.

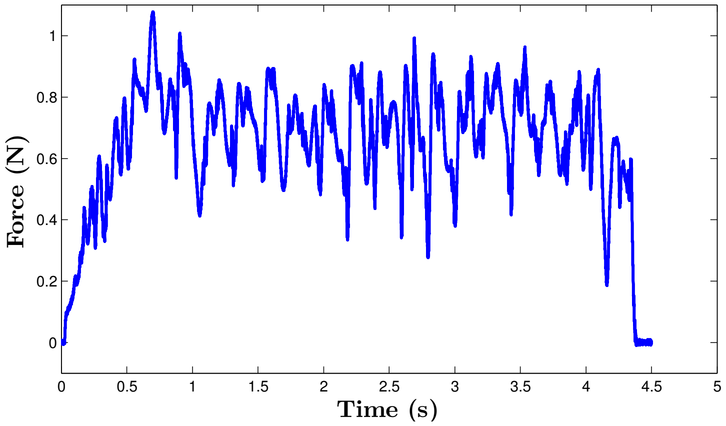

Figure 5.30: *Force profile during manual abrasion of test sample with abrasive paste and cotton bud*

Manual abrasion impedance spectra

The impedance across frequency before and after abrasion (figure 5.31) fell from approximately 30 kΩ to 4.5 kΩ at 1 Hz and the spectra decreased monotonically to 5 kΩ and 800 Ω respectively.

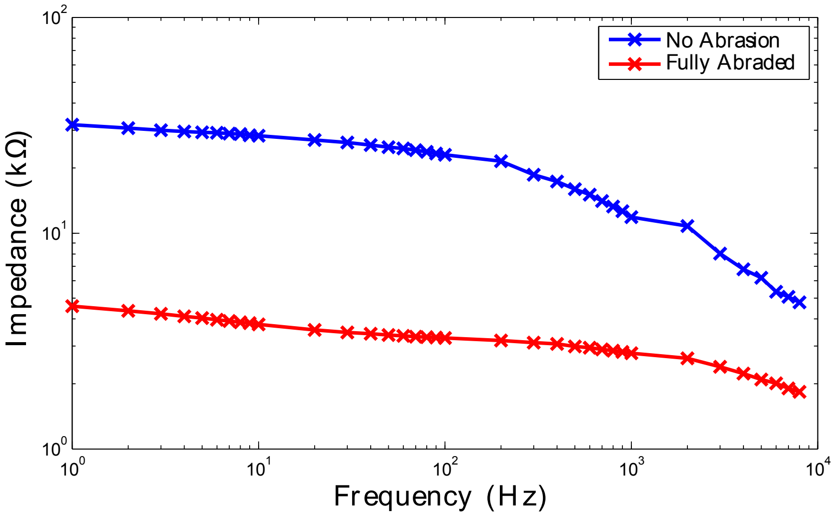

Figure 5.31: *Impedance spectra of orange skin test samples before and after manual abrasion*

5.3.2 Contact impedance as a function of applied force

As the electrode was advanced onto the test object the impedance decreased exponentially with increasing force (figure 5.32).

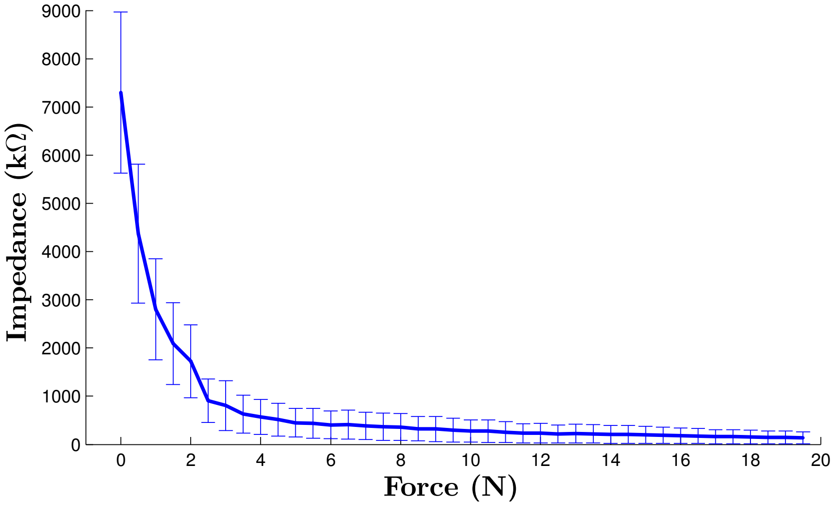

Figure 5.32: *Impedance as a function of force applied normal to surface*

5.3.3 Impedance during abrasion over a range of applied forces

The results demonstrate a similar monotonic decrease in impedance with electrode rotation (figure 5.33, and with respect to time in figure 5.34, error bars omitted for clarity). The change in impedance per half rotation (figure 5.35) is similar for all applied forces, with a large decrease in the first rotation and small decreases in subsequent rotations.

Impedance spectra after automatic abrasion

The impedance spectra after 20 seconds abrasion for the case of 7.5 N applied force (figure 5.36) decreased by approximately two orders of magnitude across the entire spectra - from 400 kΩ to 4 kΩ at low frequencies and 90 kΩ to 1 kΩ at frequencies above 1 kHz.

Force control during abrasion

The force measured by the load cell for each test is shown in figure 5.37. The root mean square error (given in table 5.3) was found to be less than 0.32 N across the force range.

Target force (N)	2	3	5	7.5	10
RMS error (N)	0.32	0.18	0.22	0.18	0.24

Table 5.3: *RMS error of force control system during abrasion*

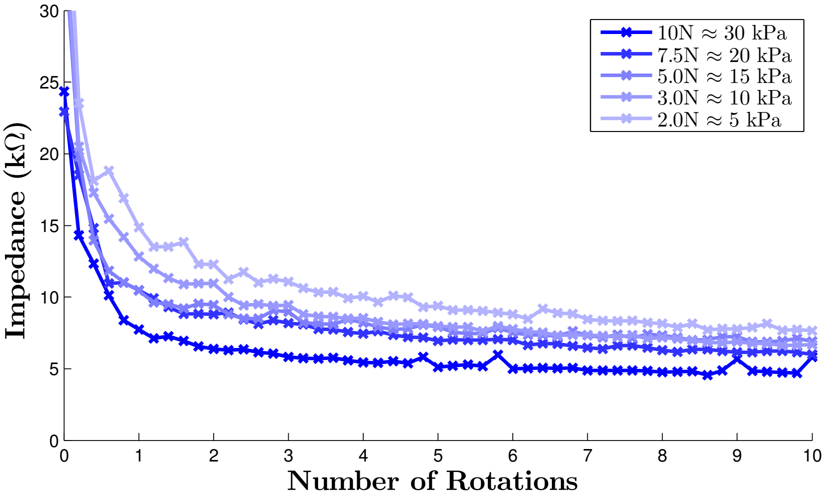

Figure 5.33: *Impedance decrease with respect to the number of rotations of the electrode, for a range of incident forces*

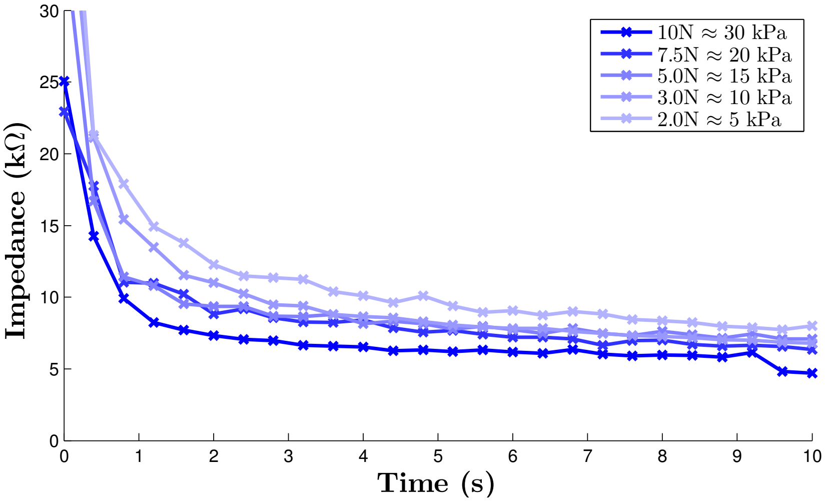

Figure 5.34: *Impedance decrease with respect to abrasion time, for a range of incident forces*

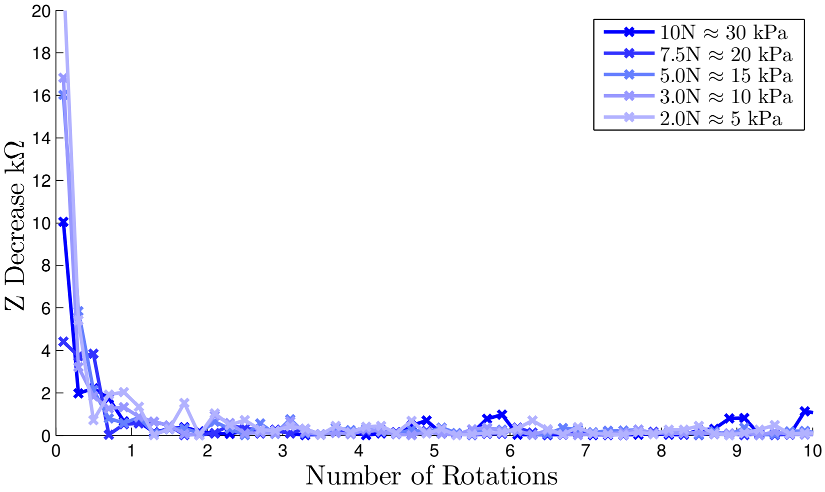

Figure 5.35: *Impedance decrease per sixth of a rotation, for a range of incident forces*

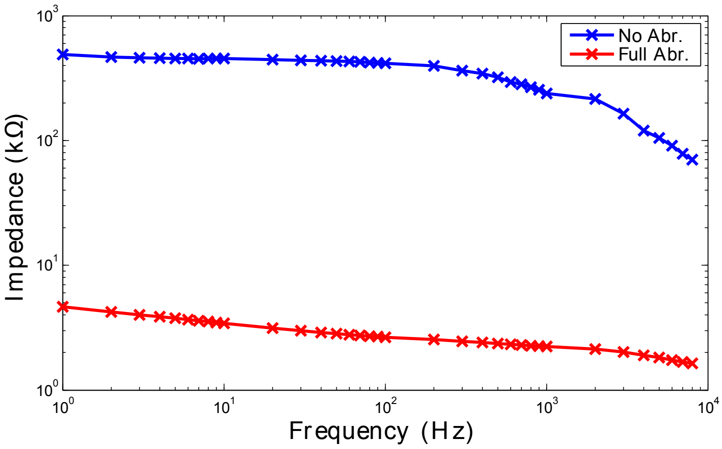

Figure 5.36: *Impedance spectra of orange skin test samples before and after 20 seconds automated abrasion with 7.5 N applied force and 90 % duty cycle*

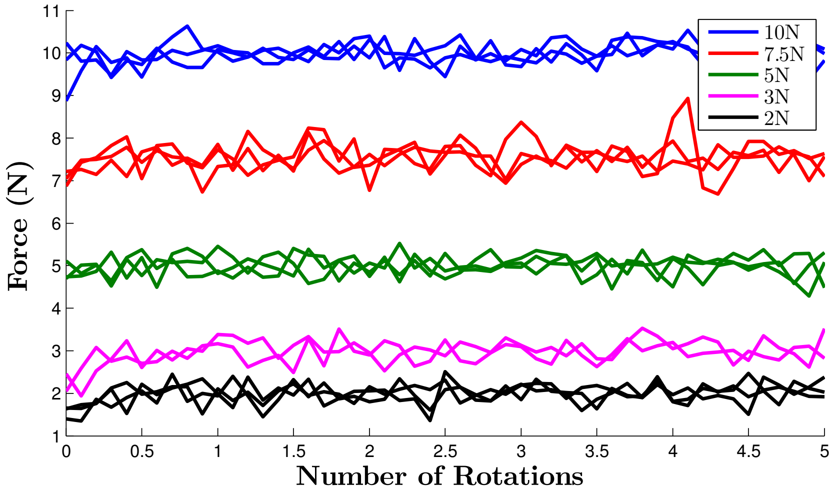

Figure 5.37: *Force control results: Measured applied force during abrasion, for set forces of 2,3,5,7.5 and 10 N*

5.3.4 Impedance during abrasion for minimum and maximum applied torque

The impedance decrease with 5 N applied force for the minimum and maximum torque, 0.3 Nm and 0.45 Nm respectively (figure 5.38 and against time in figure 5.39) show a similar monotonic decrease with increasing electrode rotation from approximately 35 kΩ to 6 kΩ.

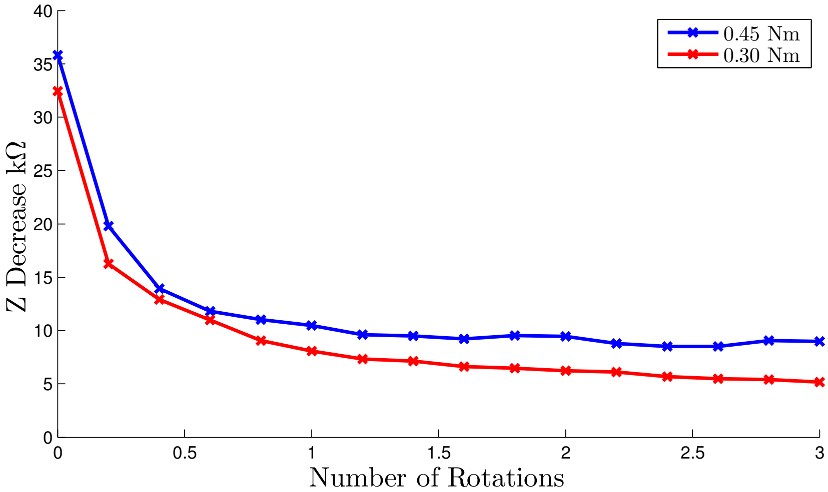

Figure 5.38: *Comparison of impedance decrease for 5 N applied force with respect to number of rotations for both minimum and maximum applied torque*

Minimum torque required to abrade

The minimum torque output required to abrade (figure 5.40) increased linearly with applied force.

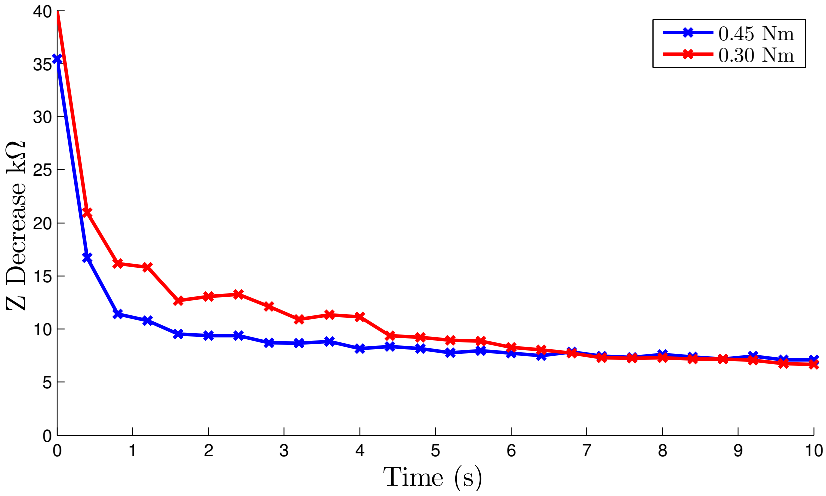

Figure 5.39: *Comparison of impedance decrease for 5 N applied force with respect abrasion time for both minimum and maximum applied torque*

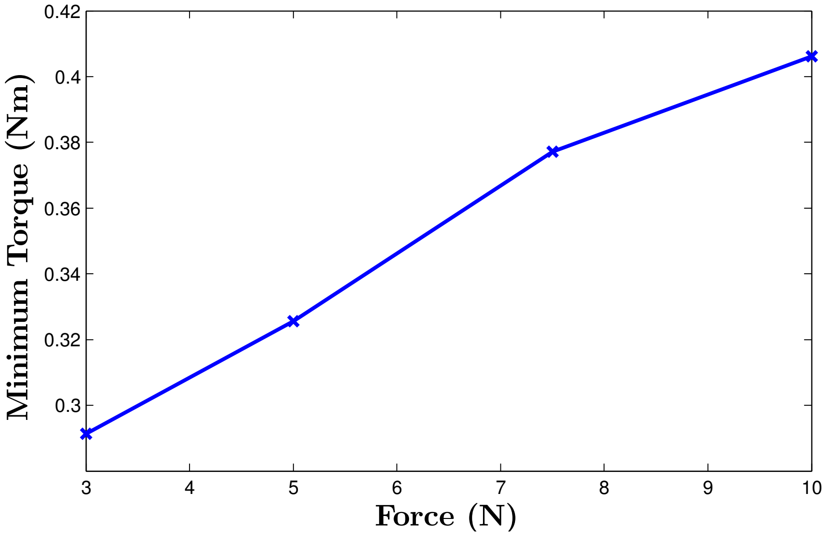

Figure 5.40: *Minimum torque necessary to rotate electrode across range of applied forces*

5.3.5 Proof of principle on human skin

Abrasion with and without conductive paste

With paste the impedance decreased from 10 kΩ to 800 Ω in less than 2 rotations, whereas without paste the decrease was from >50 kΩ to 5 kΩ in 9 rotations (5.41). The speed of rotation was 0.22 Hz or 13.2 RPM for dry abrasion, and 0.7 Hz or 42 RPM for wet abrasion with paste.

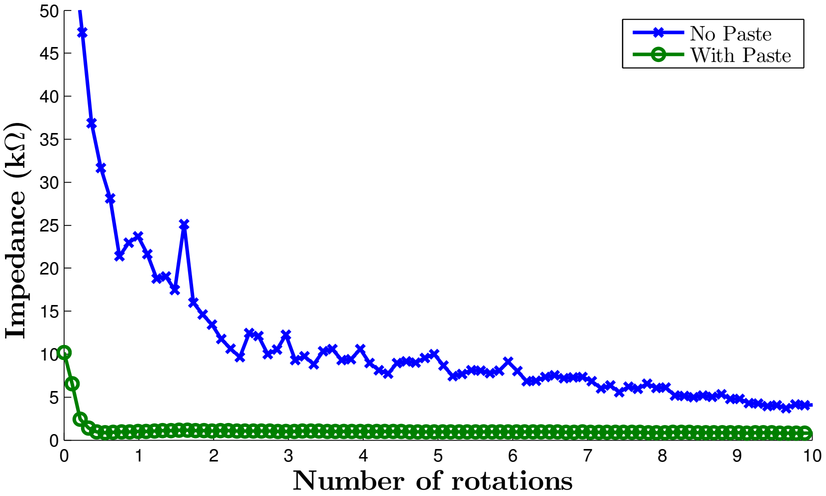

Figure 5.41: *Impedance decrease on human forearm with respect to the number of rotations of the electrode, with and without abrasive conductive paste. Note motion artefact at 1.5 rotations for without paste*

Impedance spectra

The impedance spectra with and without paste results are shown in comparison in figure 5.42.

Comparison with literature

The impedance spectra for with and without paste cases shown in comparison with the results from the Yamamoto & Yamamoto study in figure 5.43 [102]. The impedances have been corrected for the electrode impedance.

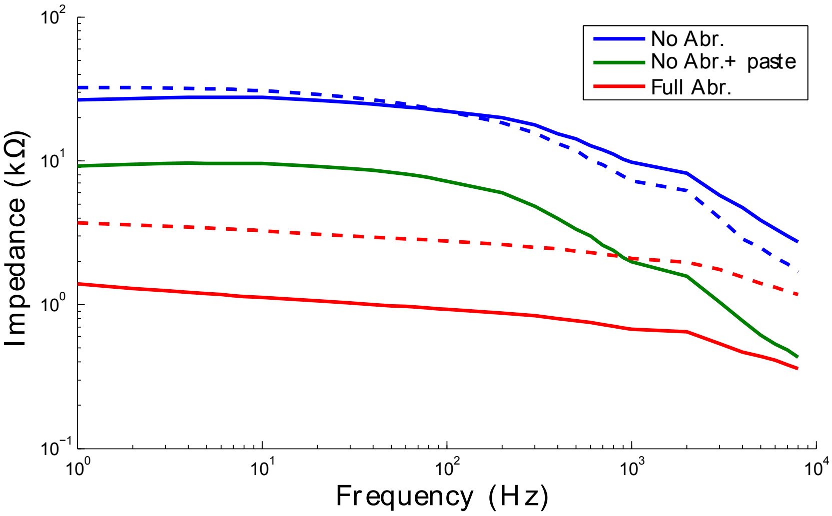

Figure 5.42: *Impedance spectra measured on human forearm: before and after abrasion without paste (dashed); before and after abrasion with paste, and with the addition of paste only (solid)*

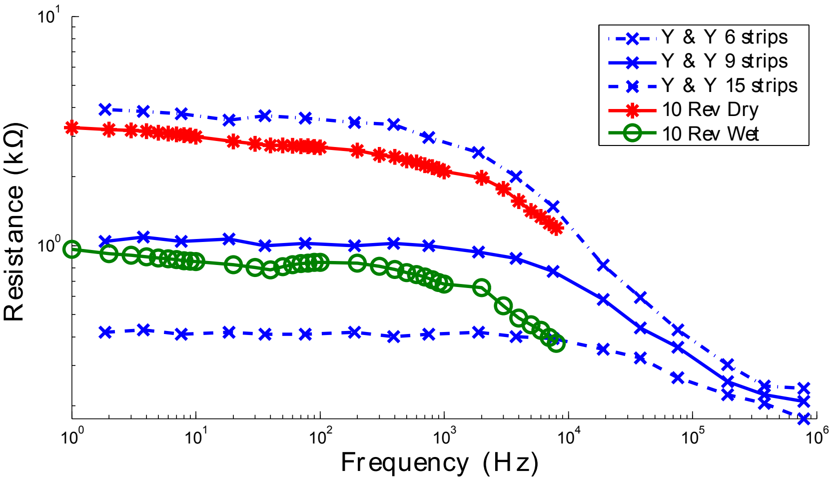

Figure 5.43: *Comparisons of corrected impedance spectra after abrasion was complete for both wet and dry abrasion in comparison with the impedance after 9 and 15 strips from [102]*

5.4 Discussion

5.4.1 Summary of results

Characterisation of manual abrasion

The average impedance spectra measured after abrasion (figure 5.31) were less than 4 kΩ above 10 Hz, which is 3 or 4 times greater than the impedances for orange skin found in section 5.2.1. This was expected as the extent of the abrasion in the preliminary experiment was much greater than that in the manual abrasion experiment, so a greater amount of the outer layer was removed. Despite this, the results from this experiment show that it is possible to reduce the contact impedance at 20 Hz to a value significantly below the 6 kΩ target. Therefore this impedance spectra is a suitable target for the automated abrasion.

Despite the empirical nature of the experiment the results demonstrate a repeatable average force applied to the surface of the test object. The force applied, 0.6 N, was substantially less than those chosen for the experiments with the prototype, however due to the small surface area of the applicator the pressures are similar. Given the area of 25mm^2, the pressure applied to the applicator was 24.8 kPa, which for the electrode used in the prototype is equates to a force of 8.7 N. This is well within the range of forces applied to the test object, which suggests that the values chosen are acceptable with respect to patient comfort.

Contact impedance as a function of applied force

As the electrode advances onto the test sample there is an exponential decrease in the contact impedance with the largest decrease occurring between 0 and 3 N (figure 5.32). This initial impedance drop is most likely caused by the penetration of the spiked electrode surface. At forces close to 0 N only the very tips of the electrode are in contact with the test sample, so the surface area is small and thus the contact impedance is very large ≈ 5000 kΩ. As the force applied increases, more of the spiked surface comes in contact and the impedance decreases rapidly until the surface is fully in contact with the electrode. Increasing the applied force further has a much less significant effect on the impedance as the decrease is due to damage of the skin due to the compression. Therefore from these results it is clear that there is a definite minimum force of 3 N which should be applied to ensure good electrode contact. Forces above 10 N do not produce a significant improvement in the contact impedance to justify the potential damage or discomfort to the patient.

Impedance during abrasion over a range of applied forces

The contact impedance demonstrates the same trend as the electrode was rotated for each value of applied force (figure 5.33). There is a large decrease in the impedance within the first three rotations, with a shallow decrease for subsequent rotations. Increasing the force applied reduces the number of rotations required to reach the 6 kΩ threshold, as well as reducing the final impedance value. However, the results from the previous experiment (figure5.32) show that prior to any rotation, the impedance decreases with applied force, so the initial impedance would be lower for higher forces before any abrasion had taken place. This is supported by the results in figure 5.33 as the impedances at zero rotations are significantly lower for 7.5 and 10 N. Additionally, after abrasion the impedance would still have a similar relationship to applied force albeit with lower overall magnitude. So for a given depth of skin removed, applying more force would also decrease the impedance. In summary, even if the abrasion with 5 N and 10 N removed exactly the same depth of Stratum Corneum, the impedance would be less with 10 N applied force.

Therefore the lower final impedances for these higher forces may not represent an improvement in the abrasion "efficacy", *i.e.* the impedance decrease per rotation, merely that by increasing the force, the initial impedance and lowest potential impedance are decreased. The impedance decrease per quarter rotation (figure 5.35), suggests this is the case. It is clear from the results that with the exception of the first rotation, there is no apparent difference between any of the results. During the first half rotation the impedance decreases by a larger amount with lower forces, this can be accounted for by the much larger initial impedance and poor electrode contact. Therefore the impedance decrease during this time will be relatively larger than the equivalent for 7.5 or 10 N applied force. These results demonstrate that applying a larger force during abrasion does not improve the impedance reducing performance, rather it reduces the initial impedance and lowest possible impedance.

Impedance during abrasion for minimum and maximum applied torque

Reducing the duty cycle and thus the output torque, in the rotary actuator did not adversely effect the performance of the prototype as the impedance decrease with respect to the number of rotations is largely unchanged (figure 5.38). The lower overall impedance of the 0.30 Nm result is within the standard error of inter-sample variations, and is thus not significant. However, the results from characterisation of the rotation stage in section 5.2.7 show that by reducing the duty cycle the speed is also reduced. So the reduction in the impedance over time is affected by the lower duty cycle as shown in figure 5.39. These results suggest that the torque output from the motor is not a crucial design issue, as long as it is sufficient to overcome the friction at the electrode surface and rotate the electrode.

The minimum torque required to abrade is related to the friction forces at the electrode surface, which in general take the form $F_{friction} = \mu F_{Normal}$ where μ is the coefficient of friction. Therefore the friction is proportional to the force applied by the electrode, and increases linearly as this normal force increases. The results shown in figure 5.40 demonstrate this trend in the minimum torque required to abrade (0.3 Nm at 3 N force). The friction torque is the summation of the friction force across the surface of the electrode, which is proportional to the normal force and scaled by the electrode geometry and the coefficient of friction.

Proof of principle on human skin

The prototype also successfully demonstrated the principle in the test on the human forearm. The force control was not as rigorous as with the test rig experiments so it was not possible to draw conclusions regarding how force affected abrasion or minimum torque. However with this set up it was possible to demonstrate that settings that were successful on the orange skin (90 % duty and 7.5 N) were also successful in the more representative test on human skin. Without paste the impedance decreases exponentially in a manner similar to the results with the orange skin. As with orange skin the majority of the impedance decrease occurs in the first 3 rotations, and the target impedance of 5 kΩ was reached after 9 rotations of the electrode. The impedance spectra shown in figure 5.42 shows that the impedance was decreased sufficiently across frequency. The addition of abrasive greatly reduced the amount of abrasion required. After only one entire rotation the impedance was reduced well below the 6 kΩ threshold impedance to a value of < 1 kΩ. The slight increase in impedance at 1.5 rotations was caused by subject movement. Further rotations did not have any significant effect, the final impedance was 800 Ω. The abrasive paste was conductive which served to significantly reduce the contact impedance before any abrasion took place, from 30 kΩ to 10 kΩ at 20 Hz as demonstrated in figure 5.42. Not only did the paste lower the initial impedance, it also facilitated the abrasion from the electrode, clearly evident in the comparison figure 5.41.

The impedances after abrasion were then corrected for the electrode impedance to enable comparison with the literature. As with the orange skin validation (section 5.2.7) the impedances were compared with those from Yamamoto and Yamamoto [102], as shown in figure 5.43. The results suggest that without paste the impedance has decreased greater than the equivalent of 6 tape strippings or the removal of 48 μm of the Stratum Corneum, whereas abrasion with paste is greater than 9 strippings or 72 μm removed.

5.4.2 Prototype performance

The prototype self abrading electrode was successful in meeting the criteria specified in section 5.1.1 of reducing the contact impedance at 20 Hz to less than 6 kΩ (modified from original 5 kΩ target, see section 5.2.7).

The results in figure 5.33 demonstrate that for forces above 5 N the contact impedance was reduced below the threshold within 10 rotations of the electrode. However, the results shown in figure 5.34 demonstrate that only the abrasion with 7.5 and 10 N applied force meet the contact impedance threshold in the desired time of 10 seconds or less. The impedance spectra shown in figure 5.36 after 20 seconds of abrasion with 7.5 N is in good agreement with the resultant impedance after manual abrasion, shown in figure 5.31. In both cases, the impedance is approximately constant between 1 Hz and 1 kHz at a value around 3 kΩ. This suggests that the automatic abrasion has matched the manual abrasion in the extent to which the outer resistive layer is removed. The impedance spectra after the automated abrasion demonstrates the same broad trend as that obtained after manual abrasion. The impedance at 20 Hz is approximately 500 Ω less after automated abrasion, so the prototype has met and exceeded the gold standard abrasion technique in terms of the resultant impedance.

The results from the test on the human forearm are similar to those obtained with the orange skin samples both in terms of the number of rotations of the electrode and the final impedance spectra. With abrasive paste each of the criteria was exceeded in terms of the final impedance, and the time taken. The final impedance, $\approx 1k\Omega$, was approximately a third of the values without paste and was obtained after only one whole rotation of the electrode. Without paste the target impedance is reached with 8 electrode rotations. However, the speed of rotation is much slower than the target 1 Hz, so this actually equates to nearly 40 seconds of abrasion, significantly longer than the 10 second target.

5.4.3 Technical considerations

The force control scheme was successful in maintaining the force applied normal to the surface to within ±0.24 N of the target force with the exception of 2 N which had an RMS error of 0.32 N. At this very low force the contact with the surface of the test sample was not as consistent, so there was more variation in force applied during rotation. Aside from this, the RMS error was close to or below the threshold of 0.2 N which suggests the control scheme was successful as could be expected.

There was substantial electrical noise induced by the DC motor at the PWM switching frequency in slip ring measurements shown in figure 5.18, and which would also be present during the impedance measurements. However this noise occurs at the PWM switching frequency and harmonics thereof, which in these experiments was set to 10 kHz, so they were out of band with the 20 Hz impedance measurements. There was also evidence of interference in the load cell measurements, even after grounding the load cell and test rig. To mitigate against any errors in the control loop, the load cell output was sampled at 1 k Hz and averaged across 10 samples, effectively filtering any potential noise. This could be further improved by shielding the electronics and the motor, but this was deemed unnecessary for the purposes of these experiments.

Work was undertaken to implement closed-loop control of the speed of rotation, however the rotation measurements were not of a sufficient resolution. The low rotation speed coupled with the coarse (18°) intervals meant that velocity calculations were not stable. Therefore the rotary actuation was executed in open-loop with respect to velocity. If closed-loop were deemed necessary then a codewheel of higher resolution would be required, which would necessitate a different encoder. Another method would be to place the codewheel on the motor shaft rather than the electrode spindle which, due to the gearing transmission (section 5.2.4) rotates 100 times faster. This would give a higher resolution position measurement, which would enable velocity to be calculated more accurately and thus it could then be used as a controlled variable in the controller.

The gear train used in the transmissions system was inefficient, which meant that much of the output power of the DC motor was lost. While this did not negatively impact the performance of the prototype, and there are no restrictions on the supply voltage and current to the motor at this stage, it is an important consideration for future designs. The transmission efficiency of spur gears is approximately 0.9 if correctly meshed [186], which gives an ideal efficiency of the entire transmission system of 4 gears $0.9^4 = 0.65$. During operation some shaft misalignment was clearly visible (and audible) so the efficiency of this system was likely below this value.

Using the impedance at 20 Hz as the controlled variable could introduce unwanted delays in the controller as several cycles are required for calculation. In the case of the prototype 3 cycles are required for a calculation of impedance, which for 20 Hz equates to an acquisition time of 0.15 s. Therefore the theoretical maximum frequency of the control loop is 6.67 Hz. Depending upon the control scheme, this may prove to be an undesirably low frequency. The impedance spectra (*e.g.* figure 5.43) show that frequencies up to approximately 200 Hz do not have dissimilar values to that at 20 Hz. Therefore it may be possible to use the impedance at this frequency in the control scheme and increase the loop rate by a factor of 10.

Two key elements required of the final miniature prototype are not present in this large scale prototype - it does not have electrode localisation, and there is no fail-safe/backdriveablity. Preliminary work was undertaken implementing electrode position feedback using a step counter for the motor position and converting the force measurement to a position through the spring constant k. However, they were not included in this study as the measurements were not required for abrasion. Also any implementation of the position measurement is highly dependent upon the design and other components in the design. As this preliminary design is not representative of the subsequent design in terms of scale or hardware, the position measurement system would not be readily transferable. Similarly with the implementation of a fail safe mechanism, the design is specific to the overall design and would require significant changes or complete redesign in the next stage. Inclusion of a fail safe system in this prototype has the additional complication that the force actuator is not backdriveable, which would not be the case in subsequent designs.

5.4.4 Future work: implications for future designs

Based on these results it is clear that the amount of electrode rotations has the greatest effect on the impedance decrease, the speed of rotation is not as important. The low rotation speed of the electrode causes difficulties when attempting to implement speed control. Therefore a position actuator would be more suitable, as the angle rotated can be controlled directly, and the position can be measured to a sufficient accuracy using encoders such as the one used in the prototype. The losses in the transmission system are undesirable in future designs as they increase the torque and power requirements which necessitate larger, heavier motors. Any gearing system designed for higher gear ratio such as a worm gear, often have lower efficiencies than spur gears so losses are inevitable. Therefore if the motor has sufficient torque output, the transmission system could be significantly simplified, thus reducing losses. The results from the experiments suggest the abrasion efficiency is independent of the applied force, thus the force does not need to be controlled as accurately as it is in this prototype. A force between 5 N and 10 N is sufficient to reach the target impedance within 10 rotations. Such a wide range of acceptable forces does not justify the added complexity of a force control loop. The tests on human skin show that abrasive paste should be used in future designs as it offers great benefits in terms of reducing the minimum contact impedance, and improving the abrasion efficiency. Reducing the number of rotations also has benefits in other areas of the design as it removes the need for complicated slip rings or other cable routing methods.

To follow on from this work, a miniature prototype should be designed which includes a simplified passive force provision, and a motor with shaft encoder for the position control. The torque output requirements can be estimated from the minimum torque to abrade based on estimations of the friction forces at the electrode-skin interface. The electrode size should be reduced as this is likely to aid access to the scalp through hair. Electrode materials with lower contact impedances, yet which still allow abrasive patterns to be machined easily should also be investigated. The test object used is idealised in that it is flat and does not have hair, and the effects these have on the performance of the prototype are not understood. Methods which allow abrasion of the scalp without removal of hair must be employed in the miniature design, thus research into these effects is necessary. Implementation of a fail safe mechanism an electrode position feedback system are also necessary tasks before the prototype can meet the specifications set out in section 5.1.1.

5.5 Conclusion

With reference to the questions set out in section 5.1.1, the following answers have been obtained:

1. **Does the prototype meet the specifications?** Yes, the contact impedance was reduced

below the threshold in sufficient time

2. **What are the optimum settings for:**
    - (a) **The applied force** Acceptable forces were 5 - 10 N
    - (b) **The speed of rotation** Does not affect abrasion thus can be any value provided threshold is reached within 10 seconds
    - (c) **The total angle rotated** Threshold can be met with less than 5 rotations
3. **What control strategy is needed? Open or closed loop, if closed which variables?** Force control loop unnecessary (with the exception of safety) as wide range of forces acceptable, closed loop with contact impedance as controlled variable only
4. **Is the finished design ready for use testing on human subjects? Or are there changes necessary?** Significant simplification and miniaturisation required before design is suitable for human testing.

Chapter 6

Self abrading servo electrode helmet for EIT measurements

6.1 Introduction

Self-abrading electrodes have been implemented successfully to reduce the contact impedance *in-situ* through manually operated rotation, section 1.4.3. The results from chapter 5 demonstrate that contact impedance can be automatically reduced through feedback controlled electromechanical rotation and force application. The experiments suggested that, given sufficient applied force, the contact impedance could be reduced to below 5 k Ω within only two complete rotations of the electrode. However, the test rig was designed to enable testing of each variable independently and was not suitable for testing on the scalp. Therefore the focus of the work within this chapter is the design, construction and validation of a miniaturised design which meets the minimum requirements found in section 1.4.3. The second focus of the work in this chapter was the design of a helmet housing 32 of the miniature electrode units, arranged according to the EEG 10-20 system. Finally, experiments were performed to assess the suitability of the helmet for EIT imaging of acute stroke and time difference imaging of epilepsy.

6.1.1 Background

Head sizes

Anthropometry is the measurement of the human body and quantification of the variations across populations [187]. Anthropometrical data has been used as the basis of ergonomic design in medical equipment as well as industry, clothing and architecture. The size and shape of the human head has been a subject of particular study for the design of helmets [188] and respirators [189]. In reality, the morphology of the human head is extremely complicated to describe accurately and is a perennial problem for designers [187].

The only truly successful quantification requires full 3D scans of a patient, which has been the focus of some military helmet designs [188], [189] but the data is not freely available. To combat these problems the Headspace project [190] at Alder Hey Childrens Hospital in Liverpool is generating an open-source database of accurate 3D scans of thousands of people. Unfortunately the data has yet to be collated and published at the time of writing. The most common methods of head measurement, using vernier calipers or tape measures, have been formalised by ISO 7250: "Basic human body measurements for technological design" [191].

The variations in sizes of the adult human head is such that designers of EEG caps, even those which are elasticated or otherwise conform to the shape of the head sell a wide range of sizes [192], [193]. Of the headnets tested by Tidswell, Bagshaw, Holder, *et al.* [78], EasyCap offer a range of five caps ranging from 54 to 62 cm circumference, and claim three sizes will cover 95 % of subjects [192]. Similarly Hydrodot offer a range of five sizes from 40 to 62 cm circumference for infants and adults [193].

To further understand the range of head sizes, a literature review was conducted of the results on anthropometric surveys. It was necessary to compare multiple sources in the literature because, despite the standardisation of measurements in ISO 7250, there was large variation between what measurements were taken as the results themselves. The majority of studies were carried out by military, [188], [189], [194], [195]. However, some large databases have been created of civilian populations covering a wider age range, the largest of which is DinBelg 2005 by Motmans and Ceriez [196], which forms the basis of the reference dimensions given in ISO 7250 [191]. The measurements are summarised in fig. 6.1. It is clear there is broad agreement between the studies, particularly in the measurements of breadth and length, with an average of approximately 146 and 190 mm respectively. The average of the circumference measurements was approximately 562 mm, with a a wider variation between studies. The likely reasons for which are that the measurements are more prone to error as they are collected using a tape measure, as opposed to a calliper, and that the circumference varies more with the *shape* of the head far more than the coarser measures of the maximum length and breadth.

Helmet applications

The main application for the helmet was to enable imaging of acute stroke with EIT in an acute setting such as an ambulance, section 1.5.1. It is not feasible for electrodes to be applied using the conventional EEG techniques [7] so an automated application process is required to enable EIT recordings. Thus the primary goal for the design of the helmet was to place the electrodes on the scalp in the correct positions and reduce the contact impedance to a level similar to that expected from manual abrasion. Specifically, <5 kΩ at below 100 Hz within 10 seconds per electrode.

Knowledge of the positions of the electrodes in space is important for reducing modelling

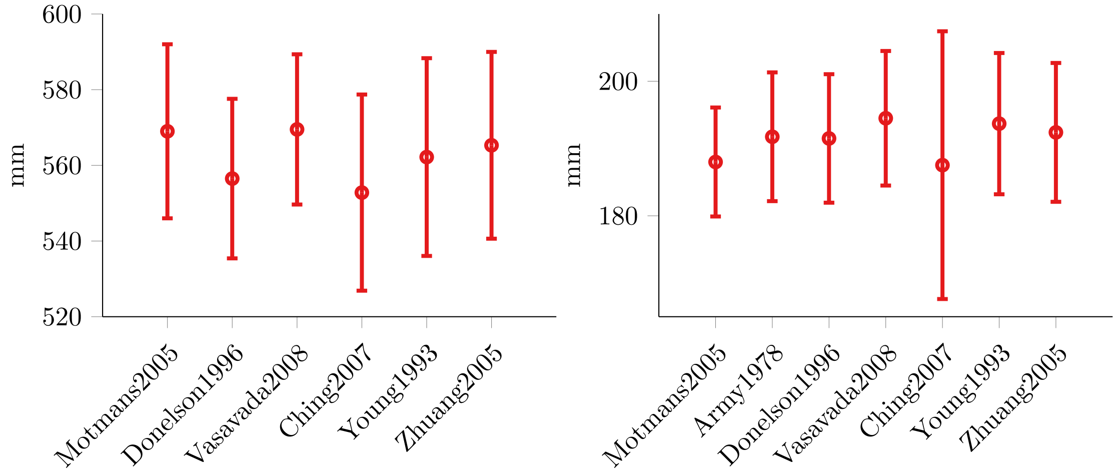

(a) *Circumference* **(b)** *Length*

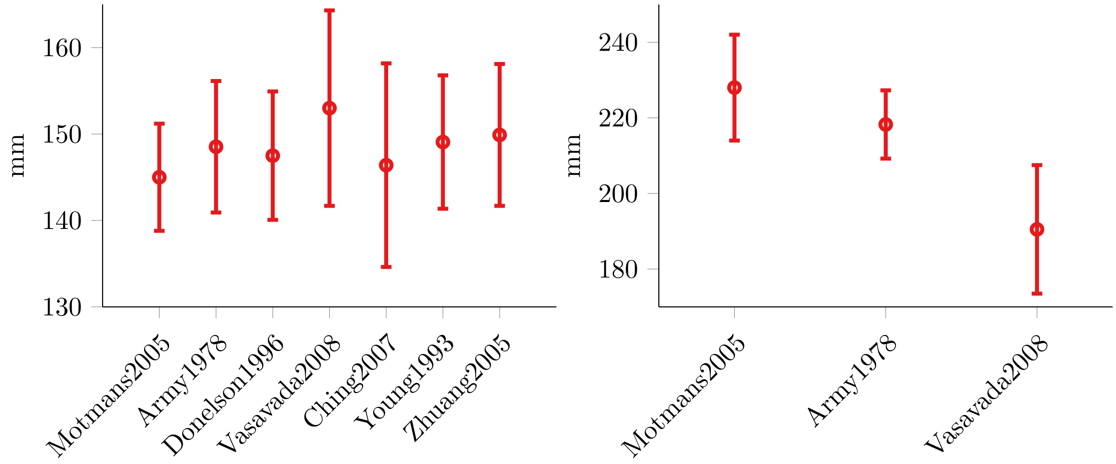

(c) *Breadth* **(d)** *Height*

Figure 6.1: *Comparison of mean and standard deviation of head measurements in anthropometric surveys*

errors [73]. Obtaining the 3D coordinates of the electrodes enables both positioning the electrodes on the mesh and for adjusting the geometry of the FEM to match the geometry of the patient. To this end, measurements of the travel of the electrode tips in relation to the body of the helmet, were used to locate the electrodes. The accuracy of 0.5 - 2 mm achieved in previous experiments using photogrammetry was the target precision for the helmet design.

The secondary application for the helmet was long term monitoring of epileptic activity with time difference EIT [58]. In this case the emphasis is on reduction of the slow changes over time, section 1.4.2, as opposed to rapid electrode application. Measurement drift, identified by Fabrizi, Sparkes, Horesh, *et al.* [30] as the critical factor limiting successful image reconstruction of long term scalp recordings. These drifts must be minimised if the improvements in imaging epileptic seizures demonstrated in chapter 4 are to be realised clinically. Therefore, control of the contact impedance over time was desirable, potentially enabling successful time difference imaging in a telemetry ward.

6.1.2 Purpose

The purpose of this study was to design and test a helmet bearing 32 self abrading servo electrodes to rapidly reduce the contact impedance on each electrode automatically. A successful proof of principle of the helmet design would constitute a significant step towards enabling imaging of acute stroke in an acute setting, such as an ambulance.

The secondary application of this helmet was for long term monitoring of epilepsy or intracranial haemorrhage, which required not only a rapid reduction of the contact impedance, but also a reduction of the measurement drift. Therefore, the performance of the electrodes over longer recordings was also investigated.

6.1.3 Experimental Design

The electromechanical requirements for each electrode unit were identified in chapter 5, but the design required significant miniaturisation and the PC controller was not scalable to 32 electrodes. The design was simplified to include a single motor to control the rotation only, with force passively applied through compression of a spring potentiometer, which also provided the positioning information. This simplified design was tested using the test rig created in chapter 5.

A controller based on the Arduino Due [162] platform was then designed which could serially control each of the 32 electrodes using contact impedance as the process variable. The performance of the impedance measurement circuit, position sensing and servo motors were each validated in the test rig and also in a simplified array of four electrodes applied to the leg. These results were used to confirm the performance of the electrode unit and controller before design of the 32 channel system.

A helmet was designed based on a reference CAD model scaled to match the average dimensions described in section 6.1.1, and constructed using a 3D printer. The electrode units were arranged in the same distribution described in section 2.2.2, a modification of the locations used in previous studies [53]. 32 electrodes were then constructed and incorporated into the helmet. The final experiment was a validation of the completed helmet on the scalp of a single subject.

6.2 Methods

6.2.1 Electrode Unit

A simplified self abrading servo electrode unit, fig. 6.2a, was designed based on the conclusions drawn from the experiments in chapter 5, which consisted of a electromechanical rotary actuator and passive force provision. The abrasion was achieved through a single motor with a rotation range of 180° which would oscillate around the central position, with a plain bearing at the opening into the helmet to maintain concentricity, fig. 6.2b. Thus the wiring to the electrode and position sensor could be connected directly without the need for a slip ring, section 5.2.6. The force was applied to the scalp through the spring inside the linear potentiometer. The compression of the spring also translated the contact wiper inside the potentiometer X_P, from which it was possible to obtain the position of the electrode along the axis of rotation X_E. The electrodes were then placed in a rigid helmet where the reference positions X_S were known with high precision *a priori*. Therefore, when placed on the scalp fig. 6.2d, the positions of the electrode tips could be calculated from the single potentiometer measurement. Each of the units were self contained individual 3D printed casings fig. 6.2e, which enabled simple replacement or transfer of the units.

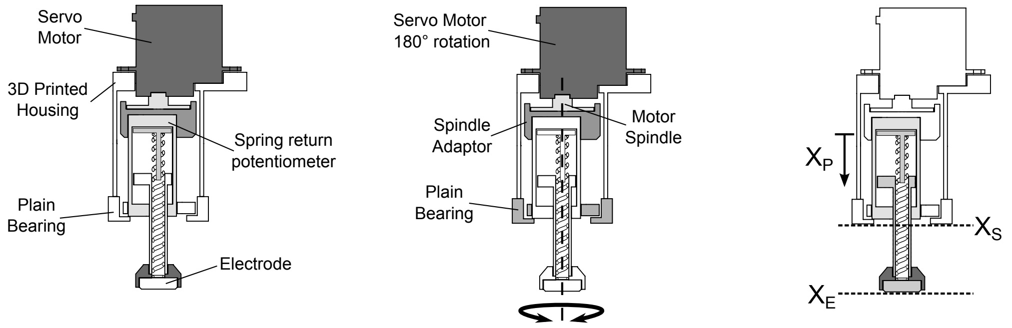

(a) *Overview* **(b)** *Rotation* **(c)** *Position Feedback*

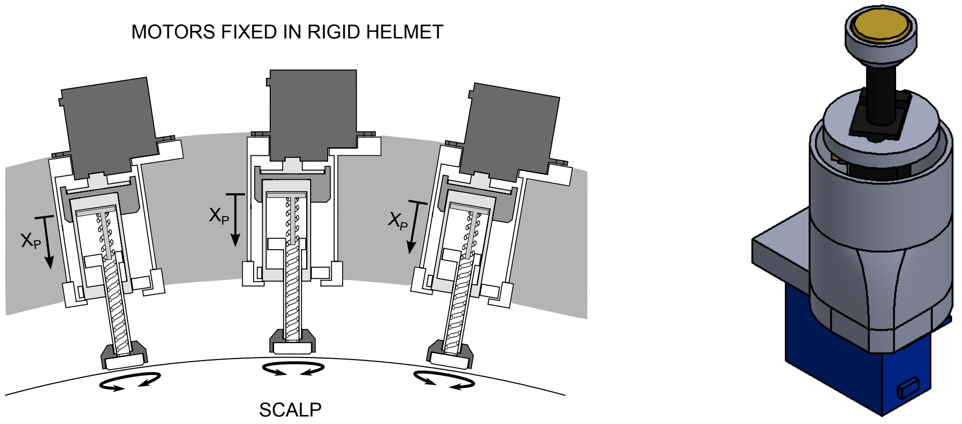

(d) *Helmet* **(e)** *Complete Unit*

Figure 6.2: *Miniaturised servo electrode unit.* ***(a)****, overview of components,* ***(b)*** *concentric rotary actuation via servo motor with pain bearing and plain bearing,* ***(c)*** *feedback of electrode position* X_E *through measurement of displacement* X_P*,* ***(d)*** *units placed in rigid helmet at known positions,* ***(e)*** *isometric view of complete unit*

Motor

To further simplify the design of the unit, a servo motor fig. 6.3a was employed as the rotary actuator. Servos are motors with incorporated position feedback and control, with all controlling electronics in the same housing [197]. Using an incorporated "off-the-shelf" servo such as this, removes the need for design and validation of the gear train, rotary encoder and control circuitry. The motor chosen for this design was the "Tower Pro MG90s", a common hobbyist level servo comprised of a DC motor, metal gear train, rotary potentiometer and position controller.

(a) *Servo* **(b)** *Position sensor*

Figure 6.3: *Off the shelf components adapted for electrode unit,* ***(a)*** *Tower Pro MG90s Servo Motor,* ***(b)*** *BEI 9605 spring return linear position sensor*

The MG90s has a rated maximum torque of 0.22 Nm which is less than the 0.3 - 0.4 Nm minimum torque required to abrade, fig. 5.40 found in the previous chapter. However, the friction expected at the electrode interface is less with the miniature design, as the area of the electrode is less than half, and the inclusion of paste significantly reduces the coefficient of friction μ. The stall torque of the motor was verified using the methodology in section 5.2.7, and was found to vary from 0.203 to 0.234 Nm across a range of 10 motors. The entire weight of the servo inclusive of motor, gears and controller was 14 g.

Position sensor

The position sensor used in the electrode unit was a 9605 spring return linear position sensor, fig. 6.3b from BEI Sensors [198], which is effectively a spring loaded potentiometer. Movement of the actuator compresses the internal spring and adjusts the position of the wiper on the resistive strip. Therefore the voltage across the wiper gives a measure of the distance travelled, from which the force can also be calculated using the spring constant k.

The 9605 potentiometer has a travel of 13 mm and a rated linearity of 0.5 % across the travel range. To confirm these results, calculate the spring constant and the range of forces applied across the range of travel, a characterisation experiment was performed using the test rig fig. 5.4 and a laser displacement sensor (LDS) (optoNCDT 1607, micro-epsilon, UK), fig. 6.4. The 9605 was attached to the spindle of the stepper motor using via a 3D printed holder, which also served as a target for the LDS. The spring was then advanced onto the load cell whilst voltages were recorded from the LDS, potentiometer and load cell simultaneously with a Labview DAQ. The process was repeated 10 times to determine the repeatability error.

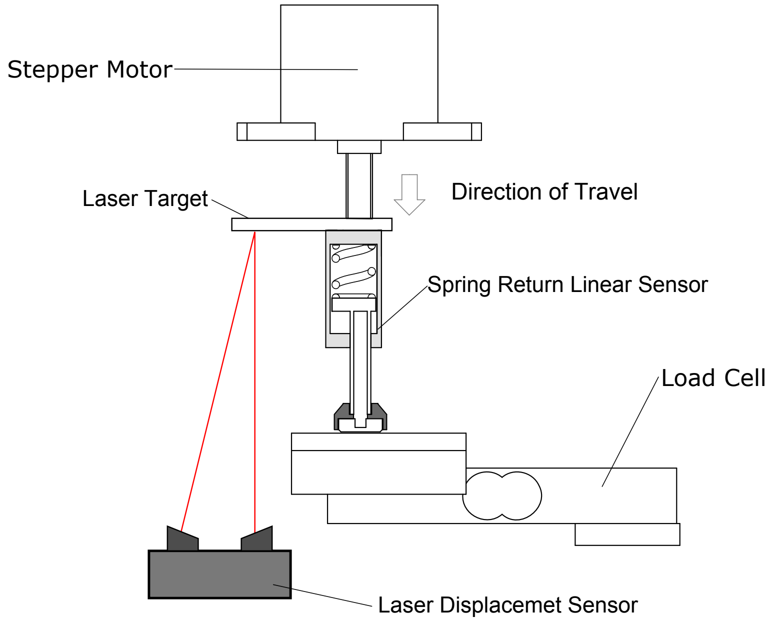

Figure 6.4: *Characterisation of spring return linear sensor. Stepper motor advances to compress spring onto load cell. Measurements of displacement obtained from laser displacement sensor*

The experiment demonstrated the potentiometer had a low repeatability error , fig. 6.5a, with a maximum of 0.78 % across the complete travel, just above the rated value. Thus the maximum error expected in the position measurements of the electrodes is ≈ 0.5 % of the travel or 0.1 mm.

Some fluctuations in the applied force were observed, fig. 6.5b, which are a result of the stiction of the potentiometer wiper. The spring was preloaded with a force of 0.5 N measured at 0 mm travel. The maximum force applied at full compression was 4.6 N, which for an electrode of 10 mm diameter equates to a pressure of 28.6 kPa, close to the maximum used in chapter 5. Thus adequate force is applied for ideal abrasion for over half of the travel of the electrode.

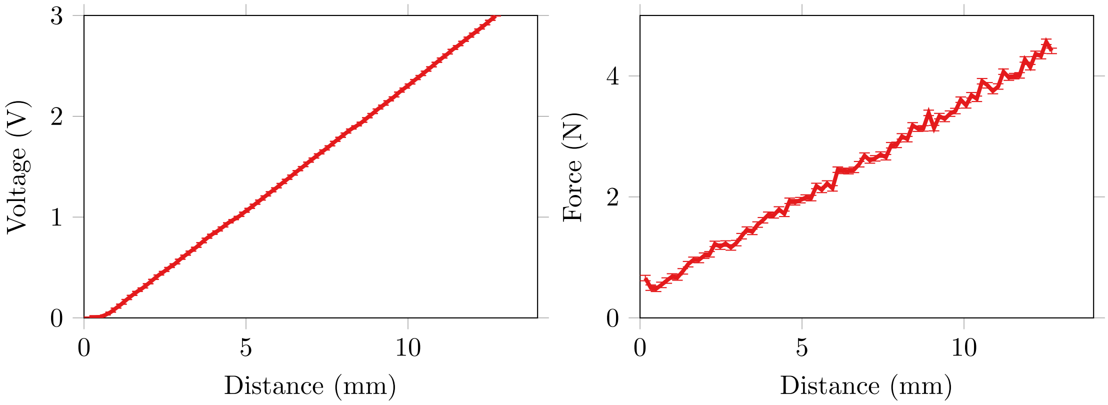

(a) *Circumference* **(b)** *Length*

Figure 6.5: *Characterisation of spring potentiometer, **(a)** voltage across compression mean±std, **(b)**, force as function of distance mean±std*

Electrode

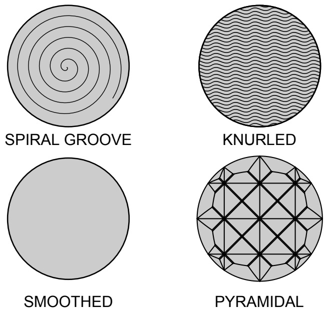

Figure 6.6: *Abrasive electrode patterns*

The results from chapter 5 demonstrated that the most efficient abrasion was achieved with a combination of pyramidal pattern and abrasive paste. A prototype miniaturised electrode with a pyramidal pattern was created using a CNC machine fig. 6.6, however during preliminary testing it was found to cause discomfort after only a few minutes after abrasion. Therefore a controlled study was required to ascertain if effective abrasion could be achieved with a simpler design, section 6.2.4. The results from the control study, fig. 6.20 demonstrated effective abrasion could be achieved through abrasive paste and a smoothed electrode. Therefore, the smoothed electrode was chosen as the design for future design iterations and experiments.

The electrodes were constructed from 10 mm diameter 316 stainless steel, with a 0.5 mm chamfer on the edge in contact with the subject. This material was chosen as opposed to Ag/AgCl based on the same considerations outlined in section 2.2.5, namely practicality and durability, and the potential damage of sintered Ag/AgCl via abrasion. The electrode diameter was decreased compared to one used in the test rig in chapter 5, to match those of commonly available EEG electrodes [7].

The electrode was wired to the controller via the spring within the potentiometer, fig. 6.7. The electrode fastened into the adapter using an interference fit, which compressed the spring directly onto the back of the electrode. A wire which protruded out of the potentiometer into the central body of the unit was glued to the base of the spring using silver epoxy. This wire then passed out of the main body of the unit through an opening next to the servo motor.

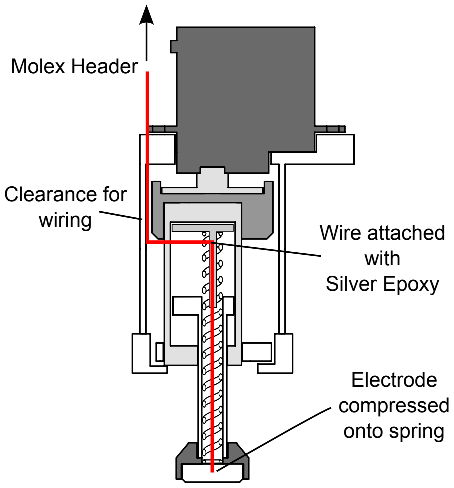

Figure 6.7: *Wiring path to electrode*

Construction

Construction of the electrode unit required modification of the potentiometer and printing of custom components. The end of the spring potentiometer actuator was cut and filed to a flat surface. Which allowed for the electrode adaptor to sit aligned with the direction of travel and was subsequently glued with epoxy. Three wires were soldered onto the contacts to the potentiometer and passed out of the body of the unit using the same path as the electrode wiring, fig. 6.7. The electrode was then placed within the adaptor using an interference fit. The potentiometer was then connected to the spindle of the servo motor via a 3D printed adaptor and the complete unit placed in an individual housing. The mass of the complete electrode unit inclusive of all 3D printed adaptors and housings was measured as 31.4 g.

6.2.2 Controller

As with the electrode design, the controller used in the test rig could not be feasibly scaled to 32 channels, and thus required miniaturisation. The overall strategy of the controller, fig. 6.8, was to employ a single controller based on the Arduino platform and small sub-controllers for the servo motors and potentiometer measurements, and a single multiplexed impedance measurement circuit. This strategy reduced the number of additional wires sent to the helmet,

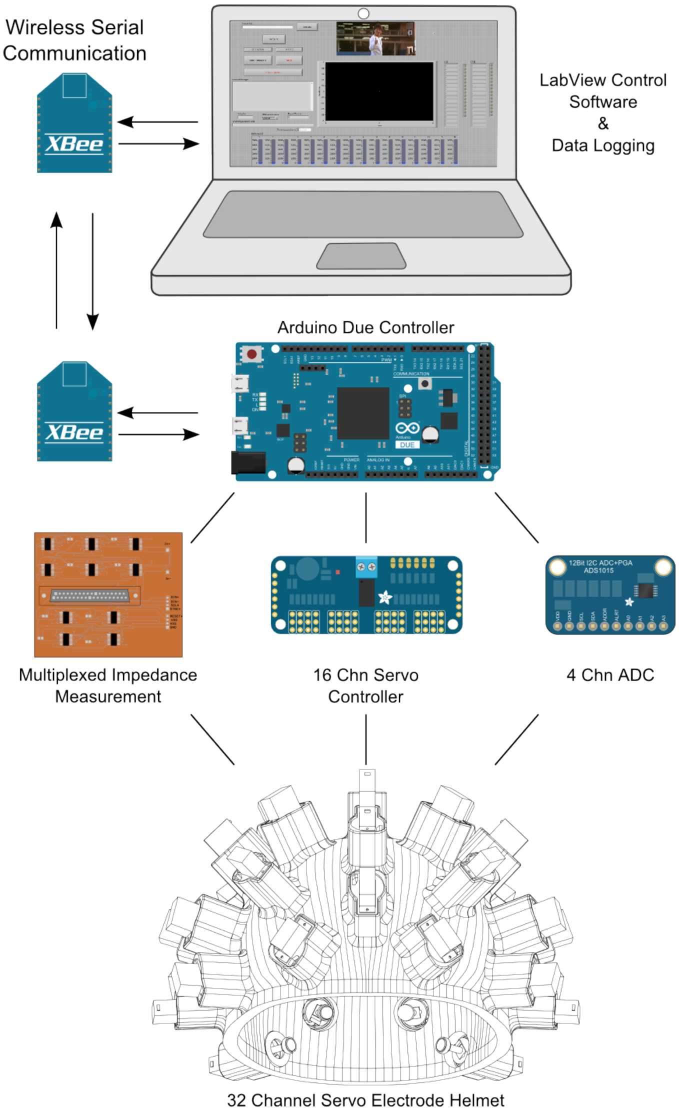

Figure 6.8: *Overview of helmet controller. Labview software controlling Arduino Due through wireless serial communication. Ardruino controls impedance measurement, servo rotation and electrode position measurements*

three for power and three for the I2C communication. The Arduino controller was battery powered, and isolated via wireless serial communication.

The impedance control loop was a simple on/off controller with a deadband of 2 % to prevent limit cycling, section 5.2.3. The initial target impedance was 5 k Ω. If this impedance was not achieved within 10 rotations, the abrasion was stopped, and the target impedance for subsequent iterations was set to the lowest impedance measured during initial abrasion.

Servo Control

Servo motors are controlled by Pulse Width Modulation (PWM). The inbuilt controller maps duty cycles from 0 to 50 % to the minimum and maximum angles of rotation. Whilst generating these pulses is simple with the Arduino, problems would arise scaling the circuit up to 32 channels whilst keeping the weight to a minimum. Therefore control of the servo motors was achieved using the Adafruit 815 16-Channel 12-bit PWM/Servo Driver, fig. 6.9 which is based on the PCA9685 PWM chip from NXP Semiconductors. Two Adafruit 815s were daisy chained together on the same I2C bus and employing the corresponding Arduino library, the servos could each be separately controlled, without considerable wiring.

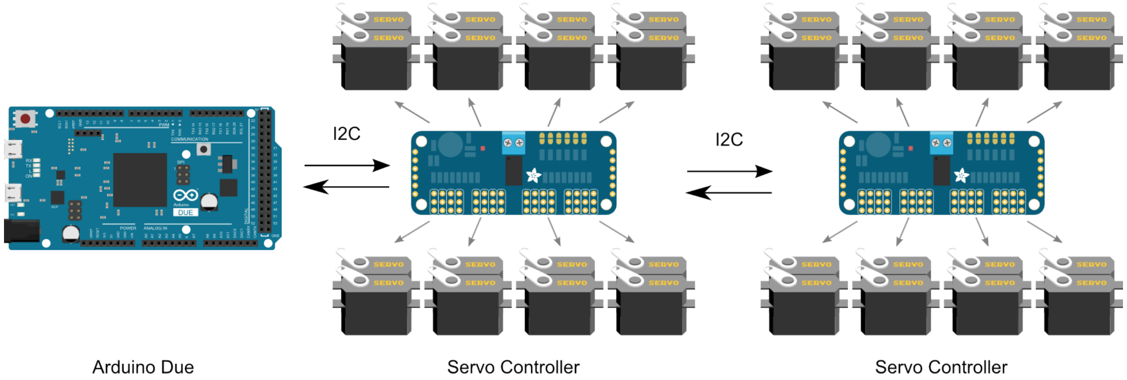

Figure 6.9: *Control of 32 Servos using PCA9685 breakout boards*

To limit battery drain the power to the servos was switched off when not in use using a high side p-channel MOSFET switch. The servo controllers were placed in 3D printed housings, fig. 6.10, which were subsequently attached to the helmet.

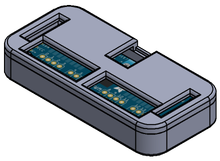

Figure 6.10: *Adafruit 815 servo controller in 3D printed casing*

Position sensing

Daisy chained breakout boards were also implemented to measure the voltages across each of the potentiometers. The Adafruit ADS1015 12-Bit ADC is a breakout board for the the 4-Channel ADS1015 ADC from Texas Instruments. Eight of these breakout boards were daisy-chained together on the same I2C bus used for the servo controllers.

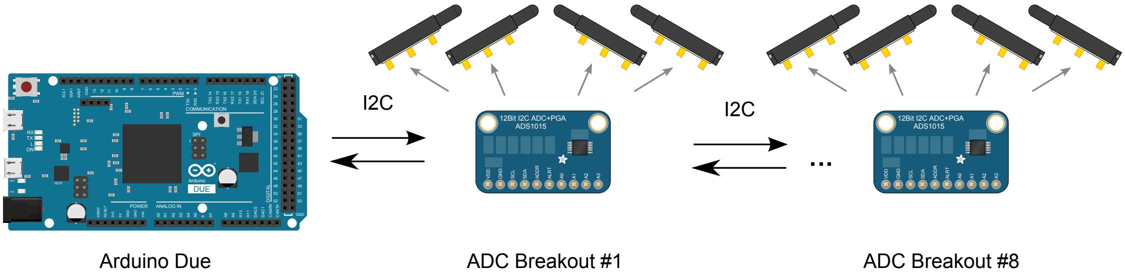

Figure 6.11: *Control of 32 Servos using PCA9685 breakout boards*

Initial position measurements were averaged over 1000 samples for each electrode. During the “idle” state, the positions were re-sampled every second, and the user was warned if any large changes were detected.

Impedance measurement

The simple impedance measurement circuit used in chapter 5 was adapted for use with the Arduino Due, fig. 6.12. As the Arduino could only supply and measure voltages between ground and +3.3 V, the 1 V amplitude sine wave signal was generated using the on-board DAC with a 1.65 V DC offset set in software. This DC bias was removed with a DC blocking capacitor before the electrodes. A bias voltage was then added to the voltages $Vknown$ and $Vload$ at the input to the Arduino ADCs. MOSFETs were used to discharge all capacitors to ground between measurements.

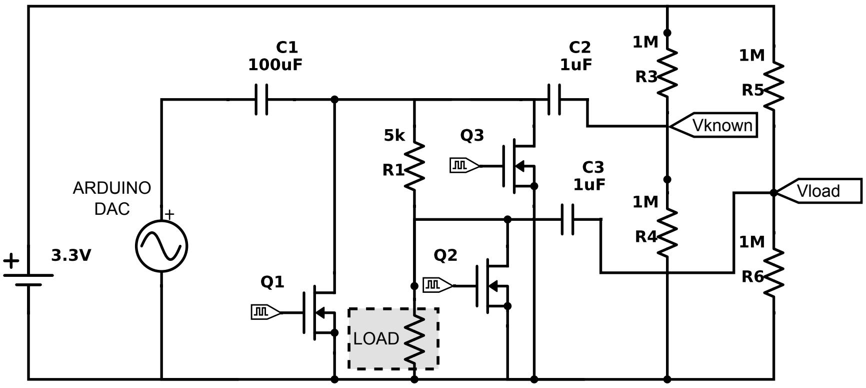

Figure 6.12: *Impedance measurement circuit for helmet controller*

Impedance measurement at 20 Hz was identified as the limiting factor in the speed of the control loop, chapter 5, but the low sampling rate of the impedance measurement loop precluded increasing the measurement frequency. Writing a value to the DAC and reading the voltages Vknown and Vload took $\approx 90\ \mu$s, which was fixed at a constant rate for 100 μs for stability. Therefore a single 20 Hz period could be represented by 500 samples, whereas only 100 were possible for a 100 Hz wave. Measurements on a 10 k Ω resistor demonstrated that a decrease in SNR as a consequence of a lower number of samples masked the benefits of shorter measurement time, fig. 6.13. A single period at 20 Hz had a lower standard deviation that the average of 15 100 Hz cycles. Thus 20 Hz was maintained as the frequency of interest for impedance measurements.

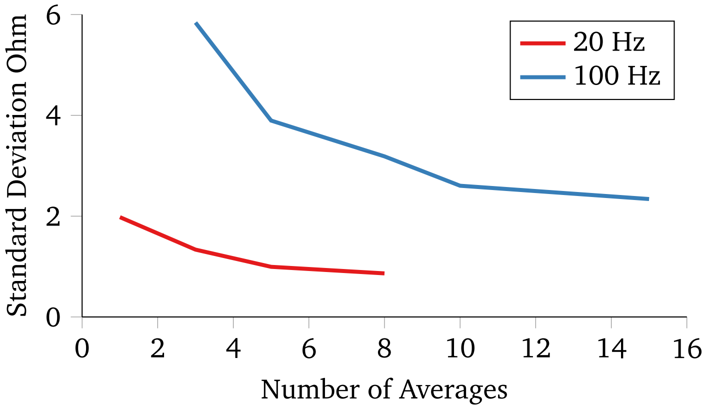

Figure 6.13: *Standard deviation of impedance measurement for frequency of 20 and 100 Hz for increasing number of periods averaged*

The voltages recorded were band passed filtered with a 3rd order Butterworth filter using the "Direct Form 2 Transposed" implementation [199]. The filter coefficients were initialised based on the methods outlined by Ream [199] to reduce edge artefacts. The filter was then reversed, to correct phase distortions. The amplitude of each sine wave was determined by the root mean square of the filtered signal. Finally, the impedance was again calculated from the ratio of the two voltages:

$$Z_{load} = \frac{V_{load} R_{sense}}{v_{known} - V_{load}}. \tag{6.1}$$

The accuracy of the impedance measurement circuit was testing on a single channel with range impedances from 10 to 1 M Ω, with 10 repetitions for each measurement. The error in the measurements, fig. 6.14, was less than 1 % from loads between 100 and 50 k Ω, the maximum noise recorded within this range was a standard deviation of 1.2 %. Thus the performances of this simplified circuit is similar to that of the impedance measurement circuit used in the test rig, despite the fewer averages and lower resolution ADC.

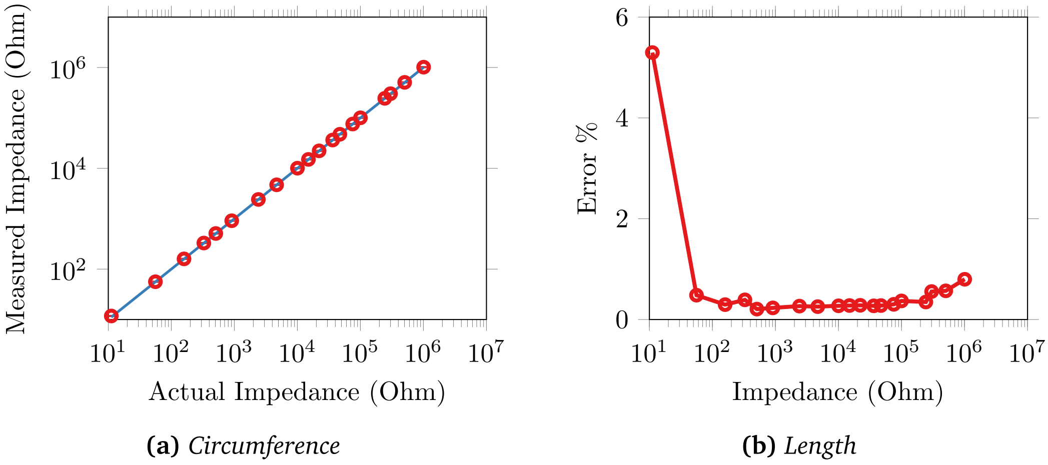

(a) *Circumference* **(b)** *Length*

Figure 6.14: *Validation of impedance measurement circuit based on Arduino Due.* ***(a)****, mean±std across expected measurement range compared to ideal,* ***(b)*** *percentage error*

Multiplexing and ground electrode The switch network designed for the UCL Scousetom [125], fig. 3.15, was used to address each of the electrodes on the helmet. Impedance measurements were collected with respect to a shared reference electrode, separate from the ground electrode of the EIT system. A traditional EEG Ag/AgCl electrode was used to minimise the contribution to the contact impedance measured and provide a stable reference over time so as not to mask the behaviour of the electrodes under test.

Four channel system

A holder was designed and 3D printed to house four electrode units in a linear array for testing on the shin. The holder was held in place with an elasticated bandage, which was adjusted to compress the electrodes to approximately 75 % of the full travel, or 10 mm.

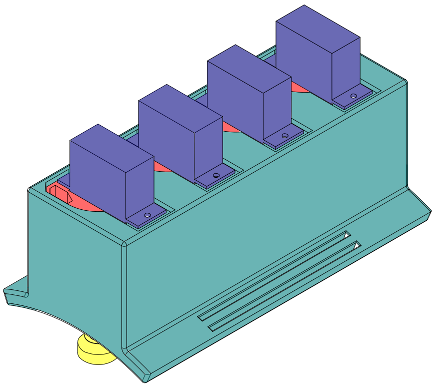

Figure 6.15: *Housing for four electrode units for testing on the shin*

6.2.3 32 Channel Helmet

Head Model

The basis of the helmet design, was a high quality, smoothed CAD model from Kappelhoff [200] created as an anthropometric reference for designers and architects fig. 6.16. The model was first scaled such that the length and breadth matched the average size as found in section 6.1.1, 189 and 146 mm respectively. The resultant circumference was 549 mm, which underestimated the average circumference as found by Motmans and Ceriez [196] by 20 mm. This was likely a result of the smoothing and lack of hair in the CAD model.

Electrode Placement

To correctly locate the electrodes in the helmet, the procedure described in section 2.2.2 which replicated the EEG 10-20 placement strategy was repeated. This provided an even coverage of the scalp, fig. 6.16 and also adequate spacing for all electrode units.

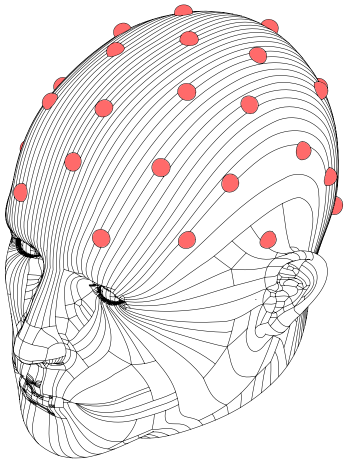

Figure 6.16: *Visualisation of the positions of the electrodes in the helmet on the reference model*

Helmet Model

The methodology of the design of the helmet model, fig. 6.17 was similar to the workflow developed for construction of the realistic head tanks, section 2.2.3. First, the reference model was trimmed below the inion-nasion plane, and the resultant surface was offset by 10 mm to provide the inner surface of the helmet. The helmet shell was then created through the combination of a further 10 mm offset surface. Vectors normal to the exemplar scalp model at each of the 32 electrode points, fig. 6.16, were created as references axes for alignment of electrode housings. As there were no constraints regarding the orientation of the electrode units, they were angled to reduce the support material and subsequent post processing required during and after 3D printing.

To create the housings for the electrodes, solid blocks were combined with the solid model through boolean addition. Then a positive mould of the central bore and motor keyslot were was subtracted from the model, fig. 6.17c, completing the frame.

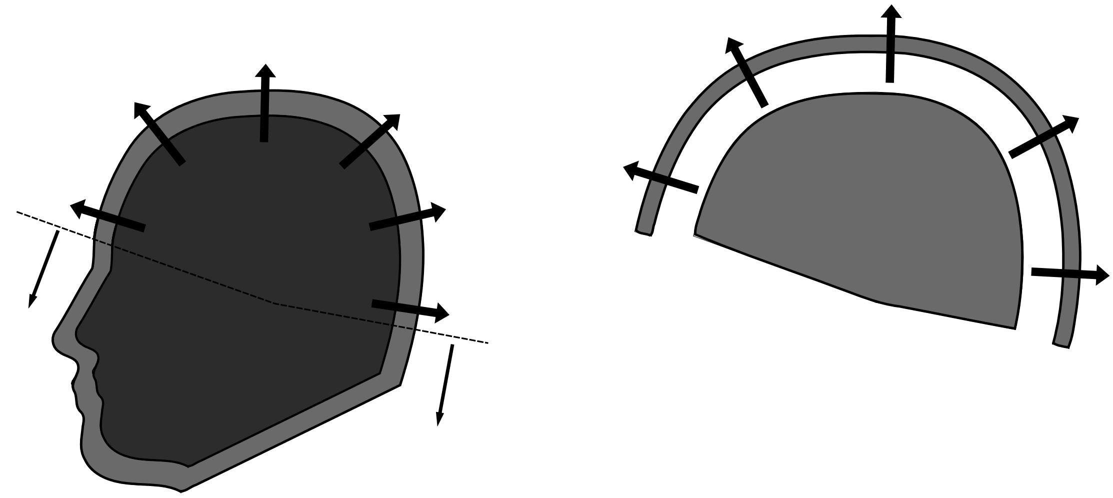

(a)

Head model is scaled and trimmed

(b)

Helmet created from reference head shape offset by 10 mm

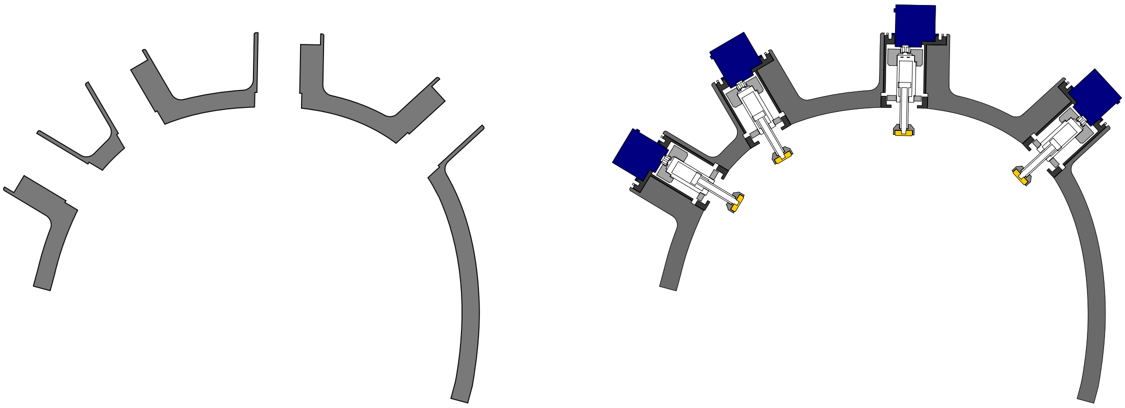

(c)

Electrode blocks and spacers added through boolean operations

(d)

Electrode units added

Figure 6.17: *Design of electrode bearing helmet* ***(a)*** *the scalp model is scaled to match the nominal head dimensions section 6.1.1 and model trimmed below in inion-nasion line,* ***(b)*** *helmet frame constructed from 10 mm offset of nominal scalp surface,* ***(c)*** *electrode blocks are added to model and spacers then removed to create housings for each electrode unit aligned to the points in fig. 6.16,* ***(d)*** *electrode units added to complete model*

Given the offset of 10 mm from the reference surface and a travel of each electrode unit is 15 mm, the helmet covers a wide range of potential head sizes, fig. 6.18. Over a standard deviation of the breadth and lengths are within the potential range of the helmet, whereas a narrower range of circumferences are represented.

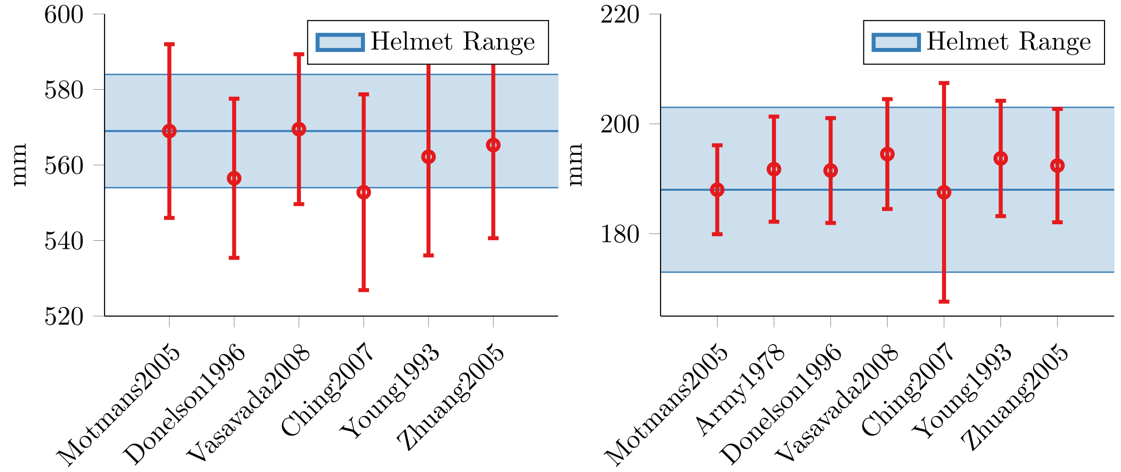

(a) *Circumference* **(b)** *Length*

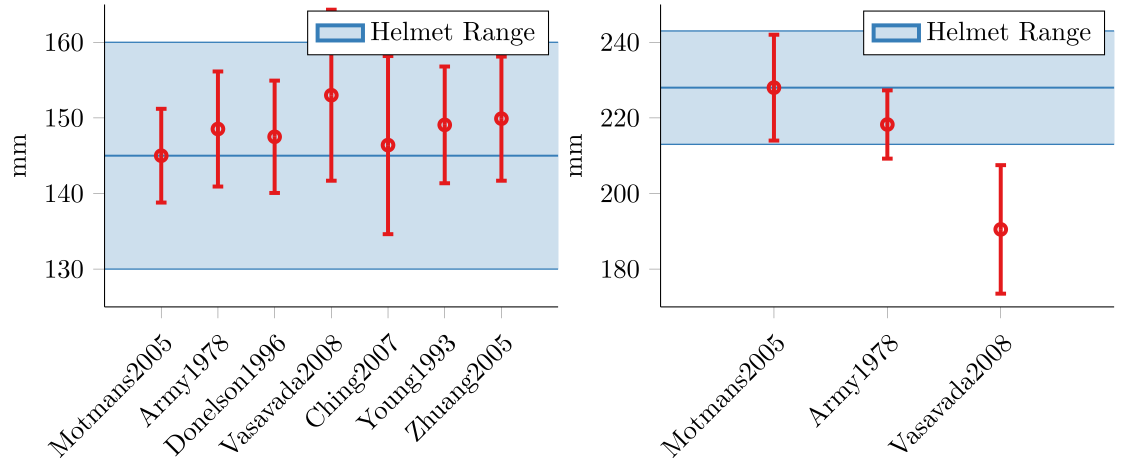

(c) *Breadth* **(d)** *Height*

Figure 6.18: *Comparison of mean and standard deviation of head measurements in anthropometric surveys*

Construction

As the completed helmet model, fig. 6.19, was larger than the maximum dimensions of the 3D printer (section 2.2.3), the model was then divided into four parts, with fastening features along each join. Each part was then printed using 10 % infill to minimise the weight of the helmet, and the support material trimmed. The cleaned parts were then slotted and bolted together to complete the helmet frame. The mass of the completed helmet frame was 604.2 g.

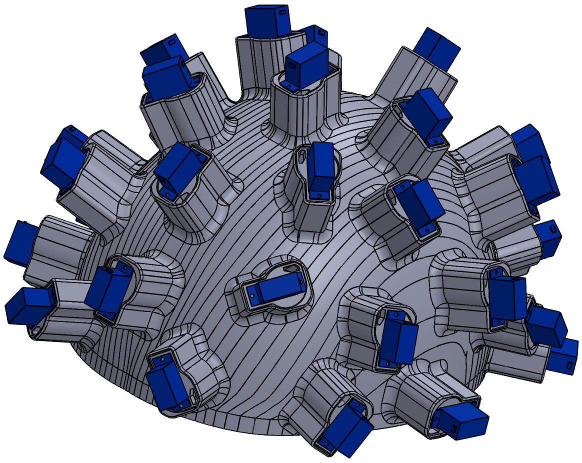

Figure 6.19: *Final helmet model inclusive of electrode assemblies*

32 electrode units, section 6.2.1 were then constructed and inserted into the helmet. The two servo controllers, fig. 6.10, and the eight ADC breakouts were attached to the helmet inside the 3D printed casings. Finally, the helmet was completed with an attachment of a 37 pin DSUB connector for the electrodes and a 9 pin DSUB connector for the servo and potentiometer wiring were housed at the posterior of the helmet.

6.2.4 Experimental Protocol

Single Unit

The experiment on the human forearm section 5.2.8, was repeated with the newly designed single electrode unit. The electrode was compressed onto the skin at 75 % of the maximum travel, equivalent to 3.45 N or 21.4 KPa. Abrasion was performed with a plain electrode, and a pyramidal patterned electrode, both with abrasive NuPrep paste.

Four Channel System

To further validate the design of the electrode units, abrasion was performed using the four electrode system on positioned on the shin of a subject aligned with the tibia. The elastic bandage was tightened such that each of the four electrodes reported $\approx$ 85 % compression, and a EEG ground electrode was positioned on the calf. Abrasion was performed with the application of NuPrep abrasive paste, and also with the addition of a layer of EleFix conductive Gel. The experimented was repeated three times for both cases on the same subject on different days, and the results presented as a mean and standard deviation.

A four channel long term recording was also collected on the shin to directly compare the measurement drift of the actuated electrodes with conventional EEG cup and paste electrodes.

The third and fourth channels on the actuated system were replaced with two EEG electrodes which were manually abraded with NuPrep paste. EEG conductive paste was added for a single channel. Measurements were collected over the course of half an hour, with the impedance control loop reactivated every 30 seconds.

32 Channel Helmet Measurement

Finally, the complete 32 channel helmet was tested on the scalp of a 27 year old volunteer. Before placement of the helmet, a ground EEG electrode was placed on the nasion of the subject with conductive EleFix gel. The skin which had previously been abraded with NuPrep paste to reduce contact impedance. Abrasive NuPrep paste was then applied to each electrode on the helmet, and positioned on the scalp of the subject. The abrasion routine was then activated for each electrode in turn. The results were expressed as a mean and standard deviation across all channels. Finally, the minimum impedance during the initial abrasion as a function of electrode position was calculated and averaged into 0.5 mm bins.

6.3 Results

6.3.1 Single Unit

Abrasion with a single unit on the forearm, fig. 6.20, was similarly effective with both a pyramidal and smoothed electrode. Both electrodes achieved a contact impedance less than 8 kΩ after one rotation. After two complete rotations, the pyramidal electrode continued to decrease the contact impedance, whereas no further significant decrease was observed with the smoothed electrode.

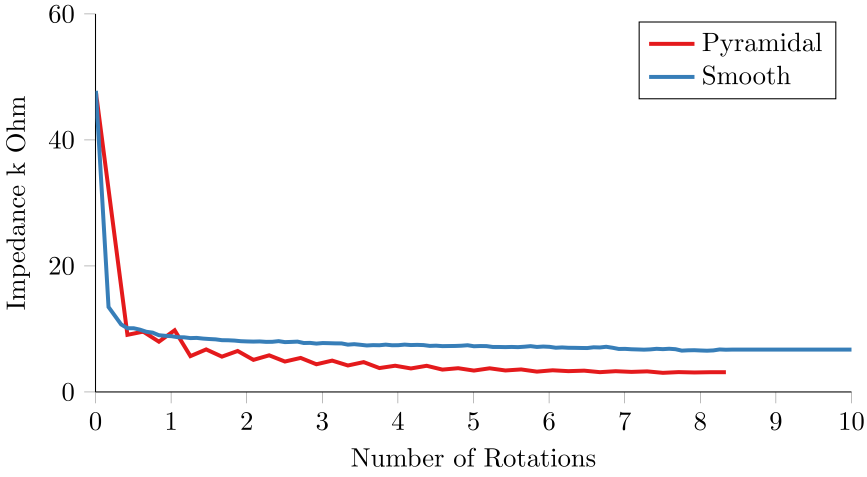

Figure 6.20: *Abrasion with single miniature unit on orange skin test rig, for both pyramidal electrode as in chapter 5, and smoothed electrode*

6.3.2 Four channel system

The four channel system reduced the contact impedance rapidly using the NuPrep paste only, decreasing the impedance by 25 kΩ to 6.7 kΩ with one half rotation, fig. 6.21. Only a further reduction of 1.3 k Ω was achieved with the remaining four complete rotations, with a minimum of 5.4 kΩ. The addition of a layer of conductive Elefix paste between the electrode and NuPrep abrasive reduced the initial impedance by 12 kΩ but reduced the efficiency of the abrasion, achieving a minimum impedance of 8.1 kΩ.

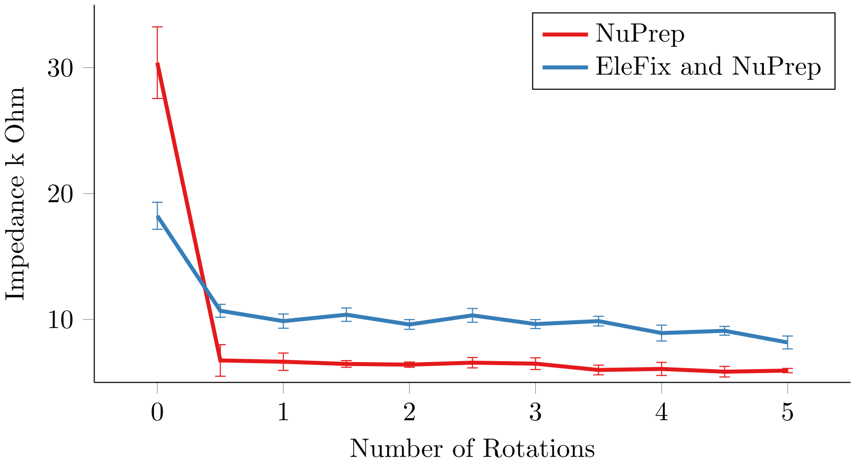

Figure 6.21: *Abrasion with four channel system with application of abrasive Nuprep paste and with EleFix EEG gel and Nuprep paste*

During the half hour recording the abrasion was continuously reactivated for the actuated electrode with NuPrep only, fig. 6.22, whereas it was not repeated beyond the initial application with the addition of the EleFix. In each instance, only an additional half rotation was required to reduce the contact impedance to its previous minimum. The impedance of both the actuated electrodes decreased over the course of the experiment, despite no additional abrasion in the case of the EleFix and Nuprep electrode.

The impedance of EEG electrode with NuPrep linearly increased over the course of the recording from 3.91 kΩ to 4.35 kΩ. The EEG electrode with the conventional combination of NuPrep and EleFix was more stable over time, with an increase of only 100 Ω from the inital 2.3 k Ω.

6.3.3 32 Channel Helmet

The contact impedance was successfully reduced through automated abrasion on all 32 electrodes, within five complete rotations or nine seconds. The entire abrasion routine was completed in 4.6 minutes. In all cases the largest decreases occurred within the first complete rotation, and comparatively little contact impedance decreases in subsequent rotations. In

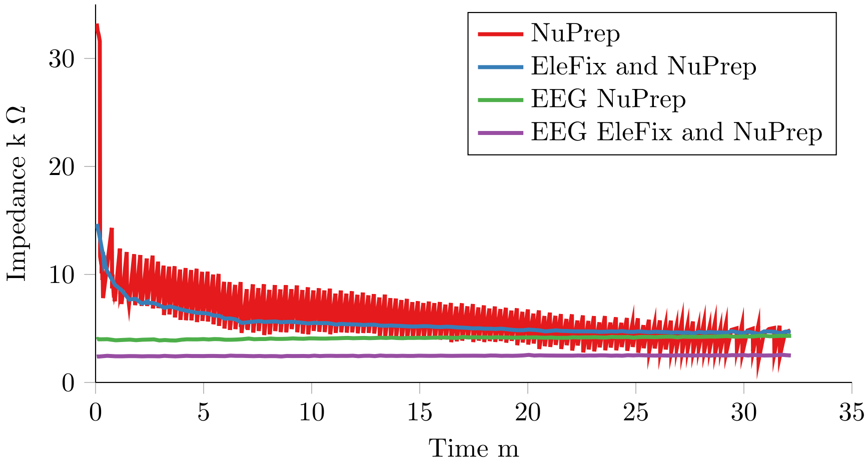

Figure 6.22: *Long term recording with four channel system, with two actuated electrodes and two conventional EEG electrodes, application of abrasive Nuprep paste and with EleFix EEG gel and Nuprep paste only*

general the impedance was reduced to approximately 8 kΩ or less for all electrodes, fig. 6.23. There was however, considerably larger variation between channels than that observed in the measurements on the leg, fig. 6.21.

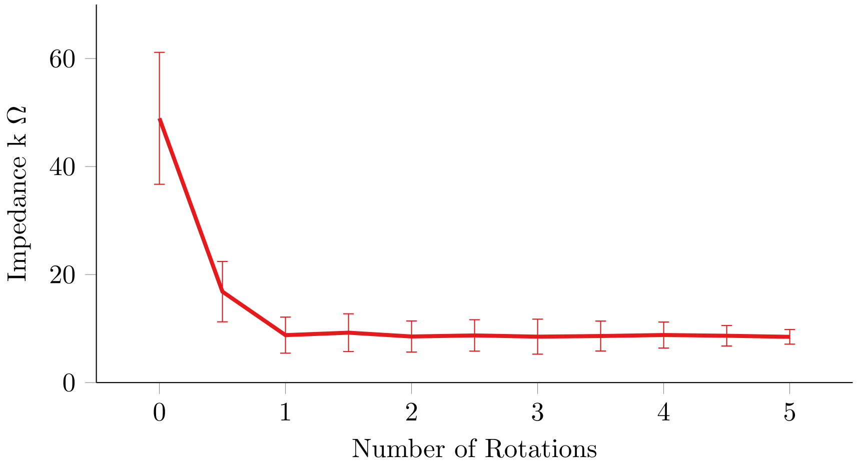

Figure 6.23: *Abrasion with 32 channel helmet on the scalp*

The minimum impedance achieved was strongly dependent upon the compression of the spring, fig. 6.24. Abrasions at locations where the spring was compressed by 2 mm or less, were significantly less effective. Beyond 8 mm, or ≈ half the potential force applied, there was little improvement in the minimum impedance achieved.

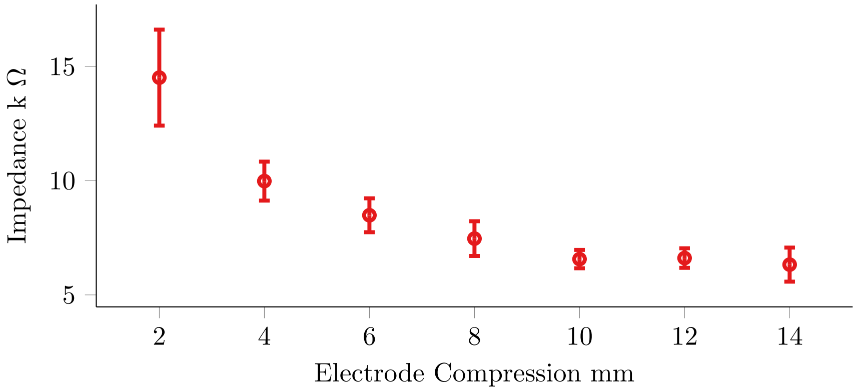

Figure 6.24: *Minimum impedance with abrasion across range of compressions*

6.4 Discussion

6.4.1 Summary of results

Based on the large scale prototype from chapter 5 the miniaturised electrode unit was designed and validated in proof and principle experiments. Initial experiments demonstrated the performance of the unit was similar to that of the larger prototype, reducing the contact impedance to less than 5 kΩ in less than two rotations when using a pyramidal patterned electrode. The simplified plain electrode did not achieve a decrease in contact impedance to the same extent but the performance was sufficient to be carried forward to the helmet design.

The four channel experiments further demonstrated the impedance reduction achieved through the miniaturised electrode unit, while simultaneously offering a more stringent test of the controller. Experiments demonstrated a repeatable 25 kΩ decrease in impedance within one half rotation, and a minimum of 5.4 kΩ within five rotations. The results of the long term recordings were less encouraging, as drifts close to 5 kΩ were measured between iterations of the impedance control loop. This effect was not visible in the electrode with a layer of EleFix paste, and is therefore likely a function of the electrochemical interaction of the electrode-gel-skin interface, and errors in the impedance measurement. Large changes in impedance were observed in all electrodes, with the exception of the traditional EEG electrode with conductive paste.

The contact impedance of 32 electrodes was automatically reduced to approximately 10 kΩ within five minutes on the scalp of a single subject. Below 8 mm travel, the performance of the electrode units was proportional to the compression of the internal spring, which correlates with the results from chapter 5 on the test rig. In locations where the compression was greater than 8 mm, there was no significant difference in minimum impedance.

6.4.2 Assessment of helmet design

For the primary application of imaging acute stroke in an acute setting, the results obtained represent a clear proof of principle, if not establishing a methodology for recording EIT in an ambulance. Specifically, the helmet met the requirements for reducing the contact impedance on 32 electrodes automatically within five minutes. However, the mean minimum impedance was 8.2 kΩ, which did not meet the target 5 kΩ. The modifications required to further reduce the impedance should not be substantial. The design of the electrode has potential for further optimisation, potentially including an abrasive pattern fig. 6.21 or using Ag/AgCl electrodes, provided the resistance to abrasion could be demonstrated.

An electrode localisation accuracy of 0.1 mm was achieved, a potential improvement upon the localisation achieved through photogrammetry, section 1.3.4. Currently, the limiting factor in the precision of the measurements is correct positioning of the electrode unit within the helmet, which is used as a reference during the position calculation, section 6.2.1. The tolerance of the 3D printer is approximately 0.2 mm section 2.3.1, which represents a systematic error in the localisation of the electrode. This could be compensated either through calibration against a known object, accurate measurement of the real reference locations with another high resolution sensor, or improved manufacturing tolerances.

Unfortunately, it was not possible to draw any strong conclusions regarding suitability of the design in the secondary application of long term monitoring as the measurements were contaminated by significant drift artefacts. Between iterations of the abrasion control loop, relatively large increases in impedance $\approx$ 5 kΩ were observed. The impedance control loop successfully reduced the impedance each time, but any benefits in the reduction of electrode drift were masked.

The helmet was demonstrated to cover a range of potential head sizes fig. 6.18, however the reduction in performance of the abrasion below 2 mm travel reduces the range in which the helmet would be effective by at least 4 mm. Therefore, following an optimisation of the design, at least two additional sizes should be produced ± 20 mm circumference, to provide a wider coverage of the population in clinical trials. The methodology developed and implemented to create the helmet in this chapter could readily be redeployed to create new helmets of varying sizes, even based on a different reference model.

There are other issues with the helmet in its current form which must be addressed before attempting clinical measurements. Namely the weight and sterilisation of the electrodes. Considerable effort was taken to minimise the material in all 3D printed components, and incorporate low mass options for the servo motor and linear sensor, however, the overall mass of the helmet was approximately 1.8 kg inclusive of all wiring and connectors, which exceed the target mass of $<$ 1.5 kg. The contribution of the helmet and the electrodes was 604.2 g and 1004 g respectively. The required reduction in the mass could be achieved through optimisation of the geometry and printing of the helmet models. However, any significant reductions would require a significant redesign of the electrode unit, or a reduction of the number of electrodes.

6.4.3 Technical Considerations

Helmet

Whilst care was taken during design to keep the centre of mass aligned with the vertical axis of the head, when the wiring and breakout boards were incorporated the helmet became unbalanced towards the posterior of the head. The volunteer was seated with neck support to compensate for this effect, but future experiments and iterations of the design should begin with a more careful analysis of the weight and centre of mass of the helmet.

Controller

The Arduino Due was chosen for the development of the servo-electrode controller, as it was user friendly with a multitude of precompiled libraries were available, including those for the servo and ADC IC breakouts. However, this simplicity comes at the expense of speed and precision. This is highlighted particularly in the impedance measurement circuit. The output of the DAC of the Due is not rail to rail, and could not be internally routed to ground. Thus even after calibration, the DC offset was 0.8 mV larger than expected. The slow update rate of the waveform generation and measurement limited the impedance measurement to 20 Hz. This limited the speed of the controller, and also had negative consequences on the noise in the measurements by limiting the number of samples used in the amplitude calculation. The Arduino Due does not have any native DSP libraries for the ARM Cortex-M3 CPU on the board and no third party libraries were available at the start of this project. Therefore, the amplitude of the voltages across the electrodes was estimated through the RMS of the completed wave. This approach has poor noise rejection is sensitive to phase errors. This it is the likely cause of the sharp changes observed in the long term recording fig. 6.22.

Recommendations for Future Work

Whilst results are encouraging, it is not possible to draw strong conclusions due to the technical limitations. Therefore the initial focus of future work should be in addressing the problems identified, particularly the impedance measurement circuit accuracy. Implementing the newly released custom FFT libraries for the Arduino Due could form the basis of a more robust measurement of the amplitude. Replacing the Arduino with another compatible controller such as the Teensy 3.1 [201] could be a benefit as which has full DSP capabilities and is compatible with Arduino code. Another solution would be to use a dedicated impedance measurement IC, such as the AD5339 from Analogue Devices, which has been adapted for use in low frequency EIT by Margo, Katrib, Nadi, *et al.* [202]. Implementation of this IC would significantly reduce the footprint of the controller, provide more accurate impedance measurement and reduce the computation necessary on the Arduino itself. If this were to be pursued, delegating the impedance measurement to the AD5339 IC would reduce the size of the controller such that it could fit onto the helmet itself.

If one of the solutions above were to be implemented, the next step would be to repeat the four-channel drift experiments to investigate the causes of the artefactual impedance increases seen in fig. 6.22. From the results of these experiments it would be possible to assess the suitability of the helmet design for long term measurements.

The application time of the electrodes could be reduced further through implementation of multiple impedance measurement circuits with distinct carrier frequencies. A further extension would be to employ multiple separate controllers for subsets of the electrodes. This would reduce the memory and computation requirements for the controller, further aiding the miniaturisation necessary to incorporate the controller onto the helmet.

The electrode alignment was not normal to the surface across the entire scalp as a consequence of variations in the morphology on the reference model and the subject. Variations such as these are inevitable with a rigid body design, and may lead to poor contact and undesirably high pressures. The gel on the electrode goes some way to improving contact with electrode misalignment, but this could be further mitigated with an spherical bearing or ball joint type arrangement at the electrode tip. Finally, an improved helmet design should be created following the publication of the detailed reference models from the Headspace project [190], to better represent the range of head morphologies.

Chapter 7

Discussion and future work

7.1 Summary of studies

The overall objective of the work in this thesis is to advance the imaging of brain pathology and function with EIT, with a particular focus on improvements in experimental methodology. This work has encompassed most aspects of experiments with EIT, with the aim of addressing some of the fundamental limitations of successful imaging; namely modelling errors, instrumentation and electrode contact. Modelling errors in tank studies were addressed in chapter 2 through the design and construction of anatomically realistic head tanks. Two modern EIT systems were modified for the specific application of brain imaging in chapter 3. Low signal to noise and modelling errors are consistent problems in experiments both in tanks and on the human scalp, limiting success of reconstructed images. Therefore, the results of these two studies, coupled with advances in imaging within the UCL group provided an opportune moment to reassess the feasibility of time difference imaging in the head, which formed the basis of chapter 4. The next two chapters concern the design of a helmet bearing 32 self abrading servo electrodes, with the aim to enable impedance measurements to be collected in an ambulance, and to reduce measurements drift during long term recordings. A prototype helmet was constructed which demonstrated the principle successfully, but requires considerable work before it is ready for clinical experiments.

7.2 Head tanks

The experiments in chapter 2 demonstrated a substantial reduction of modelling errors compared to previous studies. This is as much a reflection of the accuracy of the tank as of the improvements in forward modelling by Jehl, Dedner, Betcke, *et al.* [63] and Aristovich, Santos, Packham, *et al.* [61]. The majority of the work in this chapter, which was true throughout the thesis, was in development of the methodology. The workflow to create a new tank from a new geometry or to alter the electrode positions is comparatively trivial. It came as a disappointment to the author that the replication of the workflow using Open-Source software was not feasible within the time frame of the project, as the benefits of bespoke accurate head tanks to the wider EIT community was clear from the literature review. However, the tank models as developed can be replicated by any researcher with access to a 3D printer.

7.3 EIT systems

Both the UCL ScouseTom [125] and the KHU Mk 2.5 EIT system [110] present a considerable improvement to the systems used in previous experiments [30], [68]. The conclusion of the study in chapter 3 was that with the UCL ScouseTom generally performed best, although both systems were suitable for use in future experiments. Possibly the most important benefits of the UCL ScouseTom are that it is highly configurable and consistent across all parameters. This versatility is particularly important, as some fundamental questions in MFEIT of acute stroke regarding the optimal frequency remain unanswered. Hardware which is reliable across a wide range of parameters enables investigation into these fundamental questions. The similarity of the noise measured on the scalp with both systems, despite the improved performance of the UCL ScouseTom in all other tests, suggests the physiological noise is the main contributor.

7.4 Time difference imaging in the head

The images produced in chapter 4 show a clear improvement upon previous work in head tanks, as much a consequence of the advances in imaging by the UCL group as the tank and hardware improvements within this thesis. The results were especially encouraging regarding the comparative lack of boundary voltage processing, previously a subject of particular focus [58], [68]. The simulation study showed, on average, perturbations could be localised within 20 mm and 5 mm throughout the adult head and neonatal head respectively. The increases signal size as a consequence of the higher sensitivity inside the brain, suggests that neonatal epilepsy would represent an ideal initial clinical test for brain EIT.

7.5 Electrode helmet

The helmet designed in chapter 6 broadly met the identified criteria for application of electrodes in an acute setting. The contact impedance was consistently reduced on all 32 electrodes, to within a few kΩ of the target impedance 5 kΩ, and the electrode tips could be located with an accuracy of 0.2 mm. However, it was not possible to determine any benefits to long term time difference recordings from the results due to large linear drifts on the electrodes between abrasions. The results from chapter 5 placed less stringent requirements on the suitable parameters for effective abrasion than was expected. Subsequently the simplification and miniaturisation of the design was the subject of considerable focus in chapter 6. Despite this effort, the final design is still complex, and the weight of the helmet is close to the maximum 2 kg. Therefore at least one more iteration of the design is required before the helmet could be used in clinical measurements.

7.6 Future work

The helmet will require some considerable optimisation before it will be ready for clinical recordings. However, given an improved impedance measurement controller to remove the artefactual drifts between abrasions, an important study could be performed with the helmet in its current state. The comparison of the drift during a long term recording could be made between a subset of the servo electrodes, electrodes applied by an expert technician and electrodes applied by an inexpert user. The results of this study would properly validate the concept of automated control of contact impedance, as well as quantify the extent to which the servo electrodes replicated the “gold standard”.

Design of the helmet was made more challenging as the requirements which it was to meet were inadequately quantified. The contact impedance values, localisation error, number and position of electrodes, were based on the best practice at the time. However, using these best practices, no successful images have been reconstructed of a stroke from scalp recordings. A recent simulation study by Malone, Jehl, Arridge, *et al.* [59] found that electrode mislocations of as little as 0.25 mm on the correct mesh geometry were sufficient to prevent image reconstruction. Therefore the original target of 0.5 to 1 mm, likely represents a significant underestimation of the required precision. The extent to which the geometry of the patient must be represented still needs to be addressed, and patient specific meshes from MRI and CT segmentations did not yield successful reconstructions [93]. It is likely therefore, that electrode localisation of sufficient precision is not achievable with the current helmet and may require a more elaborate solution which may necessitate sensors too heavy to be comfortably incorporated within a helmet

Time difference imaging is much more robust to these modelling errors, and may represent the best chance of success in a clinical setting. As chapter 4 highlighted, the advances in EIT imaging and hardware have improved the feasibility of imaging physiological changes from scalp recordings. The issue of measurement drift described by Fabrizi, Sparkes, Horesh, *et al.* [30] has not been sufficiently addressed within this thesis, and still requires investigation. However, ongoing experiments within the UCL group with EEG headnets, have not demonstrated the large changes over the course of several minutes previously observed. Therefore it may be possible with the methodology now available to successfully reconstruct images of epileptic activity from scalp recordings.

Bibliography

[1] T. Thom, N. Haase, W. Rosamond, *et al.*, *Heart disease and stroke statistics–2006 update: a report from the American Heart Association Statistics Committee and Stroke Statistics Subcommittee.* 6. Feb. 2006, vol. 113, e85–151. DOI: 10.1161/CIRCULATIONAHA.105.171600.

[2] DoH, "Reducing Brain Damage: Faster Access to Better Stroke Care," Deptartment of Health, Tech. Rep. November 2005, 2005, pp. 1–60.

[3] A. Stemer and P. Lyden, "Evolution of the thrombolytic treatment window for acute ischemic stroke.," *Current neurology and neuroscience reports*, vol. 10, no. 1, pp. 29–33, Jan. 2010. DOI: 10.1007/s11910-009-0076-8.

[4] J. a. Sattin, S. E. Olson, L. Liu, R. Raman, and P. D. Lyden, "An expedited code stroke protocol is feasible and safe.," *Stroke*, vol. 37, no. 12, pp. 2935–9, Dec. 2006. DOI: 10.1161/01.STR.0000249057.44420.4b.

[5] M. J. Reeves, S. Arora, J. P. Broderick, *et al.*, "Acute stroke care in the US: results from 4 pilot prototypes of the Paul Coverdell National Acute Stroke Registry.," *Stroke*, vol. 36, no. 6, pp. 1232–40, Jun. 2005. DOI: 10.1161/01.STR.0000165902.18021.5b.

[6] Royal College of Physicians, "Immediate management of ischaemic stroke Immediate management of ischaemic stroke," Royal College of Physicians, Tech. Rep., 2012, pp. 1–17.

[7] a. Romsauerova, a. McEwan, L. Horesh, R. Yerworth, R. H. Bayford, and D. S. Holder, "Multifrequency electrical impedance tomography (EIT) of the adult human head: initial findings in brain tumours, arteriovenous malformations and chronic stroke, development of an analysis method and calibration," *Physiological Measurement*, vol. 27, no. 5, S147, May 2006. DOI: 10.1088/0967-3334/27/5/S13.

[8] H. Thompson, "Traumatic brain injury in older adults: epidemiology, outcomes, and future implications," *Journal of the American Geriatric Society*, vol. 54, no. 10, pp. 1590–1595, 2006.

[9] J. Langlois, "The epidemiology and impact of traumatic brain injury: a brief overview," *The Journal of Head Tauma Rehabilitation*, pp. 11–14, 2006.

[10] G. Teasdale and B. Jennett, "Assessment of coma and impaired consciousness: a practical scale," *The Lancet*, pp. 81–84, 1974.

[11] NICE, "Triage, assessment, investigation and early management of head injury in children young people and adults," *NICE clinical guideline*, no. January, 2014.

[12] W. Matsuda, K. Sugimoto, N. Sato, T. Watanabe, A. Fujimoto, and A. Matsumura, "Delayed onset of posttraumatic acute subdural hematoma after mild head injury with normal computed tomography: a case report and brief review.," *The Journal of trauma*, vol. 65, no. 2, pp. 461–3, Aug. 2008. DOI: 10.1097/01.ta.0000202465.13784.2a.

[13] D. Murphy, P. Burton, R. Coombs, L. Tarassenko, and P. Rolfe, "Impedance imaging in the newborn.," *Clinical physics and physiological measurement*, vol. 8 Suppl A, pp. 131–140, 1987. DOI: 10.1088/0143-0815/8/4A/017.

[14] P. K. Manwaring, K. L. Moodie, A. Hartov, K. H. Manwaring, and R. J. Halter, "Intracranial electrical impedance tomography: A method of continuous monitoring in an animal model of head trauma," *Anesthesia and Analgesia*, vol. 117, no. 4, pp. 866–875, 2013. DOI: 10.1213/ANE.0b013e318290c7b7.

[15] M. Dai, L. Wang, C. Xu, L. Li, G. Gao, and X. Dong, "Real-time imaging of subarachnoid hemorrhage in piglets with electrical impedance tomography.," *Physiological measurement*, vol. 31, no. 9, pp. 1229–39, Sep. 2010. DOI: 10.1088/0967-3334/31/9/012.

[16] M. Dai, B. Li, S. Hu, *et al.*, "In vivo imaging of twist drill drainage for subdural hematoma: a clinical feasibility study on electrical impedance tomography for measuring intracranial bleeding in humans.," *PloS one*, vol. 8, no. 1, e55020, Jan. 2013. DOI: 10.1371/journal.pone.0055020.

[17] A. K. Ngugi, C. Bottomley, I. Kleinschmidt, J. W. Sander, and C. R. Newton, “Estimation of the burden of active and life-time epilepsy: a meta-analytic approach.,” *Epilepsia*, vol. 51, no. 5, pp. 883–90, May 2010. DOI: 10.1111/j.1528-1167.2009.02481.x.

[18] W. H. Organization, *The Global Burden of Disease: 2004 update*. WHO, 2008, vol. 2010, p. 146. DOI: 10.1038/npp.2011.85.

[19] A. T. Berg, S. F. Berkovic, M. J. Brodie, *et al.*, “Revised terminology and concepts for organization of seizures and epilepsies: report of the ILAE Commission on Classification and Terminology, 2005-2009.,” *Epilepsia*, vol. 51, no. 4, pp. 676–85, Apr. 2010. DOI: 10.1111/j.1528-1167.2010.02522.x.

[20] S. D. Shorvon, “The etiologic classification of epilepsy.,” *Epilepsia*, vol. 52, no. 6, pp. 1052–7, Jun. 2011. DOI: 10.1111/j.1528-1167.2011.03041.x.

[21] I. A. W. Kotsopoulos, T. Van Merode, F. G. H. Kessels, M. C. T. F. M. De Krom, and J. A. Knottnerus, “Systematic Review and Meta-analysis of Incidence Studies of Epilepsy and Unprovoked Seizures,” *Epilepsia*, vol. 43, no. 11, pp. 1402–1409, Nov. 2002. DOI: 10.1046/j.1528-1157.2002.t01-1-26901.x.

[22] G. Regesta and P. Tanganelli, “Clinical aspects and biological bases of drug-resistant epilepsies,” *Epilepsy Research*, vol. 34, no. 2-3, pp. 109–122, Apr. 1999. DOI: 10.1016/S0920-1211(98)00106-5.

[23] P. Kwan and M. J. Brodie, “Clinical trials of antiepileptic medications in newly diagnosed patients with epilepsy,” *Neurology*, vol. 60, no. Issue 11, Supplement 4, S2–S12, Jun. 2003. DOI: 10.1212/WNL.60.11_suppl_4.S2.

[24] J. Schramm and H. Clusmann, “The surgery of epilepsy,” *Neurosurgery*, vol. 62, no. 2, pp. 463–481, 2008. DOI: 10.1227/01.NEU.0000297106.65002.1F.

[25] J. S. Duncan, “Selecting patients for epilepsy surgery: synthesis of data.,” *Epilepsy & behavior*, vol. 20, no. 2, pp. 230–2, Feb. 2011. DOI: 10.1016/j.yebeh.2010.06.040.

[26] F. Rosenow and H. Lüders, “Presurgical evaluation of epilepsy,” *Brain*, pp. 1683–1700, 2001.

[27] D. L. Schomer and F. L. Da Silva, *Niedermeyer’s electroencephalography: basic principles, clinical applications, and related fields*. Lippincott Williams & Wilkins, 2012.

[28] A. Rao, A. Gibson, and D. Holder, “EIT images of electrically induced epileptic activity in anaesthetised rabbits,” *Medical and Biological Engineering and Computing*, vol. 35, no. 1, p. 327, 1997.

[29] K. Boone, A. Lewis, and D. Holder, “Imaging of cortical spreading depression by EIT: implications for localization of epileptic foci,” *Physiological measurement*, vol. 189, 1994.

[30] L. Fabrizi, M. Sparkes, L. Horesh, *et al.*, “Factors limiting the application of electrical impedance tomography for identification of regional conductivity changes using scalp electrodes during epileptic seizures in humans.,” *Physiological measurement*, vol. 27, no. 5, S163–74, May 2006. DOI: 10.1088/0967-3334/27/5/S14.

[31] R. M. Pressler, “Neonatal seizures,” in *Epilepsy 2013 from Membranes to Mankind - A Practical Guide to Epilepsy*, F. Rugg-Gunn and J. Smalls, Eds., Epilepsy Society; 14th edition, 2013.

[32] D. M. Murray, G. B. Boylan, I. Ali, C. a. Ryan, B. P. Murphy, and S. Connolly, “Defining the gap between electrographic seizure burden, clinical expression and staff recognition of neonatal seizures.,” *Archives of disease in childhood. Fetal and neonatal edition*, vol. 93, no. 3, F187–91, May 2008. DOI: 10.1136/adc.2005.086314.

[33] A. Gibson, R. Bayford, and D. Holder, “Two-dimensional finite element modelling of the neonatal head,” *Physiological measurement*, vol. 45, 2000.

[34] J. J. Volpe, *Neurology of the Newborn*. Elsevier Health Sciences, 2008.

[35] J. Roth, C. Carlson, O. Devinsky, D. H. Harter, W. S. Macallister, and H. L. Weiner, “Safety of staged epilepsy surgery in children.,” *Neurosurgery*, vol. 74, no. 2, pp. 154–62, Mar. 2014. DOI: 10.1227/NEU.0000000000000231.

[36] T. Tang and R. J. Sadleir, “Quantification of intraventricular hemorrhage with electrical impedance tomography using a spherical model.,” *Physiological measurement*, vol. 32, no. 7, pp. 811–21, Jul. 2011. DOI: 10.1088/0967-3334/32/7/S06.

[37] K. Boone and D. Barber, “Imaging with electricity: report of the european concerted action on impedance tomography,” *Journal of medical*, vol. 21, no. 6, pp. 201–232, 1997.

[38] D. Holder, “Introduction to biomedical electrical impedance tomography,” in *Electrical Impedance Tomography: Methods, History and Applications*, ser. Series in Medical Physics and Biomedical Engineering, vol. null, Taylor & Francis, Dec. 2004.

[39] ——, “Brief introduction to bioimpedance,” in *Electrical Impedance Tomography: Methods, History and Applications*, ser. Series in Medical Physics and Biomedical Engineering, D. Holder, Ed., Taylor & Francis, Dec. 2004, ch. Appendix A.

[40] K. S. Cole and R. H. Cole, "Dispersion and Absorption in Dielectrics I. Alternating Current Characteristics," *The Journal of Chemical Physics*, vol. 9, no. 4, p. 341, 1941. DOI: 10.1063/1.1750906.

[41] K. G. Boone and D. S. Holder, "Current approaches to analogue instrumentation design in electrical impedance tomography.," *Physiological measurement*, vol. 17, no. 4, pp. 229–47, Nov. 1996.

[42] R. H. Bayford, "Bioimpedance tomography (electrical impedance tomography)," *Biomedical Engineering*, vol. 8, no. 1, p. 63, 2006.

[43] R. D. Cook, G. J. Saulnier, D. G. Gisser, J. C. Goble, J. C. Newell, and D. Isaacson, "ACT3: a high-speed, high-precision electrical impedance tomograph.," *IEEE transactions on bio-medical engineering*, vol. 41, no. 8, pp. 713–22, Aug. 1994. DOI: 10.1109/10.310086.

[44] A. S. Ross, G. J. Saulnier, J. C. Newell, and D. Isaacson, "Current source design for electrical impedance tomography.," *Physiological measurement*, vol. 24, no. 2, pp. 509–516, 2003. DOI: 10.1088/0967-3334/24/2/361.

[45] T. I. Oh, E. J. Woo, and D. Holder, "Multi-frequency EIT system with radially symmetric architecture: KHU Mark1.," *Physiological measurement*, vol. 28, no. 7, S183–96, Jul. 2007. DOI: 10.1088/0967-3334/28/7/S14.

[46] T. Oh, O. Gilad, a. Ghosh, M. Schuettler, and D. S. Holder, "A novel method for recording neuronal depolarization with recording at 125-825Hz: implications for imaging fast neural activity in the brain with electrical impedance tomography.," *Medical & biological engineering & computing*, vol. 49, no. 5, pp. 593–604, May 2011. DOI: 10.1007/s11517-011-0761-z.

[47] S. Franco, *Design with operational amplifiers and analog integrated circuits*. McGraw-Hill, 2002, p. 658.

[48] a. McEwan, A. Romsauerova, R. Yerworth, L. Horesh, R. Bayford, and D. Holder, "Design and calibration of a compact multi-frequency EIT system for acute stroke imaging.," *Physiological measurement*, vol. 27, no. 5, S199–210, May 2006. DOI: 10.1088/0967-3334/27/5/S17.

[49] T. I. Oh, H. Wi, D. Y. Kim, P. J. Yoo, and E. J. Woo, "A fully parallel multi-frequency EIT system with flexible electrode configuration: KHU Mark2.," *Physiological measurement*, vol. 32, no. 7, pp. 835–49, Jul. 2011. DOI: 10.1088/0967-3334/32/7/S08.

[50] A. F. Frangi, P. J. Riu, J. Rosell, and M. a. Viergever, "Propagation of measurement noise through backprojection reconstruction in electrical impedance tomography," *IEEE Transactions on Medical Imaging*, vol. 21, no. 6, pp. 566–578, 2002. DOI: 10.1109/TMI.2002.800612.

[51] a. J. Wilson, P. Milnes, a. R. Waterworth, R. H. Smallwood, and B. H. Brown, "Mk3.5: a modular, multi-frequency successor to the Mk3a EIS/EIT system.," *Physiological measurement*, vol. 22, no. 1, pp. 49–54, 2001. DOI: 10.1088/0967-3334/22/1/307.

[52] A. Adler, P. O. Gaggero, and Y. Maimaitijiang, "Adjacent stimulation and measurement patterns considered harmful.," *Physiological measurement*, vol. 32, no. 7, pp. 731–44, Jul. 2011. DOI: 10.1088/0967-3334/32/7/S01.

[53] T. Tidswell, a. Gibson, R. H. Bayford, and D. S. Holder, "Three-dimensional electrical impedance tomography of human brain activity.," *NeuroImage*, vol. 13, no. 2, pp. 283–94, Feb. 2001. DOI: 10.1006/nimg.2000.0698.

[54] L. Fabrizi, a. McEwan, T. Oh, E. J. Woo, and D. S. Holder, "A comparison of two EIT systems suitable for imaging impedance changes in epilepsy.," *Physiological measurement*, vol. 30, no. 6, S103–20, Jun. 2009. DOI: 10.1088/0967-3334/30/6/S07.

[55] S. RUSH and D. DRISCOLL, "Current distribution in the brain from surface electrodes," *Anesthesia & Analgesia*, pp. 717–723, 1968.

[56] C. D. Binnie, A. J. Rowan, and T. Gutter, *A Manual of Electroencephalographic Technology*. CUP Archive, 1982, p. 363.

[57] A. Gibson, "Electrical Impedance Tomography of Human Brain Function," PhD Thesis, UCL, 2000.

[58] L. Fabrizi, a. McEwan, T. Oh, E. J. Woo, and D. S. Holder, "An electrode addressing protocol for imaging brain function with electrical impedance tomography using a 16-channel semi-parallel system.," *Physiological measurement*, vol. 30, no. 6, S85–101, Jun. 2009. DOI: 10.1088/0967-3334/30/6/S06.

[59] E. Malone, M. Jehl, S. Arridge, T. Betcke, and D. Holder, "Stroke type differentiation using spectrally constrained multifrequency EIT: evaluation of feasibility in a realistic head model.," *Physiological measurement*, vol. 35, no. 6, pp. 1051–66, Jun. 2014. DOI: 10.1088/0967-3334/35/6/1051.

[60] E. Somersalo, M. Cheney, and D. Isaacson, "Existence and Uniqueness for Electrode Models for Electric Current Computed Tomography," *SIAM Journal on Applied Mathematics*, vol. 52, no. 4, pp. 1023–1040, 1992. DOI: 10.1137/0152060.

[61] K. Y. Aristovich, G. S. dos Santos, B. C. Packham, and D. S. Holder, “A method for reconstructing tomographic images of evoked neural activity with electrical impedance tomography using intracranial planar arrays.,” *Physiological measurement*, vol. 35, no. 6, pp. 1095–109, Jun. 2014. DOI: 10.1088/0967-3334/35/6/1095.

[62] A. Adler and W. R. B. Lionheart, “Uses and abuses of EIDORS: an extensible software base for EIT.,” *Physiological measurement*, vol. 27, no. 5, S25–42, May 2006. DOI: 10.1088/0967-3334/27/5/S03.

[63] M. Jehl, A. Dedner, T. Betcke, K. Aristovich, R. Klofkorn, and D. Holder, “A Fast Parallel Solver for the Forward Problem in Electrical Impedance Tomography.,” *IEEE transactions on bio-medical engineering*, vol. 9294, no. c, pp. 1–13, Jul. 2014. DOI: 10.1109/TBME.2014.2342280.

[64] A. P. Bagshaw, A. D. Liston, R. H. Bayford, *et al.*, “Electrical impedance tomography of human brain function using reconstruction algorithms based on the finite element method.,” *NeuroImage*, vol. 20, no. 2, pp. 752–64, Oct. 2003. DOI: 10.1016/S1053-8119(03)00301-X.

[65] M. Vauhkonen, D. Vadász, P. a. Karjalainen, E. Somersalo, and J. P. Kaipio, “Tikhonov regularization and prior information in electrical impedance tomography.,” *IEEE transactions on medical imaging*, vol. 17, no. 2, pp. 285–93, Apr. 1998. DOI: 10.1109/42.700740.

[66] P. J. Vauhkonen, M. Vauhkonen, T. Savolainen, and J. P. Kaipio, “Static Three Dimensional Electrical Impedance Tomography,” *Department of Applied Physics, University of Kuopio*, pp. –3, 1992.

[67] V. Kolehmainen, M. Vauhkonen, P. a. Karjalainen, and J. P. Kaipio, “Assessment of errors in static electrical impedance tomography with adjacent and trigonometric current patterns.,” *Physiological measurement*, vol. 18, no. 4, pp. 289–303, 1997. DOI: 10.1088/0967-3334/18/4/003.

[68] B. Packham, H. Koo, A. Romsauerova, *et al.*, “Comparison of frequency difference reconstruction algorithms for the detection of acute stroke using EIT in a realistic head-shaped tank,” *Physiological Measurement*, vol. 33, no. 5, pp. 767–86, May 2012. DOI: 10.1088/0967-3334/33/5/767.

[69] J. K. Seo, J. Lee, S. W. Kim, H. Zribi, and E. J. Woo, “Frequency-difference electrical impedance tomography (fdEIT): algorithm development and feasibility study.,” *Physiological measurement*, vol. 29, no. 8, pp. 929–44, Aug. 2008. DOI: 10.1088/0967-3334/29/8/006.

[70] S. Ahn, T. I. Oh, S. C. Jun, J. K. Seo, and E. J. Woo, “Validation of weighted frequency-difference EIT using a three-dimensional hemisphere model and phantom.,” *Physiological measurement*, vol. 32, no. 10, pp. 1663–80, Oct. 2011. DOI: 10.1088/0967-3334/32/10/013.

[71] E. Malone, G. Sato Dos Santos, D. Holder, and S. Arridge, “Multifrequency electrical impedance tomography using spectral constraints.,” *IEEE transactions on medical imaging*, vol. 33, no. 2, pp. 340–50, Feb. 2014. DOI: 10.1109/TMI.2013.2284966.

[72] P. C. Hansen, “Regularization Tools: A Matlab Package for Analysis and Solution of Discrete Ill-Posed Problems,” *Numerical algorithms*, vol. 6, no. 1, pp. 1–35, 1994.

[73] A. Boyle and A. Adler, “The impact of electrode area, contact impedance and boundary shape on EIT images,” *Physiological Measurement*, vol. 32, no. 7, pp. 745–754, Jul. 2011. DOI: 10.1088/0967-3334/32/7/S02.

[74] a. T. Tidswell, a. Gibson, R. H. Bayford, and D. S. Holder, “Validation of a 3D reconstruction algorithm for EIT of human brain function in a realistic head-shaped tank.,” *Physiological measurement*, vol. 22, no. 1, pp. 177–85, Feb. 2001.

[75] R. Magjarevic, A. Romsauerova, A. Ewan, *et al.*, “A comparison of Multi-Frequency EIT systems intended for acute stroke imaging,” in *World Congress on Medical Physics and Biomedical Engineering 2006*, R. Magjarevic and J. H. Nagel, Eds., ser. IFMBE Proceedings, vol. 14, Springer Berlin Heidelberg, 2007, pp. 3918–3920.

[76] A. Romsauerova, A. Ewan, L. Horesh, *et al.*, “A comparison of Multi-Frequency EIT systems intended for acute stroke imaging,” in *World Congress on Medical Physics and Biomedical Engineering 2006*, R. Magjarevic and J. H. Nagel, Eds., ser. IFMBE Proceedings, vol. 14, Springer Berlin Heidelberg, 2007, pp. 3918–3920.

[77] T. Doru, J. Avery, K. Aristovich, and D. Holder, “A new 3D head shaped tank containing a human skull phantom construction for Electrical Impedance Tomography,” in *14th Int. Conf. Biomedical Applications of EIT*, 2013.

[78] a. T. Tidswell, a. P. Bagshaw, D. S. Holder, *et al.*, “A comparison of headnet electrode arrays for electrical impedance tomography of the human head.,” *Physiological measurement*, vol. 24, no. 2, pp. 527–44, May 2003.

[79] B. Packham, “Imaging fast neural activity in the brain with Electrical Impedance Tomography,” PhD thesis, UCL, 2013, p. 306.

[80] D. S. Holder, “Electrical impedance tomography with cortical or scalp electrodes during global cerebral ischaemia in the anaesthetised rat.,” *Clinical physics and physiological measurement*, vol. 13, no. 1, pp. 87–98, Feb. 1992.

[81] D. S. Holder, a. Rao, and Y. Hanquan, “Imaging of physiologically evoked responses by electrical impedance tomography with cortical electrodes in the anaesthetized rabbit.,” *Physiological measurement*, vol. 17 Suppl 4, A179–86, Nov. 1996.

[82] L. Horesh, “Some Novel Approaches in Modelling and Image Reconstruction for Multi-Frequency Electrical Impedance Tomography of the Human Brain,” PhD thesis, University College London, 2006.

[83] D. Holder and T. Tidswell, “Electrical impedance tomography of brain function,” in *Electrical Impedance Tomography: Methods, History and Applications*, 2004, pp. 127–166.

[84] Z. Elazar, R. Kado, and W. Adey, “Impedance changes during epileptic seizures,” *Epilepsia*, pp. 291–307, 1966.

[85] A. V. Harreveld and J. Schade, “Changes in the electrical conductivity of cerebral cortex during seizure activity,” *Experimental neurology*, vol. 400, pp. 383–400, 1962.

[86] A. Rao, “Electrical Impedance Tomography of brain activity: studies into its accuracy and physiological mechanisms,” PhD Thesis, UCL, 2000.

[87] M. Broberg, K. J. Pope, T. Lewis, T. Olsson, M. Nilsson, and J. O. Willoughby, “Cell swelling precedes seizures induced by inhibition of astrocytic metabolism.,” *Epilepsy research*, vol. 80, no. 2-3, pp. 132–41, Aug. 2008. DOI: 10.1016/j.eplepsyres.2008.03.012.

[88] R. Andrew and B. Macvicar, “Imaging cell volume changes and neuronal excitation in the hippocampal slice,” *Neuroscience*, vol. 62, no. 2, pp. 371–383, Sep. 1994. DOI: 10.1016/0306-4522(94)90372-7.

[89] F. Seoane, K. Lindecrantz, T. Olsson, I. Kjellmer, A. Flisberg, and R. Bågenholm, “Spectroscopy study of the dynamics of the transencephalic electrical impedance in the perinatal brain during hypoxia.,” *Physiological measurement*, vol. 26, no. 5, pp. 849–63, Oct. 2005. DOI: 10.1088/0967-3334/26/5/021.

[90] D. K. Binder and S. R. Haut, “Toward new paradigms of seizure detection.,” *Epilepsy & behavior*, vol. 26, no. 3, pp. 247–52, Mar. 2013. DOI: 10.1016/j.yebeh.2012.10.027.

[91] K. Klivington and R. Galambos, “Resistance shifts accompanying the evoked cortical response in the cat,” *Science*, vol. 157, no. 3785, pp. 211–213, 1967.

[92] A. Vongerichten, “Imaging Physiological and Pathological Activity in the Brain using Electric Impedance Tomography,” PhD thesis, UCL, 2014, p. 208.

[93] M. Vonach, B. Marson, M. Yun, *et al.*, “A method for rapid production of subject specific finite element meshes for electrical impedance tomography of the human head,” *Physiological Measurement*, vol. 33, no. 5, pp. 801–816, May 2012. DOI: 10.1088/0967-3334/33/5/801.

[94] R. J. Yerworth, R. H. Bayford, G. Cusick, M. Conway, and D. S. Holder, “Design and performance of the UCLH mark 1b 64 channel electrical impedance tomography (EIT) system, optimized for imaging brain function.,” *Physiological measurement*, vol. 23, no. 1, pp. 149–158, 2002. DOI: 10.1088/0967-3334/23/1/314.

[95] E. T. McAdams, J. Jossinet, A. Lackermeier, and F. Risacher, “Factors affecting electrode-gel-skin interface impedance in electrical impedance tomography,” *Medical and Biological Engineering and Computing*, vol. 34, no. 6, pp. 397–408, Nov. 1996.

[96] a. Taktak, P. Record, R. Gadd, and P. Rolfe, “Practical factors in neonatal lung imaging using electrical impedance tomography.,” *Medical & biological engineering & computing*, vol. 33, no. 2, pp. 202–5, Mar. 1995.

[97] B. Brown, R. Smallwood, D. Barber, P. Lawford, and D. Hose, *Medical Physics and Biomedical Engineering (Medical Science Series)*. Taylor & Francis, 1998, p. 736.

[98] D. Boone, KG and Holder, “A model of the effect of variations in contact and skin impedance on electrical impedance tomography measurements artefacts,” *Innovation et technologie en biologie et medecine*, vol. 16, pp. 61–70, 1995.

[99] K. G. Boone and D. S. Holder, “Effect of skin impedance on image quality and variability in electrical impedance tomography: a model study.,” *Medical & biological engineering & computing*, vol. 34, no. 5, pp. 351–4, Sep. 1996.

[100] A. McEwan, G. Cusick, and D. S. Holder, “A review of errors in multi-frequency EIT instrumentation,” *Physiological Measurement*, vol. 28, no. 7, S197, 2007.

[101] P. Griss, P. Enoksson, H. K. Tolvanen-Laakso, P. Merilainen, S. Ollmar, and G. Stemme, “Micromachined electrodes for biopotential measurements,” *Journal of Microelectromechanical Systems*, vol. 10, no. 1, pp. 10–16, 2001. DOI: 10.1109/84.911086.

[102] T. Yamamoto and Y. Yamamoto, “Electrical properties of the epidermal stratum corneum,” *Medical and Biological Engineering and Computing*, vol. 14, no. 2, pp. 151–158, 1976.

[103] Y. Yamamoto and T. Yamamoto, “Characteristics of skin admittance for dry electrodes and the measurement of skin moisturisation,” *Medical and Biological Engineering and Computing*, vol. 24, no. 1, pp. 71–77, 1986.

[104] R. Cardu, P. H. W. Leong, C. T. Jin, and A. McEwan, “Electrode contact impedance sensitivity to variations in geometry,” *Physiological Measurement*, vol. 33, no. 5, pp. 817–830, May 2012. DOI: 10.1088/0967-3334/33/5/817.

[105] E. T. McAdams, P. Henry, J. M. Anderson, and J. Jossinet, “Optimal electrolytic chloriding of silver ink electrodes for use in electrical impedance tomography.,” *Clinical physics and physiological measurement*, vol. 13 Suppl A, pp. 19–23, Jan. 1992.

[106] A. Bard and L. Faulkner, *Electrochemical methods: fundamentals and applications*. Wiley New York, 1980.

[107] L.-D. Liao, I.-J. Wang, S. S.-F. Chen, *et al.*, “Design, Fabrication and Experimental Validation of a Novel Dry-Contact Sensor for Measuring Electroencephalography Signals without Skin Preparation,” *Sensors*, vol. 11, no. 6, pp. 5819–5834, May 2011. DOI: 10.3390/s110605819.

[108] C. W. D. Dodds, M. Schuettler, T. Guenther, N. H. Lovell, and G. J. Suaning, “Advancements in electrode design and laser techniques for fabricating micro-electrode arrays as part of a retinal prosthesis,” *Proceedings of the Annual International Conference of the IEEE Engineering in Medicine and Biology Society, EMBS*, pp. 636–639, 2011. DOI: 10.1109/IEMBS.2011.6090141.

[109] N. Dias, J. Carmo, a. F. da Silva, P. Mendes, and J. Correia, “New dry electrodes based on iridium oxide (IrO) for non-invasive biopotential recordings and stimulation,” *Sensors and Actuators A: Physical*, vol. 164, no. 1-2, pp. 28–34, Nov. 2010. DOI: 10.1016/j.sna.2010.09.016.

[110] H. Wi, H. Sohal, A. L. McEwan, E. J. Woo, and T. I. Oh, “Multi-frequency electrical impedance tomography system with automatic self-calibration for long-term monitoring,” *IEEE Transactions on Biomedical Circuits and Systems*, vol. 8, no. 1, pp. 119–128, 2014. DOI: 10.1109/TBCAS.2013.2256785.

[111] J. Schlappa, E. Annese, and H. Griffiths, “Systematic errors in multi-frequency EIT,” *Physiological measurement*, vol. 111, 2000.

[112] N. Goren, J. Avery, and D. S. Holder, “Feasibility study for monitoring stroke and TBI patients,” in *16th International Conference on Biomedical Applications of Electrical Impedance Tomography*, vol. 1, 2015.

[113] D. Holder, “Design and electrical characteristics of an electrode array for electrical impedance tomography of the female breast,” *Innovation et technologie en biologie et medecine*, vol. 16, pp. 143–150, 1995.

[114] Cardiac Science, “The QUINTON ® Quik-Prep ™ Automated Patient Prep System,” Cardiac Science, Tech. Rep., 2008.

[115] P. Griss, H. K. Tolvanen-Laakso, P. Merilainen, and G. Stemme, “Characterization of micromachined spiked biopotential electrodes,” *IEEE Transactions on Biomedical Engineering*, vol. 49, no. 6, pp. 597–604, 2002. DOI: 10.1109/TBME.2002.1001974.

[116] G. Ruffini, S. Dunne, E. Farres, *et al.*, “ENOBIO dry electrophysiology electrode; first human trial plus wireless electrode system.,” *Conference proceedings : ... Annual International Conference of the IEEE Engineering in Medicine and Biology Society. IEEE Engineering in Medicine and Biology Society. Conference*, vol. 2007, pp. 6690–4, Jan. 2007. DOI: 10.1109/IEMBS.2007.4353895.

[117] M. Silva, N. Dias, A. Silva, *et al.*, “NON INVASIVE DRY ELECTRODES FOR EEG,” in *21st Micromechanics and Micro systems Europe Workshop*, vol. 9, 2010, pp. 243–246.

[118] W. Ng, H. Seet, K. Lee, *et al.*, “Micro-spike EEG electrode and the vacuum-casting technology for mass production,” *Journal of Materials Processing Technology*, vol. 209, no. 9, pp. 4434–4438, May 2009. DOI: 10.1016/j.jmatprotec.2008.10.051.

[119] R. Luttge, S. N. Bystrova, and M. Putten, “Microneedle array electrode for human EEG recording,” in *4th European Conference of the International Federation for Medical and Biological Engineering*, Springer, 2009, pp. 1246–1249.

[120] H. Sherwood, A. DONZE, and J. GIEBE, “Mechanical vibration in ambulance transport,” *Journal of Obstetric, Gynecologic, & Neonatal Nursing*, vol. 23, no. 6, pp. 457–463, 1994.

[121] S. Shah, A. Rothberger, M. Caprio, P. Mally, and K. Hendricks-Munoz, “Quantification of impulse experienced by neonates during inter- and intra-hospital transport measured by biophysical accelerometery.,” *Journal of perinatal medicine*, vol. 36, no. 1, pp. 87–92, Jan. 2008. DOI: 10.1515/JPM.2008.009.

[122] Department of Health, *Statistical press notice: Ambulance Quality Indicators – monthly update for England*, 2012.

[123] K. B. Arbogast, S. S. Margulies, M. Patlak, H. Fenner, and D. J. Thomas, “Review of Pediatric Head and Neck Injury : Implications for Helmet Standards,” The Childrens Hospital of Philadelphia, Tech. Rep., 2003.

[124] WebBikeWorld, *Motorcycle Helmet Weight Comparisons*, 2012.

[125] T. Dowrick, C. Blochet, N. Chaulet, and D. Holder, "A Custom EIT System Based On Off-The-Shelf Equipment," in *Proceedings of the 15th International Conference on Biomedical Applications of Electrical Impedance Tomography*, 2014, p. 2014.

[126] T. Doru, B. Packham, H. Koo, and D. S. Holder, "Evaluation of reconstruction algorithms and imaging acute stroke with multi-frequency electrical impedance tomogra- phy in a head-shaped tank with a real human skull," in *World Congress on Medical Physics and Biomedical Engineering*, 2012.

[127] a. D. Liston, R. H. Bayford, and D. S. Holder, "The effect of layers in imaging brain function using electrical impedance tomograghy," *Physiological Measurement*, vol. 25, no. 1, pp. 143–158, Feb. 2004. DOI: 10.1088/0967-3334/25/1/022.

[128] C. Tang, F. You, G. Cheng, *et al.*, "Correlation between structure and resistivity variations of the live human skull.," *IEEE transactions on bio-medical engineering*, vol. 55, no. 9, pp. 2286–92, Sep. 2008. DOI: 10.1109/TBME.2008.923919.

[129] S. K. Law, "Thickness and resistivity variations over the upper surface of the human skull.," *Brain topography*, vol. 6, no. 2, pp. 99–109, Jan. 1993.

[130] M. Akhtari, H. C. Bryant, a. N. Mamelak, *et al.*, "Conductivities of three-layer human skull," *Brain topography*, vol. 13, no. 1, pp. 29–42, Jan. 2000.

[131] M. Akhtari, H. C. Bryant, a. N. Mamelak, *et al.*, "Conductivities of three-layer live human skull.," *Brain topography*, vol. 14, no. 3, pp. 151–67, Jan. 2002.

[132] R. Sadleir and A. Argibay, "Modeling skull electrical properties," *Annals of Biomedical engineering*, vol. 35, no. 10, pp. 1699–1712, 2007.

[133] S. Pant, T. Te, A. Tucker, and R. J. Sadleir, "The conductivity of neonatal piglet skulls.," *Physiological measurement*, vol. 32, no. 8, pp. 1275–83, Aug. 2011. DOI: 10.1088/0967-3334/32/8/017.

[134] J. Kiesler and R. Ricer, "The abnormal fontanel," *American family physician*, pp. 2547–2552, 2003.

[135] P. W. Murray, "Field calculations in the head of a newborn infant and their application to the interpretation of transcephalic impedance measurements.," *Medical & biological engineering & computing*, vol. 19, no. 5, pp. 538–46, Sep. 1981.

[136] L. a. Geddes and L. E. Baker, "The specific resistance of biological material–a compendium of data for the biomedical engineer and physiologist.," *Medical & biological engineering*, vol. 5, no. 3, pp. 271–93, May 1967.

[137] I. Despotovic, P. J. Cherian, M. De Vos, *et al.*, "Relationship of EEG sources of neonatal seizures to acute perinatal brain lesions seen on MRI: a pilot study.," *Human brain mapping*, vol. 34, no. 10, pp. 2402–17, Oct. 2013. DOI: 10.1002/hbm.22076.

[138] M. Odabaee, A. Tokariev, S. Layeghy, *et al.*, "Neonatal EEG at scalp is focal and implies high skull conductivity in realistic neonatal head models.," *NeuroImage*, Apr. 2014. DOI: 10.1016/j.neuroimage.2014.04.007.

[139] N. Roche-Labarbe, A. Aarabi, G. Kongolo, *et al.*, "High-resolution electroencephalography and source localization in neonates.," *Human brain mapping*, vol. 29, no. 2, pp. 167–76, Feb. 2008. DOI: 10.1002/hbm.20376.

[140] T. Tang, S. Oh, and R. J. Sadleir, "A robust current pattern for the detection of intraventricular hemorrhage in neonates using electrical impedance tomography.," *Annals of biomedical engineering*, vol. 38, no. 8, pp. 2733–47, Aug. 2010. DOI: 10.1007/s10439-010-0003-9.A.

[141] M. Sperandio, M. Guermandi, and R. Guerrieri, "A four-shell diffusion phantom of the head for electrical impedance tomography.," *IEEE transactions on bio-medical engineering*, vol. 59, no. 2, pp. 383–9, Feb. 2012. DOI: 10.1109/TBME.2011.2173197.

[142] T. Tang, S. Oh, and R. Sadleir, "A robust current pattern for the detection of intraventricular hemorrhage in neonates using electrical impedance tomography," *Annals of biomedical engineering*, vol. 38, no. 8, pp. 2733–2747, 2010. DOI: 10.1007/s10439-010-0003-9.A.

[143] T. J. Collier, D. B. Kynor, J. Bieszczad, W. E. Audette, E. J. Kobylarz, and S. G. Diamond, "Creation of a human head phantom for testing of electroencephalography equipment and techniques.," *IEEE transactions on bio-medical engineering*, vol. 59, no. 9, pp. 2628–34, Sep. 2012. DOI: 10.1109/TBME.2012.2207434.

[144] J.-B. Li, C. Tang, M. Dai, *et al.*, "A new head phantom with realistic shape and spatially varying skull resistivity distribution.," *IEEE transactions on bio-medical engineering*, vol. 61, no. 2, pp. 254–63, Feb. 2014. DOI: 10.1109/TBME.2013.2288133.

[145] P. Vauhkonen, M. Vauhkonen, T. Savolainen, and J. Kaipio, "Three-dimensional electrical impedance tomography based on the complete electrode model," *IEEE Transactions on Biomedical Engineering*, vol. 46, no. 9, pp. 1150–1160, 1999. DOI: 10.1109/10.784147.

[146] E. Bock, “On the solubility of anhydrous calcium sulphate and of gypsum in concentrated solutions of sodium chloride at 25 C, 30 C, 40 C, and 50 C,” *Canadian Journal of Chemistry*, vol. 39, no. 1061, 1961.

[147] R. Oostenveld and P. Praamstra, “The five percent electrode system for high-resolution EEG and ERP measurements.,” *Clinical neurophysiology*, vol. 112, no. 4, pp. 713–9, Apr. 2001.

[148] F. Rengier, a. Mehndiratta, H. von Tengg-Kobligk, *et al.*, “3D printing based on imaging data: review of medical applications.,” *International journal of computer assisted radiology and surgery*, vol. 5, no. 4, pp. 335–41, Jul. 2010. DOI: 10.1007/s11548-010-0476-x.

[149] D. N. Silva, M. Gerhardt de Oliveira, E. Meurer, M. I. Meurer, J. V. Lopes da Silva, and A. Santa-Bárbara, “Dimensional error in selective laser sintering and 3D-printing of models for craniomaxillary anatomy reconstruction.,” *Journal of cranio-maxillo-facial surgery*, vol. 36, no. 8, pp. 443–9, Dec. 2008. DOI: 10.1016/j.jcms.2008.04.003.

[150] M. Cassetta, M. Giansanti, A. Di Mambro, S. Calasso, and E. Barbato, “Accuracy of two stereolithographic surgical templates: a retrospective study.,” *Clinical implant dentistry and related research*, vol. 15, no. 3, pp. 448–59, Jun. 2013. DOI: 10.1111/j.1708-8208.2011.00369.x.

[151] M. Suzuki, a. Hagiwara, Y. Ogawa, and H. Ono, “Rapid-prototyped temporal bone and inner-ear models replicated by adjusting computed tomography thresholds.,” *The Journal of laryngology and otology*, vol. 121, no. 11, pp. 1025–8, Nov. 2007. DOI: 10.1017/S0022215107006706.

[152] M. Inc., *MakerBot | 3D Printers | 3D Printing*.

[153] *Objet24 Desktop 3D Printer | Stratasys*.

[154] A. Vongerichten, K. Aristovich, G. S. dos Santos, A. W. McEvoy, and D. S. Holder, “Design for a three-dimensional printed laryngoscope blade for the intubation of rats.,” *Lab animal*, vol. 43, no. 4, pp. 140–2, Apr. 2014. DOI: 10.1038/laban.463.

[155] T. Várady, R. R. Martin, and J. Cox, “Reverse engineering of geometric models—an introduction,” *Computer-Aided Design*, vol. 29, no. 4, pp. 255–268, Apr. 1997. DOI: 10.1016/S0010-4485(96)00054-1.

[156] *Portable 3D Scanners for 3D Scanning | Go!SCAN 3D by Creaform*.

[157] N. Makris, L. Angelone, S. Tulloch, *et al.*, “MRI-based anatomical model of the human head for specific absorption rate mapping.,” *Medical & biological engineering & computing*, vol. 46, no. 12, pp. 1239–51, Dec. 2008. DOI: 10.1007/s11517-008-0414-z.

[158] A. Vongerichten, G. Sato dos Santos, J. Avery, M. Walker, and D. Holder, “P889: Electrical impedance tomography (EIT) of epileptic seizures in rat models – a potential new tool for diagnosis of seizures,” *Clinical Neurophysiology*, vol. 125, S282–S283, Jun. 2014. DOI: 10.1016/S1388-2457(14)50924-8.

[159] H. Sohal, H. Wi, A. L. McEwan, E. J. Woo, and T. I. Oh, “Electrical impedance imaging system using FPGAs for flexibility and interoperability.,” *Biomedical engineering online*, vol. 13, p. 126, Jan. 2014. DOI: 10.1186/1475-925X-13-126.

[160] BioSemi, *ActiveTwo User Manual*, Jul. 2007.

[161] *Model 6221 AC and DC Current Source*.

[162] *Arduino - Home*.

[163] *Biosemi EEG ECG EMG BSPM NEURO amplifier electrodes*.

[164] L. Fabrizi, a. McEwan, E. Woo, and D. S. Holder, “Analysis of resting noise characteristics of three EIT systems in order to compare suitability for time difference imaging with scalp electrodes during epileptic seizures.,” *Physiological measurement*, vol. 28, no. 7, S217–36, Jul. 2007. DOI: 10.1088/0967-3334/28/7/S16.

[165] *Swisstom AG*.

[166] I. E. C. Committee, “IEC601-1 Medical Electrical Equipment Part I - General Requirements for Safety,” Tech. Rep.

[167] F. J. Harris, “On the use of windows for harmonic analysis with the discrete Fourier transform,” *Proceedings of the IEEE*, vol. 66, no. 1, pp. 51–83, 1978. DOI: 10.1109/PROC.1978.10837.

[168] L. Horesh, O. Gilad, A. Romsauerova, A. McEwan, S. Arridge, and D. Holder, “Stroke type differentiation by multi - frequency electrical impedance tomography - a feasibility study,” in *3rd European Medical and Biological Engineering Conference*, 2005.

[169] H. Gagnon, M. Cousineau, A. Adler, and A. E. Hartinger, “A resistive mesh phantom for assessing the performance of EIT systems,” *IEEE Transactions on Biomedical Engineering*, vol. 57, no. 9, pp. 2257–2266, 2010. DOI: 10.1109/TBME.2010.2052618.

[170] W. Lionheart, N. Polydorides, and A. Borsic, “The reconstruction problem,” in *Electrical Impedance Tomography: Methods, History and Applications*, D. S. Holder, Ed., Taylor & Francis, 2004, ch. 1, pp. 3–64.

[171] G.tec, *G.tec medical engineering*.

[172] *actiCHamp - Brain Vision LLC - Solutions for neurophysiological Research*.

[173] N. Goren, J. Avery, and D. Holder, “Long term scalp EIT recordings for noise modelling to use in intracranial bleeding monitoring,” *sce.carleton.ca*, p. 2009, 2013.

[174] R. Oostenveld, P. Fries, E. Maris, and J.-M. Schoffelen, “FieldTrip: Open source software for advanced analysis of MEG, EEG, and invasive electrophysiological data.,” *Computational intelligence and neuroscience*, vol. 2011, p. 156 869, Jan. 2011. DOI: 10.1155/2011/156869.

[175] T. Tidswell, “Functional Electrical Impedance Tomography of Adult and Neonatal Brain Function,” Ph.D Thesis, UCL, 2002.

[176] J. Abascal, Arridge, R. Bayford, and D. Holder, “Comparison of methods for optimal choice of the regularization parameter for linear electrical impedance tomography of brain function,” *IEEE transactions on medical imaging*, vol. 1, no. 11, pp. 1–11, 2008.

[177] G. Samandouras, *The Neurosurgeon’s Handbook*. Oxford: Oxford University Press, 2010, p. 930.

[178] W. Adey, R. Kado, and J. Didio, “Impedance measurements in brain tissue of animals using microvolt signals,” *Experimental neurology*, vol. 66, pp. 47–66, 1962.

[179] H. W. Tam and J. G. Webster, “Minimizing electrode motion artifact by skin abrasion.,” *IEEE transactions on bio-medical engineering*, vol. 24, no. 2, pp. 134–9, Mar. 1977. DOI: 10.1109/TBME.1977.326117.

[180] B. Shackel, “Skin-drilling: a method of diminishing galvanic skin-potentials,” *The American Journal of Psychology*, vol. 72, no. 1, pp. 114–121, 1959.

[181] D. P. Burbank and J. G. Webster, “Reducing skin potential motion artefact by skin abrasion.,” *Medical & biological engineering & computing*, vol. 16, no. 1, pp. 31–8, Jan. 1978.

[182] H. S. Gill, S. N. Andrews, S. K. Sakthivel, *et al.*, “Selective removal of stratum corneum by microdermabrasion to increase skin permeability.,” *European journal of pharmaceutical sciences : official journal of the European Federation for Pharmaceutical Sciences*, vol. 38, no. 2, pp. 95–103, Sep. 2009. DOI: 10.1016/j.ejps.2009.06.004.

[183] B. Siciliano and L. Villani, *Robot force control*. Springer, 1999.

[184] W. Thomson, *Theory of Vibration with Applications*. Taylor & Francis, 2004, p. 560.

[185] a. Romsauerova, a. McEwan, L. Horesh, R. Yerworth, R. H. Bayford, and D. S. Holder, “Multifrequency electrical impedance tomography (EIT) of the adult human head: initial findings in brain tumours, arteriovenous malformations and chronic stroke, development of an analysis method and calibration.,” *Physiological measurement*, vol. 27, no. 5, S147–61, May 2006. DOI: 10.1088/0967-3334/27/5/S13.

[186] F. Faulhaber, “Gearbox efficiencies,” MicroMo, Clearwater, Tech. Rep., 2002.

[187] S. Pheasant and C. M. Haslegrave, *Bodyspace: Anthropometry, ergonomics and the design of work*. CRC Press, 2005.

[188] M. E. Gross and B. Bradtmiller, “U.S. Navy Head Anthropometry for Helmet Design,” *Proceedings of the Human Factors and Ergonomics Society Annual Meeting*, vol. 43, no. 20, pp. 1070–1074, Sep. 1999. DOI: 10.1177/154193129904302003.

[189] M. Friess and D. Ph, “A HEAD-AND-FACE ANTHROPOMETRIC SURVEY OF U . S . RESPIRATOR USERS,” Tech. Rep. 11, 2004.

[190] *The Headspace Project | 26th September – 1st December*.

[191] I. ISO, “7250: Basic human body measurements for technological design,” *Geneva: International Standard Organization*, no. 20, 1995.

[192] F. Minow, *EASY CAP | Product List | Modular EEG Recording Caps and Utilities*, en.

[193] *EEG System | Disposable EEG | Stat EEG - HydroDot, Inc.*

[194] S. Donelson and C. Gordon, “1995 Matched Anthropometric Database of US Marine Corps Personnel: Summary Statistics.,” United States Army Soldier Systems Command, Tech. Rep., 1996.

[195] Department of Defense Human Factors Engineering Technical Advisory Group Washington, “Human engineering design data digest,” Tech. Rep., 2000.

[196] R. Motmans and E. Ceriez, “DinBelg 2005: Body dimensions of the Belgian population,” Ergonomie RC, Leuven, Tech. Rep., 2005.

[197] D. Sawicz, “Hobby servo fundamentals,” 2001.

[198] *Home | BEI Sensors - Robust Sensor Encoder Products for Motion Control*.

[199] N. Ream, *Discrete-Time Signal Processing*, 2. 1977, vol. 23, p. 157. DOI: 10.1049/ep.1977.0078.

[200] K. Kappelhoff, *3D Human Model CAD Tool for ergonomical design, validated human measurements*.

[201] *Teensy 3.1: New Features*.

[202] C. Margo, J. Katrib, M. Nadi, and a. Rouane, “A four-electrode low frequency impedance spectroscopy measurement system using the AD5933 measurement chip.,” *Physiological measurement*, vol. 34, no. 4, pp. 391–405, Apr. 2013. DOI: 10.1088/0967-3334/34/4/391.